CRANFIELD UNIVERSITY

Ahad Mehdi

Effect of Swirl Distortion on Gas Turbine Operability

SCHOOL OF ENGINEERING

PhD Thesis

CRANFIELD UNIVERSITY

SCHOOL OF ENGINEERING

POWER AND PROPULSION DEPARTMENT

PhD

Academic Year: 2010-2014

Ahad Mehdi

Effect of Swirl Distortion on Gas Turbine Operability

Supervised by: Dr V.Pachidis, Dr D.G.MacManus

May 2014

This report is submitted in fulfilment of the requirements for the Degree of Doctor of Engineering

To my loving parents Mehdi and Shagufta,
And also to my special best friend (Pindu).

The premise

"The opposite of a correct statement is a false statement. But the opposite of a profound truth may well be another profound truth." *-Niels Bohr(1912-1962)*

Abstract

The aerodynamic integration of an aero-engine intake system with the airframe can pose some notable challenges. This is particularly so for many military aircraft and is likely to become a more pressing issue for both new military systems with highly embedded engines as well as for novel civil aircraft configurations. During the late 1960s with the advent of turbo-fan engines, industry became increasingly aware of issues which arise due to inlet total pressure distortion. Since then, inlet-engine compatibility assessments have become a key aspect of any new development. In addition to total temperature and total pressure distortions, flow angularity and the associated swirl distortion are also known to be of notable concern. The importance of developing a rigorous methodology to understand the effects of swirl distortion on turbo-machinery has also become one of the major concerns of current design programmes.

The goal of this doctoral research was to further the current knowledge on swirl distortion, and its adverse effects on engine performance, focusing on the turbo-machinery components (i.e. fans or compressors). This was achieved by looking into appropriate swirl flow descriptors and by correlating them against the compressor performance parameters (e.g loss in stability pressure ratios). To that end, a number of high-fidelity three-dimensional Computational Fluid Dynamics (CFD) models have been developed using two sets of transonic rotors (i.e. NASA Rotor 67 and 37), and a stator (NASA Stator 67B). For the numerical purpose, a boundary condition methodology for the definition of swirl distortion patterns at the inlet has been developed. Various swirl distortion numerical parametric studies have been performed using the modelled rotor configurations. Two types

of swirl distortion pattern were investigated in the research, i.e. the pure bulk swirl and the tightly-wound vortex.

Numerical simulations suggested that the vortex core location, polarity, size and strength greatly affect the compressor performance. The bulk swirl simulations also showed the dependency on swirl strength and polarity. This emphasized the importance of quantifying these swirl components in the flow distortion descriptors. For this, a methodology have been developed for the inlet-engine compatibility assessment using different types of flow descriptors. A number of correlations have been proposed for the two types of swirl distortion investigated in the study.

Keywords: Bulk swirl, CFD, flow descriptors, Rotor 37, Rotor 67, Stator 67B, swirl distortion, tightly-wound vortex, turbo-machinery

Acknowledgements

This has been the most difficult section for me to write in the document. These last few PhD years of my life have changed me a lot as a person. It has taught me both good and bad facts about life, which i am glad will remain in my memory forever. There are so many people that I would like to express my gratitude who directly or indirectly contributed to this research.

First and foremost I offer my sincerest gratitude to my academic supervisors, Dr V.Pachidis and Dr D.G.MacManus, who gave me an opportunity for the doctoral research within the Cranfield Roll-Royce UTC. I am very grateful for all their moral and technical support throughout, whilst also allowing me the space to work on my own pace. I really admire the devotion and the dedication that you guys give to your students. I would also like to say many thanks to my industrial supervisors, Mr B.Moore , Mr R.Tunstall, and Mr G. Warnes for all the informative discussions in various technical meetings held over the years.

I would like to pay my greatest thanks and well-wishes to some people without whom I wouldn't have survive the stress of a PhD life. I have made some of my best friends over the years in Cranfield. Thanks a lot Serena (always the best), Giovanna, Egoitz, Nick, Claire, Rajib, and Anita. I am very grateful for all your support in my rough times, as you always guided me in the right direction, even withstanding my stubbornness sometimes. All the good or bad times, our trips, ferocious discussions, night outs etc. will always remain in my memory and wouldn't have experienced some of the best times without you all. I would also like to pay my greatest regards to my old best friends, Jatin and Bhabhi (Shefali), who always gave me an outsider view of my life situations. I love you all as a

part of my big family, and hope all the best for your respective futures.

I would also like to thank my PhD research team colleagues and friends Domenico, and Grant. The success of this research is part because of them as well. Thanks for all the productive discussions, the late night outs, and also the late office hours that we all shared trying to motivate each other during the PhD.

I would also like to thank Thierry, Akarsh and Karthik for being there during the first few years of my PhD. The time we all shared is unique and amazing at the same time. I will never forget the famous Thierry bbq nights and trips that we all share. I would also like to thank Alice for positive advices in much needed times.

During this research I have had the opportunity to work with a number of very talented MSc students: Javier, Darshan, Roberto, Taieb and Alejando. They all have contributed great new ideas in to my research, and had great working relationship with all of them.

To conclude, a very special thanks to my parents, my sisters and their families for always being there for me. Thank you especially Abu, Ami, Baji, Naureen and Wajeeh bhai for being there and believing in me. I love all and always feel proud for being a part of this family.

Contents

List of Figures

List of Tables

Nomenclature

General

(ρ, ξ, σ)	Cylindrical unit vectors	$[-]$
(r, θ, z)	Cylindrical coordinates	$[m]$
(x, y, z)	Cartesian coordinates	$[m]$
A	Cross sectional area	$[m^2]$
c_p	Pressure coefficient	$[J/kg^{-1}K^{-1}]$
$CSKE$	Coefficient of secondary kinetic energy	$[-]$
D	Diameter	$[m]$
DC_{60}	Total pressure distortion descriptor	$[-]$
KE	Kinetic energy	$[kgm^{-2}s^{-2}]$
KS_i	Sensitivity elements of flow descriptors	$[-]$
H	Inlet height from the ground	$[m]$
M	Mach number	$[-]$
MFR	Mass flow ratio	$[-]$
$NDMF$	Non-dimensional mass flow	$[-]$
n	Vatistas shape factor	$[-]$
N	Number of rings	$[-]$
P	Total pressure	$[Pa]$
p	Static pressure	$[Pa]$
PAV	Face average total pressure	$[Pa]$
PR	Total pressure ratio	$[-]$
PRS	Area-averaged stability total pressure-ratio	$[-]$
PCP	Circumferential intensity of total pressure	$[Pa]$

PRP	Radial intensity of total pressure	$[Pa]$
ΔPRS	Change in area-averaged stability total pressure-ratio	$[-]$
r	Radius	$[m]$
r_c	Vortex core radius	$[m]$
Re	Reynolds number	$[-]$
s	Total entropy	$[-]$
SC_{60}	Swirl distortion descriptor	$[-]$
SD	Swirl directivity	$[-]$
SFI	Face-averaged swirl directivity	$[-]$
SFC	Specific Fuel Consumption	$[-]$
SI	Swirl intensity	$[-]$
SI_R	Radial swirl intensity	$[-]$
SKE	Secondary kinetic energy	$[kgm^{-2}s^{-2}]$
SM	Surge margin	$[-]$
ΔSM	Change in Surge margin	$[-]$
SP	Swirl pairs	$[-]$
SS	Sector swirl	$[-]$
T	Total temperature	$[K]$
t	Time step	$[s]$
TR	Total temperature ratio	$[-]$
V	Velocity	$[m \cdot s^{-1}]$
W	Mass-flow	$[kg \cdot s^{-1}]$

Greek Symbols

α	Swirl angle	$[deg]$
Δ	Change in	$[-]$
γ	Adiabatic index	$[-]$
Γ	Circulation	$[m^2s^{-1}]$
η	Isentropic efficiency	$[-]$

ν	Kinematic viscosity	$[m^2 s^{-1}]$
ω	Loss coefficient,	$[-]$
ω	Rotational speed,	$[ms^{-1}]$
ρ	Density	$[kgs^{-1}]$
θ	Swirl angle extend	$[deg]$

Subscripts

60	60[deg] sector
∞	Free-stream conditions
abs	Absolute value
amb	Ambient conditions
C	Clean case
$correc$	Corrected
D	Distorted case
i	Ring number
op	Design point
r	Radial component
rel	Relative value
ref	Reference conditions
s	static or swirl distortion
sp	Combined swirl and total pressure distortion
T	Total
v	Span-wise position
x or z	Axial Direction
$+$	Co-rotating
$-$	Counter-rotating

Superscripts

$\bar{-}$ Area-average or mean quantity

$+$ Positive content

$-$ Negative content

$*$ Non-dimensional variable

Acronyms

AGARD	Advisory Group for Aerospace Research and Development
AIP	Aerodynamic Interface Plane
APU	Auxiliary Power Unit
ASME	American Society of Mechanical Engineers
BASH	Bourne-Again Shell
BC	Boundary conditions
BL	Boundary layer
BPF	Boundary passing frequency
CD	Controlled Diffusion
CEL	CFX Expression Language
CFD	Computational Fluid Dynamics
CHPC	Cranfield High Performance Computing facility
DCA	Double-Circular Arc
DP	Design point
FOD	Foreign Object Damage
GE	General Electric
HPC	High Pressure Compressor
IGTI	International Gas Turbine Institute
IGV	Inlet Guide Vane
LES	Large Eddy Simulation
LE	Leading Edge
LPC	Low Pressure Compressor
NASA	National Aeronautics and Space Administration

OGV	Outlet Guide Vane
R67	NASA Rotor 67
RANS	Reynolds-Averaged Navier-Stokes
RPM	Revolutions per Minute
RR	Rolls-Royce
S67B	NASA Stator 67B
SAE	Society of Automotive Engineers
SNECMA	Société Nationale d'Etude et de Construction de Moteurs d'Aviation
SLCC	Streamline Curvature Codes
TE	Trailing Edge
TEACC	Turbine Engine Analysis Compressor Code
TLV	Tip Leakage Vortex
UAV	Unmanned Air Vehicle
UCAV	Unmanned Combat Air Vehicle
URANS	Unsteady Reynolds-Averaged Navier-Stokes
UTC	University Technology Centre
VTOL	Vertical Take-Off and Landing

Chapter 1

Introduction

The aim of this chapter is to introduce the reader to the main topic, and the objectives of the doctoral research programme, that is the inlet flow distortion effects on the gas turbine performance.

1.1 Background

The research was carried out to investigate the adverse effects of inlet flow distortion on the gas turbine's compressor performance. Inlet flow distortion can be defined as some non-uniformity in flow properties at the engine face. This can have a wide range of ramifications on the fan or compressor operability. Thus, the overall performance of a gas turbine unit can be hugely deteriorated, even causing the engine to early surge in some distorted conditions[78]. The current methodology used by industry to account for the non-uniform inlet flows is mainly based on the circumferential, and the radial variations in the total pressure[67,68], and to some extent the total temperature[69] flow fields at the engine inlet. The past few decades have seen a variety of experimental work carried out on the total pressure distortion, testing known amounts of the circumferential, and the radial total pressure deficits[68]. These have been examined to improve the methodologies for the inlet-engine compatibility assessments. It has proven to be a very helpful tool for the industry to equate the losses in the engine stability under such distortion scenarios.

Once the database for the engine stability is generated, it can be then correlated against the flow descriptors. Thus, in this way a full inlet-engine compatibility assessment can be performed for the particular engine installation. This practice has been successful for many years, when the intakes had low levels of swirl due to the modest inlet curvatures[70].

With the advent of high bypass ratio gas turbines, and the stealth aircraft, the aviation industry is going through a drastic change in the shapes, and the requirements of the current, and the future intake configurations. This is applicable for both civil and military aircraft. The desire of the civil engine manufacturers to increase the bypass ratio of turbofans, and to reduce the overall engine length have raised the risk of ingesting high levels of non-uniform angular flows, commonly known as the swirl distortion. Military embedded engines with more convoluted inlet ducts, and also the future conceptual designs, may also encounter the problem of the intense swirling flows been ingested at the engine face. New turboprop designs have similar issues of the swirl distortion being ingested at the inlet[70,86].

Previously swirl distortion was thought to be predominately induced by the pressure distortion, and was not independently considered during the inlet-engine compatibility assessments. It was considered to be a small contributor to flow distortion distribution at the Aerodynamic Interface Plane (AIP)[1], when compared with the total pressure distortion. Firstly, the use of Inlet Guide Vanes (IGVs) could mitigate a large bulk of angular flow before reaching the leading edge of the first blade row. Secondly, the total pressure distortion was the main concern of the day, and was thought to be the most important flow distortion variable[67,68].

However, the Tornado aircraft case[79], and the Tomahawk inlet-engine compatibility study by Ludwig[51] showed the classic examples of a modest pure bulk swirl generated at the inlet, and causing the engine surge problem. During the development phase of the Tornado fighter aircraft (see Figure 1.1), swirl distortion for the first time was identified as a major instability problem. The amounts

[1]AIP is regarded as a flow measurement plane between the engine inlet and compressor, where the flow properties are nearly identical to the flow that is encounter by first blade row.[68]

of counter-rotating swirl flow produced by the S-shaped ducts was the reason of inception of the instability[79]. At subsonic speeds, the port engine caused the engine to surge early and at supersonic speeds, the starboard engine had the aerodynamic instability issues. The problem was tackled by including a straightening vane upstream of the low pressure compressor to reduce the bulk swirl amounts to manageable levels. Thus, the development of the project was setback due to the high levels of swirling flow found during the inlet-engine compatibility assessment.

This brought the gas turbine industry's attention into understanding the effects of swirl distortion phenomena, and also independently from the total pressure distortion. Especially, for the future civil and military configurations, which may have highly convoluted intakes, the swirl-distortion effects on the engine stability may exceed the latter.

When comparing the existing knowledge of the two types of flow distortion, swirl distortion and its physical effects on the gas turbine are still poorly understood. The Society of Automotive Engineers (SAE) S-16 committee recognises the swirl problem, and has collected the related swirl distortion information with a series of flow characterization techniques. They have also proposed some preliminary methodologies to correlate the swirl patterns with losses incurred in the compression system[70]. The methodology for the swirl distortion is based on a previously published SAE report for the total pressure distortion from the 1980s (SAE AIR 1419)[68]. However, these proposed swirl characterisation techniques are in early stages, and still have to be tested, and also validated against the stability losses by means of experiments and/or numerical techniques.

Thus, the motivation of the research study came from the fact that very little knowledge exists of the swirl distortion phenomena. Thus, by even tackling some of the primary concerns, such as researching about the effect of various types of swirling flow on the performance of axial flow compressors, would be very beneficial for the entire industry.

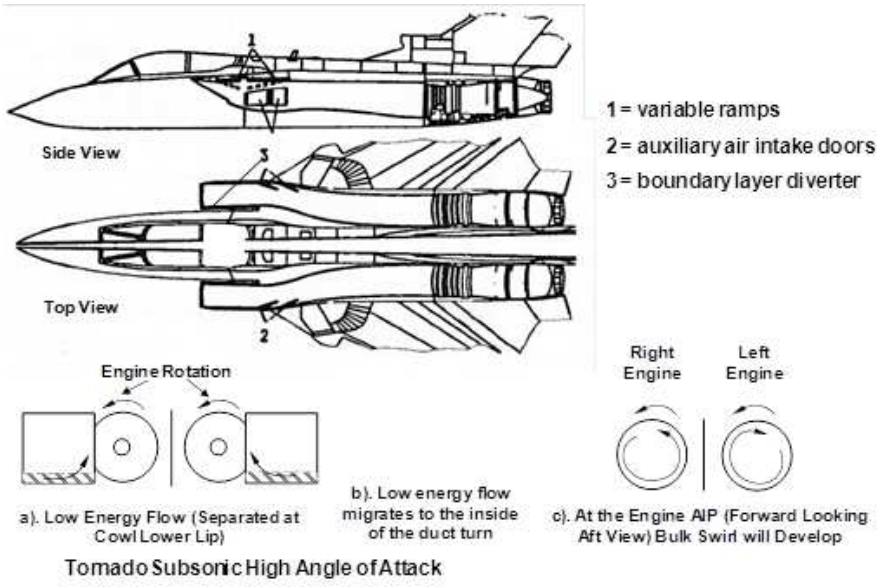

Figure 1.1: Tornado fighter aircraft; Side inlets.[70]

1.2 Research aims and objectives

This three-year doctoral research was undertaken within the Cranfield University Technology Centre (UTC) in Performance Engineering, and was sponsored by Rolls-Royce. The overall work focusses into the external intake aerodynamics, the integration of s-shaped intakes with compression systems, and finally *the effects of swirl distortion* (external or self-induced) on the turbo-machinery.

The main aim of this particular project was to understand the underlying flow physics of how various types of swirl patterns affect the turbo-machinery aerodynamics, and consequently result in the undesirable instabilities, such as the onset of rotating stall and/or surge. Overall the objective was to develop a rigorous numerical, Computational Fluid Dynamics (CFD), tool kit in order to correlate, against via appropriate flow descriptors, the loss in stability pressure ratio due to different types of swirl distortion.

Within this context, the following tasks were recognized:

1. Build an appropriate robust numerical tool kit using the CFD for modern transonic compressor rotor configurations, and validate against the experimental results.

2. Establish a methodology to define the appropriate boundary conditions for two types of swirl distorted patterns, i.e., the pure bulk swirl, and the tightly wound vortices, which can be numerically simulated at the engine face.

3. Establish the appropriate CFD methods, and the procedures to model swirl ingestions, and to analyse their effects on the performance of transonic rotors.

4. Build in-house capability to perform high-fidelity transient CFD simulations up to the onset of rotating stall, when operating under swirl distortion.

5. Carrying out an extensive parametric study to enhance the knowledge on the various flow features of a pure bulk swirl, and the tightly-wound vortex, and their adverse effects when ingested in a compression system.

6. Correlate the outcomes of the above parametric study in terms of the changes in stability limits against the suitable flow descriptors for the inlet-engine operability assessments.

7. Propose the correlation methods for characterizing the swirl distortion in terms of the flow descriptors, and utilizing them to build up a robust methodology for the inlet-engine assessments.

1.3 Project plan

Various aspects of the swirl distortion problem is currently being investigated under the Cranfield UTC, as shown in Figure 1.2. The list of tasks stated in Section 1.2 were developed, and updated over the course of research study. But the overall approach adopted in the correlation work is based on a methodology that has been proposed previously to assess the engine sensitivity[70] to the flow distortion. It is illustrated in Figure 1.3.

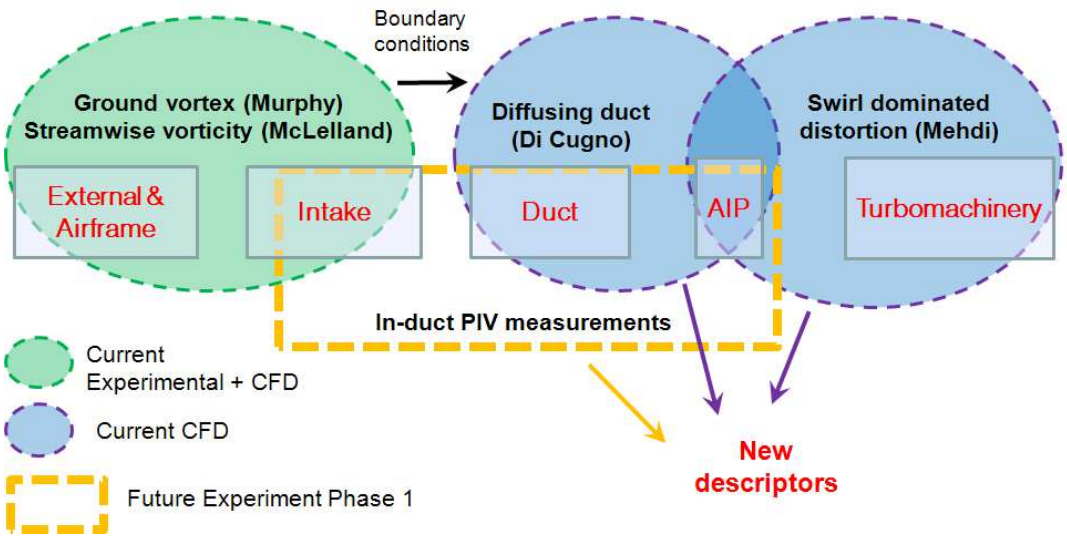

Figure 1.2: Cranfield UTC activities; Inlet flow distortion group.[52]

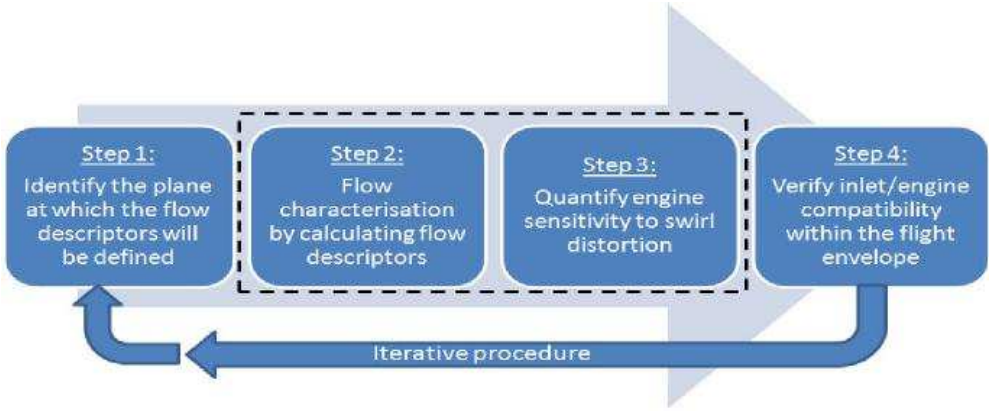

Figure 1.3: Swirl methodology to assess engine stability.[70]

Step 2 and step 3 were the main goals that have been focused, and incorporated in the current work. The tools used to quantify the engine sensitivity to flow distortion consisted of numerical CFD tools to generate the swirl distortion database. It was then combined with the in-house analytical codes created for the post-processing of results, and the correlations against the appropriate flow descriptors. Modern transonic rotors were selected for the study to make it applicable under the current industry requirement. The procedure can be summarised as follows:

- Procedure for characterizing the distorted flow at the engine inlet,

- Numerical methods to calculate the compressor rotor instabilities due to the various types of swirling flows at the inlet,

- Correlation of the rotor performance parameters with the flow descriptors.

This above procedure has been utilized in the study, and divides the PhD technical programme into two main research areas; performing the numerical CFD simulations, and generating appropriate flow descriptor correlations for the swirl distortion. A summary of the roadmap for the research programme is shown in Figure 1.4. The work in the roadmap was performed after carrying out an extensive literature survey, ranging from inlet flow distortion theory to the numerical/analytical methods already applied to quantify their effects on the compression systems. Familiarization with the required tools, and finalizing the overall project objectives took almost the entire first quarter of the research. This was clearly an essential, and a tough task due to the lack of open literature available on the topic. The next step focused on the generation of the rotor geometries, building up the CFD tools, and the methods for defining swirl distortion as boundary conditions. But once the initial methodology was set, work in both research areas has been performed in an iterative manner, and resultantly provided useful feedbacks for the final descriptor correlation analyses.

1.4 Novelty of research

The previous mentioned concerns of the swirling flow, and the lack of knowledge in the area, have resulted in a vacuum, which needs to addressed. Therefore, this study was solely dedicated to enhance the current knowledge of swirl distortion phenomena, and its effects on the performance of compression systems.

This project focused on the turbo-machinery aerodynamics, and the rise of instabilities due to the ingestion of two types of swirl distortion namely, the pure bulk swirl, and the tightly-wound vortex. The motivation came in pursing this goal as it's still one of the least looked upon research areas, especially when a vortex ingestion is concerned. Very little technical knowledge exists on the various

aerodynamic, and the thermodynamic adverse effects that the swirling flow has on the turbo-machinery's uniform flow dynamics. Any new information on the two types of swirl flow investigated, which have a direct impact on the stability of a gas turbine can prove to be very beneficial analysis. Also, recommendations on the development of appropriate flow descriptors, and their swirl distortion correlations against the compression losses may shed some new information in the topic.

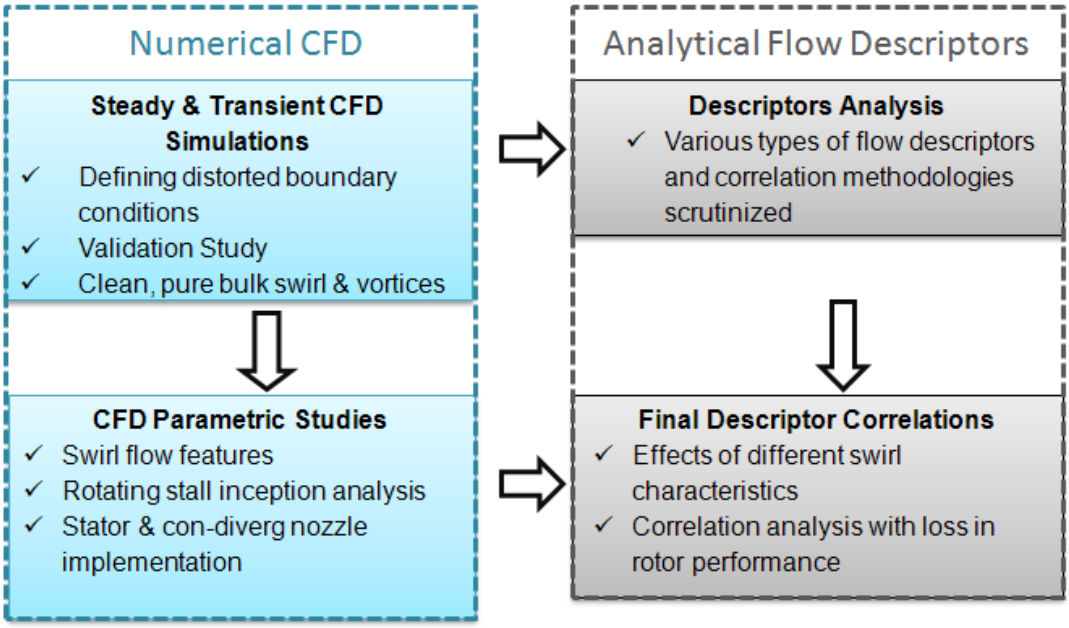

Figure 1.4: Summary of PhD technical roadmap.

1.5 Thesis structure

This document is divided into seven chapters including this *Chapter 1*, which introduces and builds the concept of inlet flow distortion problem. A list of the project objectives, and the project plan is also explained here.

Chapter 2 is the literature review regarding an explanation about various types of swirl distortion, and the previous work done in the field of the inlet/engine stability assessment under these flow conditions. It also summarises the outcomes of the work carried out on the inlet flow distortion in other research establishments.

Chapter 3 first describes the characteristics, and the mesh topologies of the test geometries. Then, the numerical CFD methodology, which had to be implemented to carry out the swirl distortion study is explained in this chapter.

Chapter 4 is dedicated to the validation study of the test geometries. The results were compared against the experimental, and the previous researchers studies on similar rotor configurations.

In *Chapter 5*, the swirl distortion results both in terms of the global performance effects, and also the local aerodynamic changes that the compressor experiences is explained. It has been sub-divided in to two key sections, first explaining the effect of a pure bulk swirl, and then going in to the detailed flow analysis of a vortex ingestion in a compression system.

In *Chapter 6*, the development of appropriate flow descriptors, and their correlations against the performance changes in the compression system is illustrated.

In *Chapter 7*, the key conclusions from the research are drawn out, and some recommendations are made for future work.

Chapter 2

Literature Review

This chapter summarizes the definition, the different types, and the effects of flow distortion on an aero gas turbine engine. Some examples of the previous work done on the topic, numerically and experientially, to understand the adverse effects of flow distortion is also illustrated.

2.1 Types of flow distortion

Inlet flow distortion may be defined as the presence of a spatial or temporal deviation from a uniform, steady, and mainly one dimensional flow at the inlet-engine Aerodynamic Interface Plane (AIP)[68]. The consequence of a non-uniform flow at the inlet can be disastrous to the engine's safe operability. The classical four types of flow distortion that have been defined in the past few decades are:

1. Total pressure distortion
2. Total temperature distortion
3. Static pressure distortion
4. Planar waves

From the above list, the most common kind of flow distortion is the total pressure distortion, and is considered during the development of new gas turbine engines. The total temperature distortion[69] is mainly an issue for the military

applications, and arises from the ingestion of hot gases when the aircraft is operating in the thrust reverser, or during the vertical take-off and landing (VTOL) operations. However, the total pressure distortion may also entail the total temperature distortion for the downstream engine components (e.g. the combustor performance). This is due to the compressor output work that can result in the total temperature flow-field to be non-uniformly distributed around the annulus, thus can be hazardous for the downstream engine components. The static pressure distortion is a very rare scenario of flow distortion, and as presented by Goldsmith and Seddon[30], Williams[84], Harrier aircraft's engine had some issues of the static pressure distortion.

The most investigated flow distortion until now has been the total pressure distortion. The generation mechanisms, and the effects on the engine performance have been extensively investigated by the individual establishments[13,17,28,38,40,48,49,64], and also jointly through the Society of Automotive Engineers (SAE)[67,68]. Many procedures have been developed to take into account the presence of total pressure distortion during the inlet-engine compatibility assessment. This includes carrying out essential experiments in order to carry out the sensitivity analysis for different prescribed distortion patterns[17,21,38,43].

Also, a number of numerical and analytical codes, e.g. parallel compressor method, have been developed to reduce the need for more expensive experimental facilities[10,39]. As a result, a number of flow descriptors have been proposed to predict the engine behaviour reducing the overall cost of a new engine development. The methodology adopted is to use these flow descriptors, which basically captures the key features of the distorted flow. Descriptors are then used to correlate, and consequently predict the engine behaviour under various operating conditions. This technique have been proven to be acceptable for many years[67].

Although, the purpose of this research study is to develop a methodology for a fifth kind of flow distortion facing the industry today, which is the **swirl distortion**. Nonetheless, the total pressure and the swirl distortion can not be decoupled so easily. In fact, in the past swirl was taken into account with the total pressure distortion as a single problem, interacting in a non-linear fashion

as stated by Fidalgo et al.[28], Gorrel et al.[32], Yao et al.[87]. However, with the advent of very high by pass ratio turbofans, and the complex s-shaped intakes, more attention have been given in the last few years to decouple the flow angularity variable with the total pressure distortion. The need for developing and analysing the flow descriptors solely for the swirl distortion is the way forward, especially for the future conceptual aircraft, such as shown in Figure 2.1. Therefore, the focus will be on swirl distortion problem only; it's types and causes, and the ways to quantify using flow descriptors.

Figure 2.1: Conceptional commercial aircraft designs by NASA[77].

2.2 Swirl distortion

High levels of flow angularity can be produced in many modern gas turbine installations. Swirl distortion can be defined by the presence of a circumferential velocity component in the inlet flow at the AIP. This velocity component is an important flow feature as it can alter the blade loading, due to increasing or decreasing the local blade incidence[70].

Nowadays, the need to use much more convoluted inlet shapes, wrapping

inlets for turboprops, and the problem of ground vortex for high bypass ratio civil engines, all had lead the necessity of structuring an appropriate methodology to address the swirl problem. There have been as many as twelve different categories of swirl distortion identified till date[70]. However, these can be grouped into four main types of swirl pattern. These are differentiated by means of a parameter, known as the swirl angle (α) (Eq.2.1), the angle between circumferential (V_θ) and the axial (V_x) velocity components. It is defined with a positive sign when it coincides with the direction of blade rotation (see Figure 2.2), and vice versa if the direction is counter to the blade rotation.

$$\alpha = tan^{-1}(\frac{V_\theta}{V_x}) \tag{2.1}$$

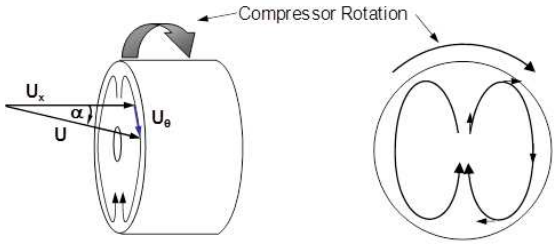

Figure 2.2: Definition of swirl angle[70].

2.2.1 Types of swirl distortion

The four main categories that distinguish the various swirling flow patterns are:

1. **Bulk swirl:** Swirl distortion is defined as the bulk swirl (or the pure bulk swirl) when the entire flow approaching the compressor is rotating in one circumferential direction, consisting of a constant swirl angle. If the flow is rotating in the same direction as the compressor rotation, it is referred as the co-rotating bulk swirl. Conversely, if the rotation is opposite, it is called the counter-rotating bulk swirl. A typical co-rotating bulk swirl at the engine face is illustrated in Figure 2.3. The direction of the bulk swirl pattern plays a vital role on the turbo-machinery response as it determines the local increase or decrease in blade incidence angle[74].

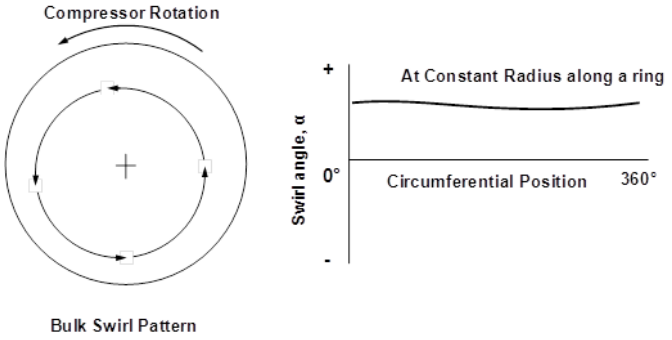

Figure 2.3: Projected velocity vectors of co-rotating bulk swirl[70].

The generation of bulk swirl can be due to a number of mechanisms, external or internal to the inlet. For example, a bulk swirl can be generated externally by a large vortex ingested into a Pitot-style inlet system or internally by the intakes that features inlet plenum chambers. Figure 2.4 show a typical example of an inlet plenum of an aircraft, and the bulk swirl is generated internally before entering the compressor unit. These kinds of inlet systems are found in the Auxiliary Power Units (APUs) or even the S-shaped intakes are also found to be a cause of the pure bulk swirl.

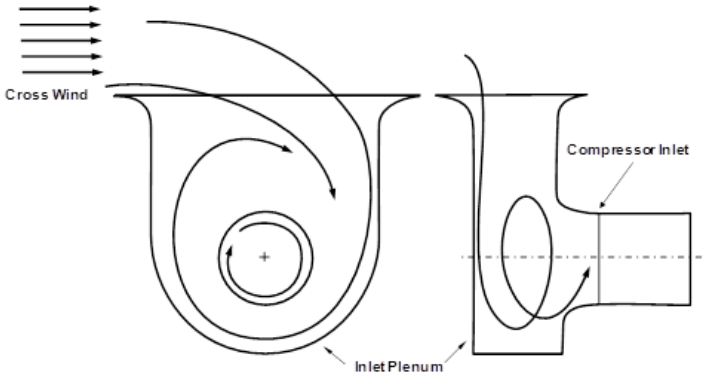

Figure 2.4: Plenum-style inlet in cross wind generating bulk swirl[70].

2. **Paired swirl:** This is most common type of swirl distortion consisting of a sinusoidal wave characteristics. One explanation of the formation mechanism is illustrated in Figure 2.5(a). It is a classic example of a paired swirl formed due to turning of the flow in a S-shaped duct. The velocity gradients caused by the boundary layer formation along the duct end walls is the

source of vorticity. The paired swirl pattern is consequently formed as the flow turns normal to the axial flow direction. Figure 2.5(a) illustrates the formation of a twin paired swirl, consisting of two vortices of equal magnitudes but opposite directions. It will have a zero circumferential swirl angle average around the annulus. In more general cases the flow will interact with the non-uniform boundary layers, thus producing two vortices of opposite direction, and also unequal magnitudes. Figure 2.5(b) show two distributions of the paired swirl, and the swirl angle average in a ring around the annulus.

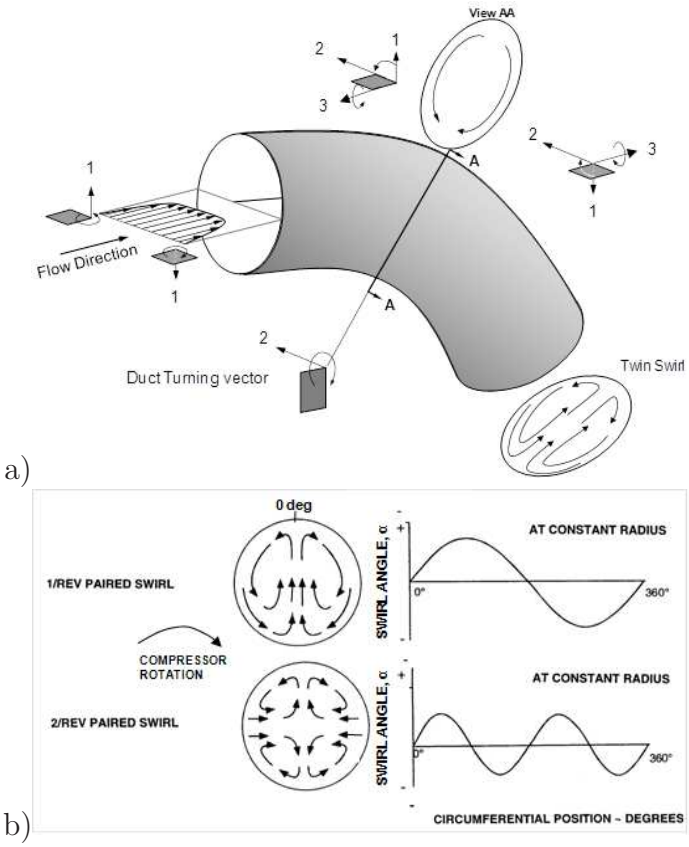

Figure 2.5: a) Mechanism of formation[70]. b) Example of two different paired swirl patterns[70].

Another source of the paired swirl pattern is when the flow is passed through a plenum style intakes that are usually used for the APUs. Sheoran et al.[73, 74] adapted such inlet geometries in order to generate different swirls, and

could alter the strength and the number of paired swirl patterns.

3. **Cross flow swirl:** It is very similar to the paired swirl pattern. It differs from the paired swirl in terms of the radial distribution of swirl angle. There is no change of the flow direction along the radial axis, as can be observed from Figure 2.6. Cross flows are typically formed in short and straight inlet ducts but the entry of the flow is normal to the motion of the aircraft, as shown in a sketch in Figure 2.6. This causes the flow to turn 90 degrees generating the swirl distribution before entering the inlet. This type of swirl is usually experienced in the lift fans configurations.

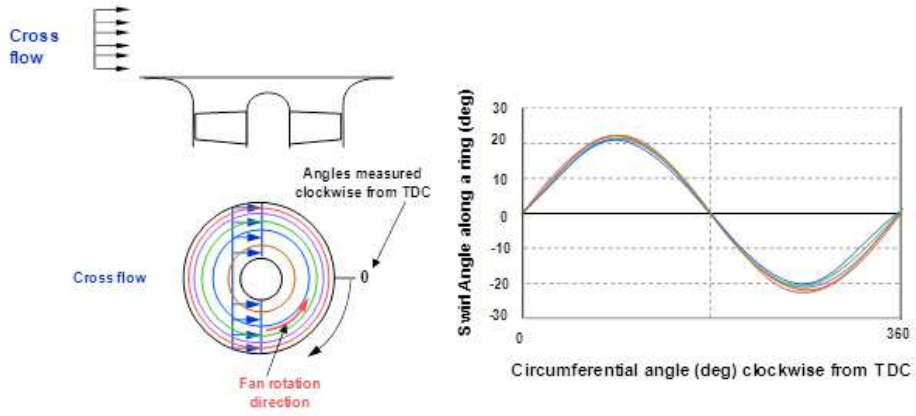

Figure 2.6: Cross-flow swirl distribution in a lift-fan installation[70].

4. **Tightly wound vortices:** These are highly dynamic in location, size, and strength and is one of the key focus of the research. There are many types, and formation mechanisms for the tightly wound vortices. For example, for a ground vortex to form there are usually three key necessary elements: a flow sink, a stagnation point, and a source of vorticity in the surrounding flow field. Figure 2.7(a) show a vortex formation, and the ingestion of ground vortex during the thrust reverser operation, where the flow sink and stagnation point is on the ground, and the cross wind causes the vortex to be ingested at the intake[59,60]. On the other hand, Figure 2.7(b) show an example of how tightly-wound vortices are generated within the S-shaped intake. The bend of the S-shaped configuration causes the adverse pressure

gradients, spilling out the discrete vortices along with a paired swirl pattern upstream of the AIP. Figure 2.8, also illustrates the ingestion of fuselage and wing tip vortices, these are usually generated due to the upstream disturbances in the flow field.

a)

b)

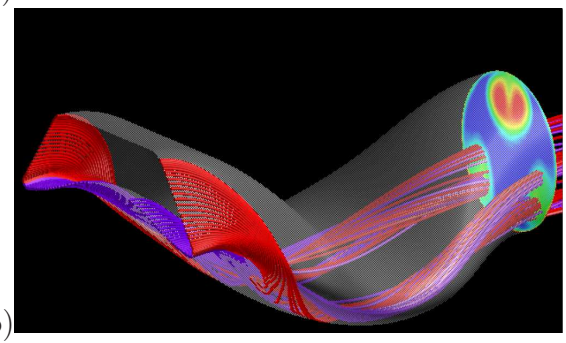

Figure 2.7: Types of tightly-wound vortices: **a)** Ground vortex ingestion[70]. **b)** Discrete vortices within the S-shaped intakes[70].

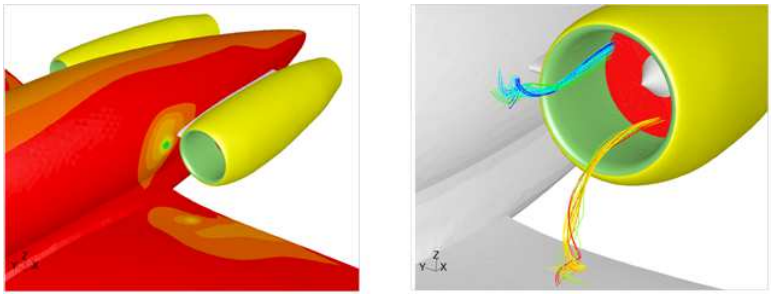

Figure 2.8: Tightly-wound vortices sucked from the fuselage body[70].

The main concern about tightly wound vortices is not only the high level of flow angularity but also in some cases the total pressure distortion inside the

vortex core. Combination of both type of distortions can indeed result in the engine to surge earlier than in normal uniform flow conditions. This is reported by Motycka[56], Motycka and Walter[57], Motycka et al.[58], where the ingestion of a ground vortex caused the engine surge, especially during the thrust reverser operation.

The project primarily focused on the ground vortex as a datum case to generate boundary conditions for the numerical simulations. To achieve this, the experimental work carried out in the past[59,60] proved very useful. Appendix A and Appendix C provide background on the different types of ground vortices, and the method proposed to estimate the vortex characteristics. Just to clarify, the dynamic behaviour, and the structure of a tightly wound vortex are almost identical regardless of the formation mechanisms[4,85]. Therefore, during the research some of the vortex characteristics were modified, as a boundary condition, which helped to analyse the effects of various vortex patterns on the compression system performance.

2.3 Effects on engine operability

Having introduced the types of swirl distortion, the implications of the distorted flows on a gas turbine life cycle can now be addressed. The consequences of the inlet flow distortion range from mechanical issues such as the blade resonance[50], to the engine operability issues, such as limitations on the transient performance. This research study focusses on the engine operability effects due to the ingestion of flow distortion[70]. This includes loss in the surge margin (SM), and is highly dependant on the various distorted characteristics. In fact, as presented in Table 2.1, it can be noticed that the surge margin loss associated only with the distortion effects can be the highest within the list; although actual values of surge margin impact of inlet distortion vary substantially. Apart from the global performance effects, there are other side effects that are linked with the inlet flow distortion. Some of them are illustrated below having been divided in to the total pressure, and the swirl distortion scenarios.

Engine stability analysis	
Item	**Percent compressor surge margin used**
Control-system performance	1.0
Engine scatter	1.0
Deterioration	0.5
Acceleration	4.0
Reynolds number	2.0
Power off-take	2.5
Inlet flow distortion	**4.5**
Remaining surge margin	3.0

Table 2.1: Possible surge margin engine technical specification[84].

2.3.1 Total pressure distortion

- **Effect on global performance:** A lot of work has been performed in the past to predict the compressor performance under the total pressure distortion conditions[13,17,21,28,38–40,48,49,64]. Figure 2.9 show a classic example of the total pressure distortion deteriorating the compressor performance map. It is mainly due to the total pressure deficit at the blade's leading edge (LE) that reduces the compressor work output. The main influence of the total pressure distortion on the compressor characteristic is a reduction in the mass-flow, and the pressure ratio. It also affects the surge line, reducing the safe operating range of the compressor. Therefore, the key physical parameter is the total pressure distribution at the Aerodynamic Interface Plane (AIP), and is taken into account during most of the total pressure distortion research studies[68]. The loss in overall stability pressure ratio has been reported to vary from 6%[21] to 16% (see[27] pg.7), when encountered by a distortion level varying from 90-180[deg] around the annulus. Therefore, inevitably the coupled effect of the flow distortion producing a new compressor map is the re-matching of the entire engine. This can cause a

considerable drop in the compressor efficiency, which may lead to a drop in the engine thrust, and a rise in the specific fuel consumption (SFC). For more details refer[68].

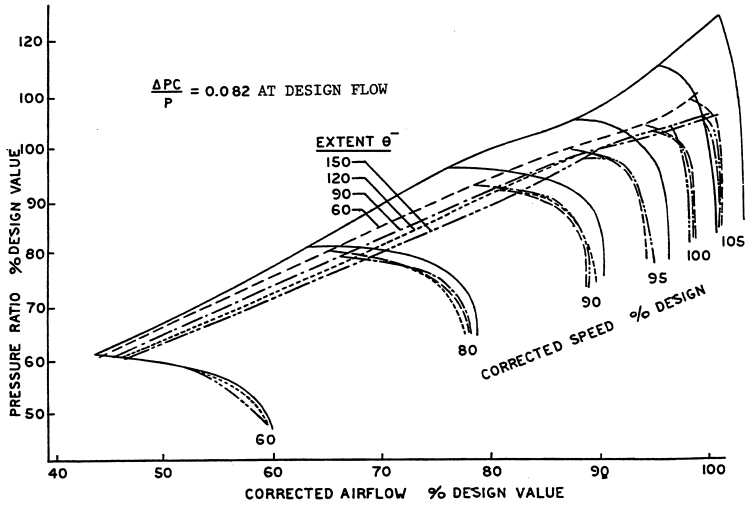

Figure 2.9: Sketch of a compressor map illustrating the typical effect of one-per-rev square wave circumferential total-pressure distortion screens with different extents (θ^-)[68].

- **Flow redistribution:** This is the most common undesirable side effect that accompanies the total pressure distortion. The imposition of the non-uniform total pressure distribution, and a uniform static pressure field far upstream the engine face causes a static pressure defect. Loss in the static pressure field over the distorted region causes cross-flow from the clean (uniform flow) to the former region, thus attenuating the axial velocity deficit before reaching the compressor entrance. This flow redistribution is a consequence of the compressor behaviour in order to handle the distortion pattern. To highlight, the cross-flow can also cause an induced swirl over the engine face which can aggravate the compressor performance. From Figure 2.10, one can observe two high swirl regions located at the interface between the clean, and the spoilt regions. These regions are contra rotating to each other, thus a co-rotating and a counter-rotating swirl is generated, and can affect the turbo-machinery performance. Many researchers including

Fidalgo et al.[28], Gorrel et al.[32], Longley and Greitzer[48] have worked in this area, and have also developed analytical approaches to capture this phenomena.

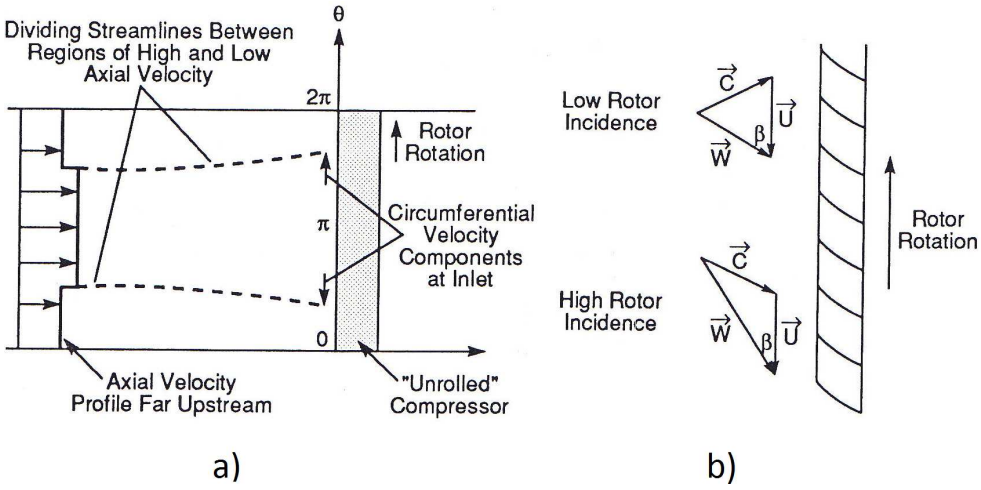

Figure 2.10: a) Induced crossflow due to static pressure[48]. b) Induced swirl upstream of compressor blade row[48].

- **Component coupling:** During distortion ingestions, coupling between the fan and the high pressure compressor (HPC) in a gas turbine can severely alter the stability of each other. Longley and Greitzer[48] stated that the static pressure field upstream of the HPC can stabilize the rotor blade hub of the HPC, reducing slightly the loss in stability pressure ratio. It has been reported by Hercock[40] for some highly coupled spools the reduction factor can be as high as 3. However, the effect of the fan is to worsen the stability of the HPC. The depletion of total pressure distortion along the low pressure compressor (LPC) or fan may also entail the total temperature distortion, which can also severely affect the downstream engine components.

- **Non-uniform blade loadings:** During the ingestion of circumferential total pressure distortion, each blade works at different operating points as it crosses the large deficits of total pressure around the annulus. This temporary throttling caused by the distortion can result in values of total pressure beyond the stability limit of the compressor[38]. However, in most

occasions there are still sufficient blades operating below the stability limit, thus causing the compressor not to surge.

2.3.2 Swirl distortion

For the swirl distortion, reasons behind the arising compressor instabilities, and the effect on the compressor aerodynamics slightly differs from the total pressure distortion. As asserted by Sheoran et al.[73], an inlet swirl distortion can cause engine to surge but the instability mechanism depends largely on the type of swirl pattern, and it varies significantly from the total pressure distortion. Although the effect of the pure bulk swirl is fairly understood, a huge lack of knowledge still exists for the other types of swirl flow.

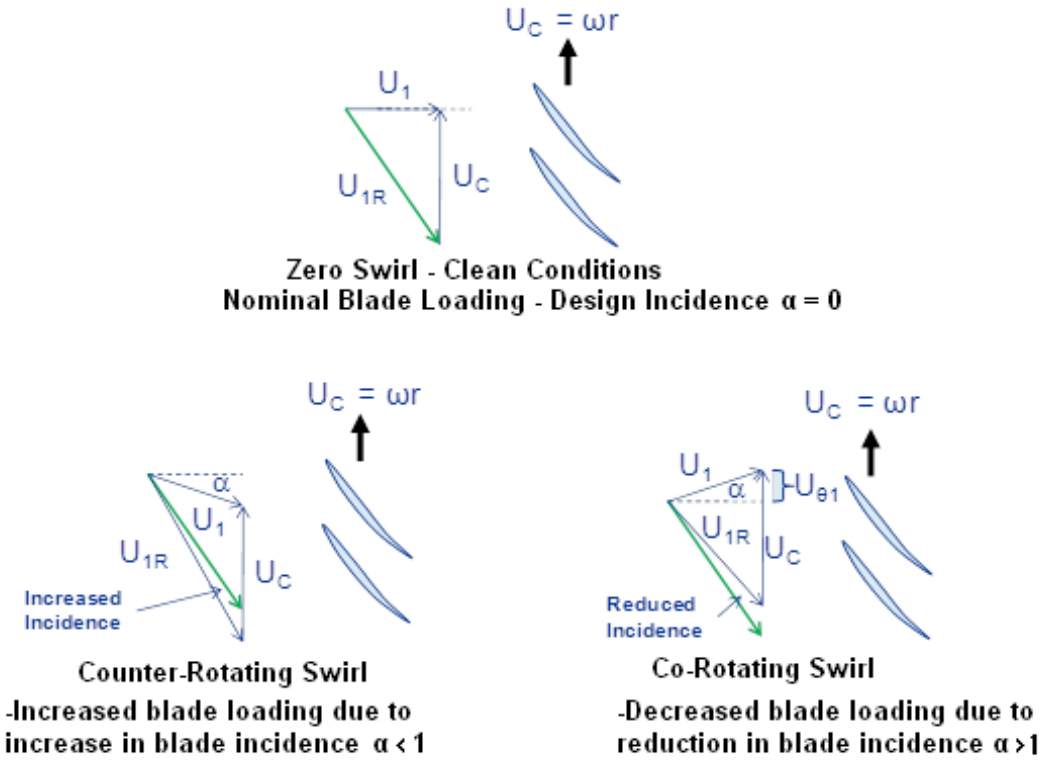

Figure 2.11: Compressor velocity triangles in clean (uniform flow) and swirl conditions.

In general, the total pressure deficit in some types of the swirl distortion (e.g. paired swirl due to the s-shape bend) can contribute to the overall loss

in the compressor performance. However, until now the key parameter is the swirl or tangential velocity component (V_θ) of the flow[70]. The direction, the magnitude, and the location of this swirl velocity component at the engine face have a distinguished effect on the compressor response.

The change in the velocity triangles in Figure 2.11 can be used to explain the effects of swirling flow. As it can be noticed, the swirl angle (α) can increase or decrease the local blade incidence angle, thus altering the blade loading. If the direction of the swirl flow coincides with compressor rotation, it is called a co-rotating swirl, and if the direction is opposite, it is defined as a counter-rotating swirl. A co-rotating swirl decreases flow incidence on the blade, thus the compression system handles this reduction by means of reducing the mass-flow and hence, the height of the inlet velocity triangle. The effect of a falling incidence is dominant, and the pressure ratio diminishes. Therefore, it deteriorates the compressor performance, and shifts the compressor speed-line downwards from the undistorted (clean) flow conditions.

The vice versa is applicable for the counter-rotating swirl, where the engine handles an increase in the incidence by increasing the compressor mass-flow and pressure ratio. An experimental work carried out on the Lazarc-04 engine by Pazur and Fottner[63] with various intensities of the co-rotating bulk swirl showed similar outcomes(see Figure 2.12). As far as more complex swirl patterns (i.e. the paired swirl, and the tightly wound vortex) are concerned, only the changes in swirl angle intensity, and the direction doesn't completely clarify the effect on the compressor performance. It is due to the fact that both the co-rotating, and the counter-rotating swirl components are present at the engine face. Figure 2.13 compares the effect of the pure bulk and the paired swirl patterns using the parallel compressor theory[18,20,70]. However, there is still a huge lack of information into the effect of these complex swirl patterns, and much more novel research can be done in the field.

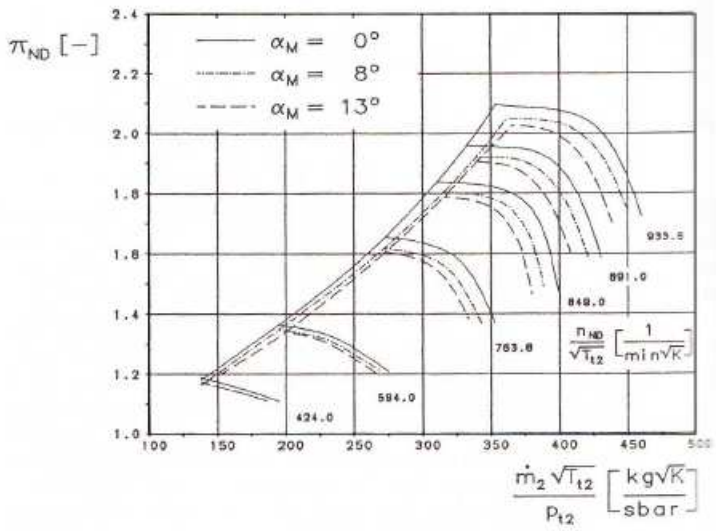

Figure 2.12: Effect of pure co-rotating bulk swirl on the Larzac-04 performance[63].

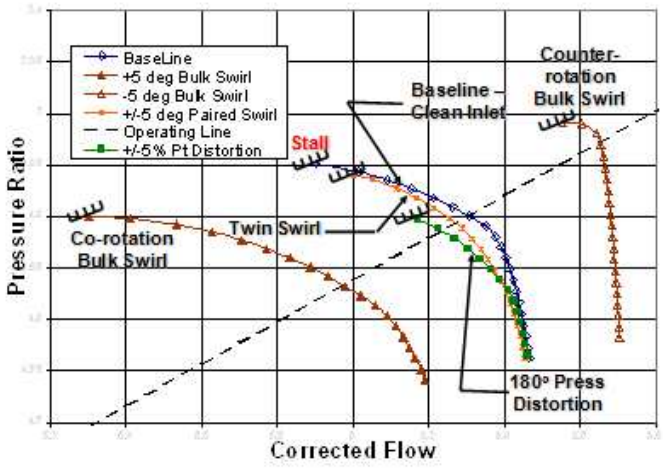

Figure 2.13: Effect of various swirl patterns on the compressor performance[70].

2.4 Flow descriptors

During the development of a new gas turbine, the role of the airframe-engine integration team is to accomplish a propulsion system that satisfies all the stability requirements within the flight envelope. The main goal of the engine stability assessment is to make sure all the distortion scenarios within the flight envelope are tested, and will not cause any major engine stability related issues during its life

cycle[68]. New modern intakes, and the aircraft's extreme manoeuvring requirements are more likely to generate more distortion at the engine inlet. Nowadays, both the experimental, and the numerical or the analytical testing takes place during most of the engine development process; from the initial design phase to final test bed certification, the airframe manufacturers are linked closely with the engine performance group to reach a safe sustainable engine operating range for the worst distortion scenarios. Use of the flow descriptors to analyse the effects of distortion was found to be very beneficial for this purpose[68].

To utilize the flow descriptors within the inlet-engine assessment is an effective way to describe the flow field ahead of the compressor face. It is basically a method to characterize the distorted flow using a measurable parameter that is relevant to the compressor or fan blade's aerodynamic performance. This has been proven very useful for both the airframe, and the engine manufacturers as a medium of passing distortion information between each other. In addition, these parameters can be used to correlate the compressor losses to provide an additional analytical tool during the development of a new gas turbine as recommended by the SAE[67,68,70]. This is achieved by characterizing the engine sensitivity to distortion using the flow descriptors, and correlating the loss in engine stability (surge) margin with the descriptor values quantified in that specific inlet-engine installation. However, the flow descriptor must be generic, and should capture all the key flow-field features of the distorted pattern. It should also be independent of the inlet, and the engine installation[68]. Once enough database is generated for a particular distorted pattern, the rest of the losses with different flow-field patterns can be extrapolated from the same correlation methodology. The results, and the analysis perform within one engine development can also later be utilize by similar engine programs, thus reducing the need of expensive experimental tests. These descriptors are usually calculated at the Aerodynamic Interface Plane (AIP) of the compression system, and from hub to tip on a ring-by-ring basis.

The AIP is selected by considering the specific inlet configuration, the engine installation, and the measurement system installation. It has been extensively

examined by the SAE[70]. In the past, for the total pressure distortion cases in conventional inlets, it has been defined up to 1.5 fan diameters upstream of the compressor fan face[67]. However, for the swirl distortion patterns due to the complex aerodynamics inside the intake systems, the AIP location is still highly debated.

Following is a list of the flow descriptors proposed for the total pressure and the swirl distortion sensitivity analysis by the industry. Correlation methodologies using these flow descriptors are also explained in the next section.

2.4.1 Total pressure distortion

1. **DC60**

   A number of studies to analyse the effect of varying the extent of the distorted pattern on the compressor performance losses have been performed in the past[44]. For this, the annulus can be divided into sectors of different distorted extents. It was noticed that the loss in surge pressure ratio did not change a lot, when using more than a 60-degree spoilt sector, thus defining a critical extent. Equation 2.2 is mostly used to calculate the DC_{60} parameter. It is the difference between the entire face-average pressure (PAV), and the 60[deg] spoilt sector average pressure (PAV_{60}). However, the simplicity of the descriptor brought some limitations, as in some engine installations, the circumferential extent more than 60[deg], and applying also the radial distortion is important, and is not covered by this flow descriptor. It is still one of the most common low-order analytical approaches used mainly in parallel compressor theory for ascertaining the effect of the total pressure distortion.

$$DC_{60} = \frac{(PAV) - (PAV_{60})}{0.5\rho V_x^2} \tag{2.2}$$

2. **S-16 committee proposed descriptors**

   SAE S-16 committee was formed in the 1980's to carry out an essential

in-detail analysis on the effects of the total pressure distortion on a gas turbine performance. Most aero gas turbine related industry represented in this committee, and have jointly published two reports, the Aerospace Information Report (AIR) 1419[68], and the Aerospace Recommended Practice (ARP) 1420[67]. These two reports consists of some essential work done on the total pressure distortion, and also contains the proposed methodologies to tackle the issue using the flow descriptors. They proposed an idea of de-structuring the distortion problem into smaller flow feature fragments. They defined these elements through a number of flow descriptors, and then linked each other through what they refer as the sensitivity analysis of the elements. The output trends are then correlated against the losses in stability pressure ratio (PRS) for each individual engine installation. The main features taken into consideration were as follows[68]:

Extent: The circumferential distortion extent element (θ_i) is the angular region defined in degrees. It is a flow region where the pressure is below the ring average pressure as shown in Figure 2.14, and described in the Equation 2.3.

$$\theta_i = \theta_2 i - \theta_1 i \tag{2.3}$$

Intensity: The circumferential distortion intensity element $(\Delta PC/P)_i$ is a numerical indication of the magnitude of the pressure defect in each measured ring (see Equations 2.4-2.6). Area-weighted integral of the extent element (θ_i^-), and the difference between the face average pressure $(PAV)_i$ and the low pressure region $(PAVLOW)_i$ is performed to determine this parameter. Therefore, the intensity element is equal to the shaded area of Figure 2.14 divided by the product of θ_i^- and $(PAV)_i$.

$$(\frac{\Delta PC}{P})_i = \frac{(PAV)_i - (PAVLOW)_i}{(PAV)_i} \tag{2.4}$$

where:

$$(PAV)_i = \frac{1}{360}\int_0^{360} P(\theta)_i d\theta \tag{2.5}$$

and

$$(PAVLOW)_i = \frac{1}{\bar{i}}\int_0^{\bar{i}} P(\theta)_i d\theta \tag{2.6}$$

Multiple-per-Revolution(MPR): This distortion element enumerates the "effective" number of the low-pressure regions in each i^{th} ring. It is linked with the above descriptors to quantify the overall circumferential distortion intensity for each measurement ring.

There is also an additional **radial intensity** element $(\Delta PR/P)_i$ that describes the difference between the ring-average pressure and the face-average pressure for each i^{th} ring (see Equation 2.7). This helps to take into account the sensitivity of the radial distortion in both the positive, and the negative extents. Positive values reflect a ring-average pressure that is below the face-average pressure.

$$(\frac{\Delta PR}{P})_i = \frac{(PFAV) - (PAVLOW)_i}{(PFAV)} \tag{2.7}$$

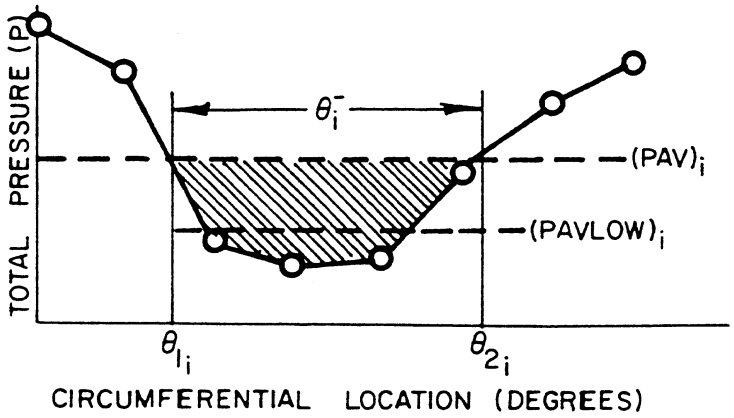

Figure 2.14: Ring circumferential distortion for a one-per-rev pattern[68]

All these descriptors are linked together, and a number of methodologies have been structured[67] for the sole purpose of correlating against the losses in the compressor performance.

2.4.2 Swirl distortion descriptors

1. **SC60:**

   For the case of swirl distortion, there is also a more classical swirl descriptor, the SC60[86]. Although, it has to be mentioned that it is not as well known as the DC60 parameter. The simplistic approach again adopted for the SC60 limits its usability to the pure bulk swirl patterns only. It has been incorporated into the analytical tools, such as the parallel compressor theory. It is defined in the Equation 2.8.

   $$SC_{60} = \frac{\overline{V_\theta}_{60\,\mathrm{deg}} - \overline{V_\theta}}{\overline{V_\theta}} \tag{2.8}$$

2. **S-16 committee proposed descriptors:**

   Flow descriptors for the swirl distortion problem were firstly introduced by Sheoran and Bouldin[71], as also reported by the SAE[70]. It consists of three swirl descriptors and two sub-parameters. The similarity with the total pressure distortion descriptors is noticeable in terms of the formulation approach. It should also be noted that these descriptors have just been proposed, and not yet validated. Work is in progress under the S-16 committee, and the correlations against the stability changes still need to be published.

   The proposed flow descriptors are derived from the swirl angle data at the AIP, which is obtained by the means of numerical or experimental testing. The data is generated using the area-weighted average of the measured swirl angle in a given instrumentation ring. Two sub parameters are necessary to illustrate the swirl angle distribution, which are the extents(θ_i^+, θ_i^-), and the sector swirls (SS_i^+, SS_i^-).

   Extents(θ_i): Figure 2.15 show a typical sinusoidal swirl pattern example in one measurement ring. The circumferential extent of the positive swirl

region is defined by θ_i^+ (Equation 2.9), and the negative swirl region is defined by θ_i^- (Equation 2.10). The subscript i refers to the i^{th} instrument ring.

$$\theta_i^+ = \theta_{2i} - \theta_{1i} \tag{2.9}$$

$$\theta_i^- = \theta_{3i} - \theta_{2i} \tag{2.10}$$

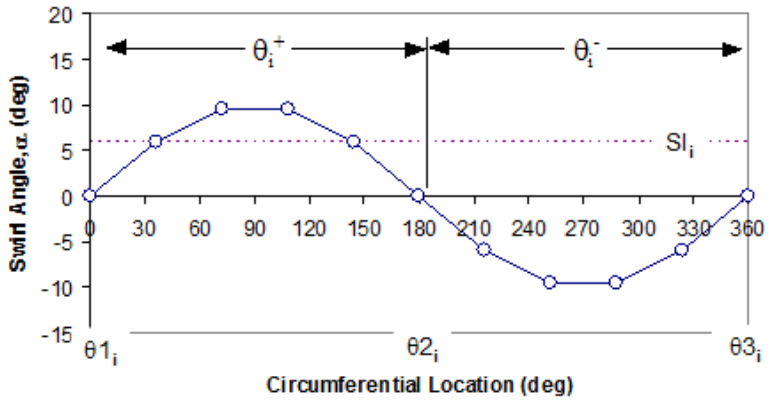

Figure 2.15: Typical one-per-rev symmetric paired swirl pattern.[70]

Sector swirl(SS): Taking the area integral of the swirl angle for each extent curve, sector swirls can be quantified. The value can be either positive (SS_i^+) in the case of the co-rotating swirl, or negative (SS_i^-) in the case of the counter-rotating swirl, as shown in the following expressions.

$$SS_i^+ = \frac{1}{\theta_i^+} \int_{\theta_i^+} \alpha(\theta)_i d\theta \tag{2.11}$$

$$SS_i^- = \frac{1}{\theta_i^-} \int_{\theta_i^-} \alpha(\theta)_i d\theta \tag{2.12}$$

The above distribution of the extents(θ_i^+, θ_i^-), and the sector swirls(SS_i^+, SS_i^-) for each circumferential ring at the AIP is used to define the following swirl descriptors:

Swirl intensity(SI): It is very similar to the circumferential intensity $(\Delta PC/P)_i$ descriptor for the total pressure distortion. SI calculates an average of the absolute circumferential swirl angle (in degrees) for each ring at the AIP, and can be observed from Equation 2.13. It uses the positive

sector swirl, and absolute of the negative sector swirl, thus SI value is always positive. Therefore, it only indicates the strength of the swirl pattern.

$$SI_i = \frac{SS_i^+.\theta_i^+ + |SS_i^-|.\theta_i^-}{360} \tag{2.13}$$

Swirl directivity (SD): Swirl directivity describes the rotational direction of the swirl with reference to the rotation of the compressor in each ring. It can also described as the equivalent bulk swirl rotational direction. The value of the swirl directivity varies between -1 and +1. For example, when considering the sinusoidal swirl distribution as illustrated in Figure 2.15, the value of the swirl directivity will be zero. This indicates that the positive, and the negative swirl components are equally distributed along the circumference of the measurement ring. Only the pure bulk swirl will have a swirl directivity value of +1 for the co-rotating bulk swirl, and -1 for the counter-rotating bulk swirl (see Figure 2.16).

$$SD_i = \frac{SS_i^+.\theta_i^+ + SS_i^-.\theta_i^-}{SS_i^+.\theta_i^+ + |SS_i^-|.\theta_i^-} \tag{2.14}$$

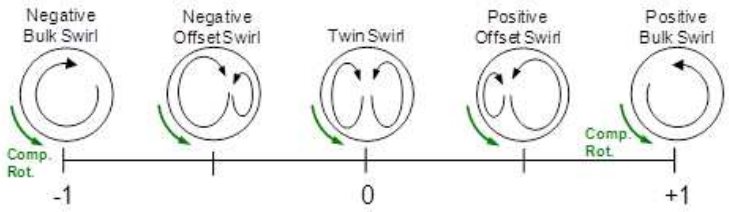

Figure 2.16: Spectrum of swirl directivity.[70]

Swirl pair(SP): This is the last flow descriptor that has been put forward. This effectively indicates the number of alternating swirl pairs present in a given ring (Equation 2.15). For example from Figure 2.17, a range of one-per-rev and bulk-swirl patterns can be described in terms of SP. It is similar to Multiple-per-Rev (MPR) descriptor for total pressure distortion.

$$SP_i = \frac{SS_i^+.\theta_i^+ + |SS_i^-|.\theta_i^-}{2Max.[(SS_i^+.\theta_i^+)or(|SS_i^-|.\theta_i^-)]} \tag{2.15}$$

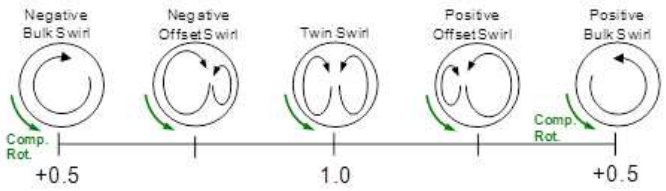

Figure 2.17: Spectrum of swirl pair. [70]

Some examples of the implementation of these flow descriptors using mainly numerical data can be found in the SAE swirl report [70].

More details of the correlation methodologies using these flow descriptors with the stability losses is discussed below.

2.5 Quantification of compressor response

Having defined the flow descriptors for the inlet flow distortion problem, the correlation methods to capture the flow distortion effects on a compressor performance can now be addressed. The main consequences of the inlet flow distortion have been previously explained in the Section 2.3. This includes notably foreign object damage due to the ingestion of debris on a runway, the mechanical excitation of the turbo-machinery parts, and the reduced compressor stability margin. The research focuses on compressor aerodynamic losses, and a reduction in the stability (surge) margin due to the inlet flow distortion.

2.5.1 Methods

SAE AIR 1419[68] have proposed two approaches to calculate the loss in surge margin (ΔSM), and the stability pressure ratio (ΔPRS). These two parameters have been identified as key elements in analysing a compressor response to flow distortion from clean (uniform flow) conditions. The database have to be generated through the numerical or the experimental methods.

The two approaches are:

1. **Constant corrected airflow:** The calculation of the ΔSM, and the ΔPRS of a compressor at constant corrected airflow has advantages for the inlet-engine airflow matching, and the stability assessment. In this case, both the inlet distortion, and the engine response can be defined as a function of constant airflow. Thus, they have the same denominator, resulting in an easier distortion, and the airflow matching during the stability assessment.

2. **Constant corrected rotor speed.** This approach is advantageous to the compressor designers, and the engine manufactures, as most compressor designs and rig tests are carried out at constant rotor speed. Also, the ΔPRS of a particular rotor speed can be calculated without extrapolation, thus saving considerable time for the stability assessments.

   Both definitions are illustrated in Figure 2.18.

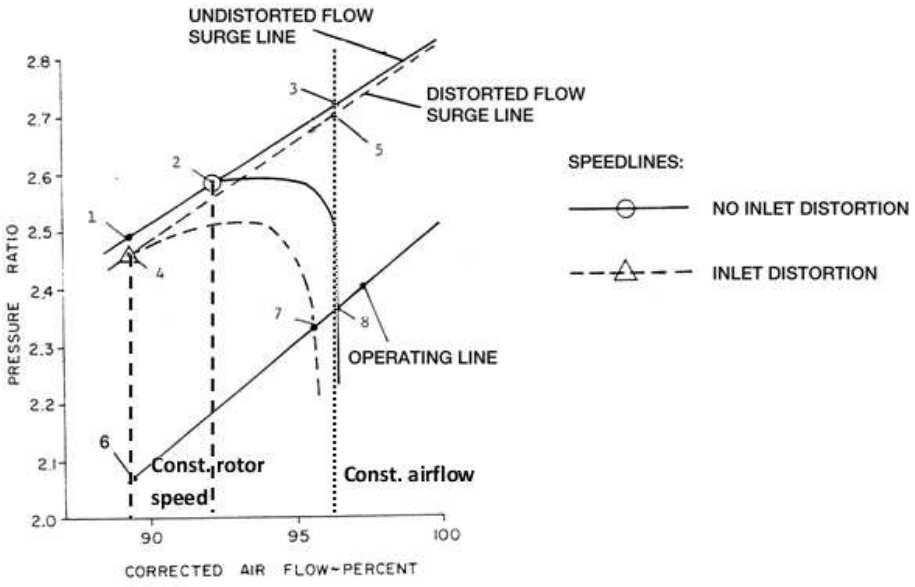

Figure 2.18: Surge margin definition map.[68]

Moreover, a wide variety of the surge margin (SM), and the loss in stability pressure ratio (ΔPRS) expressions exist in the literature[68]. Some of these are specified in the Table 2.2, and the Table 2.3. As long as one is consistent with the definitions during the entire data set, any of the expressions can be used for the above two approaches. In this way, no compatibility issues should be encountered.

Surge margin (SM)

Number	Definition	Condition
1	$\frac{PR_3-PR_8}{PR_8} \cdot 100$	Constant airflow
2	$\frac{PR_3-PR_8}{PR_3} \cdot 100$	
3	$\frac{PR_3-PR_8}{PR_8-1} \cdot 100$	
4	$\frac{(PR/W)_2-(PR/W)_8}{(PR/W)_8} \cdot 100$	Constant rotor speed
5	$\frac{\left(PR/W\sqrt{TR}\right)_2-\left(PR/W\sqrt{TR}\right)_8}{\left(PR/W\sqrt{TR}\right)_2} \cdot 100$	
6	$\frac{(PR/W)_2-(PR/W)_8}{(PR/W)_2} \cdot 100$	
7	$\frac{PR_2-PR_8}{PR_8} \cdot 100$	
8	$\frac{PR_2-PR_8}{PR_2} \cdot 100$	
9	$\frac{PR_2-PR_8}{PR_8-1} \cdot 100$	

Table 2.2: Surge margin definitions.[68]

Loss in surge pressure ratio (ΔPRS)

Number	Definition	Condition
1	$\frac{PR_1-PR_4}{PR_1} \cdot 100$	Constant airflow
2	$\frac{PR_1-PR_4}{PR_6} \cdot 100$	
3	$\frac{PR_1-PR_4}{PR_6-1} \cdot 100$	
4	$\frac{(PR/W)_2-(PR/W)_4}{(PR/W)_8} \cdot 100$	Constant rotor speed
5	$\frac{\left(PR/W\sqrt{TR}\right)_2-\left(PR/W\sqrt{TR}\right)_4}{\left(PR/W\sqrt{TR}\right)_2} \cdot 100$	
6	$\frac{(PR/W)_2-(PR/W)_4}{(PR/W)_2} \cdot 100$	
7	$\frac{PR_2-PR_4}{PR_8} \cdot 100$	
8	$\frac{PR_2-PR_4}{PR_2} \cdot 100$	
9	$\frac{PR_2-PR_4}{PR_8-1} \cdot 100$	

Table 2.3: Loss in surge pressure ratio definitions.[68]

Once, the required database of the ΔPRS, and the ΔSM is calculated from the above approach, it can then be used for the distortion correlation analysis with the help of flow descriptors. Section 2.4.2 introduced a number of flow descriptors

that have been proposed forward for the total-pressure, and the swirl distortion problem. Table 2.4 and 2.5 summarizes list of the proposed flow descriptors for the total-pressure, and the swirl distortion respectively.

SAE proposed descriptors	
Extent	θ
Circumferential intensity	ΔPCP
Radial intensity	ΔPRP
Multiple-per-Revolution	MPR
Other	
Total-pressure 60 deg descriptor	$DC60$

Table 2.4: Total-pressure descriptors.[68]

SAE proposed descriptors	
Extents	θ_i^+, θ_i^-
Sector swirls	SS_i^+, SS_i^-
Circumferential swirl intensity	SI
Swirl directivity	SD
Swirl pair	SP
Other	
Swirl 60 deg descriptor	$SC60$

Table 2.5: Swirl descriptors.[70]

2.5.2 SAE S-16 inlet-engine compatibility assessments

During the 1980's, a report[68] on the total-pressure distortion was published containing all the relevant information of the time, and number of methodologies were proposed for the inlet-engine compatibility assessments. One of the main correlation between the total pressure distortion descriptors, and the loss in stability pressure ratio ΔPRS is illustrated in Figure 2.19.

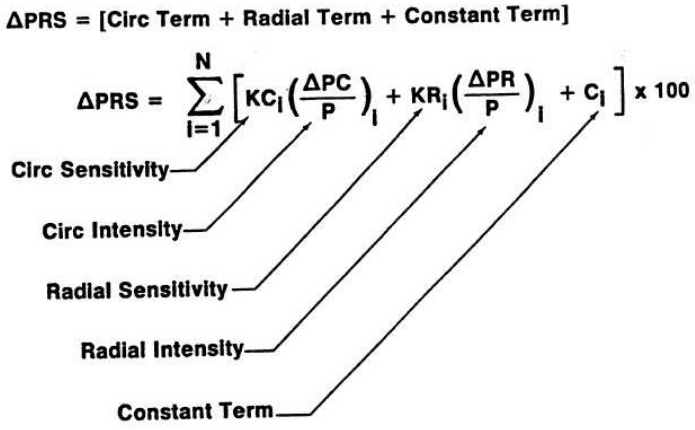

Figure 2.19: Total-pressure distortion correlation for determining ΔPRS.

It can be observed from the above correlation that with each total-pressure descriptor, there is an associated engine sensitivity element (K_i). Certain steps have been proposed to develop these sensitivity elements using the numerical or experimental tests. This helps to perform the engine sensitivity analyses with different distortion screens later. This has to be done for the individual airframe-engine installation, and some additional offset coefficients are also needed to calibrate the final correlations. More information on the other proposed correlation methodologies, and steps needed to generate the engine sensitivities for the total pressure distortion can be found in the report [68].

The recent SAE swirl report [70] also contains some preliminary proposed correlations for the swirl distortion. This is due to the rising need of also taking into account the swirl content during the inlet-engine compatibility assessments. A general agreement has been reached that the total loss in stability pressure ratio is, in fact, due to the combined effect of total pressure and swirl distortion, which can be expressed as:

$$\Delta PRS = \Delta PRS_S + \Delta PRS_P + B \cdot \Delta PRS_{SP} \tag{2.16}$$

The ΔPRS_P, and the ΔPRS_S represent the individual effects of total pressure and swirl distortion respectively. Whereas, the ΔPRS_{SP} quantifies the stability pressure ratio loss due to the interactions between the total pressure and the

swirl distortion, in flow conditions where both are present closely at the engine face. In Equation 2.16, B is a constant that indicates whether the interactions are stabilising or destabilising, and can be positive or negative. An explicit definition of the ΔPRS_{SP} is the subject of future research, as currently the S-16 committee is still focussing on proposing and validating the appropriate ΔPRS_S correlations.

This research also focused on the adverse effects due to the swirl distortion only. For this, two correlations of the ΔPRS_S with the swirl descriptors has been suggested by the SAE, and is shown in Equation 2.17. It is a somewhat optimistic approach to preclude the total pressure distortion effect from the swirl but some types of swirl distortion does acts on its own, e.g. the pure bulk swirl, and the small tightly-wound vortices. These two types of swirl distortion are incorporated in the current work, and doesn't contribute much towards the total-pressure distortion.

As for the case of the total pressure distortion, the swirl distortion's engine sensitivities (K_i) also have to be developed prior to the inlet-engine compatibility assessments. However, there is no structured methodology that has been proposed to calculate these engine sensitivities (K_i), which is linked with the each swirl descriptor. A comprehensive, and a consistent experimental or numerical test database is required to be able to derive the steps necessary to achieve this goal. The correlations for the ΔPRS_S have been proposed on the basis of the total-pressure distortion approach. Thus, it has not yet been validated against the swirl distortion results.

$$\begin{cases} \Delta PRS_S = \sum_{i=1}^{N} \left[KSI_i \left(SI_i \right) + KSD_i \left(SD_i \right) + KSP_i \left(SP_i \right) + C_i \right] \cdot 100 \\ \Delta PRS_S = \sum_{i=1}^{N} \left[KS_i^+ \left(SS_i^+ \right) \frac{\theta_i^+}{\theta_{ref}} + KS_i^- \left(SS_i^- \right) \frac{\theta_i^-}{\theta_{ref}} \right] \cdot 100 \end{cases} \tag{2.17}$$

Therefore, the key motivation of the current doctoral research was to generate the numerical database for the two types of swirl distortion, namely the bulk swirl and the tightly-wound vortices. NASA experimental study carried out by Mitchell[55] is the only experiment found in the open literature about the ingestion of discrete vortices in a gas turbine, and is discussed in the following section.

2.6 Example: Investigation of the effect of wing tip vortices on gas turbine performance

During the 1970's, NASA carried out an experimental test to study the generation, and the evolution of tip vortices from a wing mounted at an upstream location to a combined inlet and turbojet system[55]. A two dimensional inlet designed for Mach 2.2 connected with a J85-GE-13 turbojet engine was placed in the Lewis 10-by 10-Foot supersonic wind tunnel, as illustrated in the schematic Figure 2.20. The J85-GE-13 turbojet engine is 8-stage engine capable of running at a pressure ratio (PR) of 7, at sea level conditions.

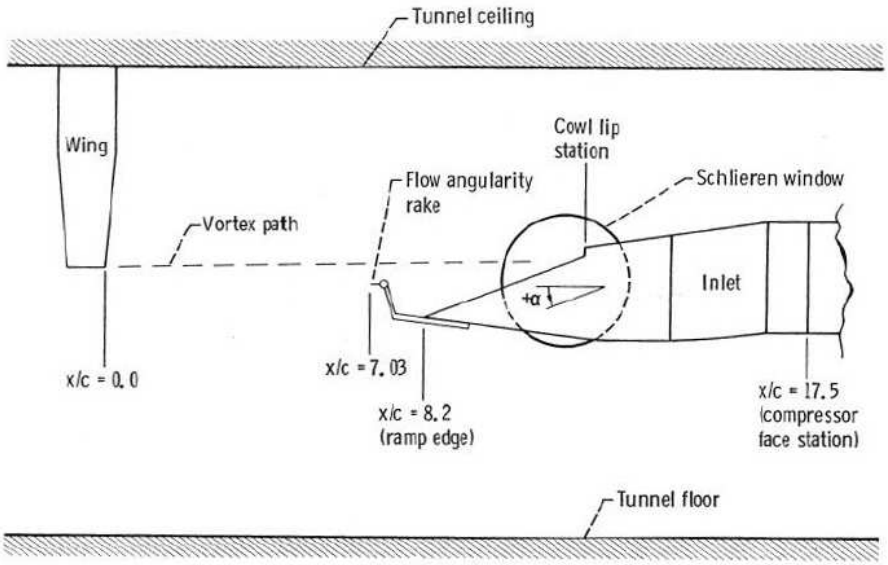

Figure 2.20: Schematic of the direct-connect engine test of tip vortices.[55]

The discrete tip vortices were initiated from a forward mounted wing, and were ingested at various radial locations across the inlet entrance. The wing angles were varied to alter the strength of the generated vortex that rotated either in the same direction (co) or opposite (counter) to the engine rotation. The vortex properties were measured at various axial locations along the test section. A shift in the vortex location, and the size was observed inside the intake before reaching the compressor face (see Figure 2.21).

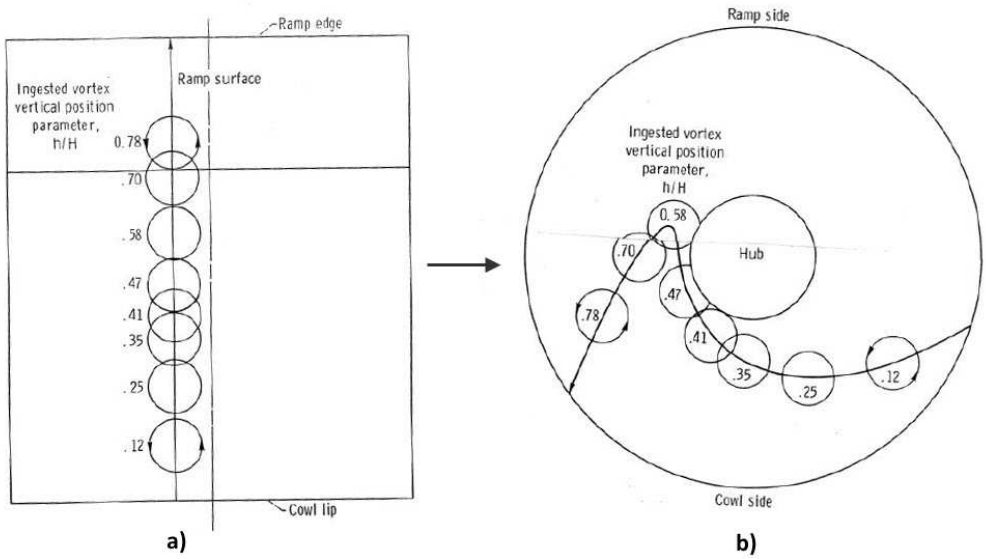

Figure 2.21: **a)** Location of vortex at inlet entrance **b)** Loction of vortex at compressor face.[55]

Following are the relevant key conclusions that can be drawn out from the study:

- Ingestion of a wing tip vortex caused a reduction in the engine surge margin (ΔSM) and the efficiency (η). Vortex location and the direction had an important effect on the turbojet performance, and as a result it varied the stability pressure ratio (PRS) significantly (see Figures 2.21 and 2.22).

- When the counter-rotating vortices were ingested, the highest loss in the stability pressure ratio (ΔPRS) was observed for a vortex ingested near the hub location. For this case, the stability pressure ratio (PRS) was 28% closer to the undistorted operating line.

- On the contrary, for the co-rotating vortices, the maximum loss in stability pressure ratio (ΔPRS) was smaller. The maximum loss for this case was observed when vortex was ingested on the cowl side of the duct that was near the mid-span at the compressor face. It was found to be 11% closer to the nominal undistorted operating line at constant rotor speed.

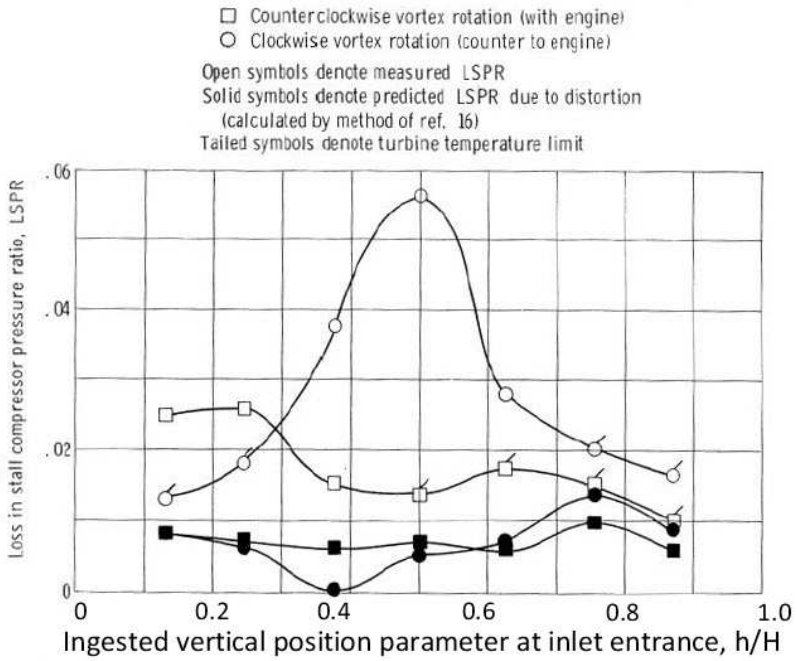

Figure 2.22: Loss in stall pressure ratio (ΔPRS) with respect to vortex radial location and direction.[55]

2.7 Previous CFD studies

Due to an increase in computational resources available in the last decade or so, numerous CFD studies have been carried out to predict the performance of full annulus compressor stages, which were once thought to be infeasible. The availability of the parallel computational power has enable many researchers to model with millions of meshing nodes to be able to accurately capture the required flow to perform not only the RANS (Reynolds Average Navier Stoke) simulations but even the unsteady LES (Large Eddy Simulation)[33,36]. Having said that, not many CFD studies have been carried out with the inlet flow distortion, and even less for the swirl distortion cases. Also, it has to be highlighted that there always have been side studies[18,20] within the available CFD framework to try to reduce the computational requirements, usually by performing low order simulations. Although, some large URANS CFD simulations have been performed in the past with hundreds of millions of nodes[33], but if a large parametric database

is required from these expensive CFD runs, the approach is merely not achievable.

Two related examples of the flow distortion cases found in literature are explained below, and some other related cases can be found in[33,37]:

1. **NASA Stage 67 under total-pressure distortion:** The purpose of this particular work was to improve the Rolls-Royce in-house CFD software "Hydra", when simulating under a typical 120[deg] total-pressure distortion screen[28]. First stage Rotor 67 was combined with the Stator 67, and a choked nozzle was used to adjust the mass-flow across the compression system, as shown in Figure 2.23(a). The URANS simulations were performed with a total mesh size of around 42 million cells. A cluster of 120 CPUs, and running time of about two months were required for the 25 rotor revolutions to reach a converged solution. The key flow field analysis stressed upon the mass-flow redistribution, along with an induced swirl ahead of the rotor's leading edge. The large pressure deficit inside the distorted sector causes the static properties from clean sectors to adjust the former, which is suggested to be the reason of this inherent swirl as shown in Figure 2.23(b). The effect on the stage performance from clean (uniform flow) conditions was also scrutinized, an increase in the overall stage losses associated with the flow distortion were observed.

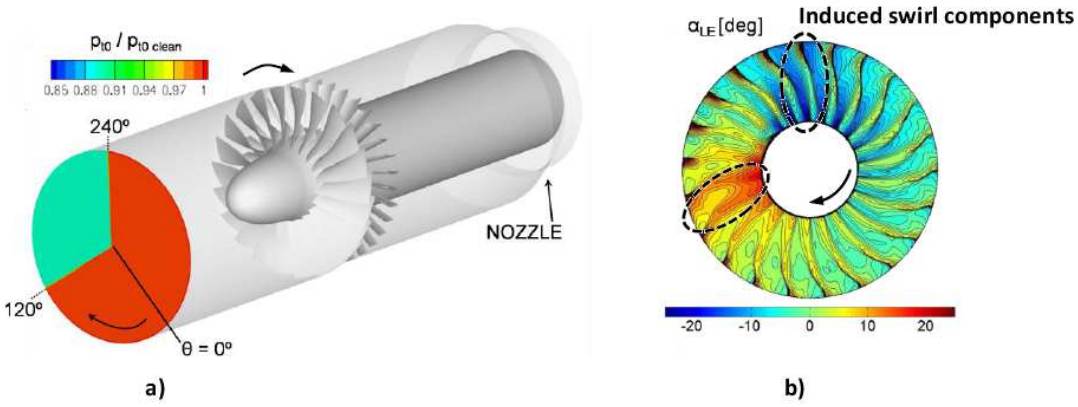

Figure 2.23: First Stage 67 total-pressure distortion: **a)** Numerical setup. **b)**Swirl angle distribution at rotor LE plane.[28]

2. **Honeywell ASE120 LPC under pure bulk and paired swirl distortion:** This study was carried out by Sheoran et al.[72], aiming to understand the effects of some types of swirl patterns on the compressor performance. Previously, they have proposed versatile designs[73] using the moveable side walls, and the splitters to produce different swirl patterns namely, the bulk, the paired and the twin swirls. The significance of the research lies on the fact that the reliable swirl generators (see Figure 2.24) were proposed. These swirl generators can be utilized for both the experimental, and the CFD purposes in order to study the sensitivity of some types of the swirl distortion.

   Later, the RANS CFD model consisting of about 11.8 million mesh cells was developed[72]. The purpose was to couple a very similar swirl generator as above with a single-stage axial compressor, and then consequently speed-lines were generated to describe the compressor performance in swirl flow conditions[72]. A sketch of the modelled domains is shown in Figure 2.25(a). The results of compressor performance changes under the co and the counter bulk, and the various paired swirl patterns are illustarted in Figure 2.25(b) and (c).

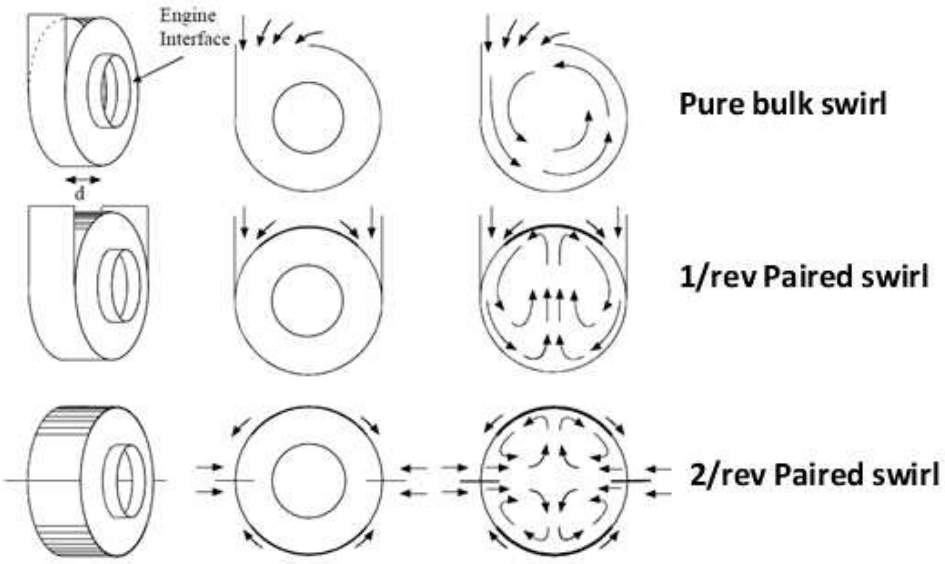

Figure 2.24: Versatile swirl generator for compressor sensitivity training.[73]

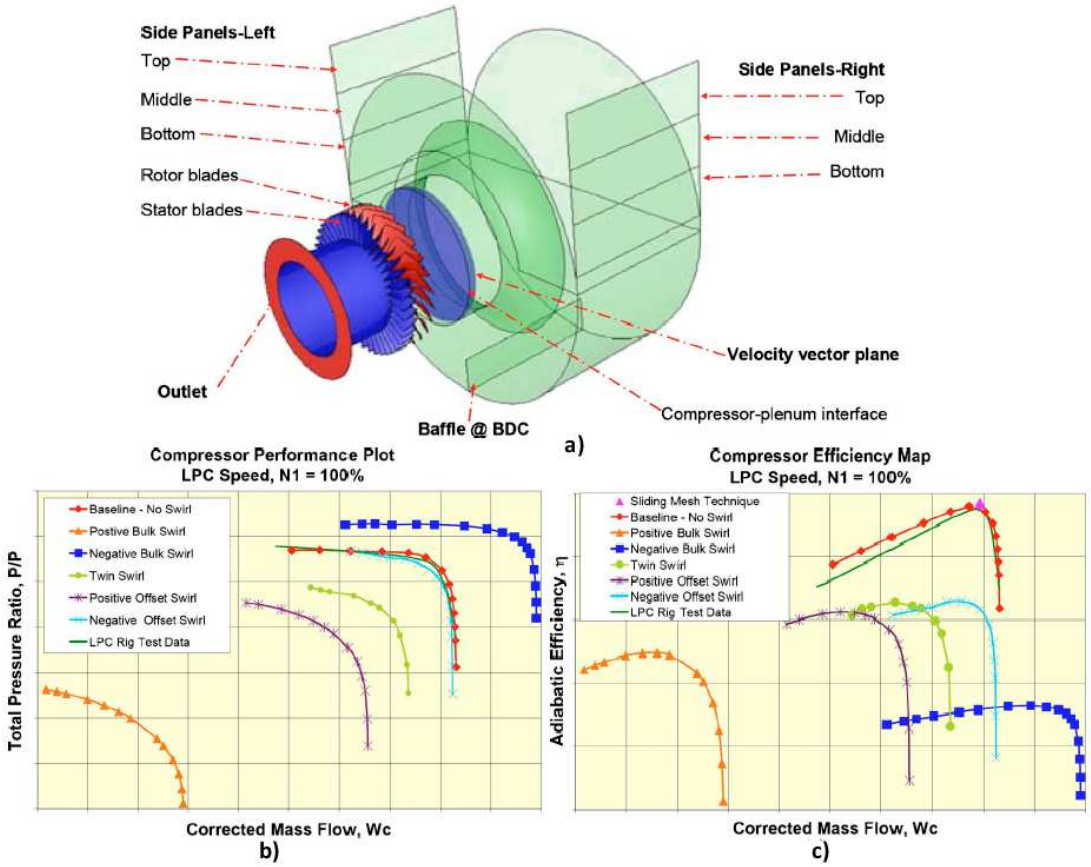

Figure 2.25: Low pressure compressor stage **a)**Example numerical/experimental with a twin swirl generator. **b)** Changes in pressure ratio. **c)** Changes in adiabatic efficiency under various swirl patterns.[72]

Some general observations can be made on the effect of swirl patterns, the counter-rotating bulk swirl show an overall increase in the stage performance, and a drop in the efficiency. The opposite takes place for the case of co-rotating bulk swirl, the shift in speed-line is downwards in terms of the pressure ratio, and the mass flow (see Figure 2.25). On the other hand, paired (also twin) swirl has a co-rotating half, and a counter-rotating half that both participate in influencing the compressor performance. Both halves induce a lower efficiency. The reduction is slightly less than in the case of pure bulk swirl. Also, the counter-rotating half was found to be reducing the efficiency more than the co-rotating half as observed for the pure bulk swirl cases. As a result, the reduction in pressure ratio and mass

flow compared to the clean conditions is smaller than the reduction in the case of pure co-rotating bulk swirl.

A comparative study between the use of a sliding mesh (URANS), and a frozen rotor (RANS) interface within the compressor stage was also undertaken. The results showed that both the methods were equally accurate as fairly uniform swirl angle distributions exists in these cases.

It should be highlighted at this stage, the swirl flows were generated using a CFD-modelled swirl generator in the above work. However, the approach adopted for the current research involved the implementation of the numerical swirl expressions as an inlet boundary conditions.

2.8 Methods for reducing swirl effects

Having noted the impact of distorted flows on a compressor, this section briefly describes some of the developed techniques, and the design modifications that may reduce the swirl distortion effects prior to the compressor face. These are:

- **Inlet guide vanes (IGVs):** Experimental tests demonstrated that the presence of the inlet guide vanes upstream of a compressor can make it less sensitive to the flow distortion. This is because the effects of the tangential velocity component are lessened by turning the incoming flow to an appropriate flow direction, this method was used for the Tornado aircraft[79]. Moreover, variable guide vanes proved to have further improved the effects, the flow can be better regulated depending on the inlet conditions.

  However, use of the inlet guide vanes at the front of an engine is not always advised due to the integration issues associated, also including an increase in the engine noise, weight, length, and the de-icing problem. Also, in some offset inlet-engine configurations, both in the military and the civil aircraft, the use of only IGVs can not always guarantee swirl free inlet[70]. Streamwise fences are also sometimes used upstream in the bend of the convoluted s-shape inlets to mitigate the swirl effects.

- **Stage geometry:** It have been demonstrated that the blades with a higher chord length reduce the compressor sensitivity to flow distortion. The surge margin was shown to be improved upto 1% when blades with higher chord lengths were fitted in the first two compressor stages[34]. Moreover, the theoretical results showed that the reduced spacing between the blade rows can influence the amount of distortion that is transferred between the stages. These results did not however take into account the effects of flow turbulence downstream of the rotor blades.

- **Flow control techniques:** Flow control methods have been tested and some used in the past, such as variable inlet lip geometries[70]. In particular, for the twin swirl as flow distortion takes place downstream in the s-shaped bend, the flow separation control is performed using the boundary layer suction or the vortex generators. There are several types of vortex generators that have been proposed for the purpose of energising the low-momentum flow near the wall[70]. This helps to negotiate the adverse pressure gradients in diffusing sections of the inlet. One example of such technique using the micro-jet air and the micro-vanes is shown in Figure 2.26. An improvement in the total-pressure recovery at the exit of the convoluted inlet is clearly visible.

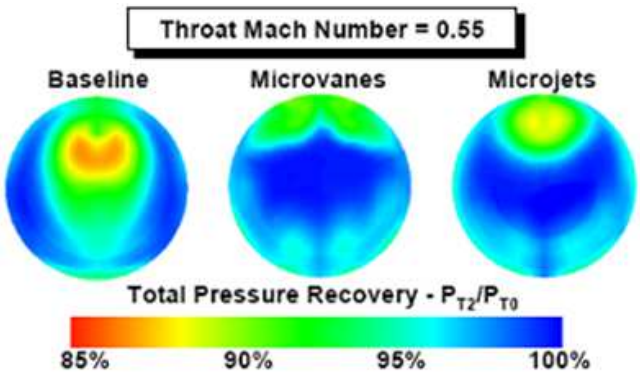

Figure 2.26: Impact of micro-vanes and micro-jets on total-pressure recovery.[70]

2.9 Other methods for swirl distortion inlet-engine compatibility assessment

Above examples showed that the CFD can be very time consuming, and also demand high computational power, especially where the modelling of full annulus or multiple compression stages becomes important. On the other hand, the experimental tests can also be very expensive, and even not feasible on some occasions, for example when highly distorted flows are involved.

Therefore, there are number of alternative low order analytical techniques that has been proposed to study the effects of flow distortion on the stability margins of a compressor. The following three methods have been proposed for the analytical prediction of some simple types of the swirl pattern, e.g. pure bulk swirl, and paired swirl.

1. ***Meanline analysis*** is a 1-D, steady-state, row-by-row simulation that uses the blade loss and the deviation correlations to solve the system performance.[74] It calculates an estimate of the overall performance of a compression system, which is characterised by the blade geometry at mean radius as shown in the velocity triangles below. This approach is limited for the pure bulk swirl patterns, as the flow can only be assumed axis-symmetric circumferentially.

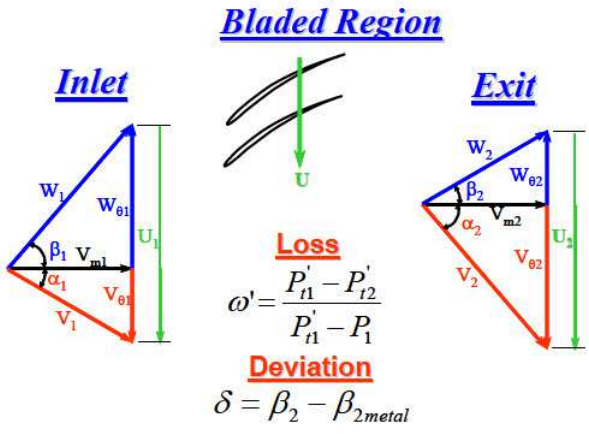

Figure 2.27: Meanline code theory.[74]

2. ***Parallel compressor*** analysis involves subdividing the compressor into a number of circumferential and parallel tubes (sectors). Each sector works as a 1-D solver but in parallel with each of the other subdivisions, and all the sections exit to a common exit boundary condition, thus making it a quasi 2-D code circumferentially. Each sector is therefore operating differently with a user specified cross-flow taking place between them. This method is illustrated in Figure 2.28, and have been extensively used in the past for the total-pressure, and the total-temperature distortion[21]. In comparison, the use of parallel approach for the swirl distortion has been recently performed for the bulk and the paired swirl patterns, showing promising results with the experimental tests[18]. An illustrative sketch of the parallel compressor approach is shown below.

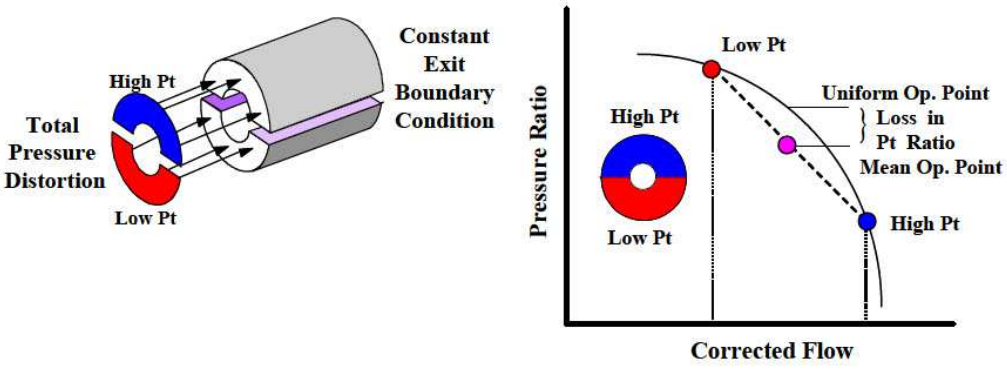

Figure 2.28: Parallel compressor theory concept.[21]

3. ***3-D Euler analysis*** is considered to be a suitable compromise between the one-dimensional methods that require a number of simplifying approximations, and the conventional CFD which needs to solve using a full annulus model. This method combines the use of streamline curvature codes (SLCC) in the complex flow regions, for example between the blades, with the implementation of conventional CFD in regions which are less complex. The Euler equations are then used by the CFD to transport the fluid properties. An example of such approach utilized to develop the Turbine Engine Analysis Compressor Code(TEACC)[39] is shown below.

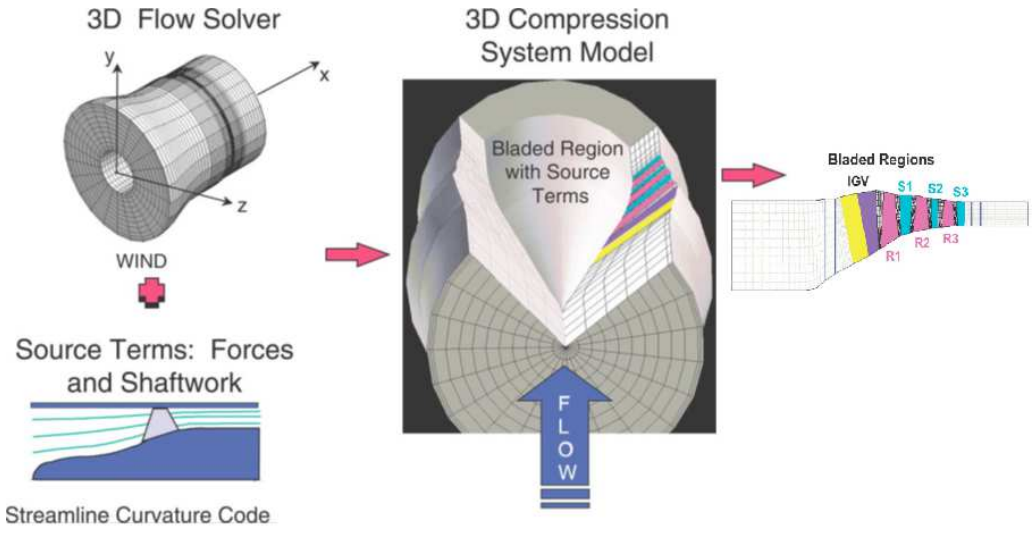

Figure 2.29: TEACC technical approach.[39]

Just to conclude regarding the methods available to assess the swirl distortion effects, the experimental methods are currently been developed to test the compressor response to distortion[70]. These are still in early stages, where the delta wings and the complex turning vanes have just been proposed to generate the desired swirl patterns[73]. However, the use of this kind of generators have been proven successful in the past for the Tornado case[70], where a number of successful tests were carried out.

2.10 Compression system instabilities

The compressor instabilities that can lead to stall or surge is also an important aspect within the framework of the current project. These instabilities emerges when the compressor reaches near to its peak characteristic, and results in the performance deterioration. This section intends to introduce with these instability phenomena of how they are incepted, and developed during the process. It is vital to understand the underlying flow physics, as it will help to scrutinize the combined effects of the ingestion of swirl distortion under such flow conditions.

In general, a compressor can have two different length and time scales[61]. The first one is short wavelength scale, which is associated with passage to pas-

sage variations of a typical compressor and at a high frequency (around 2.7kHz). Whereas, the long wavelength scale is associated with the inlet flow distortion, and the stall cells occurring at a lower frequency (around 200 Hz). Therefore, when a compressor is operating near the design point and far away from the stability limit, the flow along a compressor is steady axis-symmetric, where there are no signs of the large wavelength scales. However, when a compressor is running near its stability limit they become a part of the flow field, and two different types of flow instabilities can emerge as shown below in Figure 2.30. These are the rotating stall and the surge.

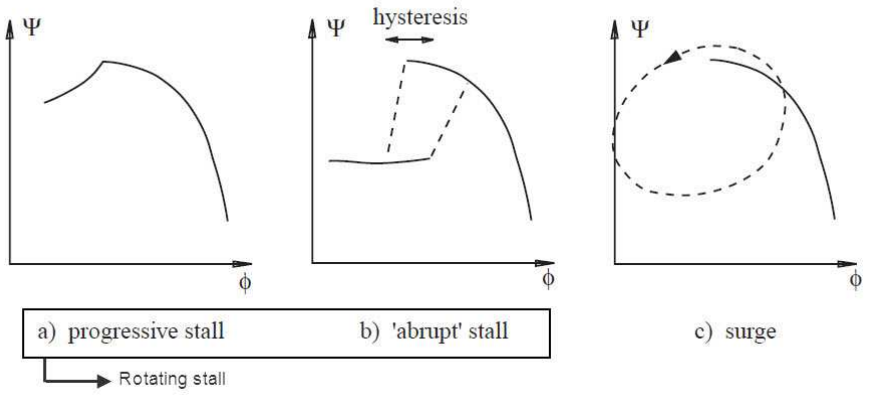

Figure 2.30: Types of compressor instabilities.[31]

2.10.1 Rotating stall

The rotating stall is a two-dimensional instability phenomena, which affects only part of a compressor annulus. The flow is unsteady in nature and non-axisymmetric as shown in Figure 2.31. The level of flow blockage can also be continuously increased as the stall cells causes the flow to spill in the adjacent blade passages. The reason of this propagation is that when one blade stalls due to some instability, the flow angle increases at its blade leading edge. Because of this angle increase, there is a blockage associated to stall, and causes the unstable flow to be diverted to the adjacent passages, as the blade rotates. Therefore, the angle of attack of the adjacent blade consequently increases, leading them to stall. On the other hand, as the blade rotates away from the disturbances, the angle of

attack decreases, and restoring normal flow over the blade passage. Thus, when observing from an inertial frame of reference, this stall cell rotates in the direction of compressor rotation but having a lower wheel speed (about $25 - 70\%$ of the compressor rotational speed). The number of stall cells depends on the blade geometry, and also the operating conditions. In general, it have been reported to vary from one to nine stall cells[23,61,75,76].

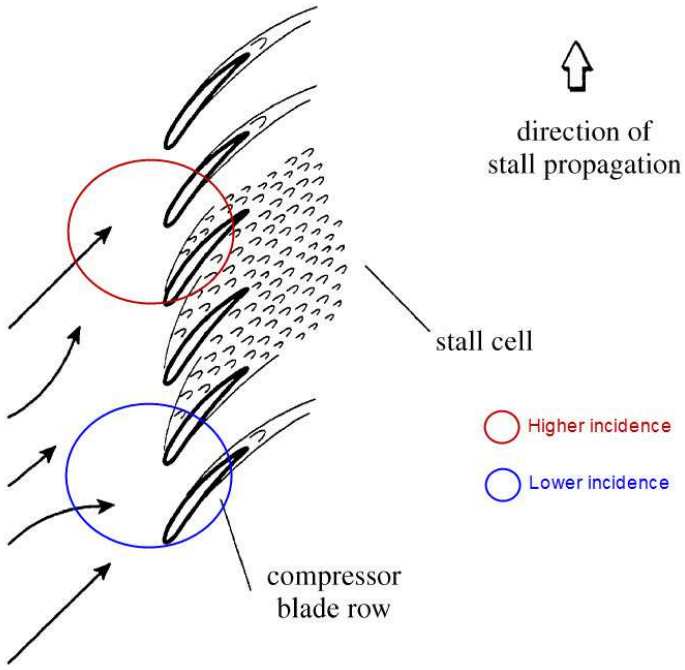

Figure 2.31: Rotating stall cell propagation mechanism.[31]

Rotating stall can be split into two further types; the progressive, and the abrupt stall (see Figure 2.32). As the name suggests, the progressive stall affects the flow in passage at certain span, also known as part-span stall, and slowly reduces the pressure ratio. Whereas, the abrupt stall causes full-span stall. Ultimately, this rotating stall may also lead to a more severe compressor instability, known as the surge.

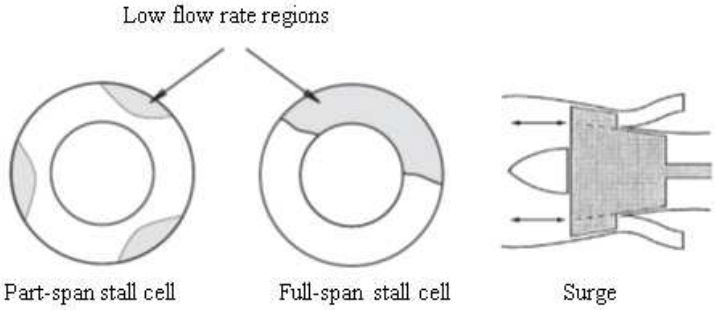

Figure 2.32: Common instabilities patterns in a compression system.[31]

2.10.2 Surge

It is a one-dimensional instability phenomena, where the flow is axisymmetric and unsteady in nature. Complete flow reversal in the compressor is well known consequence of the surge. It affects the compressor performance, and can also cause severe structural damage to the turbo-machinery components. A number of large fluctuations in the pressure are observed during the surge operation. Surge phenomenon has been be classified into four categories[31]:

1. **Mild surge:** It is always the first consequence of surge, where small pressure fluctuations arise. No flow reversal.

2. **Classic surge:** Large mass flow and pressure fluctuations are observed with no reverse flow.

3. **Modified surge:** This is the most common type of instability especially in modern transonic compressors. It starts with some blades under the rotating stall, and then forms 3D flow instabilities when combined with the classic surge.

4. **Deep surge:** A stronger version of classic surge and is characterized by a flow reversal.

Surge is a final stage of the instability process in a compression system, and is therefore beyond the scope of the current project. However, the detection of

first instabilities that can resultantly push a compressor into the rotating stall or surge is an important aspect, and is discussed in the following section.

2.10.3 Instabilities inception and causes

Most of the compressor instabilities emerges during the rotating stall process, and usually in the first few stages of a compressor. Rotating stall has three stages[31,61], the inception, the development, and the final flow pattern of the stalled cell. The first phase is the period when the disturbances start to grow. There are two kinds of inception, the spike and the modal type. The spike type is linked with the short wavelength disturbances but with high amplitude, and vice versa for the modal type disturbances.

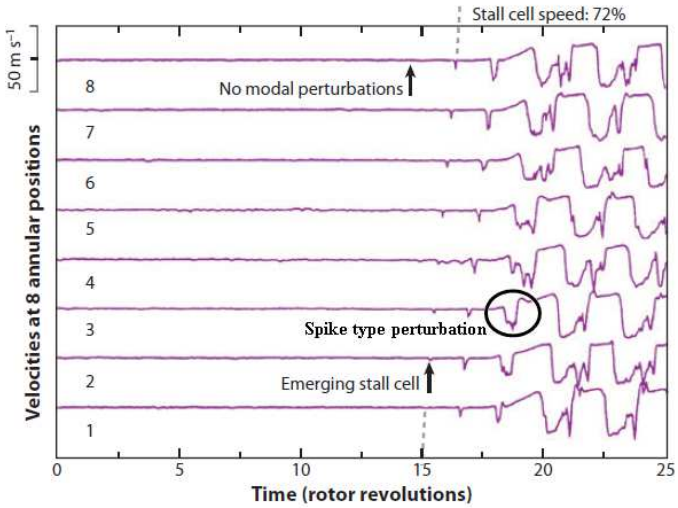

Figure 2.33: An example of spike type disturbance evolving into rotating stall.[81]

Th spike type stall inception is the most common way for the modern transonic rotors of a compressor to precede the rotating stall. Described first by Day[22], it is characterized by the emergence of a local flow disturbance, called the spike. The spike has a width between two and three blade pitches at the rotor tip. Since the disturbance is confined in the tip region, the tip clearance flow also plays an important role in this phenomenon[1]. The velocity defect of the spike is comparable to the mean velocity through the compressor, and to analyse the

fluctuations, the traces of the axial velocity at different circumferential locations are usually plotted during the transient runs. In Figure 2.33, an example of the axial velocity traces during a stalling event is shown.

There are two established criterion that usually have to be fulfilled for a local spike type disturbance to start, and grow[81,82] within a blade passage. These are:

1. **Leading-edge flow spillage:** The first criterion occurs when the interface between the tip-clearance flow, and the incoming flow lines up with the rotor leading-edge (LE) plane. The position of this interface is a consequence of the balance between the momentum of the tip-clearance flow, and that of the incoming flow. This interface moves upstream when the flow coefficient reduces because of the reduction of the momentum of the incoming flow, and thus causes an increase in the local incidence. In computations, a strong gradient of entropy reveals the position of this interface. The flow spillage at the LE takes place below the tip-clearance region of the adjacent blade, and can also propagate around the annulus. The concept of the leading-edge spillage is illustrated in Figure 2.34(a), the path of the tip-clearance fluid spilling into the next blade passage is shown.

2. **Trailing-edge flow impingement:** A sketch of the second criterion is also presented in Figure 2.34(b). It can be seen that the flow coming from the tip-clearance moves into the adjacent blade passage at the trailing-edge. As a result, it impinges on the pressure surface of the blade. This is called tip-clearance backflow, and it also implies an end-wall separation with a circumferential relative velocity component.

Tan et al.[81], Vo et al.[82] suggests that the above flow events (tip-clearance LE flow spillage and backflow impingement) sometimes may occur at the same time. But a necessary requirement for the spike formation is fulfilled even if one of the above criterion is fulfilled. More information of the phenomena will be discussed later in the results chapter.

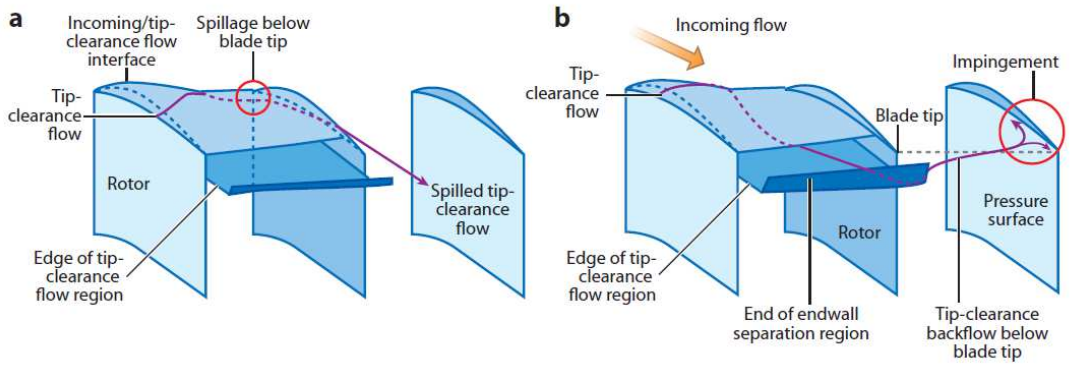

Figure 2.34: **a)** Leading-edge tip-clearance flow spillage below the blade tip. **b)** Reversal (backflow) of tip-clearance fluid below the blade tip.[82,83]

2.11 Chapter conclusions

This chapter brought together a broad collection of theories, research outcomes, and empirical observations within the research scope to assess the present state of knowledge.

This literature review provides an insight into the fundamental theoretical and the analytical aspects of the swirling flow phenomena. It should be addressed and understood before proceeding to study the effects of these types of flow distortion on the turbo-machinery performance. It was brought to light that the inlet flow distortion is not uncommon in gas turbine engines, and the risks of its occurrence are rising due to the size, and the architecture of modern designs. Especially, the risks of ingesting vortical flows, and the generation of complex swirling flows due to the convoluted inlets have risen. It can have damaging effects on the engine performance, which has urged the industry and the academia to understand this phenomena, and strive towards mitigating its risks.

A number of techniques including design modifications were first developed to prevent swirl distortion from impacting the engine. But this proved to have very limited success, and as a result, the experimental methods started to emerge to asses the impact of the swirling flow. However, because of the costs involved with such tests, the analytical and the numerical approaches also started to be

developed at many distinguished research establishments including the already established SAE S-16 committee. The reason of this research activity is to enhance the current knowledge on the swirl distortion adverse effects on the gas turbine performance, and to develop appropriate inlet-engine compatibility assessment methodologies for future use. The outline of this has been described in this chapter.

Previous numerical and the experimental work done in the related fields of flow distortion, and the stalled flow have also been summarised in this chapter. This will be used to validate, and determine the consistency with the current research's numerical simulations.

The next chapter describes the methodology developed to pursue, and tackle some aspects of the emerging swirl distortion problem. The key ambition of the project is to answer what are the main effects of the swirling flows on the turbomachinery performance, and develop a data set that can then be used for future inlet-engine distortion studies.

Chapter 3

Methodology

This chapter outlines the adopted methodology, it can be summarized as in Figure 3.1. Due to the nature of the study, a substantial effort and time went into developing a robust methodology that can be applied for the different swirl distortion studies, and using the Computational Fluid Dynamics (CFD) as a numerical tool.

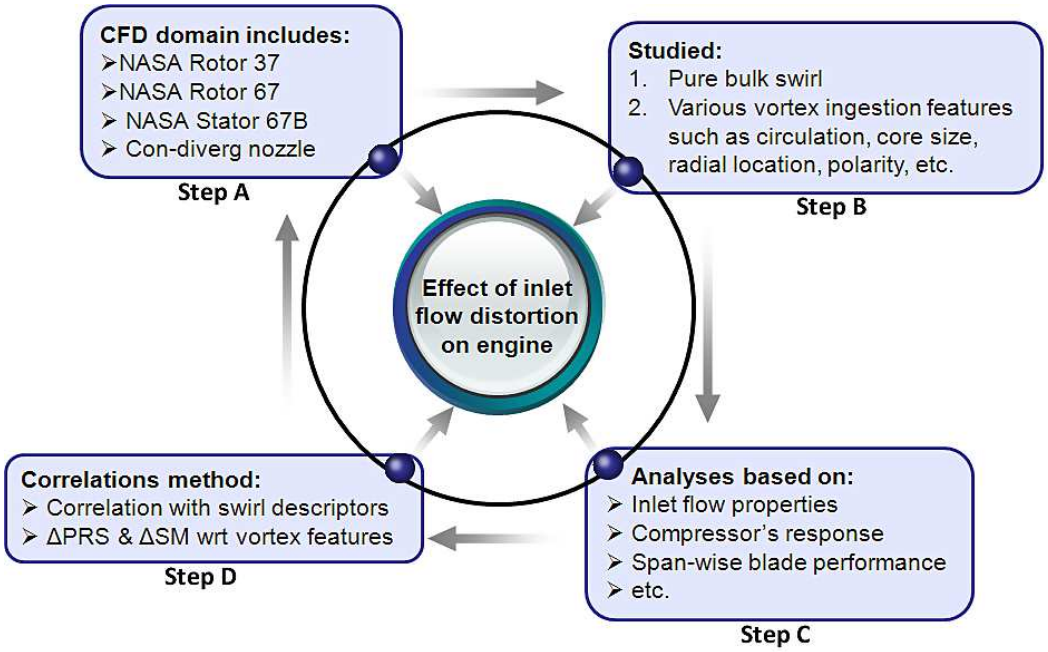

Figure 3.1: Overall project methodology.

From Figure 3.1, steps A, B and C are the key foundations on which all the analyses are based, and then used to generate the final project aim (step D).

It was an iterative procedure, which was followed throughout the course of the study.

First, the creation of the investigated geometries (i.e., Rotor 67, Rotor 37, and the Stator 67B), and their meshes were generated. The validation studies utilizing a commercial CFD software (i.e. ANSYS CFX) were performed to gain some confidence in the developed tool kit.

From the literature, methods for implementing the appropriate Boundary Conditions (BC's) for the bulk swirl, and the tightly-wound vortex were studied, and after an extensive scrutiny, the BC toolbox for distorted flows was created within the CFD software. A number of test cases were performed to check the applicability of the BC implementation method.

The intention of the developed CFD capability is the ability to perform both the steady-state Reynolds Averaged Navier Stoke (RANS), and the Unsteady Reynolds Averaged Navier Stoke (URANS) simulations. Some of the distorted cases were performed using both methods. In this way, the key differences in terms of the accuracy, and the computational requirements between them were analysed.

The two types of the swirl distortion which were studied were, the bulk swirl, and the ingestion of a tightly wound vortex. Furthermore, a RANS parametric study involving the various flow features of a vortex ingestion was conducted. The results from this study was used to define the appropriate swirl descriptors, and their correlations against the rotor instabilities.

Acquiring a sufficiently wide range of data is paramount in conducting an informative, and a reliable parametric study. The data was generated in a methodical, and a consistent manner throughout the study. A number of optimisation tools were developed, and implemented to shorten the post-processing times. This enabled the data to be processed efficiently.

All these steps are explained in this chapter, and the following tools were utilized in the project:

- Mesh generation: ANSYS TurboGrid (12.1), Blade Gen (12.1).

- CFD simulations: ANSYS CFX-Pre (12.1 and 14.0), and CFX-Solve (12.1 and 14.0).
- Post-analysis: ANSYS CFX-Post (12.1 and 14.0), MATLAB (R2008a), LINUX-Bash, Excel (2010), Animator (2012).

3.1 Investigated NASA geometries

In the aerospace sector, the exact geometric data is protected by means of stringent intellectual property laws. NASA on the other hand provides a number of experimental test data, as a form of the technical reports, which can be easily found in the public domain. NASA experimental data have been used for many decades to validate the CFD results, when using the exact generic NASA geometry. A brief summary about the two rotors, and a stator geometry investigated in this study is presented. In addition, the other researchers CFD results are also included, highlighting the main flow-field features.

3.1.1 NASA stage 67

NASA 67 geometry is comprised of a two-stage fan developed in the Lewis research laboratory[29,80]. First stage model of the two stage fan, i.e. NASA Rotor 67 (R67) and Stator 67B (S67B) was utilized in the research.

3.1.1.1 Rotor 67

Rotor 67 is a low-aspect-ratio transonic axial-flow fan rotor that has been used extensively as a test case in the validation of various CFD codes. It has a highly twisted geometry, which is a prevalent feature among the modern transonic fan blade geometries (see Figure 3.2). It is comprised of several double-circular-arc (DCA) blades sections along the span, and also features an aft-sweep near the blade tip region. The choice of the rotor was also based on the fact that Rotor 67 is a first stage fan rotor, where the ingestion of externally generated swirl patterns are most likely to occur. The following are the main specifications of the rotor.

NASA ROTOR 67	
Number of rotor blades	22
Rotational speed (rpm)	16043
Mass flow(DP) (kg/s)	33.25
Total Pressure ratio(DP)	1.63
Rotor tip speed (m/s)	429
Tip clearance (cm)	0.061
Inlet tip relative Mach Number	1.38
Rotor aspect ratio	1.56
Rotor solidity hub	3.11
Rotor solidity tip	1.29
Tip diameter inlet (cm)	51.4
Tip diameter exit (cm)	48.5

Table 3.1: Rotor 67 geometrical specifications.[80]

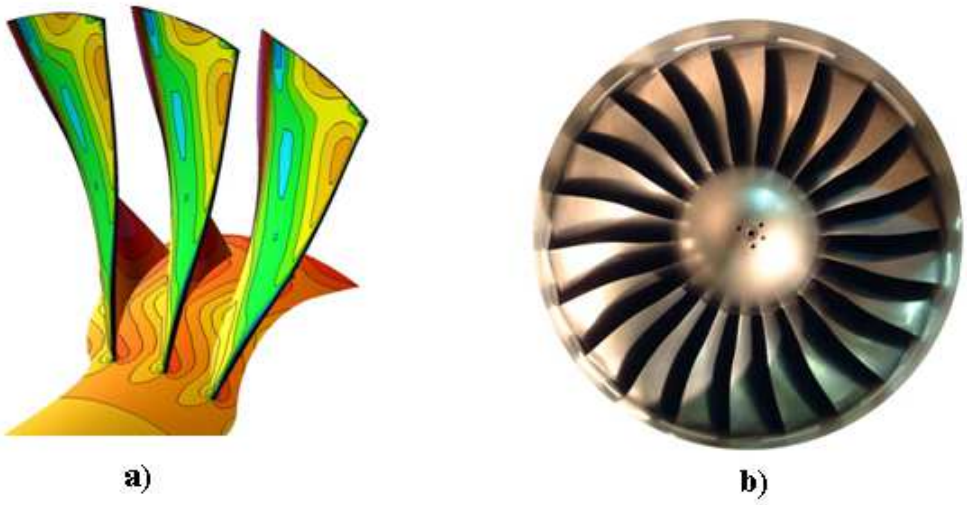

Figure 3.2: **a)** CFD Model of Rotor 67[14]. **b)** Real picture of Rotor 67.[61]

3.1.1.2 Stator 67B

For the stage calculations, the Rotor 67 was combined with the downstream Stator 67B, consisting of 17 second-generation controlled-diffusion (CD) blades[29]. CD

blade design add a level of complexity to the blade geometry as opposed to the more conventional double-circular-arc (DCA) blades. They have relatively a blunt leading, and trailing edges, as shown in Figure 3.3. The blade loading, and the turning of the flow is higher on this type of blade design but an advantage is gained in the reduced number of blades to produce the same pressure ratio. The following are the main specifications of the stator.

NASA STATOR 67B	
Number of stator blades	17
Chord length (cm)	12.7
Thickness / Chord ratio	0.5
Span (cm)	25.4

Table 3.2: Stator 67B specifications.[29]

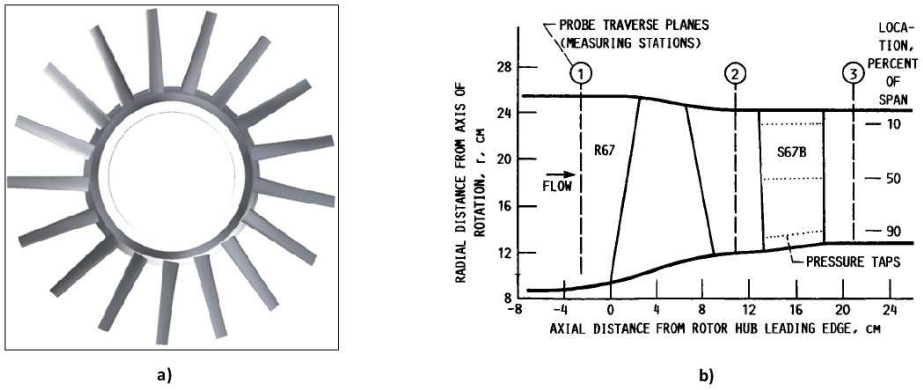

Figure 3.3: **a)** Model of Stator 67B. **b)** Flow path and instrumentation locations for the first Stage 67.[29]

3.1.2 NASA rotor 37

The NASA Rotor 37 (R37) is a transonic high pressure compressor rotor, part of an 8-stages compressor designed in the 1970'S. It was tested by Reid and Moore[65] at the NASA Lewis Research Centre. The main specifications are listed in Table 3.3 below. This test case has been employed in many CFD case studies, and the

detailed flow field analysis have been reported in the AGARD report[26]. A real test case picture, and the measurement stations of the rotor are shown in Figure 3.4.

NASA ROTOR 37	
Number of rotor blades	36
Rotational speed (rad/s)	1800
Mass flow(DP) (kg/s)	20.19
Total Pressure ratio(DP)	2.106
Rotor tip speed (m/s)	454.14
Tip clearance (cm)	0.0365
Inlet tip relative Mach Number	1.48
Rotor aspect ratio	1.19
Hub to tip ratio	0.7
Rotor solidity tip	1.228

Table 3.3: Rotor 37 geometrical specifications.[26,65]

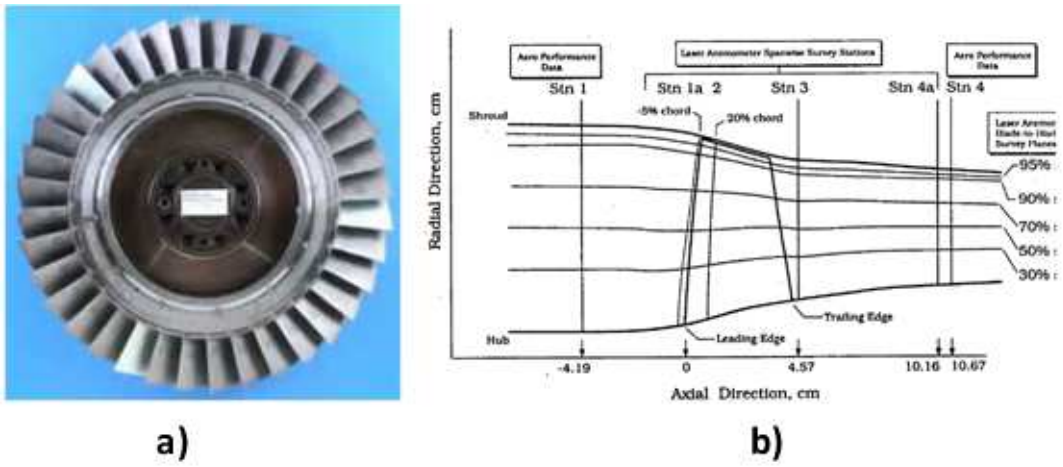

Figure 3.4: **a)**Real picture of Rotor 37.[61] **b)** Flow path and instrumentation locations for Rotor 37.[26]

3.1.3 Main flow features of Rotor 67 and Rotor 37

To summarize all the previous CFD analyses performed on these rotor geometries is merely not feasible in the space available. As both are transonic rotors, therefore main flow features found in both the rotor configurations by other researchers is presented. More detailed information on the CFD results can be found in the literature[6,15,36].

- **Shock-wave system:** A strong shock-wave system is observed in both the rotor geometries at high rotational speeds. The shock-wave extends over the majority of the blade span. For the Rotor 37, an oblique shock is observed within the blade passage, at near choke conditions. This shock moves upstream when the compressor is near the peak efficiency. At this condition, a strong shock is observed attached near the leading edge of the blade. This shock ultimately transforms in to a single strong detached bow shock near the stalling conditions, resulting in an increase of the passage flow blockage.

  In the Rotor 67 shock-wave system, as shown in Figure 3.5, a lambda shock wave pattern is observed near the peak efficiency, which consists of an oblique shock plus a passage shock wave. On the other hand, a single strong oblique shock is observed at the blade leading edge near the stalling conditions, a trajectory which was also well predicted by Chens model[1].

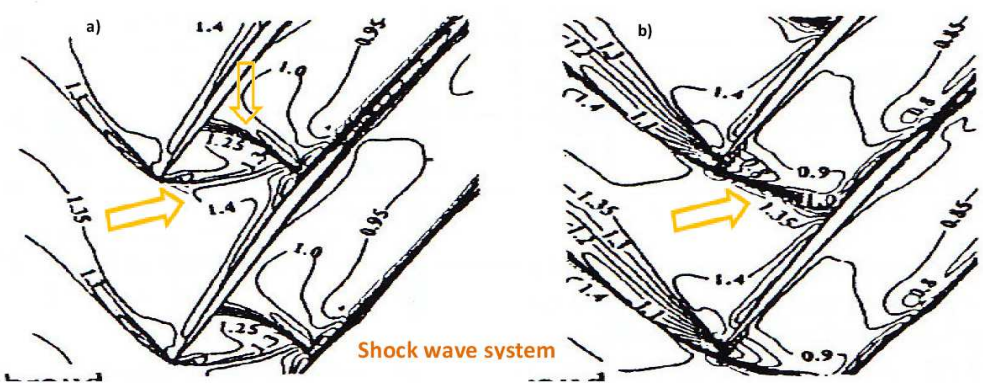

Figure 3.5: Rotor 67 shock wave system. **a)**Near peak efficiency. **b)**Near stall conditions.[61]

- **Interaction tip leakage flow/shock wave:** A lot of studies have been performed in the past to analyse the effect of the tip leakage vortex on the rotor performance, and also its interaction with the shock wave system[15]. In both the rotor geometries, the tip leakage vortex plays a vital role for the inception of the instabilities inside the blade passages. The interaction results in a certain spillage, and the mass-flow blockage. This mass-flow blockage moves upstream of the blade passage, as the rotor shifts from the near peak efficiency to the near stall operating conditions. This ultimately causes the flow spillage to move to the adjacent blade passages, which may result in the part-span stall of the annulus. Figure 3.6 is illustrating this interaction, and the breakdown of the Tip Leakage Vortex (TLV) due to the presence of passage shocks.

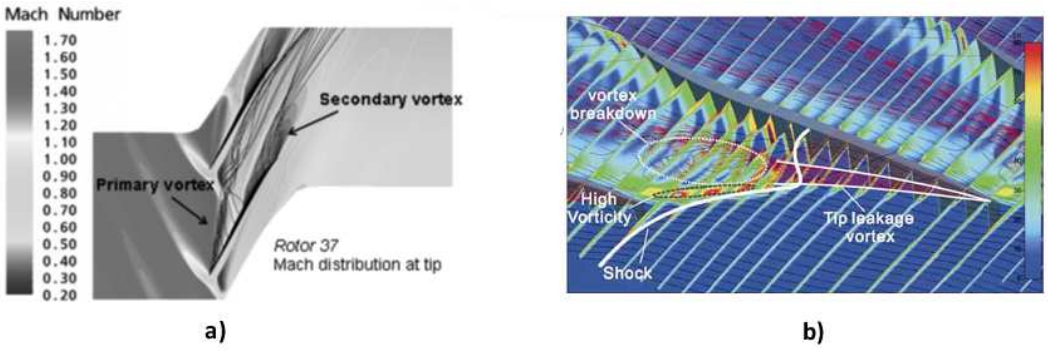

Figure 3.6: Rotor 37 CFD simulations. **a)** TLV structures due to tip clearance.[9] **b)** TLV break down due to interaction with the passage shock.[88]

- **Hub corner stall:** This flow-feature is observed at all the operating conditions near the suction surface of the blades. It grows in size as the compressor moves from choking to stalling operating conditions. However, it is reported by the other authors[2,36] that it is a common feature of transonic rotors, and the effects on the rotor performance diminishes at the higher rotor rotational speeds. Thus, this should not be the prime reason for the stall inception. Examples of the hub corner stall in the Rotor 37 near the trailing edge of the suction surface can be observed in Figure 3.7.

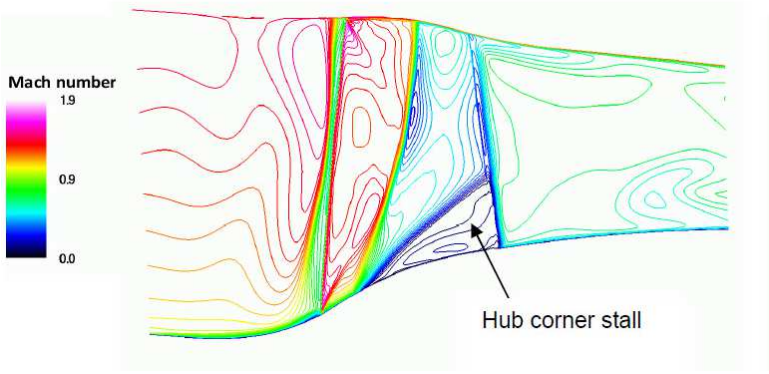

Figure 3.7: Rotor 37 meridional view illustrating hub corner stall using Mach contours.[36]

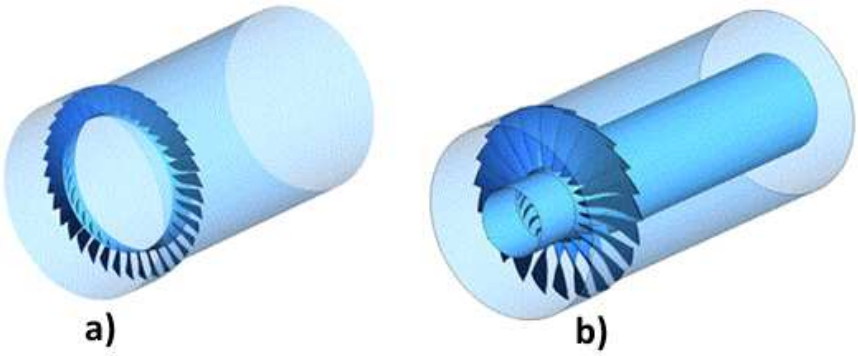

Figure 3.8: **a)** Modelled isolated Rotor 37 domain. **b)** Modelled isolated Rotor 67 domain.

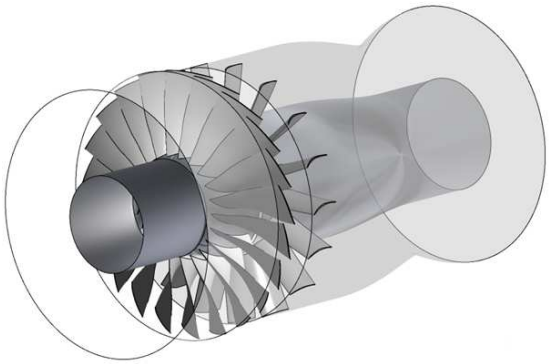

Figure 3.9: First Stage 67: the Rotor 67 and the Stator 67B with a convergent-divergent nozzle.

3.2 Mesh of modelled configurations

Figure 3.8 illustrates the computational models of the isolated rotors that were utilized in the project. During the research, the Rotor 67 configuration was upgraded by including downstream, the Stator 67B, and a choked convergent-divergent nozzle. The modelled configuration is illustrated in Figure 3.9. This section describes the mesh topologies for these three CFD configurations, which were numerically simulated during the research:

- **Configuration 1: Rotor 67**
- **Configuration 2: Rotor 37**
- **Configuration 3: Stage 67**

3.2.1 Configuration 1: Rotor 67

The mesh was created using the ANSYS Turbogrid 12.1, and the Bladegen 12.1. Because of the large change in the stagger angle along the blade span, 14 blade profile layers were used to capture the shape of the aerofoil, as shown in Figure 3.10(a). The blade's leading edge (LE) was refined using more control points to capture accurately the local surface curvature of the blade.

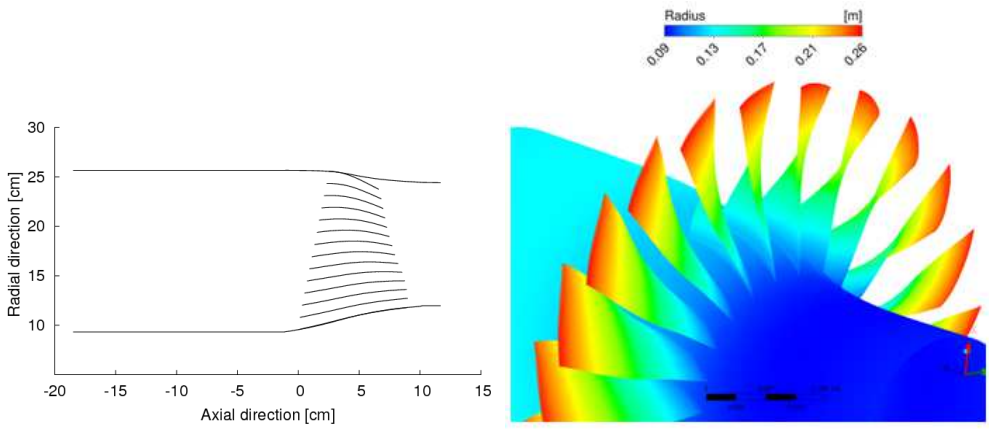

(a) (b)

Figure 3.10: **a)** Rotor 67 blade profiles in meridional view. **b)** Contours of Rotor 67 radius.

A wide variety of fully structured hexahedral meshes were created for the grid dependency study. The Table 3.4 summarizes the total number of full annulus mesh elements for each case study. The baseline model including the tip clearance was about 500,000 elements per blade passage. It was found to be a good compromise between the accuracy, and the computational resources available for the numerical calculations.

Mesh Statistics			
Mesh	**Turbulence model**	**Elements**($1x10^6$)	**Tip gap nodes**
Coarse	K-epsilon	5	0
Baseline	K-epsilon	10.8	0
Baseline tip clearance	K-epsilon	11	12
Fine	K-epsilon	18	0
Hi-fi	K-omega	35.5	0
Very fine	K-epsilon	35.5	14

Table 3.4: Full-annulus Rotor 67 mesh statistics for the grid dependency study.

Nodes definition: Figure 3.11 illustrates the baseline mesh topology of the Rotor 67, and was used for the numerical simulations. The whole passage mesh consisted of variety of mesh topologies; C/ O/ L/ J/ H/. A O-block was used around the blade to allow for modelling the boundary layer (BL). A grid dependency study was also carried out using the K-epsilon, and the K-omega turbulence models with the different values of y^+ to create the appropriate boundary layers. The H block was used to mesh the inlet and the outlet, whereas the J block topology allows the meshing of the flow passage. Tip clearance was also taken into account for some cases with a number of H blocks, within the tip gap height of $0.061cm$, value taken from the NASA report [80]. Having reached an acceptable value of the skewness, regarding both the minimum and the maximum face angles, the grid dependency study was carried out to determine the suitability of the mesh model for the CFD studies.

In Figure 3.11(b), the mesh structure around the Rotor 67 leading edge can

be observed. To keep the y^+ between 10 and 100, for the K-epsilon turbulence scheme (with the scalable wall functions)[26], a total number of 11 nodes within the O-block boundary layer had to be defined. The distance of the first node from the blade surface is about 0.12% of the blade chord (mid-span).

A total number of 65 span-wise nodes (see Figure 3.11(a)), and 60 blade-to-blade pitch-wise nodes were defined (see Figure 3.11(c)). Around 65 nodes were used to define the axial distribution of the blade passage. On the other hand, the number of mesh elements within the inlet and outlet domains depends on the individual cases, and will be discussed later in the section.

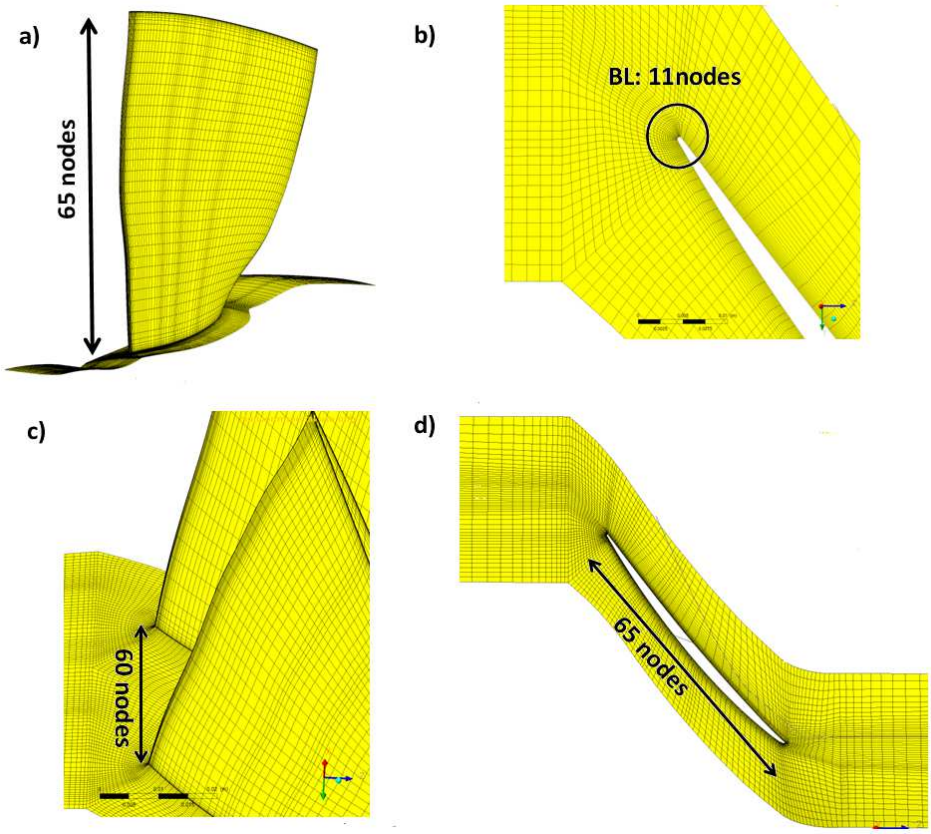

Figure 3.11: Rotor 67 baseline model showing mesh distribution: **a)** Span-wise. **b)** Blade boundary layer mesh. **c)** Blade-to-blade pitch nodes. **d)** Blade chord.

3.2.2 Configuration 2: Rotor 37

The aforementioned comments with respect to the Rotor 67 also apply to the isolated Rotor 37 configuration. The hub to tip radius of the Rotor 37 is lower,

when compared with the former. Therefore, the modelling of 6 span-wise blade sections was sufficient to accurately capture the rotor geometry (see Figure 3.12). Also, a wide range of meshes were created for the grid dependency study, as summarized in the Table 3.5.

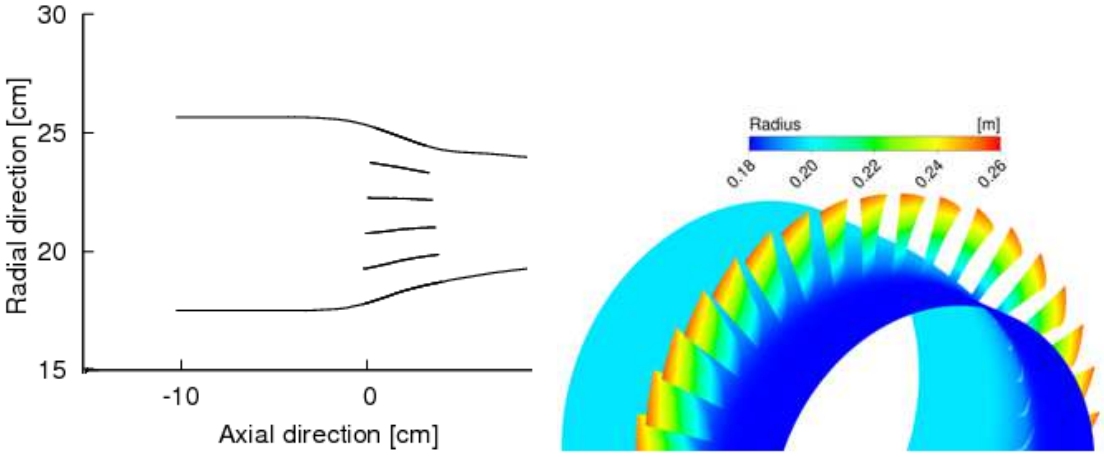

(a) (b)

Figure 3.12: **a)** Rotor 37 blade profiles in meridional view. **b)** Contours of Rotor 37 radius.

Mesh Statistics			
Mesh	**Turbulence model**	**Elements**($1x10^6$)	**Tip gap nodes**
Coarse	K-epsilon	4.5	0
Baseline	K-epsilon	11	0
Baseline tip clearance	K-epsilon	11.1	10
Fine	K-epsilon	19	0
Hi-fi	K-omega	24.2	0
Very fine	K-epsilon	22	0

Table 3.5: Full-annulus Rotor 37 mesh statistics for the grid dependency study.

Similar mesh topology as discussed for the Rotor 67 were used in this case, and are illustrated in Figure 3.13. A fully structured hexahedral mesh was utilized to create the full annulus Rotor 37 mesh model, and comprised of around 11.1

million elements. The tip gap losses were also taken into account by modelling 10 span-wise nodes at the clearance height. Figure 3.13 is illustrating the nodes distribution along each direction within the blade passage.

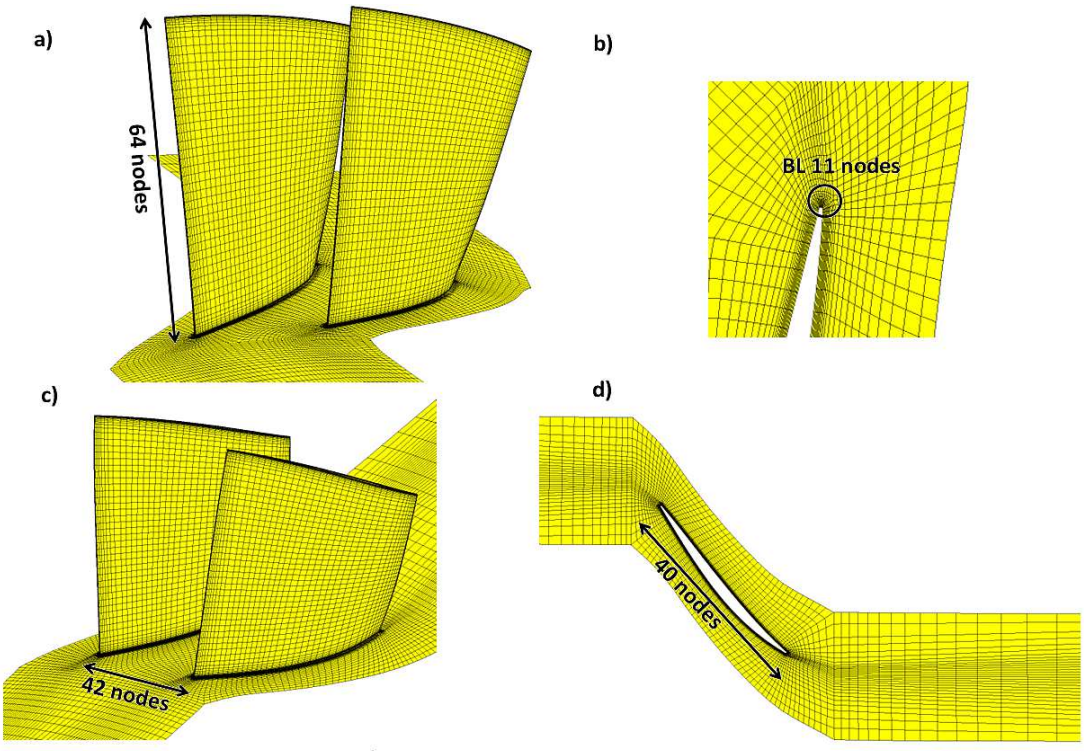

Figure 3.13: Rotor 37 baseline model showing mesh distribution: **a)** Span-wise. **b)** Boundary layer definition. **c)** Blade-to-blade pitch. **d)** Blade chord.

3.2.3 Configuration 3: Stage 67

During the course of the research, the model of Rotor 67 was upgraded by including downstream, the Stator 67B, and the convergent-divergent nozzle. The lessons learned from the grid dependency studies of the previous two rotor configurations were utilized during the modelling of this one stage geometry.

Similar mesh topology as before were used to create the three test cases for the Stator 67B grid dependency study. The K-epsilon turbulence scheme with the scalable wall functions was used in all three cases. It exhibited good compromise between the accuracy and the time required to simulate the full-annulus stage, and was therefore selected over the K-Omega SST model to save hefty computational

requirements. The Table 3.6 summarizes the full-annulus mesh size for the each case study.

Mesh Statistics		
Mesh	**Turbulence model**	**Elements**($1x10^6$)
Coarse	K-epsilon	5.9
Baseline	K-epsilon	7.7
Fine	K-epsilon	14.4

Table 3.6: Full-annulus Stage 67B mesh statistics for the grid dependency study.

The baseline model for the Stator 67B consisted of around 450,000 mesh elements per blade passage. Some illustrations of the developed mesh topology can be seen in Figures 3.14(a) and (b). An O grid made up of 10 span wise nodes was used to model the stator blade boundary layer. The outlet domain of the whole stage consists of a choked convergent-divergent nozzle. A number of meshes with different nozzle areas were created to control the mass-flow passing through the stage. A total number of 100 axial nodes were used within the conv-div nozzle section, as shown in Figure 3.14(a).

The mesh of the Rotor 67 was also upgraded from 500,000 to 850,000 elements per blade passage for this stage configuration. The key areas where the mesh density was increased is the inlet domain, the rotor blade passage, and the short rotor outlet between the rotor and the stator. Figures 3.14 (c) and (d) illustrate the new mesh for Rotor 67.

The combined full-annulus stage geometry consists of around 27 million nodes, and Table 3.7 summarizes the mesh count of the individual domains. The mesh resolutions at various parts of the stage can be observed from Figure 3.15. It highlights the differences in mesh density between the rotor mesh, and the stator domain. More details of the mesh quality differences on the overall flow field are provided in the next validation chapter.

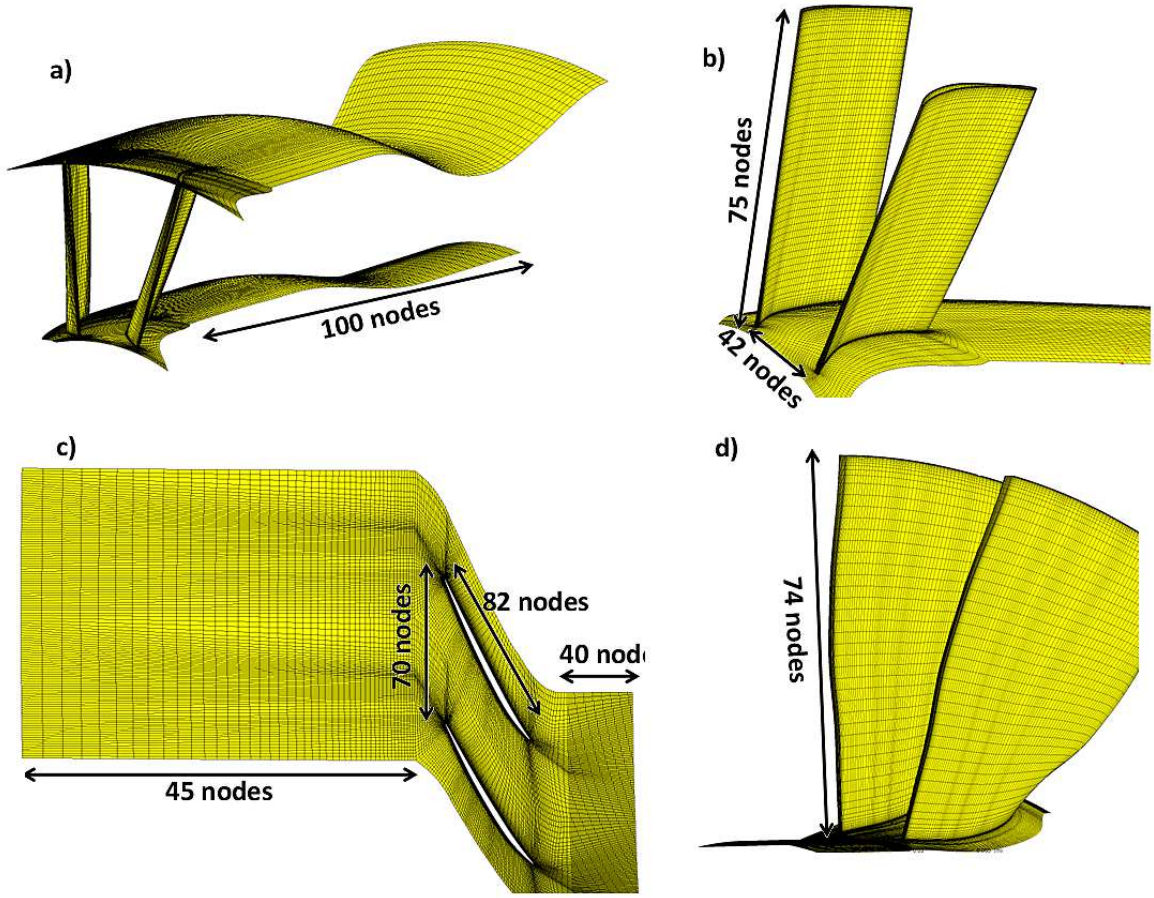

Figure 3.14: **a)** Baseline mesh of S67B with nozzle. **b)** Span-wise mesh distribution of S67B. **c)** Upgraded R67 passage mesh. **d)** Upgraded R67 span-wise mesh.

Mesh Summary	
Domain	**Elements**($1x10^6$)
Inlet domain	3
Rotor 67	16
Stator 67B(inc Nozzle)	8
Total	27

Table 3.7: Mesh summary of the full-annulus first Stage 67.

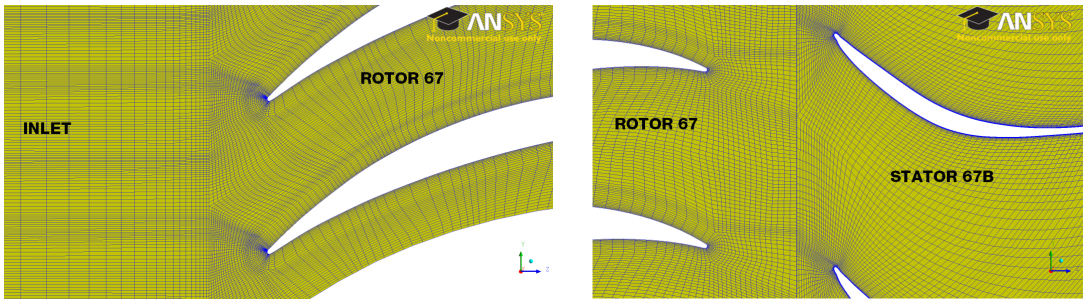

(a) (b)

Figure 3.15: Stage 67 mesh at hub span: a) Between inlet and rotor. b) Between rotor and stator.

3.3 Flow domains and interfaces

In all the above three configurations, i.e. the Rotor 67, the Rotor 37, and the Stage 67, the baseline mesh models were used for the distorted CFD simulations, although they had to be slightly adjusted depending on the boundary conditions, and the type of simulation. Firstly, the flow domains at the outlet were considerably extended for the distorted CFD cases. Also, the total number of domain interfaces, and the mesh size employed depended on whether the RANS or the URANS calculation was required.

3.3.1 Extension of the outlet domain

The configurations 1 and 2 represent the case studies for the isolated transonic rotors. The static pressure was imposed as an outlet boundary condition for these two setups. The approach adopted was to extend the outlet block a distance of around 10 times the rotor blade chord (at hub), this was done to allow the flow to be partially mixed before reaching the outlet. This is an important modification due to the lack of downstream stator for the flow straightening. Also, the imposition of highly swirling flows at the inlet can cause discrepancies in the CFD results with a short outlet, as the flow needs to be mixed for the outlet static pressure BC to work[26].

On the other hand, the Stage 67 model was created with the non-reflecting outlet boundary conditions by implementing a choked nozzle. So, for this configuration the outlet extension of 6 times the rotor blade chord (at hub) was deployed downstream of the Stator 67B, and kept constant for all the test cases. Table 3.8 below summarizes all the different domain extents for the three configurations. To note, the inlet was defined maximum around 3.5 times the rotor blade chord (at hub) for the Stage 67 configuration, and was found to be an adequate distance for all the distorted CFD cases.

Axial flow domain limits			
Configuration	**Inlet**	**Outlet**	**Elements**($1x10^6$)
Rotor 67 - Clean	$2.5 \cdot chord$	$3.5 \cdot chord$	11
Rotor 67- Distorted	$2.5 \cdot chord$	$10 \cdot chord$	12
Rotor 37 - Clean	$2 \cdot chord$	$3.2 \cdot chord$	11.1
Rotor 37- Distorted	$2 \cdot chord$	$10 \cdot chord$	14
Stage 67- Clean/distorted	$3.5 \cdot chord$	$6 \cdot chord$	27

Table 3.8: Comparison of the axial length scales for different configurations.

The number of nodes was also augmented to maintain the consistency in accordance with the outlet extension. As the outlet region far downstream of the turbo-components is not of utmost importance, therefore a low mesh grid could be used in this region, as compared with the inlet domain. The baseline meshes from the grid dependency were selected for the distorted CFD study. The full-annulus simulations have been carried out, and limited the total mesh size that could be employed. However, the mesh was considerably refined for the Configurations 1, and 2 in order to able to perform the URANS calculations. For the URANS simulations, in order to capture the required unsteady effects near the stability limit, the mesh had to be refined, especially within the blade passages and near the blade tip region[33]. Table 3.9 summarizes the mesh statistic for the full-annulus configurations.

Configuration	RANS cases ($1x10^6$)	URANS cases ($1x10^6$)
1- Rotor 67	12	18.5
2- Rotor 37	14	25
3- Stage 67	27	27

Table 3.9: Mesh sizes: Comparison of the full-annulus mesh count for the distorted RANS and URANS CFD simulations.

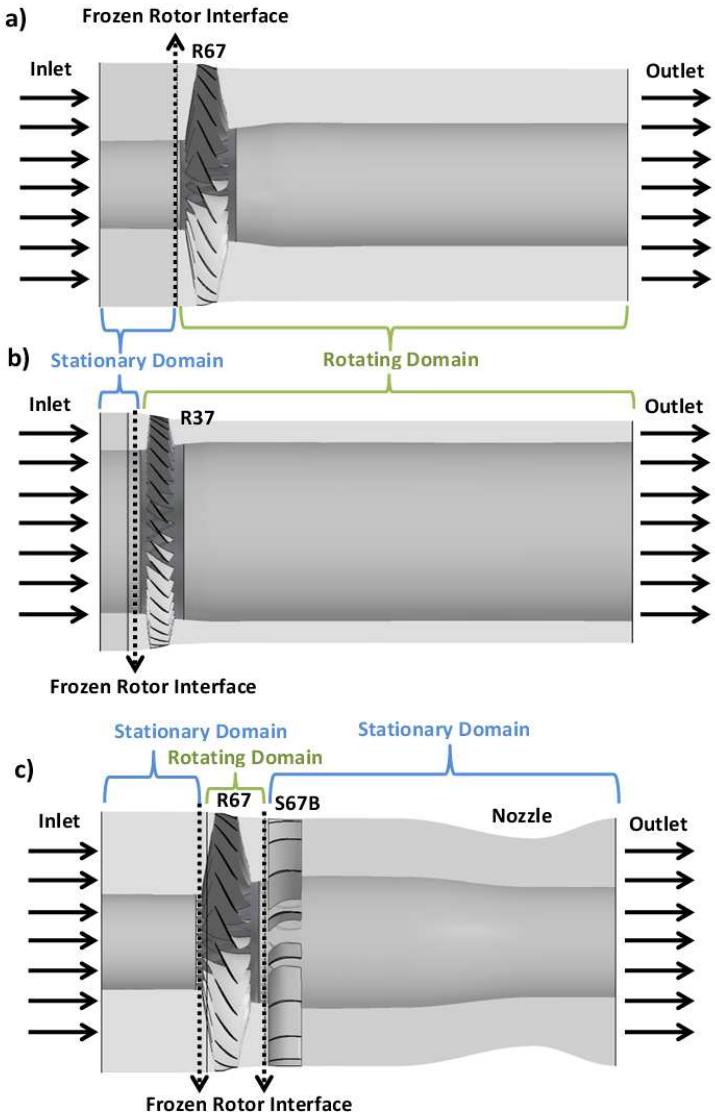

Figure 3.16: The definition of flow domains for RANS simulation. **a)** Isolated Rotor 67. **b)** Isolated Rotor 37. **c)** First Stage 67.

3.3.2 CFD domains for RANS and URANS calculations

There is one critical alteration in terms of the number of domains employed for the RANS, and the URANS simulations. As the RANS calculations produces the time-averaged motion of the fluid, a stationary domain have to be employed upstream of the rotor passage. It was a necessary requirement in order to impose the asymmetric distorted flows (e.g. ingestion of vortices) at the inlet. It is followed by a rotating domain of the rotor, and another stationary domain, if the Stage 67 is being simulated. All the stationary, and the rotating domains are separated by the frozen rotor interface as shown in Figure 3.16.

As the URANS calculations produces the real motion of the fluid depending on the user time-marching settings, the use of a single inlet rotor domain in all the above configurations was found to be more attractive. The rationale behind this was the concern about the mesh interface between the inlet domain, and the rotating rotor passage, which can cause certain disparities in the flow properties across the interface. Also, this approach would save a hefty computational time, and the mesh requirements to perform the Stage 67 simulations, where the use of already one stationary stator domain can not be avoided. The transient rotor-stator interface was deployed at this boundary. Figure 3.17 shows the set-up of the domains for the URANS simulations.

However, the use of a single domain raised an additional concern associated with the implementation of the non axis-symmetric boundary conditions at the inlet, e.g., during the ingestion of a vortex. As the whole domain was set as rotating, so did the inlet plane. For this reason, the ingestion location of vortex at the inlet was updated every time step. This was done to simulate a vortex ingestion, in the stationary position with respect to the rotating compressor, when observing from the absolute frame of reference. This was resolved by employing for the URANS cases an expression at the inlet plane. This input expression rotates the vortex position opposite to the domain rotation (ω), depending on the rotor timestep (t) value. The following expression in Equation 3.1 was integrated into the inlet boundary condition (BC) expressions.

$$\zeta(t) = \zeta(t-1) - \omega.\Delta t \tag{3.1}$$

Where, ζ is the function of the vortex inlet position in terms of the radius (r), and the angular position (θ).

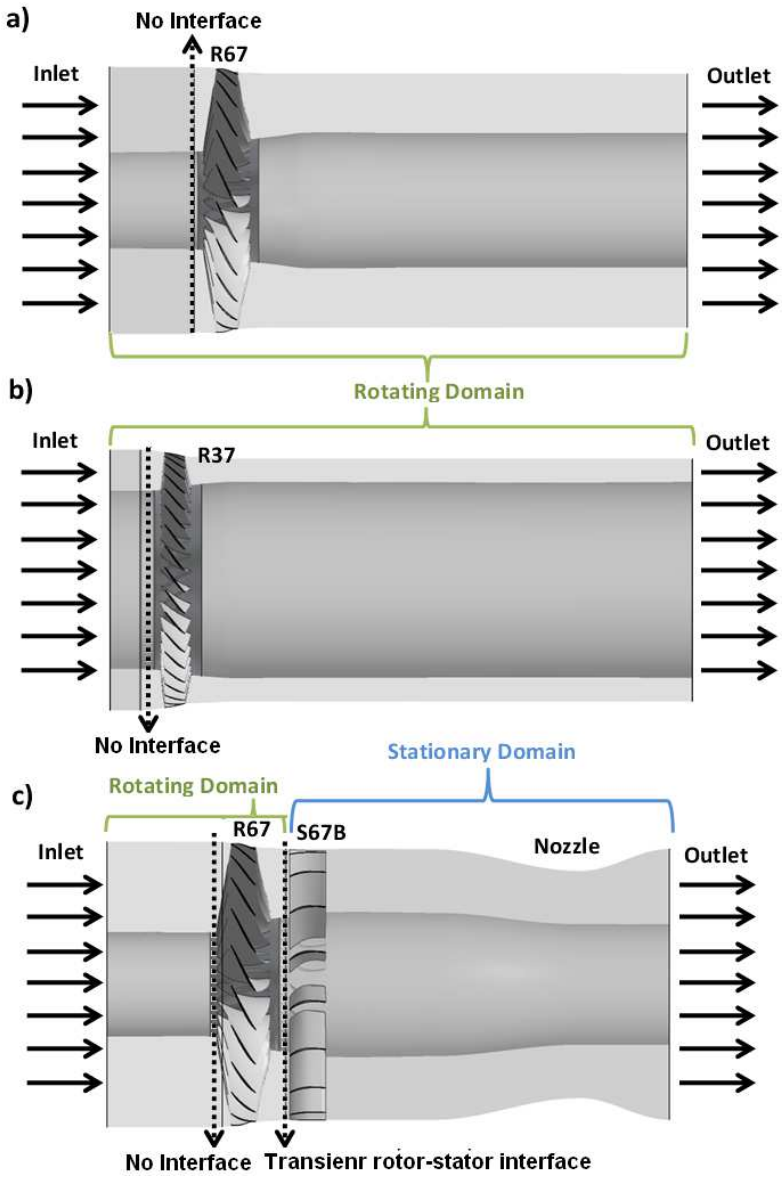

Figure 3.17: The definition of flow domains for URANS simulation. **a)** Isolated Rotor 67. **b)** Isolated Rotor 37. **c)** First Stage 67.

3.4 CFD approach

In this section, the steps taken to implement the appropriate CFD settings for the above configurations are explained. The CFD settings such as the boundary conditions (BC), the convergence criterion, the types of simulation, and the developed post-processing tools are discussed. To point out, most of the CFD approaches are totally applicable for each configuration, therefore only the differences will be highlighted where appropriate.

3.4.1 Governing equations

The mathematics of the Computational Fluid Dynamics (CFD) are based on solving the Navier-Stokes (NS) equations, which describe the processes of momentum, mass, and heat transfer. These partial differential equations were first derived in the 19^{th} century. The equations does not have a general analytical solution, therefore these can be discretized, and solved numerically[3]. Usually, an approximate set of the Navier-Stokes (NS) equations are used in conjunction with other models, e.g., the turbulence models being a particularly important one. This is done to achieve in some cases quicker, and more reliable CFD results.[3]

A commercial CFD software, CFX (12.1-14.0) was utilized to carry out the numerical simulations for the study. A number of the NS solution methods have been developed over the years. The finite volume technique to solve the NS equations is one of the most common, and the CFX is based on this method[5]. The set of equations solved by CFX are the unsteady NS equations in their conservation form. Its foundation is based on the NS transport equations, which takes into account the mass flow continuity, the conservation of momentum, and the total energy terms, as illustrated in the following expressions.

Mass flow continuity:

$$\frac{\partial \rho}{\partial t} + \nabla \cdot (\rho U) = 0 \tag{3.2}$$

Conservation of momentum:

$$\frac{\partial (\rho U)}{\partial t} + \nabla \cdot [\rho U \otimes U] = -\nabla p + \nabla \cdot \tau + S_M \tag{3.3}$$

Where the stress tensor, τ, is related to the strain rate by

$$\tau = \mu \left(\nabla U + (\nabla U)^T - \frac{2}{3} \delta \nabla \cdot U \right) \tag{3.4}$$

Conservation of total energy:

$$\frac{\partial(\rho h_{tot})}{\partial t} - \frac{\partial p}{\partial t} + \nabla \cdot (\rho U h_{tot}) = \nabla \cdot (\tau \cdot U) + \nabla \cdot (\lambda \nabla T) + U.S_M + S_E \tag{3.5}$$

Where h_{tot} is the total enthalpy, which can be related to static enthalpy h(T,p) by:

$$h_{tot} = h + \frac{1}{2} U^2 \tag{3.6}$$

The term $\nabla \cdot (\tau \cdot U)$ represents the work due to viscous stresses, and usually refers to as viscous work term. It is used to model the internal heating by viscosity in the fluid, and in most flows is negligible.

The above transport equations are modified for the Reynolds Averaged Navier-Stokes (RANS) and the Unsteady Reynolds Averaged Navier-Stokes (URANS) calculations along with the inclusion of equation of states, and the additional source terms to model the flow turbulence[3]. These set of equations can also be altered and used for a lower order 2-D or even 1-D flow problems.

In this study, the 3-D numerical simulations of turbo-machinery have been performed with either the RANS or the URANS method. RANS approach calculates the time-averaged flow solutions, and, therefore, an approximation to the real flow behaviour. URANS on the other-side, calculates the flow behaviour between the set of time-intervals, also known as the time-steps, which are defined by the user. Thus, it provides a more insightful approach in to understanding the unsteady flow behaviour. However, both these approaches have been used commonly in the past for the turbo-machinery applications, and have their own pros and cons[3,26].

More specific details of the numerical models in CFX for the turbo-machinery applications can be found in ANSYS Solver Modelling guide[5], and therefore will not be examined further.

3.4.2 General CFD settings

As mentioned, various RANS and URANS simulations were performed in the research project. The author capitalized on the valuable knowledge gained during the initial RANS and URANS runs on the Rotor 67, and the Rotor 37 to launch simulations for the swirl distortion parametric studies. The simulations of Rotor 67 and Rotor 37 were performed at, $N = 100\%$. This includes the validation studies under the undistorted uniform (clean) flow conditions, and also the various distortion simulations carried out on these two configurations. On the other hand, the Stage 67 simulations were run at two rotor speeds, which were, $N = 100\%$, and $N = 90\%$. Some of the basic settings that were implemented to create a credible numerical CFD tool are discussed below.

1. **Advection scheme and energy equation**: A high-resolution advection scheme of CFX was used for the discretization of the advection terms of Navier-Stokes equation system. This advection scheme works more time efficiently than the standard 2nd order scheme in most of the commercial CFD solvers. It uses the first order advection scheme in the domain wherever small variable gradients are present. But then switches to the second order by means of a blending factor as the gradient of the CFD solution exceeds a limit, and requires the switching for a better accuracy[5].

   The flow within the compressor domains was considered to be compressible and adiabatic at standard sea level conditions. Moreover, due to nature of the numerical studies conducted, transonic regimes were reached throughout the computational domains. Therefore, the compressibility effects couldn't be neglected for sure. Consequently, the energy equation within the CFX solver[5] was utilized to take into account the compressibility effects of the flow.

2. **Turbulence Model**: Two commonly used turbulence models were investigated during the study, namely, the K-Epsilon (with scalable wall functions)[45], and the K-Omega SST models[54]. As discussed before, the flow

physics of the swirl distortion is characterized by complex secondary flows, and adverse pressure gradients on the turbo-machinery aerodynamics. Thus, these conditions required a high demand from the turbulence modelling. Therefore, two equation turbulence model was more desirable than one equation turbulence scheme for the research study.

However, it should be highlighted here that only few simulations were performed using the K-Omega SST model due to hefty computational power requirement. The grid dependency in the next chapter discusses the feasibility of the K-Omega SST model experienced during the validation studies. The K-Epsilon (with scalable wall functions) model was found to be more suitable, as it not only achieves a good accuracy, but also the running times compared with the K-Omega SST was much less. The first transported variable is turbulent kinetic energy, k. The second transported variable in this case is the turbulent dissipation, ϵ. It is the variable that determines the scale of the turbulence, whereas the first variable, k, determines the energy in the turbulence. However, the standard K-epsilon turbulence model is known to perform poorly for the highly separated flows near the walls but is still widely used for its robustness.

To overcome the inability of K-epsilon model to model the highly separated flows, it was combined with the scalable wall functions that improves the prediction of flow separation. Launder and Spalding[45] developed a series of wall functions that can be implemented with the standard K-epsilon scheme. These wall functions switches to higher order turbulence near the regions where the flow becomes highly separated by recalculating the near wall values of turbulent kinetic energy, k , depending on the wall viscosity, by using a modified term[45]. More information on the details of the turbulence models within the CFX framework is beyond the scope of the document but can be found in the modelling guide[5], and more information of the turbulence equations can also be found in the literature[45,54].

Thus, the use of wall functions was concluded to be suitable compromise

as it can save hefty computational requirement of the SST model, and on the other side can also overcome the inefficiencies of the standard K-epsilon model. Therefore, in order to be consistent throughout the analysis, and also to be able to perform a large number of the swirl distortion simulations in the most efficient manner, the K-epsilon model with the scalable wall functions was chosen. It was used for all the swirl distortion studies within the research.

3. **Solver and the Convergence Criterion:** The average momentum, mass and energy residuals recommended value is $1x10^{-5}$. For the CFD simulations performed, the Root Mean Square (RMS) values reached as low as $1x10^{-7}$ for most of the RANS, and also the URANS simulations. The residuals were monitored together with some of the flow variables at the inlet and the outlet, for a better accurate convergence. The criterion for the convergence was not limited to monitoring the magnitudes of certain flow parameters but also checking the spatial periodicity of the variable. For example, the mass flow, which have to be conserved at the inlet and the outlet, was constantly compared to ensure a converged solution.

Figure 3.18, show example of one of the convergence criterion. The mass-flow evolution for a RANS simulation of the Rotor 67, and the Stage 67, measured at the domain inlet and outlet is illustrated. It is describing several different outlet BCs, the black vertical lines in the chart are used to distinguish the change in the outlet throttle setting. When the mass flow at the domain inlet and outlet becomes constant and equal along with the residual values, the simulation can be considered as converged. Thus, the static pressure/nozzle area at the outlet can be changed for the new case.

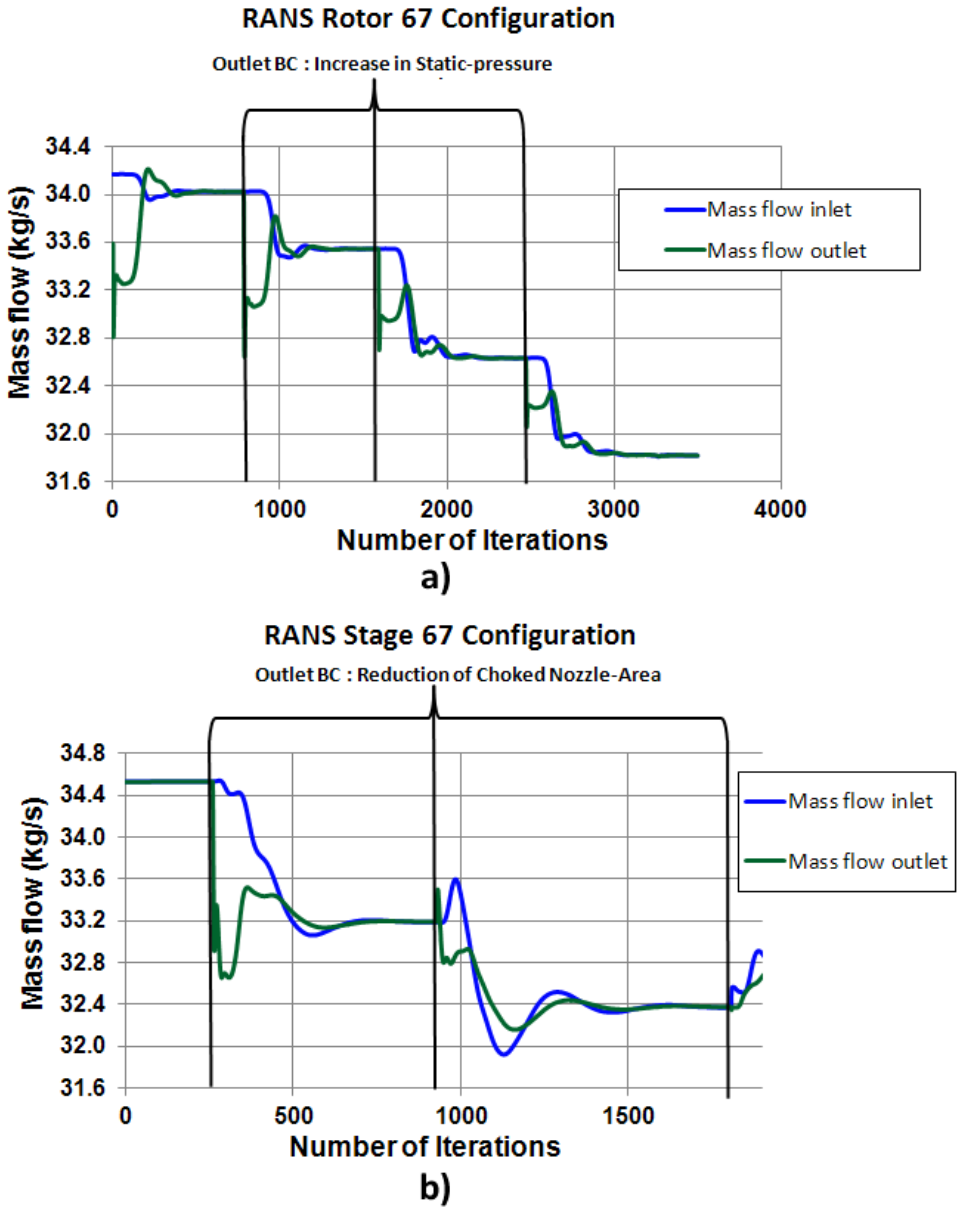

Figure 3.18: RANS simulation mass-flow evolution of **a)** Rotor 67. **b)** Stage 67.

When performing the URANS calculations, and in order to ensure convergence in this type of simulation, several monitor points within the domain were also introduced. To investigate the transient behaviour of a compressor, the use of several monitor points within the CFD domains is highly recommended[26,31]. This not only enable the user to record the transient flow behaviour and convergence within the domain but can also be used as an indication tool for the instabilities inception in the compression system. For the research study, three

monitor points per blade passage were placed to record the time traced values of the static pressure, the total pressure, and the axial velocity. Two of these monitor points were placed 30% chord (mid-span) upstream, and downstream of the rotor blade passage. These were placed at 90% blade span, and the last monitor point was positioned at the exit of the domains, as shown in the example of Stage 67 in Figure 3.19.

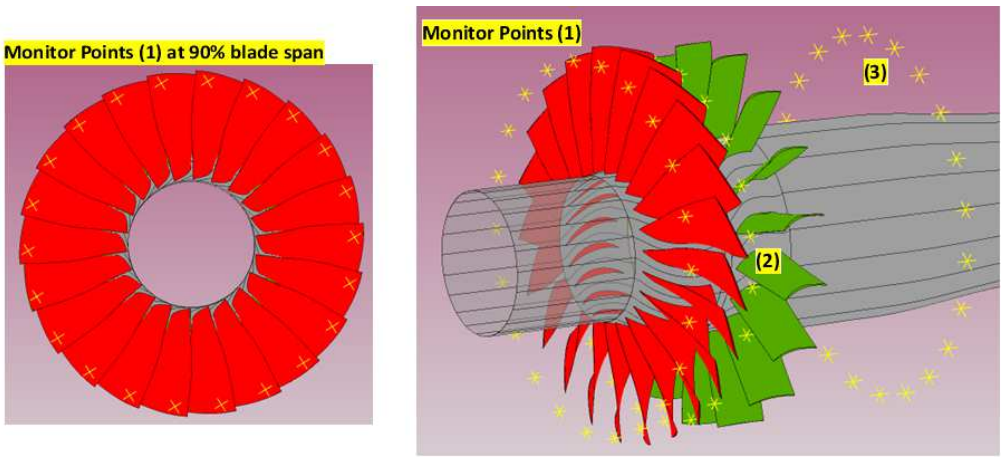

Figure 3.19: Example: NASA Stage 67 flow domain with monitor points.

As far as, the number of iterations to reach a converged solution is concerned, it was most importantly depended on the type of simulation, and the inlet BCs. To note, as the URANS simulations required two set of time-scales as a user input, the iteration scheme for the URANS was different than the former.

3.5 Boundary conditions

Definition of the accurate boundary conditions (BC) for any CFD based model is an important task. Especially, when the non-uniform distorted boundary conditions have to be implemented, this formed as one of the key tasks for the research progress. This section illustrates the methodology developed within the CFD tool kit to tackle these issues.

3.5.1 Inlet

A methodology was developed to impose the pure bulk swirl, and the tightly-wound vortex at the inlet plane of the modelled configurations. This was crucial to the project success as it saved hefty computational resources by enabling the prescription and control of the required flow distortion at the inlet. This avoided the necessity of including the source of the distortion in the CFD domain.

For all the clean (uniform axial flow) simulations, the ambient total pressure of 101325[Pa], and the total temperature of 288.15[K] was used at the inlet. The flow direction was set to be perpendicular to the inlet plane.

On the other hand, for the distorted simulations, CEL (CFX Expression Language)[5] was used to input into the pre-processor (CFX-pre 12.1-14.0) the required flow distortion patterns in terms of the velocity direction, and the total pressure distribution at the domain inlet. The inlet total temperature of 288.15[K] was kept constant for all the numerical simulations. The following section provides the explanation of the expressions developed to impose the two types of swirl distortion (i.e., the bulk and the tightly-wound vortex) using the CEL expressions.

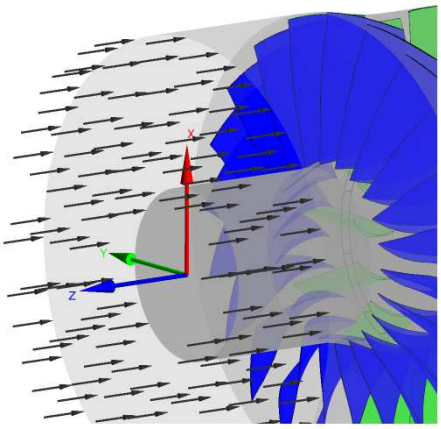

Figure 3.20: Creation of a new coordinate system for the imposition of swirl at the inlet.

Before going into the details of the distorted BC's, the Figure 3.20 is illustrating one of the model domain with a coordinate system at the center of the

compression system. This coordinate system was created for the user-defined functions of the inlet BC's, and is called the global coordinate system hereafter. This was centered on the axis of the rotor with the positive axial direction, in the same direction as the rotor rotation (anti-clockwise). The coordinate system have to be created for the implementation of CEL expressions, so the appropriate swirl pattern can be imposed at the inlet. Following are the inlet BC's for the two types of swirl patterns investigated:

1. **Pure bulk swirl:**

   The main characteristics of a pure bulk swirl pattern is the presence of a constant swirl angle (α_{Bulk}) across the engine inlet. Therefore, apart from specifying the ambient total pressure and total temperature, the following CEL expressions in Equation 3.7 were utilized to vary the direction of the circumferential velocity component (V_θ). This depends on the value, and the direction of swirl angle (α_{Bulk}).

   In CFX, the direction of the inlet flow can be altered as a BC by changing the unit velocity components (ρ, ξ, σ). These are in the polar coordinates (see Equation 3.7), which can be prescribed at the inlet plane using the global coordinate system. Thus, the unit velocity in the tangential (bulk swirl) (ξ), and consequently, in the axial (σ) direction can be varied using this method. Just to clear any ambiguity in the below formulation that the value of axial velocity (V_z) is an arbitrary, and has no effect on the velocity direction or magnitude. The key input is the value, and the direction of swirl angle α_{Bulk}, by which a range of pure bulk swirl patterns can be numerically prescribed at the inlet.

$$\begin{cases} V_z = V_\infty \\ V_r = 0 \\ V_\theta = V_z \cdot \tan\left(\pm\alpha_{Bulk}\right) \\ \|V\| = \sqrt{{V_z}^2 + {V_\theta}^2} \\ \sigma = \frac{V_z}{\|V\|} \\ \rho = \frac{V_r}{\|V\|} = 0 \\ \xi = \frac{V_\theta}{\|V\|} \end{cases} \tag{3.7}$$

2. **Tightly-wound vortex:**

   For CFD purposes, the distribution of a localized vortex topology at the inlet plane can be expressed using a series of user defined CEL expressions. However, there are some key parameters regarding the vortex characteristics that can be considered as the user inputs, and have to be prescribed in the vortex BC's, which are:

   - Vortex circulation (strength) and direction, $\pm\Gamma[m^2 s^{-1}]$.
   - Vortex core size, $r_c[m]$.
   - Vortex radial location, $r_v[m]$.
   - Excess or deficit of axial velocity within the vortex, $\pm\Delta V_z^*[-]$.

   The methods for calculating these user inputs for numerical purposes is the subject of next section. Methodology of how to implement the vortex flow-field as a part of the inlet BC's, is explained hereafter.

   Once the above four vortex flow-field features are known for a particular case study, the Vatistas vortex model (see Appendix B) can be used to generate the circumferential velocity V_θ distribution[35]. In Equation 3.8, the V_θ is expressed in relation with the vortex center. However, for the prescription as a BC for the CFD studies, it was found to be more useful to be able to prescribe the vortex structure using a global coordinate system (see Figure 3.20). This method of expressing the vortex flow-field distribu-

tion in a generalized reference system, especially for the turbo-machinery applications is also proposed by McLelland et al.[53].

$$V_\theta(r) = \left(\frac{\Gamma}{2\pi r_c}\right) \frac{\bar{r}}{\left(1+\bar{r}^{2n}\right)^{1/n}} \tag{3.8}$$

Figure 3.21 illustrates the transformation of the user coordinate system for a vortex flow-field from local, V, to the global system, O. The point O refers the axis of the global coordinate system, where the inlet BC for the rotor configurations have to be prescribed. So, for example, if a vortex having its own local coordinate frame at center V, have to be identified in the global coordinate system, it will be $({}^{G}r_v, {}^{G}\theta_v)$. The global position of a generic point P in the vortex flow-field can be described as $({}^{G}r_P, {}^{G}\theta_P)$. Similarly, the position of a generic point P in the vortex local frame is described as $({}^{L}r_P, {}^{L}\theta_P)$, and the vortex center is described as $({}^{L}r_v, {}^{L}\theta_v)$.

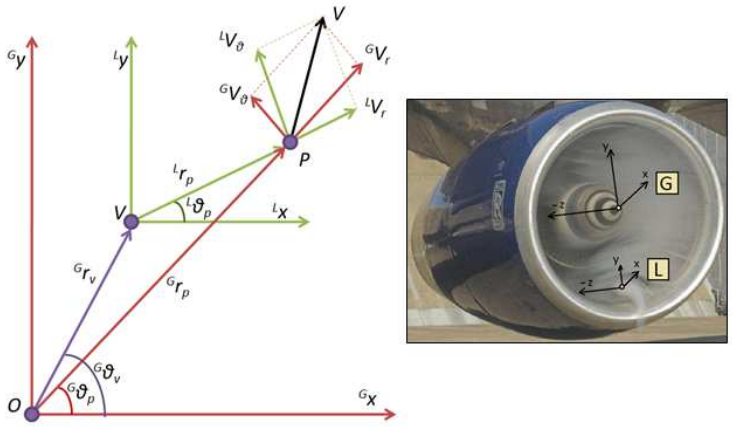

Figure 3.21: Definition of global and local coordinate systems for vortex flow-field.

Thus, once all the local vortex velocity components are identified, the transformation process can be started. The transformation of the tangential ${}^{L}V_\theta$, and the radial ${}^{L}V_r$ components from the local to the global frame can be performed using[53]:

$${}^{G}V_\theta = {}^{L}V_\theta \cos({}^{G}\theta_P - {}^{L}\theta_P) - {}^{L}V_r \sin({}^{G}\theta_P - {}^{L}\theta_P) \tag{3.9}$$

and

$$ {}^{G}V_r = {}^{L}V_\theta \sin({}^{G}\theta_P - {}^{L}\theta_P) + {}^{L}V_r \cos({}^{G}\theta_P - {}^{L}\theta_P) \tag{3.10} $$

Where, ${}^{L}V_\theta$ was derived from Equation B.6 by replacing r with ${}^{L}r_P$. The local radial velocity component ${}^{L}V_r$ of the vortex (Equation B.8 in Appendix B) is multiplied by the kinematic viscosity of the air, and results in a very small overall contribution, and therefore was neglected in the current methodology[41].

As a result, the expressions for tangential ${}^{G}V_\theta$ and radial ${}^{G}V_r$ of the vortex profiles in the global coordinate system can be generated, and used for the CFD simulations. And as expected, the expression for the axial velocity component does not change between the global and the local coordinate frames, and can be written as:

$$ {}^{G}V_z = V_\infty - \frac{A}{z}\left[1 - \frac{({}^{L}r_P)^2}{(r_c^{2n} + ({}^{L}r_P)^{2n})^{\frac{1}{n}}}\right] \tag{3.11} $$

The value of n (Vatistas shape factor) depends on the vortex flow-field, and A is known as wake axial momentum constant, whereas, z is the axial position [m].

To specify the total pressure distribution, an expression of the static pressure profile derived from the radial momentum equation can be used, which is written as[53]:

$$ p = p_\infty + \frac{\pi\rho}{4}\left[\frac{\Gamma}{2\pi r_c}\right]^2 \left[\frac{2}{\pi}\arctan\left(\frac{{}^{L}r_P}{r_c}\right)^2 - 1\right] \tag{3.12} $$

To note, the above static-pressure distribution is valid for the Vatistas shape factor $n = 1$, which was used in the current study. A vortex is assumed to be within an incompressible flow region, thus according to Bernoulli, the total pressure can be expressed as:

$$p_0 = p + \frac{1}{2}\rho\left({}^{G}V_{\theta}^{2} + {}^{G}V_{r}^{2} + {}^{G}V_{z}^{2}\right) \tag{3.13}$$

Thus, all the above four flow variables (i.e., ${}^{G}V_{\theta}$, ${}^{G}V_{r}$, ${}^{G}V_{z}$, and p_0) profiles in the global coordinate system were essentially formed into an inlet BC methodology, and written as the CEL expressions for CFX (12.1-14.0). This was found to be an efficient way of modelling the vortex for the numerical simulations. The equations illustrated above are generic, as not shown in the actual CEL form, and therefore can be implemented within any coding environment. The following Equation 3.14 illustrates the unit velocity components in the radial (ρ), circumferential (ξ), and axial(σ) direction. The global coordinate system was used to prescribe these velocity unit vectors at the domain inlet, along with the distribution of the total pressure.

$$\begin{cases} \mid {}^{G}V \mid = \sqrt{\left({}^{G}V_{\theta}\right)^2 + \left({}^{G}V_{r}\right)^2 + \left({}^{G}V_{z}\right)^2} \\ \rho = \frac{{}^{G}V_{r}}{|{}^{G}V|} \\ \xi = \frac{{}^{G}V_{\theta}}{|{}^{G}V|} \\ \sigma = \frac{{}^{G}V_{z}}{|{}^{G}V|} \end{cases} \tag{3.14}$$

3.5.2 Outlet

For the Rotor 67 and 37 configurations, a constant static-pressure (P_s) distribution was defined at the outlet boundary, to form as the throttle setting of compression system. ANSYS CFX (12.1-14.0) offers a blending factor option, which allows a certain radial variation in the outlet static pressure, depending on the user-defined value. A value of 5% was chosen and was found to be adequate for the outlet flow. The static pressure at the outlet was varied to control the mass flow entering the compression system. As stated before, the outlet domains were extended for the distorted cases. This allowed the outflow of rotor to be mixed properly prior to the domain exit. The values of the outlet static-pressure (P_s) were non-dimensionlised using the following Equation 3.15. Where, the $\overline{P}_{s,choke}$

stands for the area-averaged static pressure for the undistorted (clean) case at near choking. Using this ratio of the static-pressures allowed to follow a consistent change in the throttle setting for the different modelled configurations.

$$P_s^* = \frac{P_s}{\overline{P}_{s,near-choke}} \tag{3.15}$$

The use of a convergent-divergent nozzle was investigated to control the Stage 67 (Configuration 3) mass-flow. It also provided a method to analyse the performance changes due to the flow distortion at constant throttle settings to the nominal (uniform axial flow) conditions. The constant throttle setting means that the compression system is operating at constant outlet non-dimensional mass-flow (NDMF). This approach works due to the characteristics of a choked convergent-divergent nozzle, where a Mach number at the throat of the nozzle equals to unity.

So, a nozzle with a fixed geometry and constant gas properties (γ,c_p), will exhibit constant non dimensional mass flow ($NDMF$) at the throat. Equation 3.16 shows definition of $NDMF$, and for the choked throat, it can written as Equation 3.17. Thus, Equation 3.18 illustrates that the mass flow depends on the total pressure and total temperature, and the area of the choked nozzle.

$$NDMF = \frac{\dot{m}\sqrt{T}}{A \cdot P} = M\sqrt{\frac{\gamma}{R}}\left\{1 + \frac{\gamma - 1}{2}M^2\right\}^{-\frac{\gamma+1}{2(\gamma-1)}} \tag{3.16}$$

$$NDMF\ |_{M=1} = \sqrt{\frac{\gamma}{R}}\left\{\frac{\gamma + 1}{2}\right\}^{-\frac{\gamma+1}{2(\gamma-1)}} \tag{3.17}$$

$$\dot{m}\ |_{M=1} = \frac{A \cdot P}{\sqrt{T}}\sqrt{\frac{\gamma}{R}}\left\{\frac{\gamma + 1}{2}\right\}^{-\frac{\gamma+1}{2(\gamma-1)}} \tag{3.18}$$

Assuming air ideal gas behaviour, steady-state choked flow occurs when downstream static pressure falls below a critical value p^*. That critical value can be calculated from the dimensionless critical pressure ratio as shown in Equation 3.19. Thus, by assuming γ to be 1.4 at ideal conditions, then $p^* = 0.528P_o$, which means that, choked flow should occur at the tested throat when the downstream static pressure drops to below 0.528 times the upstream absolute total pressure.

$$\frac{p^*}{P_o} = \frac{2}{\gamma + 1}^{\frac{\gamma}{\gamma - 1}} \tag{3.19}$$

Where, p^* = critical static pressure at a choked throat, and P_o = Total pressure upstream of the convergent-divergent nozzle.

The Figure 3.22 show an example of the Stage 67 static pressure conditions near the choked nozzle. This is shown for a case study at the design conditions, when operating at $N = 100\%$ rotational speed. The upstream total pressure is in the range of 160000 [Pa], thus resulting the p^* of about 84500 [Pa]. From the Figure 3.22, it can be clearly observed that the throat static pressure in this particular case was about 72000 [Pa], which is below the required value. Thus, it satisfies the critical static pressure condition and the nozzle can be assumed as a choked nozzle. Thus, this check was performed for the all the simulated operating conditions in the compressor map to make sure the nozzle is operating under choked flow conditions.

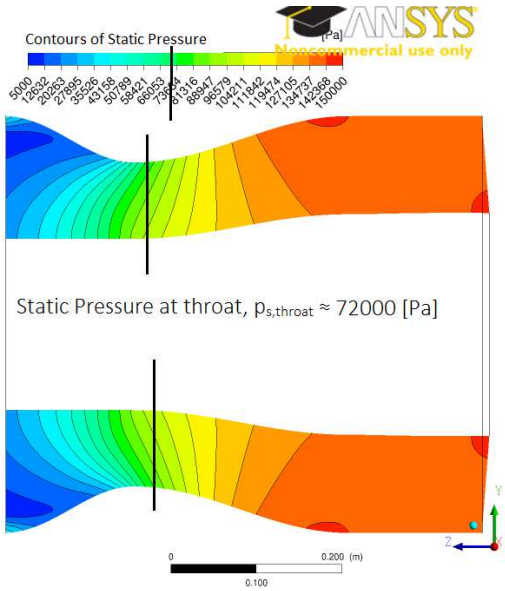

Figure 3.22: Example of static pressure contour at the throat sliced section. Stage 67 configuration operating at design conditions.

To use the convergent-divergent nozzle in a consistent manner, the important parameters were non-dimensionlised, as shown in Equation 3.20. The critical conditions have been established as the values for near choke operating conditions

of the compressor map. Thus, as the ratio of nozzle throat area $\frac{A}{A_{crit}}$ reduces, so does the mass-flow of the compression system, bringing the operating condition from near choke to near stall. The range of the $\frac{A}{A_{crit}}$ have been chosen in a consistent and a careful manner to enable a wide range of mass-flows for the flow distortion parametric studies. The size factors used in the research for the two rotational speeds of Stage 67 are shown in Table 3.10. It was important to select a wide range of nozzle areas where the stage didnt go into stall but as near to the onset of instabilities as possible. It can be notice that 13 nozzle areas were created; however, in most cases upto 6 were used for each speed-line, and is discussed further in the results.

$$\dot{m} = \dot{m}_{crit} \cdot \frac{A}{A_{crit}} \cdot \frac{\overline{PR}}{\overline{PR}_{crit}} \cdot \frac{\overline{TR}}{\overline{TR}_{crit}} \tag{3.20}$$

No.	$\frac{A}{A_{crit}}$	Throat area $[m^2]$	Mass flow$[kg/s]$	Mass flow$[kg/s]$
			$N = 90\%$	$N = 100\%$
A1	1	0.102	32.3(Near-choke)	34.53(Near-choke)
A2	0.98	0.1	-	34.44
A3	0.96	0.098	-	34.24
A4	0.95	0.0972	-	34.11
A5	0.941	0.096	-	33.97
A6	0.922	0.094	30.9(Near-design)	33.5(Near-design)
A7	0.912	0.093	-	33.14
A8	0.902	0.092	-	32.97
A9	0.892	0.091	-	32.80
A10	0.882	0.090	30.03	32.37(Near-stall)
A11	0.88	0.089	29.36	-
A12	0.86	0.087	28.646	-
A13	0.84	0.085	27.90(Near-stall)	-

Table 3.10: Stage 67 specifications of different nozzle throat areas and mass-flows.

The above approach to generate the compressor map database proved use-

ful especially for the vortex features parametric study, and helped to build a consistent methodology for the flow descriptor correlations.

3.5.3 Other

The following are the three wall boundaries imposed within the CFD domains:

- Blades
- Hub
- Shroud

For all the above three wall boundaries, no slip conditions were selected. Also, the rotor blades were set as rotating at the two rotational speeds, whereas the stator blades were set as stationary in the absolute frame. The hub associated with the rotor blades was set as a rotating no-slip wall. All the other hub and shroud regions were set as stationary no-slip walls in the absolute frame, as shown in Figure 3.23(a).

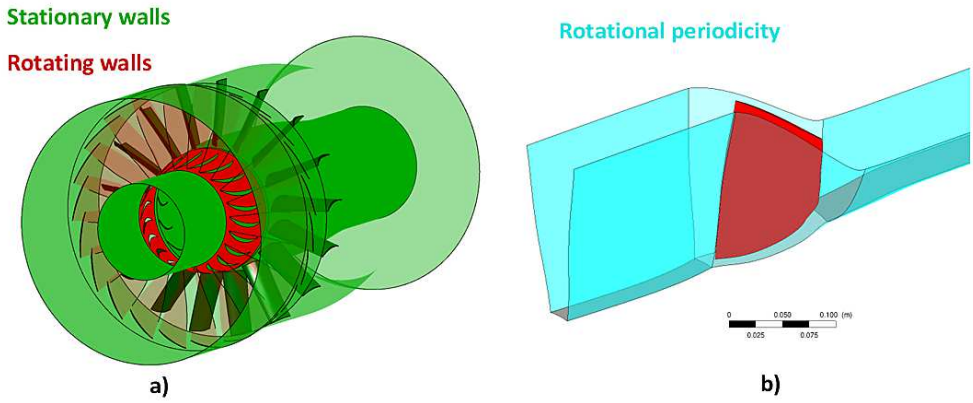

Figure 3.23: **a)** Stage 67 wall boundary conditions. **b)** Rotor 67 periodic BCs.

One flow passage simulations were carried out only on the Rotor 67 and 37 configurations. Uniform axial flow (clean), and the pure bulk swirl cases were performed modeling a single rotor passage during the study. Therefore, in these cases, periodic BC on each side of the passage was chosen to take into account the rotational periodicity (Figure 3.23(b)).

3.6 Test Matrix of the swirl distortion

In this section, the numerical test matrix of the two swirl distortion patterns, i.e., the bulk swirl, and the tightly-wound vortex, is discussed.

3.6.1 Pure bulk swirl

A number of RANS and URANS simulations were performed on the Rotor 67 and the Rotor 37 under the influence of bulk swirl. Whereas, a detailed RANS parametric study of the influence of bulk swirl on the Stage 67 was also undertaken. The complete test matrix is illustrated Table D.1 of Appendix D.

3.6.2 Tightly-wound vortex

There are many types of vortex generation mechanisms, ranging from external wing-tip vortex to the ingestion of ground vortex, and also the self-generated vortices within the s-shaped ducts. For this work, a methodology was developed to model a strong discrete vortex, which can be then used as a datum case for the vortex ingestion CFD parametric study. This strong discrete vortex datum case was chosen to be a representation of a ground vortex (see Appendix A and C). However, the parametric study involved varying many of the vortex flow features (e.g., vortex size, strength, location and polarity), thus removing the categorising factor of being only limited as a ground vortex.

3.6.2.1 Modelling the datum vortex case

Referring back to the inlet BC's section, some key inputs regarding the vortex characteristics is required by the user to be able to utilize the aforementioned inlet BC methodology (Section 3.5.1). These include the vortex circulation, size, excess velocity, the ingestion location, and the total-pressure field. Following approach has been considered to generate the datum vortex topology.

The prediction of the datum vortex circulation was carried out by using an empirical model for ground vortex ingestion developed by Murphy[59]. More

explanation of this model is presented in Appendix C. The modelled vortex is assumed to be generated by a cross-wind configuration (i.e. almost a worst case scenario for a ground vortex), considering a non-dimensional height $H/D_i \approx 0.5$, and the velocity ratio $U_{in}/U_\infty \approx 6$. These values were chosen after carrying out an detail study of varying the H/D_i and U_{in}/U_∞, as explained in more detail in [14]. The values chosen are the representation of modern intake sizes, and the velocity ratios achieved at the inlet. As a result, a datum value of vortex circulation, Γ of $22.1[m^2.s^{-1}]$ was calculated (see Table 3.12).

Other parameters that have to be specified were: the vortex core diameter ($2 \cdot r_c$), which was chosen to be 6% of the intake inner diameter D_i, and the Vastistas shape factor $n = 1$ was selected. Other researchers[41,60] have consistently found shape factor n = 1, and the vortex core diameter, $2r_c \approx 6\%D_i$, suitable for ground vortices. This value has also been reported by Murphy[59], during the sub-scale wind tunnel experiments of ground vortex ingestions.

The above information was then used in the inlet BC methodology (Section 3.5.1) for the implementation of the datum vortex pattern. However, the determination of the axial velcoity (V_z) distribution is still needed. From Equation 3.11, the knowledge of the constant A and the axial position z is an unknown. McLelland et al.[53] proposes an additional term the excess velocity ratio, ΔV_z^*, of around 50% for the case of a ground vortex ingestion, which has been determined numerically by a previous researcher[16]. Thus, by substituting the value of the excess velocity, Equation 3.21 was used to determined the $\frac{A}{Z}$ for the datum vortex case.

Where,

$$\Delta V_z^* = \frac{V_{z,max} - \overline{V}_{z,av}}{V_{z,av}} = \frac{A/z}{\overline{V}_{z,av}} \tag{3.21}$$

Table 3.12 summarizes the final datum vortex characteristics, and Figure 3.24 shows an example distribution of the inlet datum vortex flow-field, when ingested at the mid-span. The majority of the datum vortex ingestion cases, using RANS and URANS were performed on the full-annulus Rotor 67 (Configuration 1). Later in the study, full-annulus Stage 67(Configuration 3) was developed, and a RANS parametric study involving various vortex features was also performed.

Datum vortex	
Vortex circulation, Γ $(m^2 s^{-1})$	22.1
Vortex core radius, $2 \cdot r_c$ (m)	$6\% D_i$
Vatistas shape factor, n	1
Velocity excess ratio,ΔV_z^*	$50\% excess$
Vortex ingestion position, r_v	25%, 50%, 75% blade span

Table 3.11: Datum vortex characteristics.

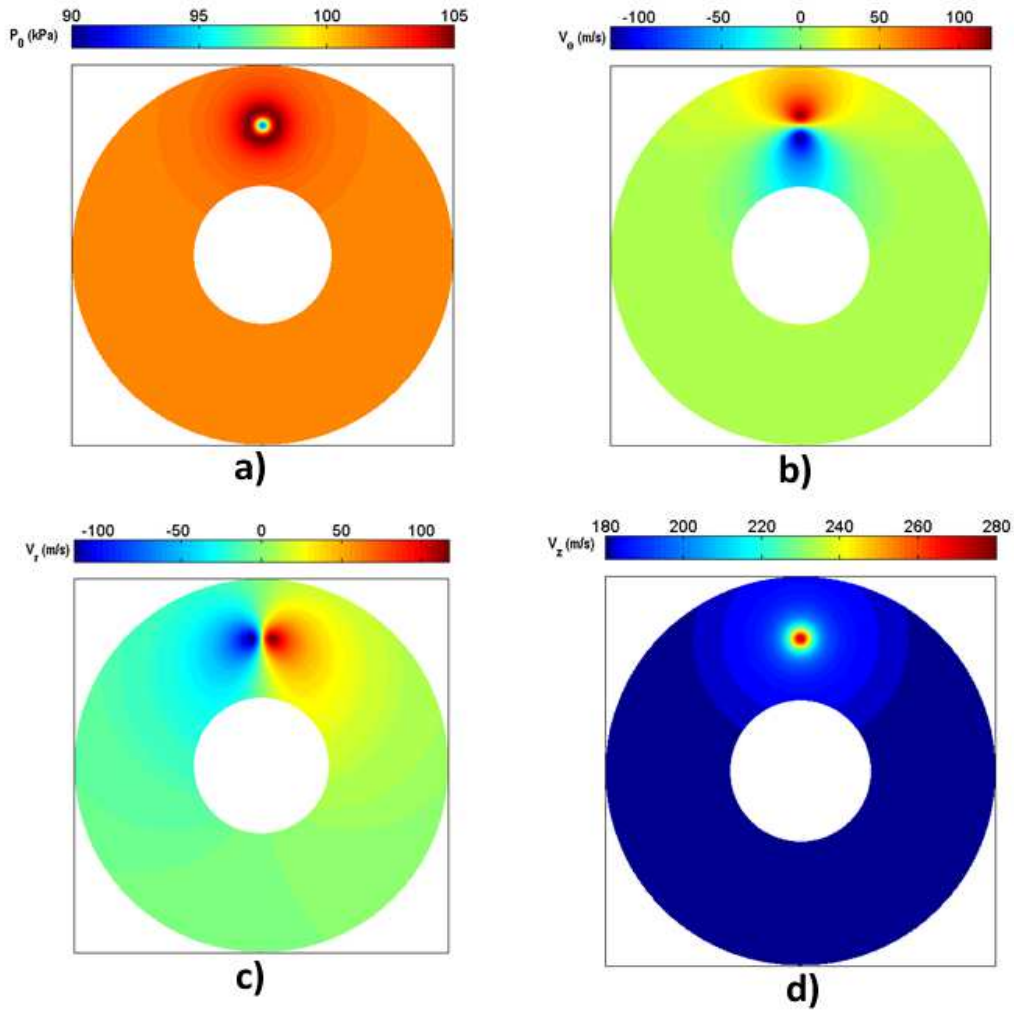

Figure 3.24: Vortex distribution at the inlet plane: **a)** Total pressure P_0, **b)** Tangential velocity V_θ, **c)** Radial velocity V_r, **d)** Axial velocity V_z.

3.6.2.2 RANS parametric study

The main vortex flow features that were investigated in the parametric study are listed in Table 3.12. In order to efficiently carry out the parametric study, one feature was varied at a time to gain confidence in to the underlying flow physics individually.

Investigated vortex features				
Vortex circulation, Γ (m^2s^{-1})	5.0	11.01	16.0	22.1
Vortex core size, $\frac{r_c}{s}$	4.5%	9%	14%	
Vortex span-wise location	25%	50%	75%	
Number of ingested vortex, N_v	1			
Vortex direction	$\pm\Gamma$			

Table 3.12: Vortex characteristics parametric study.

The developed vortex ingestion characteristics as explained in the previous section was used as the datum case for the parametric study. The complete test matrix for the vortex pametric study is illustrated Table D.2 of Appendix D.

Just to conclude the CFD methodology, all the numerical studies including the previously mentioned bulk swirl test matrix were performed using the high performance parallel computing (HPC) facility. Over the course of study, the number of computing nodes employed for each simulation has been chosen according to the total mesh size. However, the number of required HPC nodes also depends on the type of simulation. URANS simulations were most heavy in terms of both the computing nodes demand, and the run times.

3.7 Post-processing

3.7.1 Measurement stations

The flow was analysed at different measurement stations along each configuration studied in the project. For all the configurations, global performance data has

been collected at the specified station numbers provided in the NASA reports, where the actual experimental data was analysed. Table 3.13 summarizes the exact position for each configuration for the global performance measurements. The validation of the undistorted (clean) simulations were performed using these measurement stations. The values have been non-dimensionalised, using the rotor chord (c) (at hub) of each configuration, and is measured from the rotor leading edge (LE).

Configuration	**Station 1**	**Station 2**	**Station 3**
1-Rotor 67	-32% chord	125% chord	
2-Rotor 37	-93% chord	237% chord	
3-Stage 67	-32% chord	125% chord	236% chord

Table 3.13: Global performance measurement stations.

Also, some additional measurement stations were defined upstream of the rotor. This was done to capture the evolution of the ingested vortex, and also for the flow descriptors definition. An example of all these measurement station for Stage 67 is shown in Figure 3.25. In this configuration, the two additional upstream measurement planes (i.e. 01 and 12) were located at -57% chord, and -11% chord, respectively. The inlet (station 0) was also used to measure the various flow-field quantities.

The four key flow variables that were used for the global performance calculations were the area-averaged total-pressure ratio ($\overline{PR}$), the total-temperature ratio ($\overline{TR}$), the isentropic efficiency ($\overline{\eta}$), and the corrected mass-flow ($\overline{W}_{correc}$). These were formulated using the following Equations 3.22-3.25, at the measurement stations 1 (rotor in), and 2 (rotor out) or 3 (for the stage out).

$$\overline{PR} = \frac{\overline{P}_{t,out}}{\overline{P}_{t,in}} \tag{3.22}$$

$$\overline{TR} = \frac{\overline{T}_{t,out}}{\overline{T}_{t,in}} \tag{3.23}$$

$$\overline{\eta} = \frac{\overline{PR}^{\frac{\gamma-1}{\gamma}} - 1}{\overline{TR} - 1} \tag{3.24}$$

$$\overline{W}_{correc} = \overline{W}_{out} \frac{\sqrt{\frac{\overline{T_t}_{,out}}{288.15}}}{\frac{\overline{P_t}_{,out}}{101325}} \tag{3.25}$$

Where, $\overline{P_t}$ stands for the area-averaged absolute total-pressure, $\overline{T_t}$ stands for the area-averaged absolute total-temperature, and γ is the heat capacity ratio of the fluid air.

For the corrected mass flow ($\overline{W}_{correc}$) of the area-averaged mass-flow ($\overline{W}$) at the outlet, the Equation 3.25 can be used, where the ambient temperature of 288.15[K], and the ambient pressure of 101325[Pa] was used to correct the outlet mass-flow.

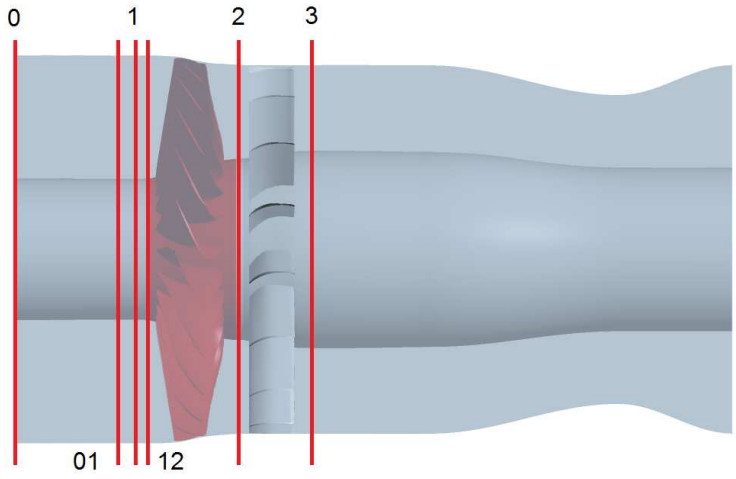

Figure 3.25: Example of Stage 67 measurement stations.

3.7.2 Tools

Numerous macros and scripts have been developed to post-process the numerical simulations. Tools such as the CFX-Post, the Matlab scripts, the Excel macros, and the Techplot is utilised within the study to create generic post-processing scripts. Due to the large size of the output files especially for the full-annulus cases, it was necessary to optimise the process to obtain consistent outputs.

Some of these are:

- Global performance scripts

A global performance macro captures relevant flow data such as the area-averaged total pressure, total temperature and mass flow at the measurement stations (Table 3.13). The variables such as total pressure ratio ($\overline{PR}$), temperature ratio ($\overline{TR}$), isentropic efficiency ($\overline{\eta}$), and, the corrected mass-flows ($\overline{W_{correc}}$) have been calculated using this method. Generation of this data is done by creating a session-file script within the CFX-Post environment. Using the script an automated program was created that exports the data to a text file, which is subsequently read by a Matlab script, and the relevant compressor maps are then plotted.

- Span-normalized charts

Session files macros have been created in CFX-Post to obtain 2-D and 3-D span normalized charts of the results. For 2-D plots, polylines at the rotor blade LE and TE in all the configurations were created (a example shown in Figure 3.26(a)). The flow properties were registered at these polylines, and were exported into a Matlab script, which reads the value of the magnitudes and plots the appropriate variables along the blade span.

For 3-D plots, using one of the blade polylines, a surface of revolution around the domain circumference was created, and was feedback into the Matlab script to create 3-D blade-span surfaces of the flow variables. The measurement station for the 2-D and 3-D span has been kept axially constant to -10% chord from the blade LE.

The blade performance study also focuses on the flow analysis in the worst affected 6 blade passages due to the localised vortex ingestions. These blade passages are shown in Figure 3.26(a). Two surfaces of revolution are created from the above 2-D polylines maintaining a constant axial distance of -10% chord from the blade LE. The exported data is subsequently imported by a Matlab script, and provides a closer indication of the nature of the vortex effects on the blade performance. This enabled to explain the outcomes from the global performance analysis.

The resolution of each 2-D line is 1000 span-wise cells from hub to tip, and

for 3-D surfaces around 1000 circumferentially distributed cells were used in each blade passage.

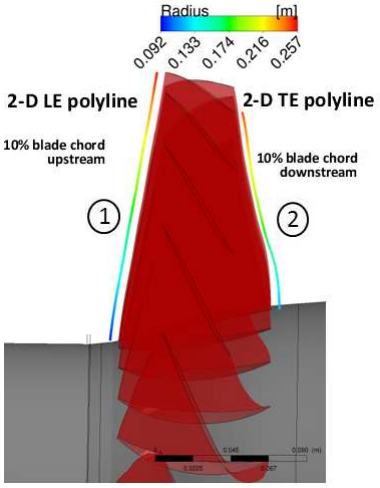

(a) 2-D span-wise polylines.

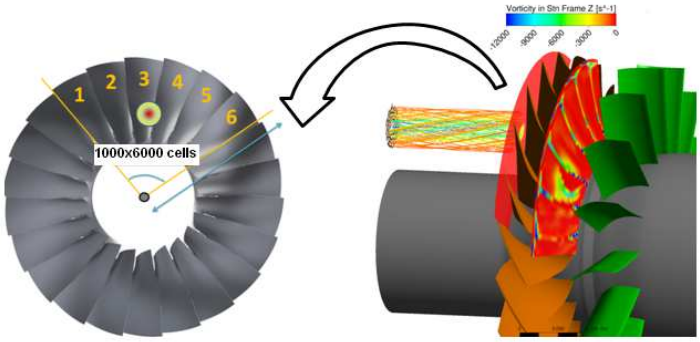

(b) 3-D span-wise for 6 blade passages along with absolute vorticity z vortex streamlines

Figure 3.26: Stage 67 example of span-normalized approaches.

- Scripts for flow descriptors definition

A number of scripts were also created to generate the data set of the flow descriptors developed for the rotor configurations. This was done at different axial locations upstream of the rotor blade LE, same planes as shown in Figure 3.25. More description of the flow descriptor definitions is presented in Chapter 6.

All the aforementioned scripts are completely modular so more plots can be added if it is required.

3.8 Concluding remarks

This chapter gave an overview on the applied methods and assumptions for the numerical simulations performed in the study. The overall CFD methodology can be summarised in a flow chart, as shown in Figure 3.27.

To summarize, the development of a CFD tool kit capable of simulating the two types of swirl distortion, i.e. the bulk swirl and the tightly wound vortex, have been presented. The generation and mesh of the three NASA test geometries were described, along with the approaches adopted to implement the swirling flows at the domain inlet. A generic BC methodology have been proposed for this purpose. Also, the determination of the datum vortex flow-field has been discussed. Finally, the test matrix of the swirl distortion parametric studies was also presented.

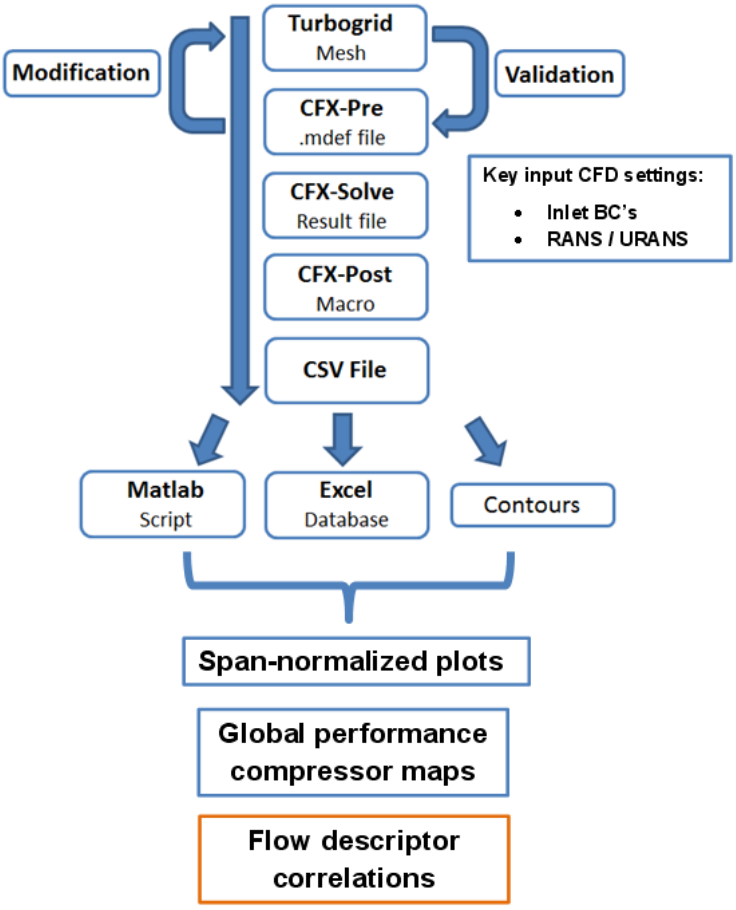

Figure 3.27: Overall CFD methodology.

Chapter 4

CFD Validation

As with any numerical based analysis, it is important to perform a mesh sensitivity investigation. A compromise between the mesh size and accuracy of the predicted flow field have to be made. The comparison was carried out with the undistorted (clean) experimental data provided by NASA[65,80]. The undistorted (clean) uniform flow results for the baseline mesh models were also compared with the data found in literature by the other authors. Moreover, typical 120[deg] total-pressure distortion simulations were also performed on the Rotor 67 and 37. The predicted flow field was compared with previous study under similar flow conditions. Only the main flow field features will be discussed in this chapter, as the detailed aerodynamic analyses of these rotors have already been done in the past, and is not the key objective of the study.

The three configurations studied in the research are:

1. Configuration 1: ***Isolated Rotor R67***

2. Configuration 2: ***Isolated Rotor R37***

3. Configuration 3: ***First Stage 67***

4.1 Configuration 1: Rotor 67

4.1.1 Compressor maps

In the last chapter, Table 3.4 summarized the Rotor 67 mesh sizes used for the grid dependency study. As the flow is clean axis-symmetric at the inlet, one flow passage simulations were sufficient to capture the key flow-field features. RANS simulations were performed with a cluster of around 16 CPU's for the clean (uniform undistorted flow) validation study. It took around 24 hours for each simulation to converge the residuals under the value of $1x10^{-6}$. All the numerical simulations were performed at $N = 100\%$ rotational speed.

Figure 4.1 illustrates the validation of the Rotor R67 CFD model in terms of the area-averaged pressure ratio ($\overline{PR}$), and the isentropic efficiency ($\overline{\eta}$) calculated at the Rotor 67 measurement stations (see Table 3.13) for the various mesh sizes. In general, a good agreement with the experimental data was achieved in most cases. The baseline mesh model including the tip clearance gap was selected, and used as a datum case for the later distorted flow-field numerical simulations. Certain observations were made, illustrating some notable differences in the flow field between the different rotor mesh models.

The relative percentage error near the peak efficiency in terms of area-averaged pressure ratio ($\overline{PR}$), the isentropic efficiency ($\overline{\eta}$), and the mass flow ($\overline{W}$) for the aforementioned cases is also illustrated in Table 4.1. The ratios of the area-averaged absolute total pressure and total temperature were calculated at the defined measurement stations 1 (rotor-in), and 2 (rotor-out). The accuracy of the developed models was calculated by comparing the CFD simulated point from the experimental speed-line using the following expression:

$$\Delta(\overline{PR}, \overline{\eta}, \overline{W})\% = \frac{Experimental(\overline{PR}, \overline{\eta}, \overline{W}) - CFD(\overline{PR}, \overline{\eta}, \overline{W})}{Experimental(\overline{PR}, \overline{\eta}, \overline{W})} \times 100 \quad (4.1)$$

Thus, the negative output values of the above expression means there is an overestimation of the variable, as compared with the experimental data, and the vice-versa for positive values of the relative percentage error.

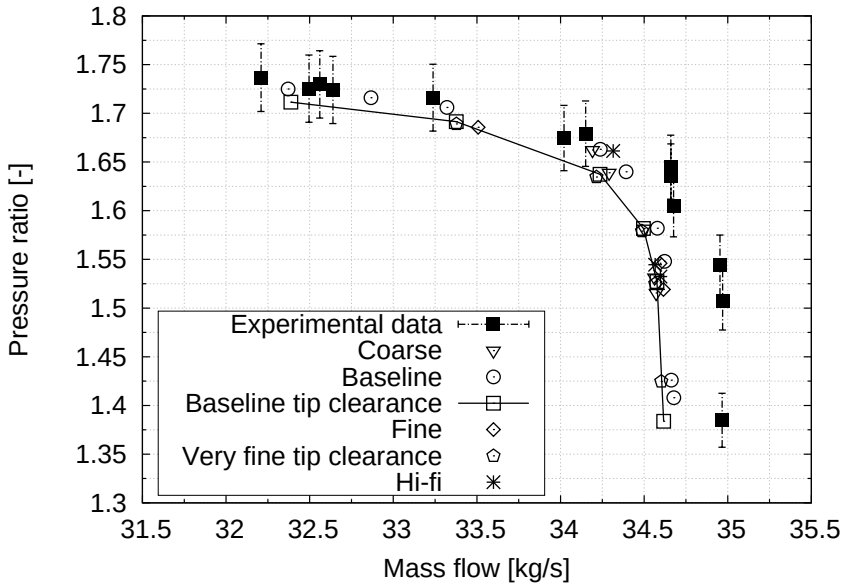

(a) Evolution of the rotor pressure ratio ($\overline{PR}$).

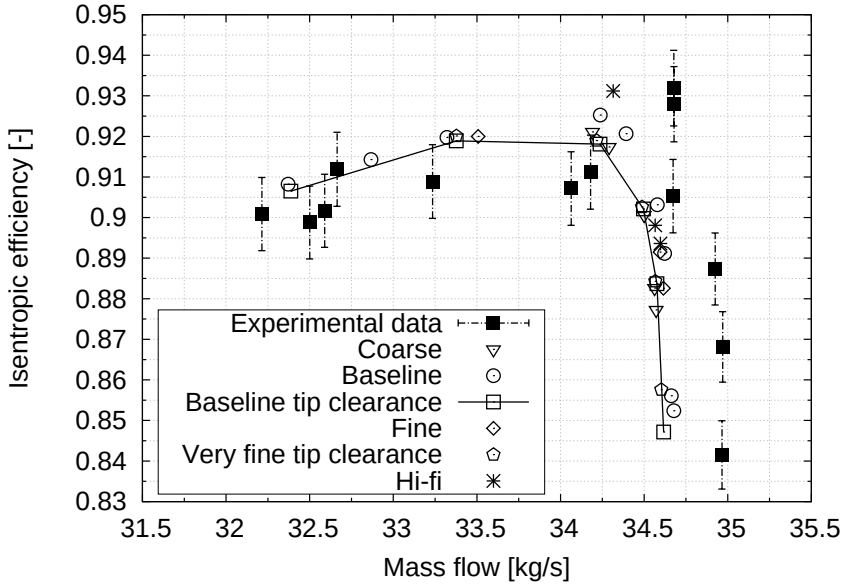

(b) Evolution of the rotor isentropic efficiency ($\overline{\eta}$).

Figure 4.1: Configuration 1: Grid dependency study of Rotor 67. Performance maps. With 1% error bars for exp. data.

From the previous Table 4.1 and Figure 4.1, it can be observed that the level of average total pressure ratio ($\overline{PR}$) for the baseline model with the tip gap is nearly the same, as in the experimental test cascade. Nonetheless, the same cannot be said about the mass flow ($\overline{W}$), and the rotor isentropic efficiency ($\overline{\eta}$). It can be

Relative % error-Near peak efficiency			
Case study	$\Delta\overline{PR}\%$	$\Delta\overline{\eta}\%$	$\Delta\overline{W}\%$
Coarse	-1.61%	1.16%	1.35%
Baseline	-1.66%	0.72%	1.22%
Baseline tip clearance	-0.087%	1.47%	1.225%
Very fine tip clearance	0.082%	1.35%	1.288%
Hi-fi	-1.55%	0.075%	0.99%

Table 4.1: Rotor 67 discrepancies in $\overline{PR}$, $\overline{\eta}$, and $\overline{W}$ with the experimental data

noticed that there is a certain shift to the left in the simulated characteristic for the mass-flow. The relative error from the experimental results of the calculated $\overline{W}$ and the $\overline{\eta}$ for the baseline model is around 1.2%, and 1.5% respectively. This is believed to be due to the extension of the inlet domain, thus increasing the boundary layer effects, which has not been modeled with a large number of mesh elements upstream of the blade passage.

This can be further confirmed by looking at the $\overline{W}$ and the $\overline{\eta}$ errors for the K-Omega SST (Hi-fi) model, which was found to be under 1% of the experimental mass-flow value. Thus, the error reduces significantly especially in terms of overall efficiency by utilizing a much more dense grid, and a more robust turbulence scheme. On other hand, the model have to compromise heavily on the CFD run times.

In terms of other case studies where mesh sensitivity study was conducted, and a much less computational demanding the K-Epsilon (with scalable wall functions) turbulence scheme was used. Not a lot of differences in terms of the $\overline{PR}$ was observed. An overall improvement in the prediction of the rotor $\overline{W}$ and the $\overline{\eta}$ was achieved by increasing the mesh size from the coarse to the baseline count.

One more very important feature that significantly improved the CFD results was the modeling of the rotor tip gap. Over-prediction of the pressure ratio by 1.6% for the baseline model with no tip clearance showed the necessity of simulat-

ing the tip gap losses. This have been also reported that the tip loss contribution is significant, and should be taken into account in the overall losses of modern transonic rotors[15], such as the simulated Rotor 67. By modeling around 10-14 span-wise nodes in the tip clearance, the $\overline{PR}$ accuracy level increased upto 95%. A slight higher mass flow blockage was also witnessed due to the tip clearance effect.

On the other side, CFD results of the very fine grid, and the baseline model showed similar outcomes by taking into account the tip clearance effects, thus showing the insignificance of the overall mesh size in this particular case. However, the baseline mesh was still refined further for the URANS full-annulus distorted simulations. The areas of major mesh improvements were the density of the axial chord mesh elements, and the tip region of the rotor. This was essential to be able to capture the small unsteady flow fluctuations near the blade surface.

The results were further validated by comparing with some other researchers cases, as shown in Figure 4.2. An acceptable agreement in terms of the $\overline{PR}$, and the $\overline{\eta}$ was achieved. However, it can be pointed out that the shape of the $\overline{PR}$ curve has been correctly captured but not the trend of the $\overline{\eta}$. Only the numerical work carried out by Niazi[61] was able to match the efficiency pattern with the experimental data. The importance of simulating numerically the tip clearance effects, especially near the stability limit has also been highlighted by the authors[1,6].

4.1.2 Other flow field

Blade span plots

The blade span-wise plots of the pressure ratio, and the temperature ratio were plotted to analyse the grid quality in the span-wise direction. An example of such plot is shown near the peak efficiency in Figure 4.3. A drastic improvement in span-wise prediction of PR and TR was achieved from coarse to the baseline model. However, an increase in the mesh size to a very fine grid didn't show better results in terms of the flow variables. For the tip gap cases, the clearance

effects can also be noticed in the form of flow losses near the blade tip region. The validation of the span-wise results against the numerical work carried out by Arima et al.[6] also show similar outcomes.

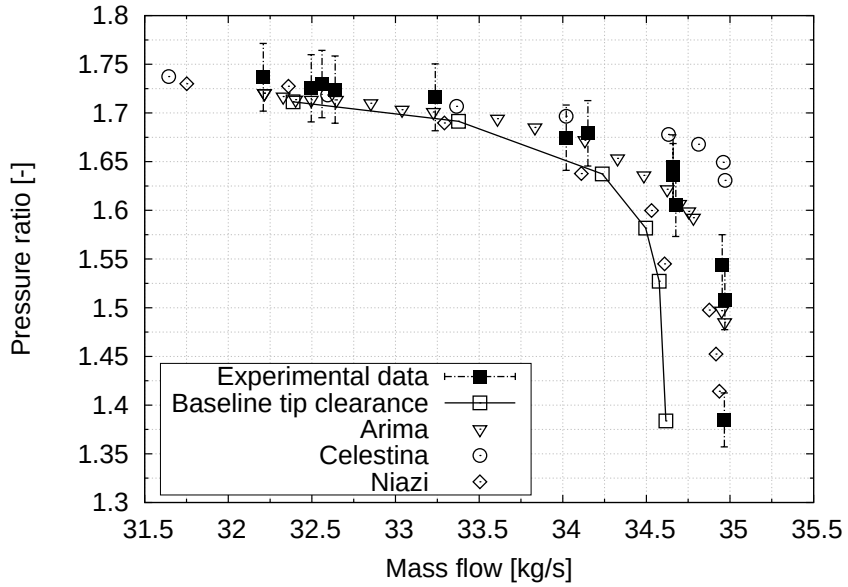

(a) Evolution of the rotor pressure ratio ($\overline{PR}$.)

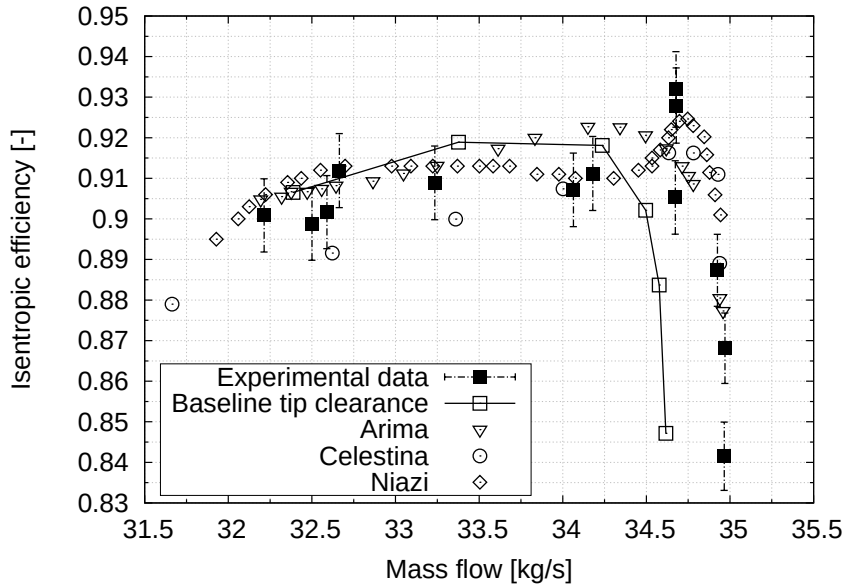

(b) Evolution of the rotor isentropic efficiency ($\overline{\eta}$.)

Figure 4.2: Configuration 1: Validation study of Rotor 67[1,6,61]. Performance maps. With 1% error bars for exp. data.

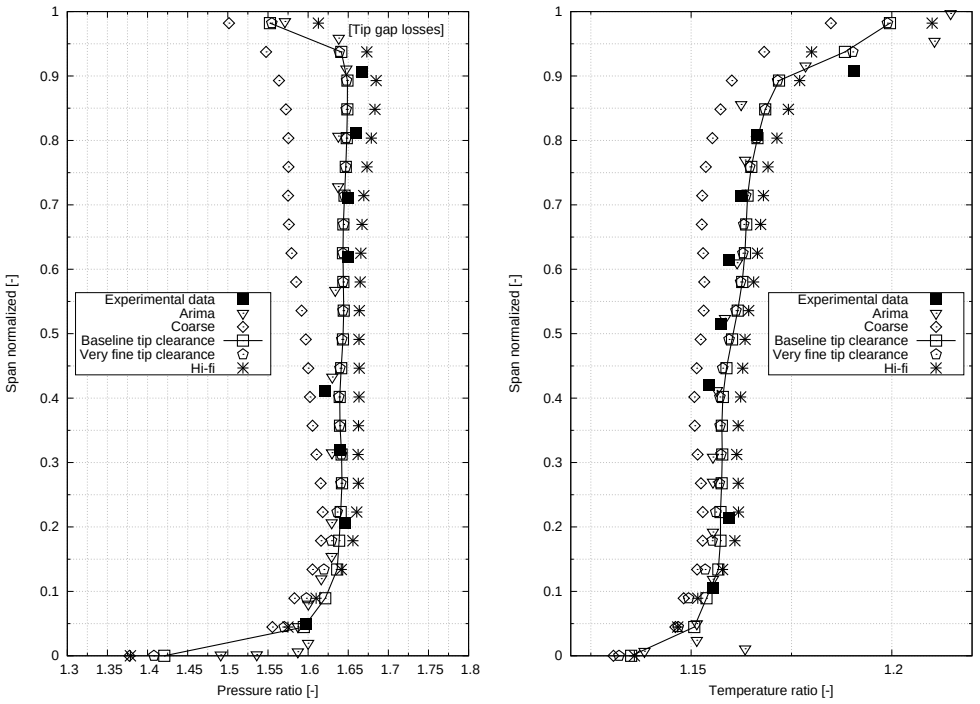

(a) Span-wise pressure ratio (PR). (b) Span-wise temperature ratio (TR).

Figure 4.3: Configuration 1: Span-wise plots near the peak efficiency of Rotor 67[6].

Turbulence scheme

The main flow variable that is usually used to validate the mesh grid using different turbulence schemes is the distribution of the non-dimensional wall distance, y^+. The value between 10 and 100 for the K-Epsilon is acceptable for the turbo-machinery, and where as, value of 1 or near for the K-Omega SST turbulence scheme is recommended. Figure 4.4 demonstrates the blade wall y^+ for both turbulence schemes investigated in the study, and the distributions exhibit within the the recommended ranges. The K-Epsilon (with walls functions) model was used for further studies, and it was adequate enough around the blade walls, and was also able to appropriately capture the boundary layer effects.

Shock-wave system

Apart from comparing the rotor global performance data, the contour plots in Figure 4.5 validates the shock-wave system at 70% blade span near the peak efficiency, and at near stall conditions. The validation of the shock-wave structure

and the strength can be done with the previous researcher contours in Figure 3.5. The major feature is the presence of the two shock waves system for higher mass flow (near peak efficiency). It comprises of a weaker blade LE oblique shock, and an additional strong passage shock much downstream of the blade passage. However at near stall conditions, the passage shock moves upstream, thus results in a very strong semi-detached oblique shock sitting just at the blade LE, as shown in Figure 4.4(b). If there is even a slight further reduction in the mass-flow, this oblique shock can become completely detached into a separated bow shock, and forms the perfect environment for triggering the rotating stall[1,61].

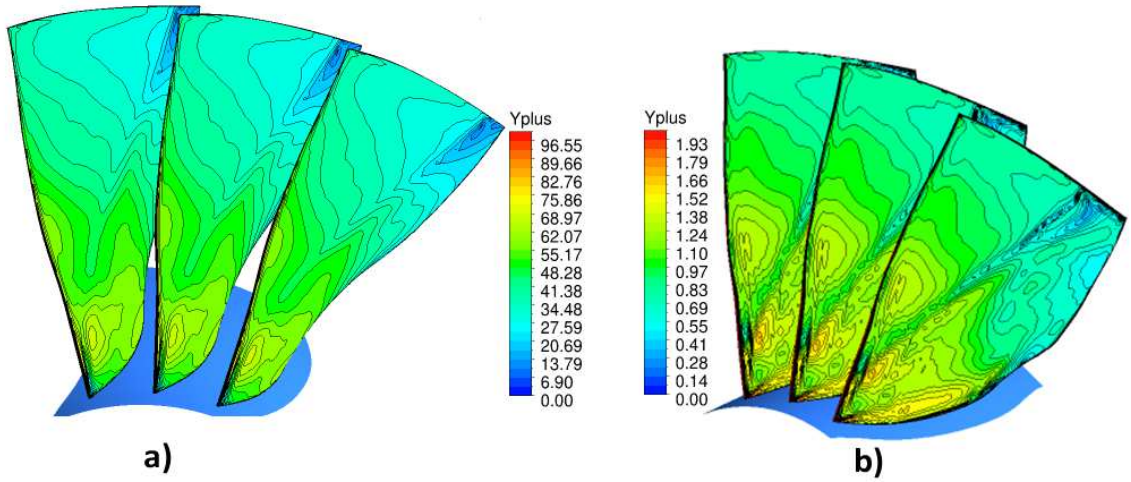

Figure 4.4: Configuration 1: y^+ near peak efficiency **a)** using K-Epsilon with wall functions. **b)** using K-Omega SST.

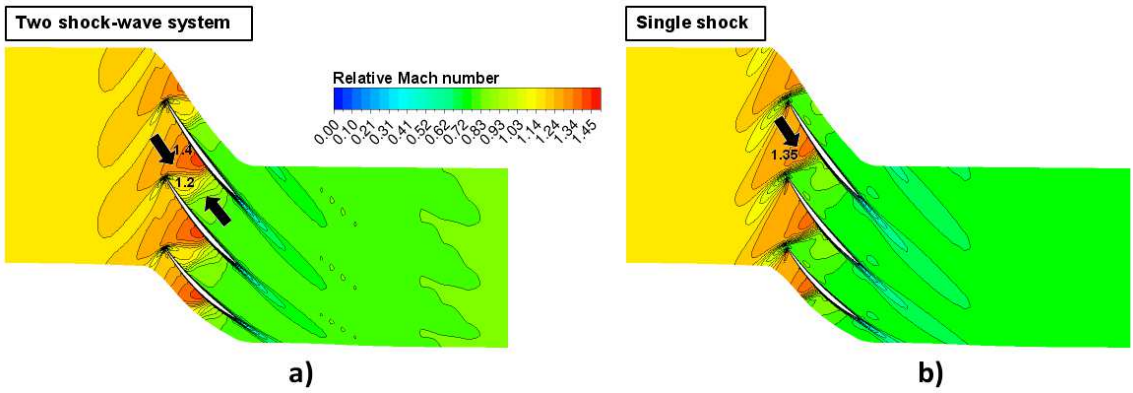

Figure 4.5: Configuration 1: Rotor 67 baseline model shock-wave system at 70% blade span: **a)** Near peak efficiency. **b)** Near stall conditions.

Rotor losses

The following form of flow losses have been identified as the main contributors to the overall loss across the transonic Rotor 67 blade passage:

1. Hub corner losses

2. Tip clearance/mixing losses

3. Shock losses

Figure 4.6 illustrates the losses near the suction side of the blade hub, both at near peak, and at near stall conditions. This is due to the viscous effects in the boundary layer, and causes the flow to separate on the suction side, and eventually migrates towards the tip wall. Moreover, there is an increase in hub losses near the stability limit, and is a typical observation found by the previous authors as well [2]. However, it can also be observed that there is an upstream movement of the shock position, which is actually found to be the prime reason that pushes the entire blade passage to its stability limit. The latter is caused due to high interactions of the passage flow with tip clearance flow. As a strong shock just sits at the blade LE near stall, vigorous interactions with the tip clearance flow detaches the shock from the blade passage, and causes flow spillage at the blade LE. These tip leakage vortex (TLV) and passage flow exchanges are illustrated in Figure 4.7.

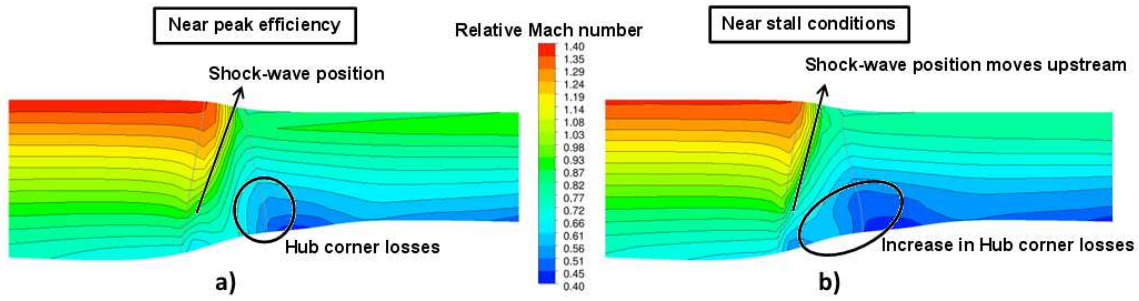

Figure 4.6: Configuration 1: Baseline model meridional view of Mach contours. **a)** Near peak efficiency. **b)** Near stall conditions.

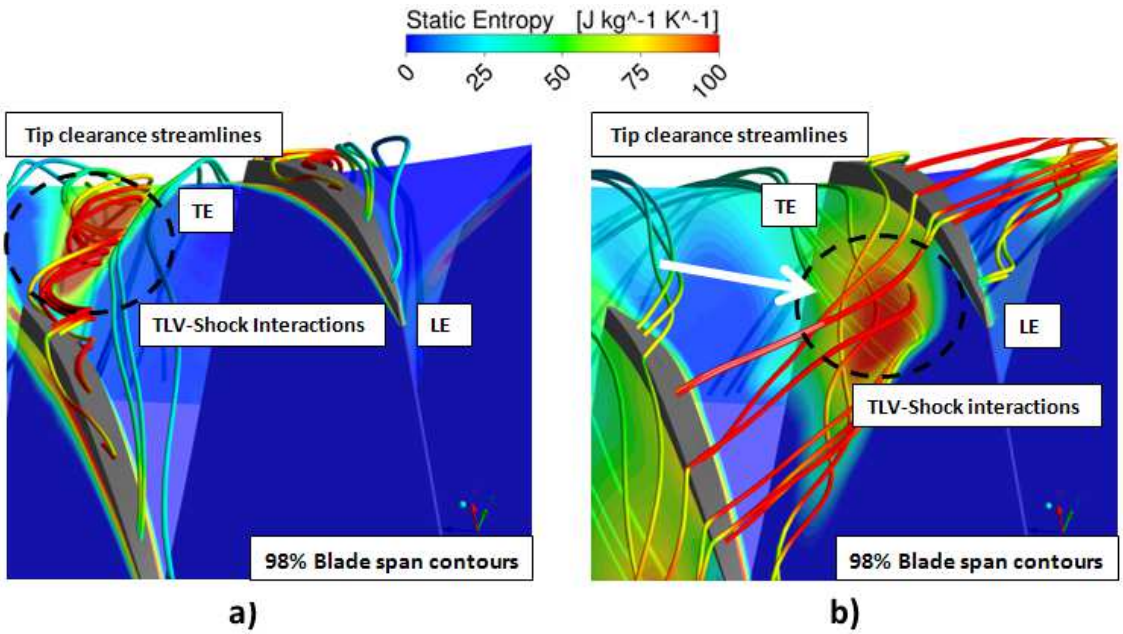

Figure 4.7: Configuration 1: Baseline model entropy contours and tip leakage streamlines interactions with the passage inlet flow. **a)** Near peak efficiency. **b)** Near stall conditions.

Lastly, the contribution of shock losses is small when compared with the formers. It is related to the flow losses associated with the heat conduction and high viscous normal stresses within the shock wave[24]. As these are few molecular free paths in thickness in majority of the blade span, these don't contribute much. However, with the ingestion of flow angularity in the distortion cases, shock losses can cause high entropy generation, and is presented in the Section 5.1.

4.2 Configuration 2: Rotor 37

4.2.1 Compressor maps

Similar aforementioned validation techniques were adopted for the Rotor 37 CFD models. Therefore, the results from the Rotor 37 validation study is not explained in much detail as the former. The mesh sensitivity study is shown in Figure 4.8 below. All the following RANS cases were performed at 100% rotational speed, and one-flow passage domain with 16 CPUs were utilized to achieve faster

convergence.

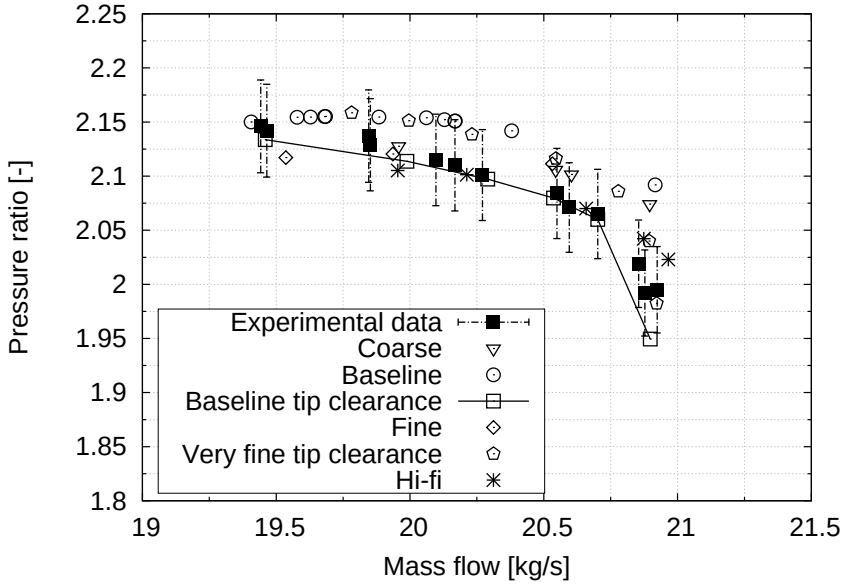

(a) Evolution of the rotor pressure ratio ($\overline{PR}$)

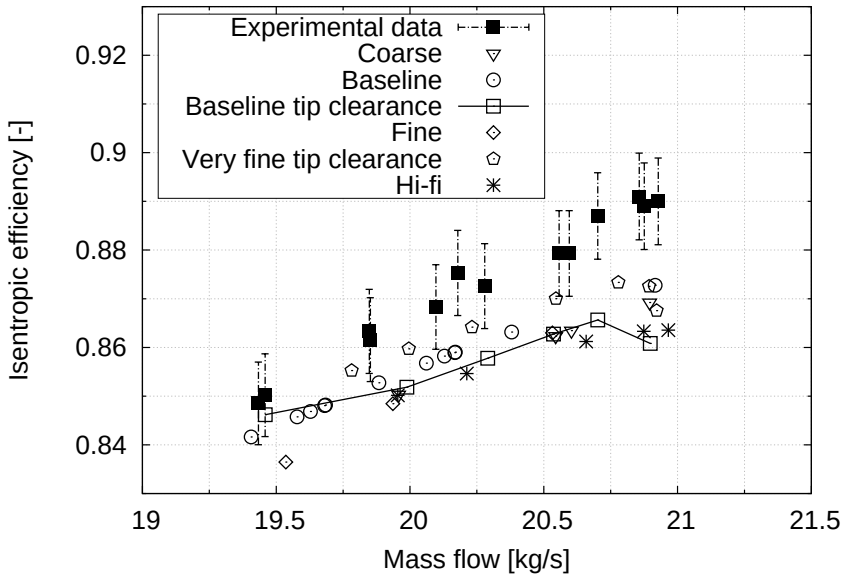

(b) Evolution of the rotor isentropic efficiency ($\overline{\eta}$)

Figure 4.8: Configuration 2: Grid dependency study of Rotor 37. Performance maps. With 1% error bars for exp. data.

Overall, a good agreement between the baseline model and the experimental data has been accomplished. Thus, the baseline model with the tip clearance was selected. However, as for the Rotor 67 configuration, the passage mesh was

particularly more refined for carrying out the quarter URANS simulations later in the study.

Table 4.2 illustrates the relative % error of the test cases from the experimental data, at near peak efficiency. In general, a good agreement in terms of the $\overline{PR}$ and $\overline{W}$ can be observed for the baseline model. However, same cannot be said for the variations in the $\overline{\eta}$, where a persistent underestimation is observed. This has been highlighted by the previous researchers as well, and is discussed in detail by Dunham[26].

A comparison with the other researchers is also demonstrated in Figure 4.9. The under-prediction of the rotor efficiency can be observed in other researchers work as well. It is reported to be mainly due to the presence of an axial gap between the non-rotating hub and the rotating blade row. Therefore, the methods adopted to measure the performance data during the experiment[26] differs from the Rotor 37 CFD models, and is observed in most CFD studies. Therefore, it has been highlighted in the previous work that this dissimilarity in the predicted efficiency should not underpinned the numerical results, if one follows similar CFD methods throughout their study.

Relative % error-Near peak efficiency			
Case study	$\Delta\overline{PR}\%$	$\Delta\overline{\eta}\%$	$\Delta\overline{W}\%$
Coarse	-0.44%	2.03%	-0.90%
Baseline	-1.30%	1.58%	-1.00%
Baseline tip clearance	0.24%	2.41%	0.04%
Very fine	-1.01%	1.54%	-0.34%
Hi-fi	-0.24%	2.91%	0.24%

Table 4.2: Rotor 37 discrepancies in $\overline{PR}$, $\overline{\eta}$, and $\overline{W}$ with the experimental data

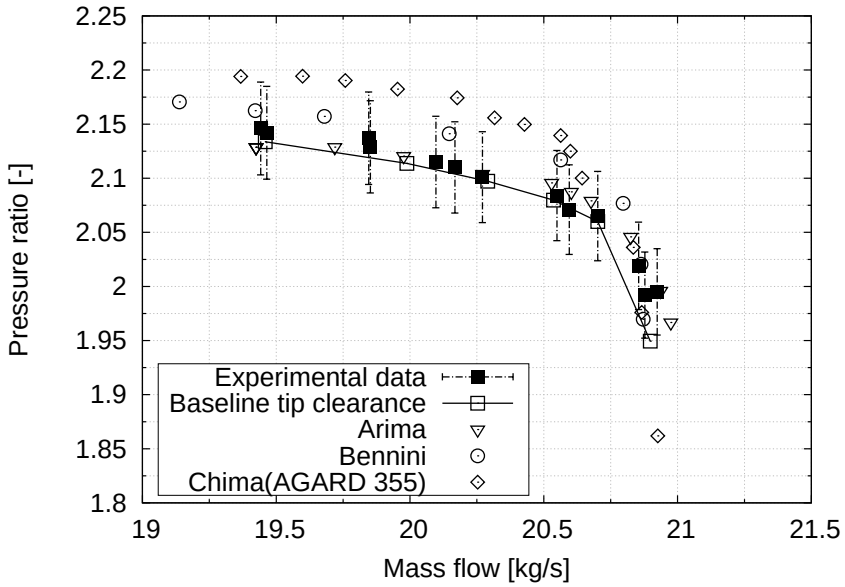

(a) Evolution of the rotor pressure ratio ($\overline{PR}$).

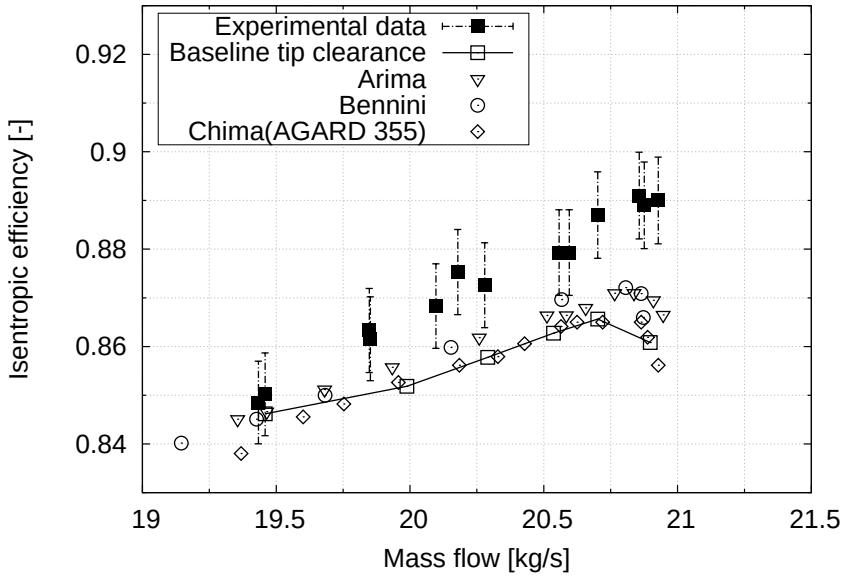

(b) Evolution of the rotor isentropic efficiency ($\overline{\eta}$).

Figure 4.9: Configuration 2: Validation study of Rotor 37[6,9,26]. Performance maps. With 1% error bars for exp. data.

4.2.2 Other flow field

Blade span plots

The span-wise plots of the PR and TR were also analyzed to validate the

span-wise mesh grid for the Rotor 37. An example of such plot is shown near the peak efficiency in Figure 4.10. As for the Rotor 67, a considerable improvement in the span-wise prediction of PR and TR was achieved, when changing from the coarse to the baseline mesh topology. However, a further increase in the number of span-wise nodes to a very fine grid didn't improve the CFD results further. Just to point out here, the cases where tip was modelled, the clearance effects can also be noticed in the form of flow losses, at the blade tip region. The validation of the span-wise distributions against the numerical work carried out by Chima[26] also showed similar results (Figure 4.10).

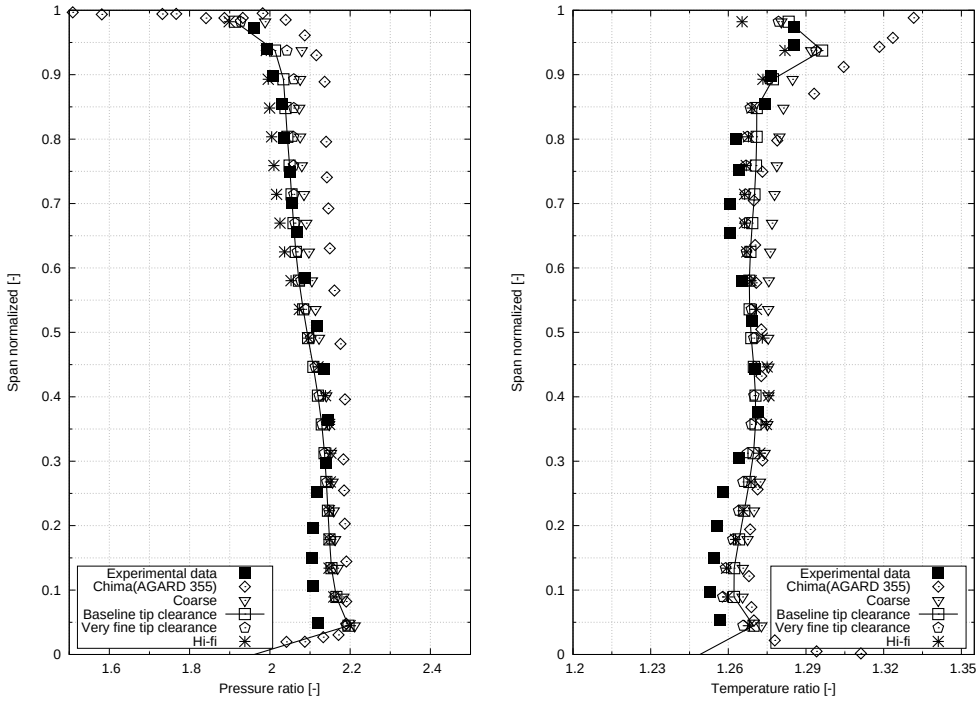

(a) Span-wise pressure ratio (PR). (b) Span-wise temperature ratio (TR).

Figure 4.10: Configuration 2: Span-wise plots near peak efficiency of Rotor 37.[26]

Blade-to-blade flow validation

Validation of the blade pitch-wise flow field was also carried out for the Rotor 37 configuration. Figure 4.11 demonstrates the pitch-wise plots of the relative Mach number (M_{rel}) at 20% mid-span chord inside the rotor, and also at the rotor downstream location ($\approx$ 50% mid-span chord). This analysis has been performed

at near choke conditions, and was compared against the available experimental and numerical data[26].

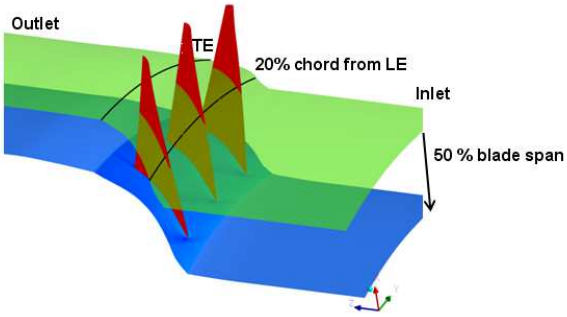

(a) Schematic of the blade-to-blade measurement stations

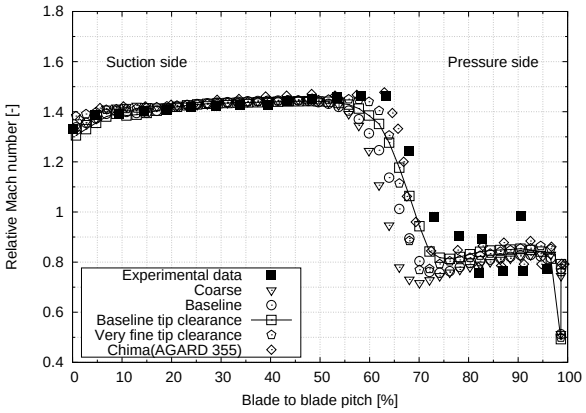

(b) At 20% chord downstream of the blade LE.

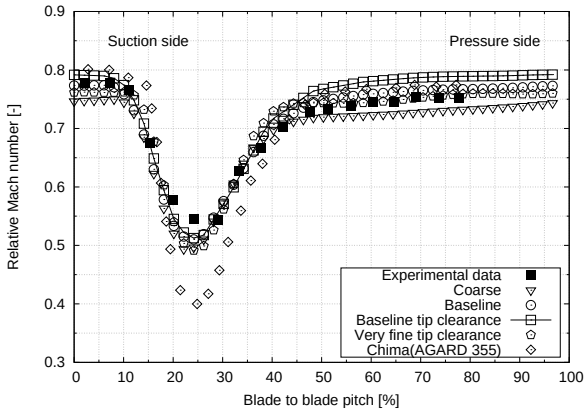

(c) At downstream of the blade TE.

Figure 4.11: Configuration 2: Validation of blade pitch-wise relative Mach number (M_{rel}).[26]

From Figure 4.11(b), it can be clearly observed that there is an improvement in the prediction of shock structure, and also the position by increasing the mesh density, when comparing with the experimental data. The baseline mesh with the tip clearance showed the best comparison of the flow-field within the blade passage.

On the other hand, Figure 4.11(c) is illustrating the downstream wake, spilling from the blade passage, and can be identified as a region of low momentum. The validation of the wake deficit with the experimental data show very similar behaviour. The results were also compared with the numerical work carried out

by Chima, they considerably over predicted the wake deficit due to the lack of fine mesh density downstream of the blade passage[26].

Turbulence scheme

The distribution of the non-dimensional wall distance, y^+ on the blade wall is shown in Figure 4.12, for the two utilised turbulence schemes. As stated for the former Rotor 67 configuration, the predicted distribution of y^+ were within the recommended ranges for the K-epsilon turbulence model. However, as the solidity of the Rotor 37 is higher, a much better y^+ could be obtained for the K-Omega SST by increasing the mesh size near the blade surface. This was beyond the limitation of available computational resources, and was therefore left out from the implemented CFD methodology. Therefore, the K-epsilon turbulence model with the wall functions was used for the further analyses.

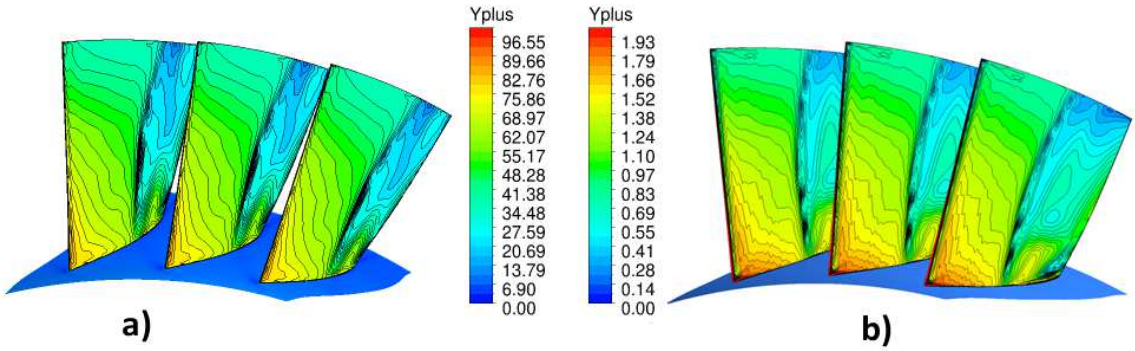

Figure 4.12: Configuration 1: y^+ near peak efficiency. **a)** Using K-Epsilon with wall functions. **b)** Using K-Omega SST.

The baseline mesh with the tip gap was again chosen, as for the Rotor 67 configuration, on the basis of computational requirements, and the level of acceptable accuracy.

In general, after the validation studies of the two rotor configuration, the CFD settings and the models were kept same to simulate the distorted non-uniform flows to build a robust methodology.

4.3 Flow-field comparison: Total-pressure distortion

To gain more confidence with the non-uniform boundary conditions at the inlet, a number of typical total-pressure distortion simulations were performed on the Rotor 67 and 37 configurations. An example of the Rotor 67 under a typical extent of 120[deg] total pressure distortion of about 10% was simulated at 100% spool speed, and is described in this section. A similar study on Rotor 67 with a stator downstream exists in literature[28], and therefore it was also helpful to compare some of the flow-field patterns qualitatively.

The global performance changes due to the ingestion of total-pressure distortion in terms of $\overline{PR}$ and $\overline{\eta}$, is illustrated in Figure 4.13. The predicted loss in stability pressure ratio (see Equation 6.2) from undistorted (clean) uniform inlet flow, ΔPRS is about 6.9%. The change in $\overline{PR}$ becomes more significant when operating conditions changes from near choking to stall. There is also a considerable loss in the rotor efficiency $\overline{\eta}$ due to the mass-flow blockage ahead of the fan blades, which reduces the $\overline{PR}$ much more than the $\overline{TR}$. Similar aforementioned comments were also observed from the work carried on Stage 67 by Fidalgo et al.[28].

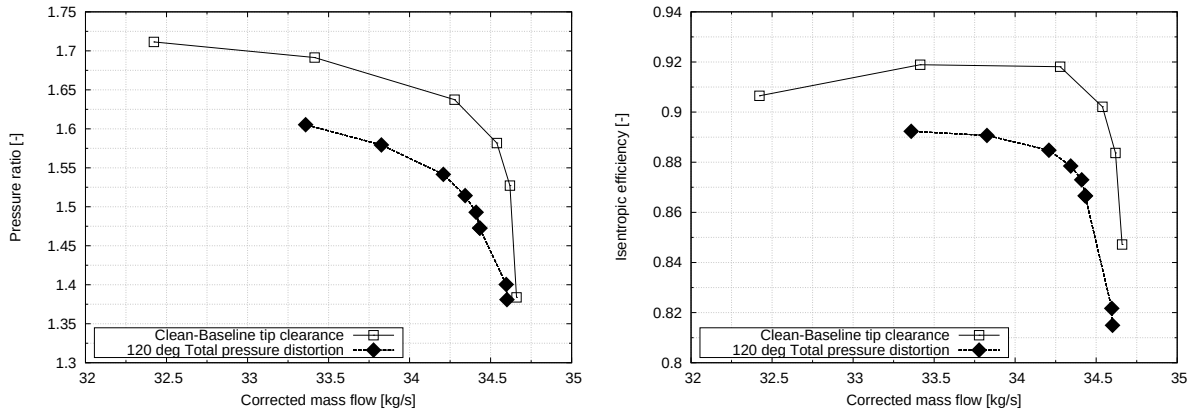

(a) Evolution of the rotor pressure ratio ($\overline{PR}$). (b) Evolution of the rotor isentropic efficiency ($\overline{\eta}$).

Figure 4.13: Configuration 1: Rotor 67 120[deg] total-pressure distortion. Performance maps.

Figure 4.14 exhibits the absolute total-pressure P_t contours along the domain, a non-uniform distribution around the annulus can be observed downstream of the rotor passage. The absolute swirl angle, α_{abs}, distribution just upstream of the rotor blade's LE show an induced cross-flow between the two regions, which is generated due to the lower axial velocity of the distorted region. The differences in the static pressure of the two regions causes flow transfer from the high pressure to a lower pressure zone. As a result, it creates a zone of counter-rotating swirl, and coherently, a zone of co-rotating swirl (see Figure 4.14(b)). Similar cross-flow zones have also been observed from the previous numerical study[28] (Figure 4.14(c)). Thus, this case study built up the confidence in the developed CFD methodology for the distorted inlet flows.

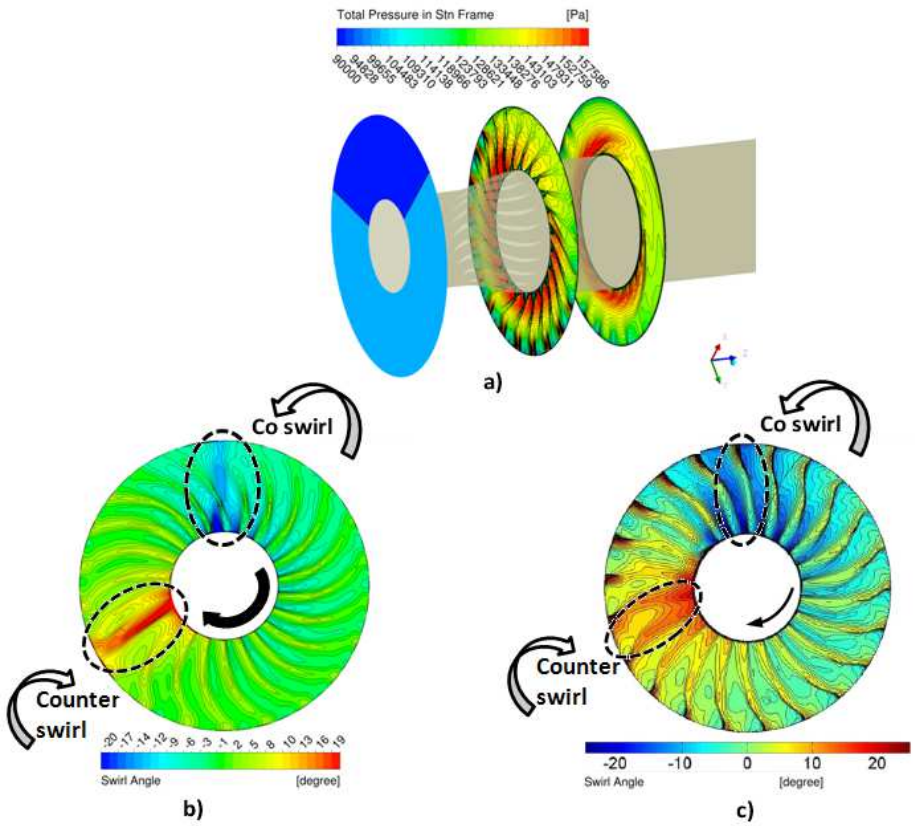

Figure 4.14: Configuration 1: 120deg total-pressure distortion **a)** Distribution of P_0 in streamwise direction. **b)** Distribution of α_{abs} ahead of fan blades. **c)** Similar α_{abs} distribution by Fidalgo et al.[28]

4.4 Configuration 3: Stage 67

4.4.1 Compressor maps

As mentioned earlier, during the research study the isolated Rotor 67 was upgraded by taking into account the rotor-stator effects. The available experimental test results of the first Stage 67 [29] were used to validate the computational model under the undistorted (clean) flow conditions, when using the RANS approach.

For the purpose of validating the already verified Rotor 67 CFD model with the new Stator 67B, a single compressor stage (R67, S67B and a Conv-diverg nozzle) was simulated with a range of choked nozzle areas (Table 3.10) to simulate from near choking to near stall conditions , at two spool speeds of 100% and 90%. The experimental values of $\overline{PR}$, $\overline{TR}$ and $\overline{\eta}$ are provided for the rotor, and also for the whole stage. Therefore, the experimental global performance data was compared with the Stage 67 CFD results, as shown in Figure 4.16.

Performance of Rotor 67

The performance of Rotor 67 in a stage environment was found to be simulated fairly accurately using the denser version of the rotor baseline mesh (see Table3.6). The predicted values of $\overline{PR}$ and $\overline{TR}$ as a function of corrected mass flow $\overline{W}_{correc}$ follow the same trend as the experimental values, within a tolerance of around 2% (see Figures 4.16(a) and 4.16(b)). Whereas, the $\overline{\eta}$ was found to be within 1% of the experimental values.

Performance of Stage 67 (coupled R67 and S67B)

The single stage performance showed a slight reduction in accuracy with the simulated values of $\overline{PR}$ reaching upto 2.5% of the experimental values (see Figures 4.16). The deviations from the experimental curve becomes higher near the stall, when compared with near choke conditions. Also, the estimated values of $\overline{TR}$ and $\overline{\eta}$ were within 2% and 4% of the experimental data respectively. This increase in the relative% error from the experimental data across the stator as compared with the rotor passage can be due to the mesh size in the former. As, the objective of the research was not only confined to perform high-fidelity stage calculations but to use the stage configuration to analyze the key interest in terms

of the compressor response to flow distortion. Therefore, this baseline CFD model was found to be robust enough to capture the required key flow features fairly accurately in an efficient manner.

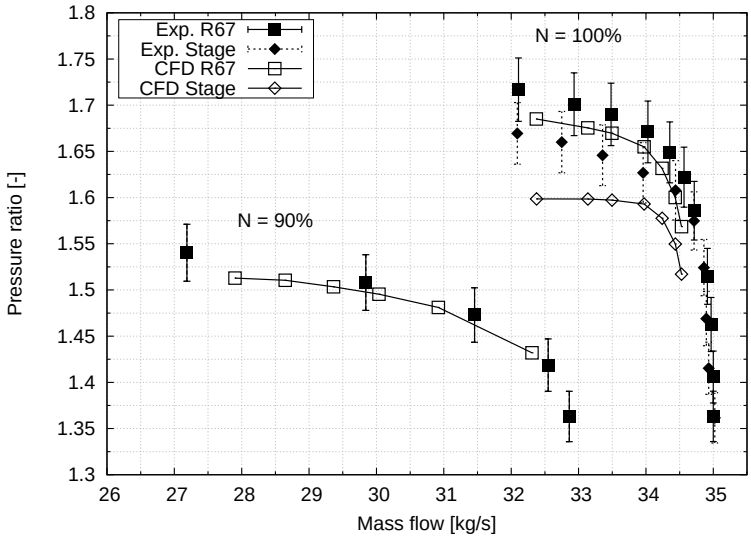

(a) Evolution of the rotor pressure ratio ($\overline{PR}$.)

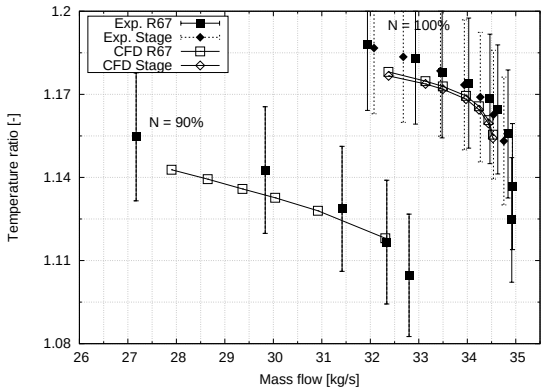

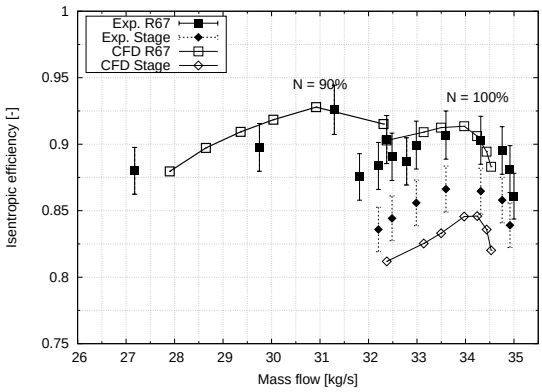

(b) Evolution of the rotor temperature ratio ($\overline{TR}$)(c) Evolution of the rotor isentropic efficiency ($\overline{\eta}$)

Figure 4.15: Configuration 3: Validation study of Stage 67[29]. Performance maps. With 1% error bars for exp. data.

The next step in the validation process was to determine the type of domain interface employed between the rotating Rotor 67, and the stationary Stator 67B.

4.4.2 Domain interfaces and stator grid dependency

Choice of domain interface

For ANSYS CFX (12.1-14.0) based numerical solutions, three methods are available to link the rotating and stationary domains with each other. These are[5]:

1. Mixing-plane method: It is a lower order interface for the RANS simulations, and transport the average quantities at the boundary of one domain to the other and the vice-versa.

2. Frozen-rotor method: It is a higher order interface for the RANS simulations, takes the real flow information at the interface boundary, and at a particular rotating relative domain position try to transport the exact flow quantities to the downstream domain, and the vice-versa.

3. Sliding mesh method (transient rotor-stator interaction): A much higher order interface than the former, and mainly used for the URANS CFD application. It takes into account the relative position of the rotating domain in real physical time scales, constantly passing the real time flow quantities to the downstream domain, and vice versa.

From above, the mixing plane method was quite evidently not suitable for the current study, as it would have weaken out the effect of swirl components, and also the large wakes between the domains. Therefore, the frozen-rotor method was implemented for the RANS simulations, which fixes the relative position of the rotor and the stator, and transport the flow properties. Hence, for the secondary flows, the rotating wakes are modelled at the exact position during the simulation, thus no transient effects are taken into account. However, besides on being dependant on the relative position of the turbo-machinery, it does offer an incentive of being robust, and also requires much less computational resources, than the third sliding-mesh option. However, the latter was limited for few URANS CFD runs only.

Some initial RANS CFD runs were also performed to analyse the use of the mixing-plane with the frozen-rotor (symbols with no fill) method, as shown in Figure 4.16. Although a better modelling of pressure ratio seems to achived using the mixing-plane method but it doesn't hide the fact that the corrected mass flow is clearly over-predicted, and the simulated point shifts towards right of the original rotor speed-line. This may be due to the circumferential averaging of the wakes in the mixing-plane method, whereas the frozen rotor takes a snapshot of the wakes, and these are subsequently transported to the next domain, hence causing more reduction in the mass flow.

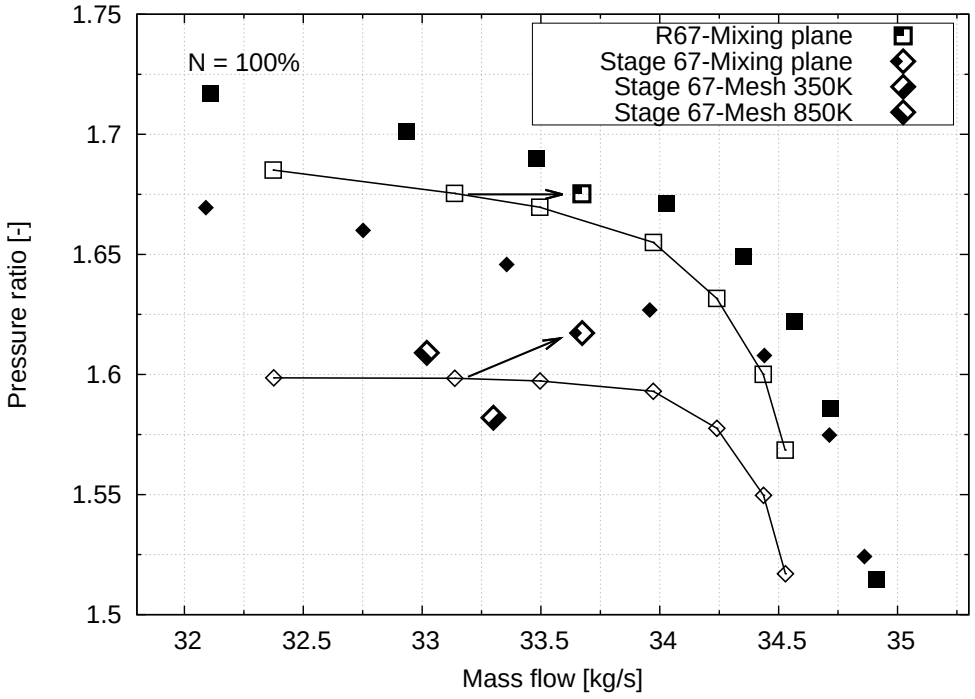

Figure 4.16: Configuration 3: Comparison between frozen-rotor and mixing-plane methods, and Stator 67B mesh sensitivity study.

Grid dependency of the stator S67B

One of the main reason for the reduced accuracy in simulating the flow field across the stator could be the mesh density in the stator domain. Just to validate the reasoning, a comparative RANS CFD study was carried out using the 450K mesh in each stator passage, which is used in this study, and two other stator passage meshes (350K element and 850K element).

The results are illustrated in Figure 4.16, an improvement in the stage performance prediction can be clearly observed in the simulated point with a denser stator passage mesh (850K element). However, the improvement in the prediction of $\overline{PR}$, $\overline{W}_{correc}$, and $\overline{\eta}$ is no more than 2% of the baseline (450K element) passage mesh. As, a large number of full-annulus Stage 67 simulations had to be performed in the study, therefore the baseline mesh was used for all the RANS, and also the URANS CFD simulations. To compare the total mesh count, the baseline mesh is about 7 million elements less in full-annulus, when using the 450K mesh elements per stator passage. This saved a considerable computational time that was required to perform a quantitative parametric study of the swirl ingestion. This method allowed to keep the Rotor 67 passage mesh much finer, as required by the research study.

4.5 Concluding remarks

The chapter was aimed at summarizing the key validation studies done for the three configurations that were utilized in the research. These were performed under undistorted (clean) uniform flow conditions, and were compared with the available experimental data.

For Configuration 1 (Rotor 67), the baseline CFD model with the tip clearance (about 11 million elements for full-annulus) was used. This mesh model was refined to around 18.5 million elements for full-annulus RANS and URANS CFD vortex ingestion cases. The maximum % error from the experimental data was found to be within 2%.

For Configuration 2 (Rotor 37), the baseline CFD model with the tip clearance (about 11.1 million elements for full-annulus) was used. This mesh model was also refined to around 25 million elements for full/quarter annulus RANS and URANS CFD pure bulk swirl, and also for some vortex ingestion cases. The maximum % error from the experimental data was found to be within 3%, it was observed in the values of the efficiency $\overline{\eta}$, which is also previously reported by other researchers[26].

The isolated Rotor 67 model from Configuration 1 was later combined with the Stator 67B to form the first Stage 67 (Configuration 3). Both the Rotor 67 and Stator 67B performance data was compared with the experimental stage performance data[29]. The maximum % error for the Rotor 67 domain was found to be within 2% for $\overline{PR}$, whereas the whole stage 67 was within $3-4\%$ of the experimental curve. The deviation of the stage performance was mainly seen in the $\overline{\eta}$ values, and have been linked with the coarser stator mesh as compared with much finer rotor mesh.

Besides undistorted (clean) uniform axial flow validation of the implemented CFD models, some non-uniform (total-pressure distortion) flows were also simulated under the reference configurations. These were performed to gain some confidence in the developed CFD models by carrying out a comparative study of the flow-field with some open literature, and similar flow-fields were observed.

To summarize, the outcome from the validation study showed positive signs in predicting the rotor performance with reasonable accuracy levels, thus justifying the requirements to carry on with the distorted CFD case studies.

Chapter 5

Swirl Distortion Results

This chapter illustrates the effects of two types of swirl distortion namely, pure bulk swirl and discrete vortices, on the turbo-machinery performance. The chapter is divided into two main sections, describing the distortion effects on the modelled configurations. The highlights of the flow-field variations are discussed along with the changes in the global performance from undistorted (clean) uniform axial-flow.

Appendix D summarizes the CFX test matrix for all the swill distortion simulations preformed during the study.

5.1 Pure bulk swirl

One of the favorable characteristics of the bulk swirl pattern regarding CFD simulations is the rotational axis-symmetry of the flow. Thus, one-flow passage RANS simulations were capable of capturing the key flow features of imposing an absolute flow angle at the inlet with periodic boundary conditions (BC's) (see Figure 3.23(b)). However, in order to capture the unsteady flows in more detail, multiple flow passage simulations were also performed using the URANS approach.

Also, the reason for choosing pure bulk swirl as the starting point was mainly due to the fact that it is one of the two types of swirl distortion investigated in the project whose turbo-machinery effects are more widely known. They have

been published[10,72,74] over the last few years, thus providing a method to judge the capabilities of the developed CFD toolkit.

In terms of the boundary conditions (BC), models were subjected to the positive (co-rotating) and the negative (counter-rotating) swirl content with respect to the rotor rotation direction. The methods for applying such BC at the inlet has been previously discussed in Section 3.5, along with the CFD settings implemented in the current approach. The post-processing of the results were carried out in terms of the global performance response, and the flow-field within the blade passages were also analyzed to understand the underlying causes of the bulk swirl effects.

The case studies discussed in this section illustrates some of the key findings found from the bulk swirl simulations. Table D.1 summarizes the test cases that were performed on the bulk swirl.

5.1.1 Configuration 1: Rotor 67 RANS Simulations

One flow passage RANS simulations of the isolated Rotor 67 were carried out to assess the overall performance effects due to the uniform (pure) bulk swirl flow. These were performed at a constant 100% rotational speed, and the rotor was throttled from near choke to near stall operating conditions by changing the back static pressure. A cluster of 48 CPUs was used for this set of analyses, and upto 2000 iterations in some cases were needed by the CFD solver to satisfy the convergence criterion (see Section 3.4.2). The following compressor maps show the results of these simulations.

As illustrated in Figure 5.1, the shift of the speed-lines is in agreement with the trends obtained previously by Sheoran et al.[72] (see Figure 2.25). A co-rotating bulk swirl reduces the overall area-average pressure ratio ($\overline{PR}$), the mass-flow ($\overline{W}$), and the temperature ratio ($\overline{TR}$) during the entire rotor operation from choking to near-stall. Thus, it shifts the speedline downwards and to the left hand side of the clean (undistorted) flow operation. On the other hand, the counter-rotating bulk swirl shifts the speedline towards right and upwards.

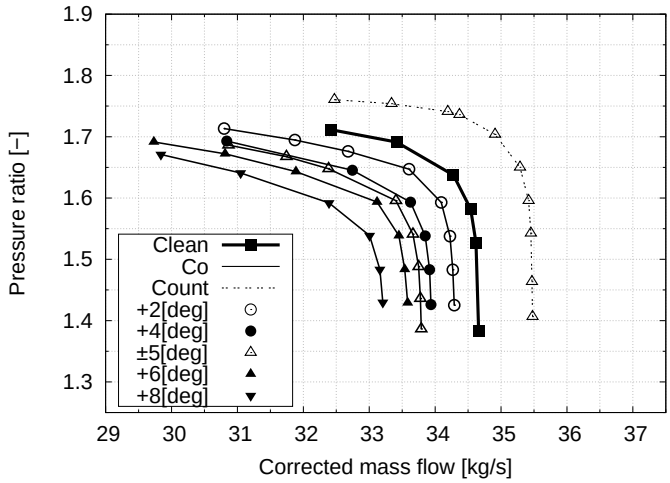

(a) Evolution of the rotor pressure ratio ($\overline{PR}$)

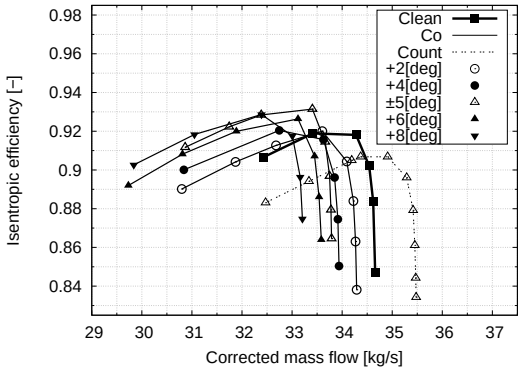

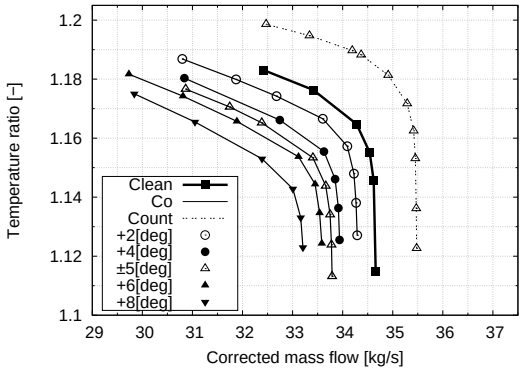

(b) Evolution of the rotor isentropic efficiency ($\overline{\eta}$)(c) Evolution of the rotor temperature ratio ($\overline{TR}$)

Figure 5.1: Configuration 1: One flow passage Rotor 67 bulk swirl CFD results. Performance maps.

The explanation of this change in position of the operational speedline can be based on the change in shape of the velocity triangles (see Figure 5.2). It describes the change in the incidence angle, (i), due to the circumferential swirl content for both the co and counter rotating swirl contents, assuming there is no or a very little change in the axial velocity upstream of the rotor. But in reality, the flow field tends to be more complex, it is indeed dependent on the compression system outlet throttle setting, but also the rotor blade aerodynamics. Rotor 67 is a twisted double circular arc transonic blade design, and half of the blade operates in sonic conditions (i.e. $M_{rel} \geq 1$ at the rotor inlet). This in return subjects the blade to work at the unique incidence[47] in clean (undistorted) flow

conditions, adjusting the inlet relative angle depending on the span-wise blade design.

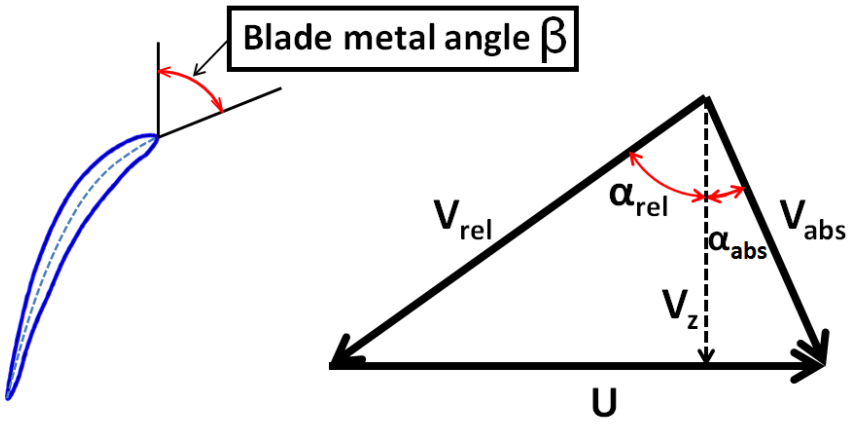

Figure 5.2: Inlet velocity triangle definition.

$$i = \alpha_{\text{rel}} - \beta \tag{5.1}$$

Thus, for example, in the case of co-rotating bulk swirl, the value of the inlet absolute swirl angle (α_{abs}) increases (see Figure 5.2), and the relative swirl angle (α_{rel}) decreases. Therefore, the incidence angle, (i), (Eq. 5.1) is smaller, and thus less work generated by the compression system, i.e. a lower $\overline{PR}$ and $\overline{TR}$. Also as it is a transonic rotor, it tends to operate at a unique incidence angle at particular blade spans, similar to the clean (uniform axial) flow conditions. To fulfill this requirement, height of the velocity triangle (i.e. the axial velocity) again have to be reduced for a co-rotating swirl. This is done in order to keep the inlet relative angle similar to the clean condition at certain blade spans, where $M_{rel} \geq 1$ at the rotor inlet. As a result, it also contributes to the overall reduction in rotor aerodynamic loading; shifting again the compressor speedline to the left and downwards in terms of PR and TR, while a slight increase in the values of $\overline{\eta}$.

Figure 5.1 also illustrates the fact that the magnitude of a co-rotating swirl content is also directly proportional to the reduction of blade loading. Thus, further reduction in $\overline{W}$, $\overline{PR}$, and $\overline{TR}$, and an increase in $\overline{\eta}$ are observed when the co-rotating swirl angle is intensified. An extensive parametric study to analyze

the effect of various bulk swirl magnitudes on a transonic rotor was carried out on the Stage 67 CFD model. It is discussed in-detail later in Section 5.1.3.

On the other hand, the case of counter-rotating swirl shows the opposite consequences; an increase in the incidence angle is compensated by an increase in the axial velocity. The latter increases the value of choking mass flow, and displaces the speedline to the right and upwards. Thus, the overall $\overline{PR}$ increases but higher flow losses are also observed. This has been found to be due to the upstream movement of the shock within the blade passage, thus compensating the increase in the inlet flow angle. More of this counter swirl phenomena is also discussed later in detail during the Stage 67 analyses in Section 5.1.3.

In terms of the mean isentropic efficiency ($\overline{\eta}$), the effect of a co-rotating bulk swirl results in a slight increase in the efficiency. A reduction in the $\overline{PR}$ is also accompanied by a drop in the $\overline{TR}$. The rise of $\overline{\eta}$ may be due to the fact that the rotor is not operating at optimal conditions due to reduction in the blade loading, thus resulting in a slightly more efficient compression system. The opposite takes place for the counter rotating swirl case, the increase in the $\overline{TR}$ due to higher loading is much more than the increase in the $\overline{PR}$ due to the accompanied blade flow losses. Thus, it dramatically reduces the overall isentropic efficiency of the compression system.

The above observations have been put into context in Table 5.1. It shows the relative percentage changes of $\overline{W}$, $\overline{PR}$, $\overline{\eta}$, and $\overline{TR}$ at the peak efficiency for the ± 5[deg] bulk swirl (both co and counter rotating) patterns. They have been calculated with respect to the uniform undistorted (clean) flow speed-line, and using the following expression:

$$\Delta(\overline{PR},\overline{\eta},\overline{W},\overline{TR})\% = \frac{Clean(\overline{PR},\overline{\eta},\overline{W},\overline{TR}) - Distorted(\overline{PR},\overline{\eta},\overline{W},\overline{TR})}{Clean(\overline{PR},\overline{\eta},\overline{W},\overline{TR})} \times 100 \tag{5.2}$$

%Δ-Near peak efficiency				
Case study	$\Delta\overline{W}\%$	$\Delta\overline{PR}\%$	$\Delta\overline{TR}\%$	$\Delta\overline{\eta}\%$
Co-rot. 5 deg	3.13%	2.58%	0.95%	−1.03%
Counter-rot. 5 deg	−2.81%	−2.63%	−1.01%	1.32%

Table 5.1: Configuration 1: Bulk swirl ±5 deg- Changes in $\overline{W}$, $\overline{PR}$, $\overline{TR}$, and $\overline{\eta}$ with the clean flow

Similar aforementioned conclusions can be drawn out from the above table. A reduction in the blade loading, and a slight increase in the isentropic efficiency can be observed for the co-rotating bulk swirl, and opposite trends for the counter rotating swirl, when compared with the undistorted flow solution. It can be noticed that the percentage increase in the magnitude of $\Delta\overline{TR}$ for the counter-rotating swirl is slightly higher than the amount of reduction in the case of co-rotating swirl. This is due to the losses incurred for the counter rotating swirl pattern dissipating in the form of heat exchange, thus compensating for the increase in the inlet flow angle. As a result, the efficiency drops dramatically in the case of counter-rotating bulk swirl ingestion.

Following points can be recognized as the key findings from this particular part of the bulk swirl CFD analyses:

- The effect of the change in inlet swirl angle in both the co and counter rotating bulk swirl cases was found to have evident effects on the turbomachinery performance (i.e. in terms of $\overline{PR}$, $\overline{W}$, $\overline{\eta}$, etc.).

- The magnitude, and the polarity of the swirl pattern exposed at the rotor inlet are the key factors in determining the rotor response. They were found to have opposing aerodynamic effects on the compression performance at low inlet swirl angles.

5.1.2 Configuration 2: Rotor 37 RANS and URANS simulations

This section is divided into two parts, first explaining the RANS simulations, and the comparison with the Rotor 67 trends, when operated under similar bulk swirl conditions. The second part of the section is devoted for the illustration of the URANS simulation results that were carried on the Rotor 37 configuration. These URANS simulations were performed to analyze the unsteady effects of the bulk swirl distortion on the flow-field, especially near the stall conditions. Also, the comparison of the RANS and URANS results of the pure bulk swirl was undertaken.

5.1.2.1 RANS results

Again, one flow passage RANS simulations of the isolated Rotor 37 were performed at a constant 100% rotational speed. The static pressure at the outlet was varied to change the throttle setting from near choke to near stall flow conditions. These were also run on a cluster of around 48 CPUS, required 24 hrs for the residuals to reach below the acceptable values. Figure 5.3 illustrates the outcome of the simulations in terms of the global performance effects.

%Δ-Near peak efficiency					
Configuration	**Case study**	$\Delta\overline{W}\%$	$\Delta\overline{PR}\%$	$\Delta\overline{TR}\%$	$\Delta\overline{\eta}\%$
1-Rotor 67	Co-rot. 5 deg	3.13%	2.58%	0.95%	−1.03%
1-Rotor 67	Counter-rot. 5 deg	−2.81%	−2.63%	−1.07%	1.32%
2-Rotor 37	Co-rot. 5 deg	1.90%	1.25%	0.95%	−2.72%
2-Rotor 37	Counter-rot. 5 deg	−2.33%	−1.09%	−0.89%	2.48%

Table 5.2: Configurations 1 and 2: Bulk swirl ±5 deg- Changes in $\overline{W}$, $\overline{PR}$, $\overline{TR}$, and $\overline{\eta}$ with the clean flow.

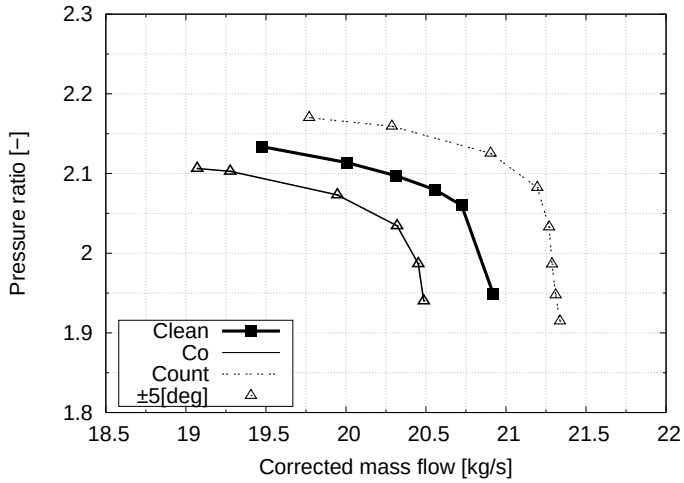

(a) Evolution of the rotor pressure ratio ($\overline{PR}$).

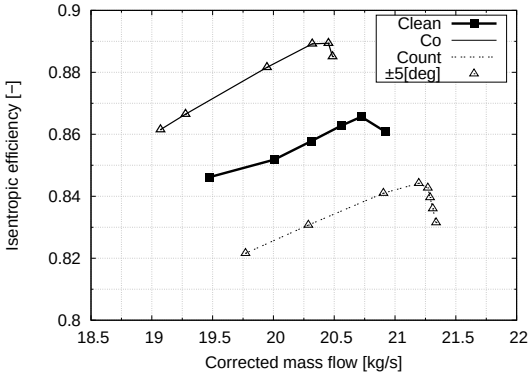

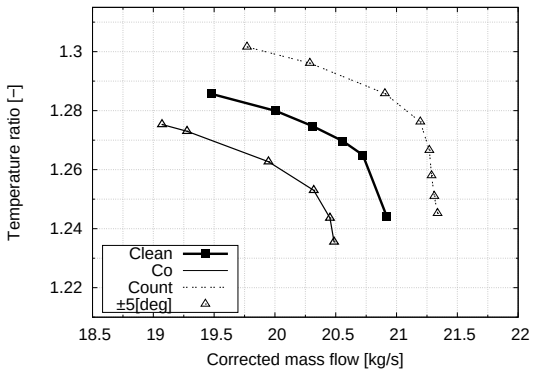

(b) Evolution of the rotor isentropic efficiency ($\overline{\eta}$)(c) Evolution of the rotor temperature ratio ($\overline{TR}$)

Figure 5.3: Configuration 2: One flow passage Rotor 37 bulk swirl CFD results. Performance maps.

From Figure 5.3, it can be noticed that the movement of the speed-lines is again in accordance with the previous Rotor 67 configuration. Since, the main comments concerning the effects of bulk swirl on the turbo-machinery have already been highlighted, the aim of this section is to differentiate between the bulk swirl results of the two rotor configurations (i.e. Rotor 67 and Rotor 37). To summarize, a co-rotating bulk swirl resulted in the reduction of blade loading, and the opposite took place for the counter-rotating bulk swirl. Table 5.2 compares the relative percentage changes of the area-averaged $\overline{W}$, $\overline{PR}$, $\overline{\eta}$, and $\overline{TR}$ at the peak efficiency for the two rotor configurations studied.

From above, similar outcomes can be observed when comparing the co and

counter rotating bulk swirl patterns comprising of ±5[deg] swirl magnitude, as for the previous rotor configuration. It can be noticed that the percentage gain in $\Delta\overline{PR}$ due to -5[deg] counter bulk swirl is lower than the percentage loss in $\Delta\overline{PR}$ due to similar $+5$[deg] co-rotating swirl. However, an increase in the $\Delta\overline{W}\%$ for the case of counter-rotating bulk swirl is much more than the loss in $\Delta\overline{W}\%$ for the co-rotating swirl. It means that the Rotor 37 requires much more mass flow in the case of counter swirl to achieve still lower $\Delta\overline{PR}\%$, when compared with the co-rotating swirl. This is due to the increment in flow losses associated with the counter-rotating swirl for the Rotor 37 configuration, and can also be seen from the values of the isentropic efficiency.

On the other hand, when comparing with the previous Rotor 67 configuration results, the dissimilarities in the isentropic efficiency between the two test cases is quite apparent. The large $\Delta\overline{\eta}\%$ for the Rotor 37 test case illustrates the fact that it is more sensitive to the bulk swirl pattern than the former. However, these changes in the efficiency doesn't correspond in the values of $\Delta\overline{W}\%$, $\Delta\overline{PR}\%$, and $\Delta\overline{TR}\%$. This shows that there are more aerodynamic changes associated with the Rotor 37 than the Rotor 67 configuration. This is maybe linked with the shape of the two transonic rotors. The Rotor 37 comprises of much higher hub to tip ratio, and also, as it is a part of a high pressure compressor (HPC), thus it reaches a value of $\overline{PR}$ much higher than the fan Rotor 67 at the design speed. This results in a much stronger shock-wave system for the Rotor 37 configuration ranging along most of the blade span, when compared with the 50% sonic blade span for the Rotor 67 configuration.

5.1.2.2 URANS results

For the URANS bulk swirl calculations, a quarter annulus was used in order to capture the unsteady effects of the flow-field more precisely. Moreover, RANS simulations on quarter annulus model of the Rotor 37 were also performed to compare the discrepancies between the two approaches. These were run on a cluster of around 48 CPUS. URANS calculations were performed using around 3600 timesteps per rotor revolution (10 timesteps/degree), and within each timestep

around 25 inner loop iterations were needed to converge the flow field at a particular rotor angular position. By convergence, it means all the residuals were below the set value (see Section 3.4.2), and the flow variables (e.g. mass flow, total pressure etc.) had reached a quasi steady-state within the domain. To summarize, it required around 24 hrs of computing to complete half a rotor revolution. It required upto 2 rotor revolutions to reach a quasi-steady state converged solution near the design point, and for near the stability limit, it needed upto 6 rotor revolutions to reach any stable solution. Each transient simulation generated about 15 GB of post data, which had to be post-process to average the transient results, and generate useful information. Therefore, a number of post-processing tools were developed to optimize the procedure for analyzing the URANS results. A co-rotating bulk swirl case having a magnitude of +5[deg] was selected for this analysis, and the results are shown in the Figure 5.4.

Just to mention, the URANS points in the performance maps were obtained once the CFD solution became quasi steady-state in terms of the flow properties (e.g. mass-flow, pressure, temperature, etc). Therefore, once oscillations in the flow properties during each transient CFD run reduced to minimal, the area-averaged global performance properties (e.g. $\overline{W}$, $\overline{TR}$, $\overline{PR}$, and $\overline{\eta}$) were measured. On the other hand, at near stall conditions the oscillations were present through out the analysis. Therefore, one cycle of the oscillation were averaged to generate the database of the flow properties for this case.

Some key observations can be drawn out from the above charts. The global effect of a co-rotating bulk swirl on the rotor performance is similar to what have been described in the previous sections (see Section 5.1.1). It reduces the overall pressure ratio, and the corrected mass flow, whilst increasing the isentropic efficiency.

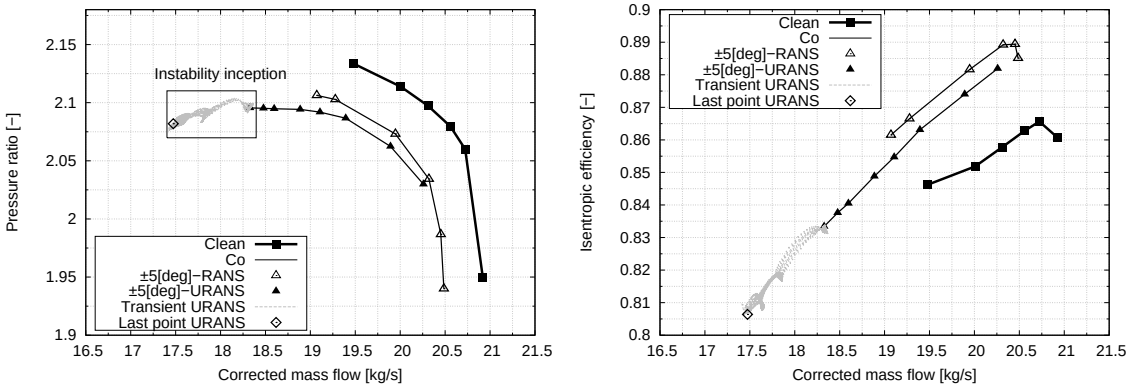

(a) Evolution of the rotor pressure ratio ($\overline{PR}$) (b) Evolution of the rotor isentropic efficiency ($\overline{\eta}$)

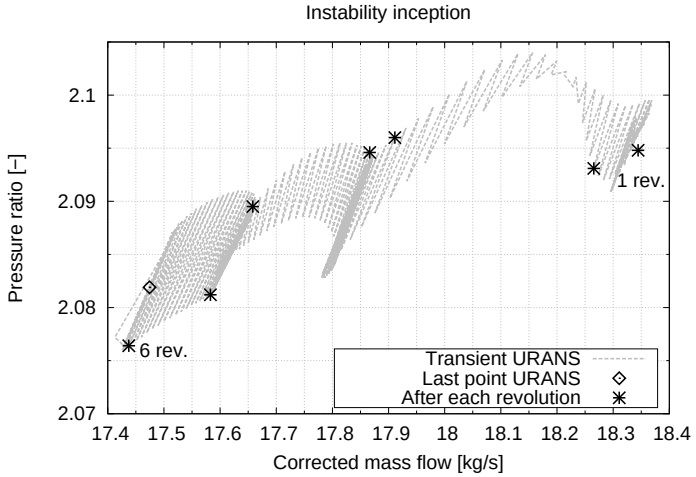

(c) Evolution of the transient stall line pressure ratio ($\overline{PR}$)

Figure 5.4: Configuration 2: Comparison of quarter-annulus bulk swirl RANS and URANS. Performance maps.

%Δ-Near peak efficiency					
Type	**Case study**	$\Delta\overline{W}\%$	$\Delta\overline{PR}\%$	$\Delta\overline{TR}\%$	$\Delta\overline{\eta}\%$
RANS-Rotor 37	Co-rot. 5 deg	1.90%	1.25%	0.95%	−2.72%
URANS-Rotor 37	Co-rot. 5 deg	2.36%	1.46%	0.85%	−1.88%

Table 5.3: Configuration 2: URANS and RANS bulk swirl +5 deg- Changes in $\overline{W}$, $\overline{PR}$, $\overline{TR}$, and $\overline{\eta}$ with the undistorted (clean) flow.

The comparison of the values of $\overline{PR}$, $\overline{W}$, $\overline{\eta}$, and $\overline{TR}$ near the peak efficiency

from the undistorted (clean) conditions were evaluated for both approaches, and is illustrated in Table 5.3. It can be noticed that the values of $\Delta\overline{PR}\%$, and $\Delta\overline{TR}\%$ near the peak efficiency are quite similar in both cases. However, the RANS calculations under predicts the $\Delta\overline{W}\%$ by 0.46%, whilst over predicting the $\Delta\overline{\eta}\%$ by 0.84%, when compared with the URANS results.

It can also be observed from Figure 5.4 that the differences are more pronounced as the flow reaches near the stall condition. It is a predictable outcome as the URANS calculates the detached flows more precisely than the latter. This detached flow is responsible for the major losses in the rotor domain, and supports the fact that the URANS predicts lower $\overline{PR}$ near stall than the RANS solution. However, the differences of less than 2.5% in the flow properties, such as the $\overline{W}$, $\overline{PR}$, $\overline{TR}$, and $\overline{\eta}$, were found over the entire rotor operation. Also, the computing requirements needed to carry out large number of URANS simulations reinforces the idea of adopting RANS approach for the bulk swirl parametric study. This parametric study was carried on the Stage 67 model, and is presented in the next section.

The flow-field of the URANS simulations was analyzed in-detail, especially near the stall conditions. This was performed to identify the key reasons of the inception of the instabilities, such as the flow spillage near the rotor tip casing. The observations made in this analyses were then used to identify the highly separated flow regions in the RANS solutions to determine whether the solution is near the last stable point, or is already inside the instability region of the rotor. These flow separation regions within the blade passages have been found to be the likelihood of the major flow instability inception, i.e. it can result into rotating stall, or even surge[1,22,23,75,76].

The Figure 5.4(c) shows the zoomed in view of the transient stall line from the Rotor 37 global performance plot of the area-averaged pressure ratio ($\overline{PR}$), operating at +5[deg] bulk swirl. These transient points were sampled after every 100 timesteps, which is around a bit more than half of the blade passing frequency (BPF). Therefore, some information of the flow field within this sampling rate could have been missed. However, the main unsteady flow features that were

responsible for the instability were captured. The chart also show that it required around 6 rotor revolutions from the last stable operating point to just enter into the rotating stall region, and oscillates near the last URANS point in the plot. This was achieved by an increment in the outlet static pressure. The global performance of the last URANS point was calculated by averaging the flow variables of the last cycle of the oscillation. The outlet throttling by increasing the static pressure by 2000$[Pa]$, from the last stable point was found to be enough to push the rotor just into the rotating stall region.

Flow Field Characteristics:

The instability criterion was based on observing the various rotor's flow field tendencies during the transient CFD run. These include analyzing the global performance properties such as the mass flow, the total pressure, etc. at certain time intervals to assess the changes in the overall rotor performance. Moreover, a number of monitor points were defined just 10% chord upstream of the blade's LE, and at 90% blade span, as shown in Figure 5.8. These points were utilized to asses the local flowfield near the blade's tip, as it is the region where inception of the instability likely to occur[22].

One of the key observable flow feature near the stability limit of typical transonic rotors is the intensified interaction between the tip clearance flow and the shock-wave system, as compared with operating conditions away from the stall. This phenomenon have been previously illustrated in the Section 4.2.2. The interactions between the Tip Leakage Vortex (TLV) and the passage shock can cause considerable flow spillage, thus initiating the instability disturbances near the rotor tip region. As Rotor 37 is a high-speed transonic rotor, spike-type disturbances[31] were expected to take effect, and drive the rotor into the rotating stall. Adamczyk et al.[1] have also reported the criterion for the spike-type disturbance to initiate within the rotor passages (see Section 2.10.3). This comprises of flow spillages either at the blade's Leading Edge (LE) or at the blade's Trailing Edge (TE). However, both the blade edges have also shown the signs of flow spillages simultaneously in the past[82,83].

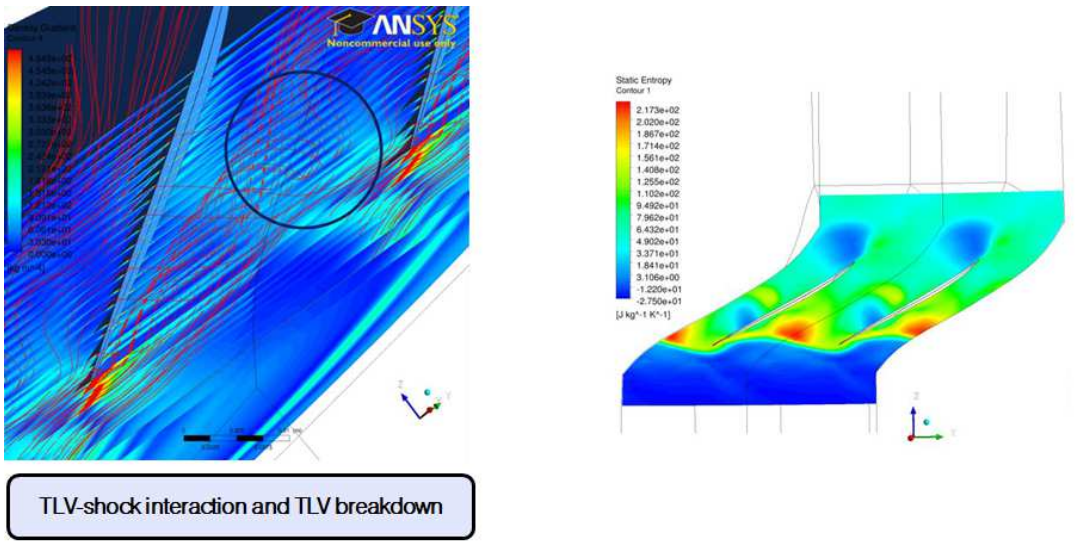

Figure 5.5: 5 deg Bulk swirl: Quarter-annulus Rotor 37 tip leakage vortex (TLV) breakdown.

Figure 5.5 illustrates the Rotor 37 entropy contour (right), and the TLV interacting with the rotor passage flow at 99% blade span (left), operating at near stall conditions. It can be observed from the static entropy contour that the interface between the incoming and the tip clearance flow is completely aligned near the blade LE. As the rotor is highly loaded, it implies that the shock-structure is also unsteady in nature. This is due to the shock movement upstream and downstream of rotor passages when interacting with TLV, thus fulfilling one of the instability criterion. Ultimately, due to this intense unsteady interaction, the TLV breaks down in the region of the high entropy interface. Consequently, the shock-structure detaches from the blade' s suction side, causing the flow separation, and thus compelling the flow to spill at the adjacent rotor passages.

Figure 5.6 shows the local relative velocity vectors at 99% blade span within one flow passage of the URANS quarter annulus model of Rotor 37. The flow spillage at the LE can be clearly observed. This disembarks just below the tip-clearance gap of the rotor passage, the flow is spilled downwards to the the adjacent blade, and can also propagate around the annulus. On the other hand, no TE flow impingement was observed for this particular rotor configuration. However, already the criteria for spike-type rotating stall inception was fulfilled by

the LE flow spillage.

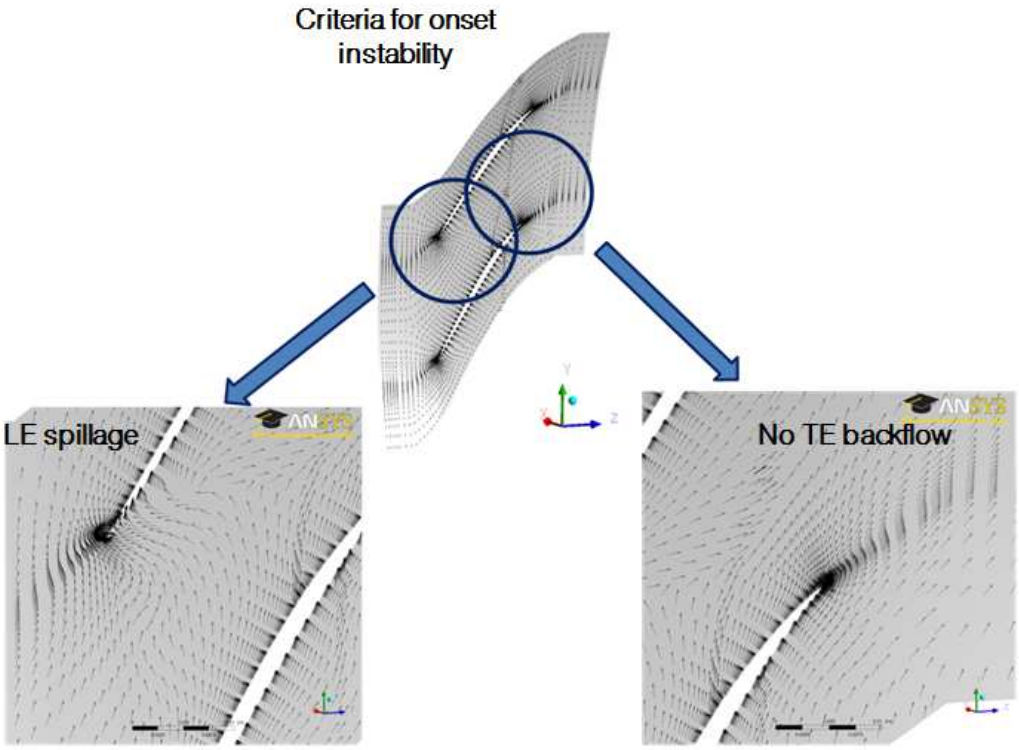

Figure 5.6: 5 deg Bulk swirl: Quarter annulus Rotor 37 LE spillage near stall operation

Figure 5.7 depicts the region of low-momentum using the 3D-Graphical representation. Axial velocity is plotted against the blade span for half of the quarter annulus Rotor 37 simulated in this study. It shows the axial velocity variation for five blade passages, when operating in both stable (away from stall) and unstable (in stall) conditions. During the unstable operation, the low-momentum region can be clearly observed near the tip part of some of the blade passages. This rotating-stall region is then propagated around the annulus at a part rotor rotational speed. This can be illustrated using the Figure 5.8.

In Figure 5.8, the evolution of the normalized pressure and axial velocity probe readings are plotted against the number of rotor revolutions. These numerical monitor probes were placed at the height 90% blade span, and were positioned 10% blade chord upstream of the leading edge. In the case of axial velocity, speed of sound at the rotor inlet was used to non-dimensionalised the probe

readings, and for the case of the static pressure, the following Equation 5.3 was utilized. Also, to note in these charts, a constant has been added to every blade measurement in order to separate the data of the individual blade from each other. In addition the measurements of the pressure and velocity were generated every timestep of the simulation.

$$p_{norm} = \frac{p_i - p_{avg}}{p_{inlet}} \tag{5.3}$$

where, p_i is the static pressure reading from each probe, p_{avg} stands for the averaged static pressure at each probe after one revolution, and p_{inlet} refers to the area-averaged static pressure at the rotor inlet.

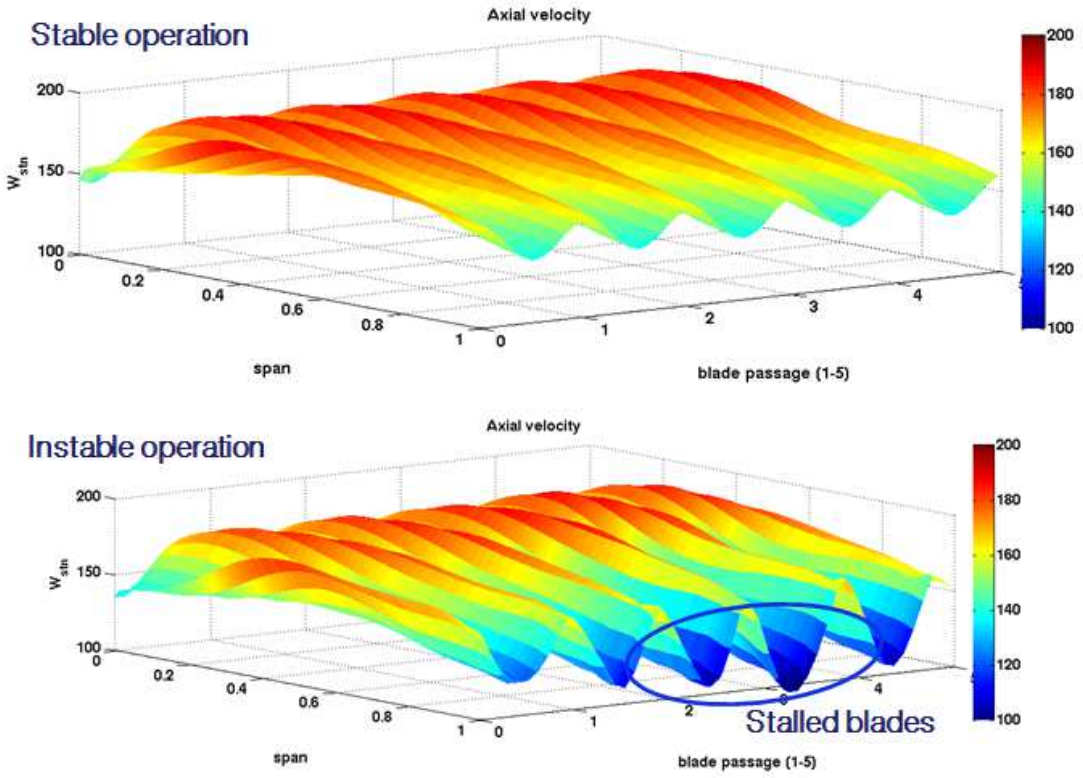

Figure 5.7: 5 deg Bulk swirl: Quarter annulus Rotor 37 axial velocity, V_z evolution

Thus, from Figure 5.8, after 0.3 rotor revolution the first disturbance can be detected in probe 1. This disturbance very slowly grows in amplitude, and at 0.75 rotor revolutions a first significant spike was detected in probe 1, and at 1.5 revs a second spike was noticed. This spike resulted in a stronger flow separation

at probe 9 (at around 2 rotor revs). This region of low momentum (also known as the rotating stall) then started to propagate around the annulus, as can be observed by the fluctuations in all the numerical probes with time. It was found to be traveling at a speed of around 35% rotor spool speed, thus recognizing itself as spike-type rotating stall, and as also found by other researchers on similar transonic rotors.

The following can be recognized as the key findings from these bulk swirl CFD case studies:

- Similar effect of the change in inlet swirl angle in both the co and counter rotating cases of the Rotor 37 configuration was found to have evident effects on the turbo-machinery performance (i.e. in terms of $\overline{PR}$, $\overline{W}$, $\overline{\eta}$, etc.) as for the previous Rotor 67 configuration.

- The differences between the RANS and URANS capability was also put into practice using the bulk swirl pattern. Not a lot of differences were found between the two approaches away from the instability region. Both showed similar flow field characteristics, and the effect on the compression system, when encountered a pure bulk swirl at the inlet.

- It was observed that in order to capture precisely the transient onset of the rotor instabilities, one has to adopt the URANS approach. In this way, the flow field behavior near the stability limit can be observed in the real physical time. However, if the objective is to broadly identify the limitations of transonic rotor under the distorted flows, even the RANS approach should suffice.

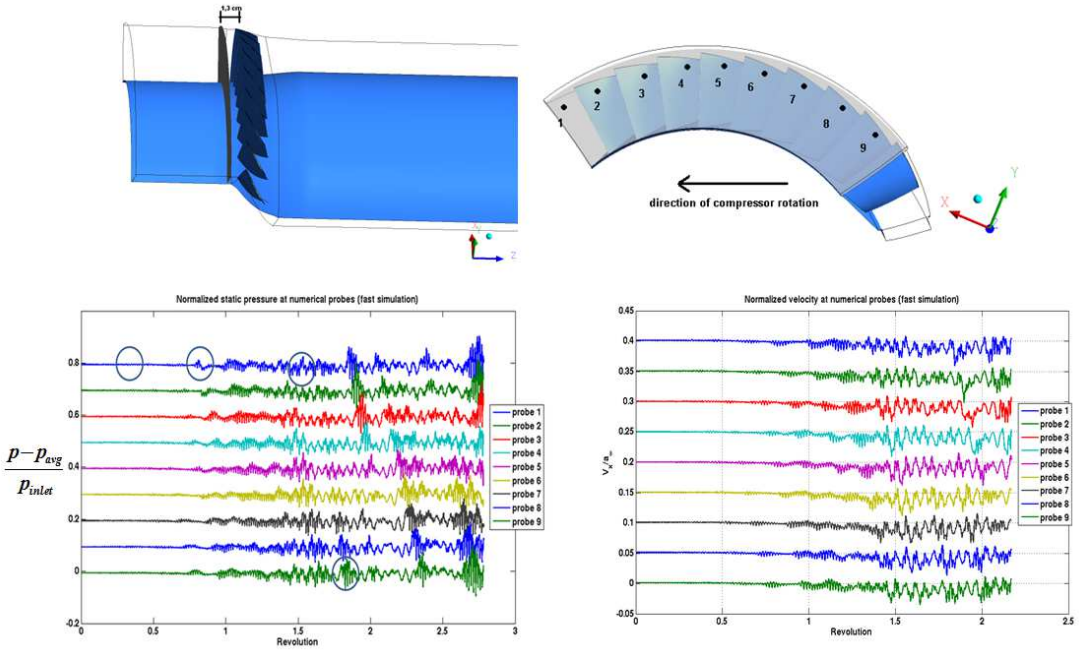

Figure 5.8: +5[deg] Bulk swirl: Evolution of the quarter annulus Rotor 37 flow field at tip probes during the transient stall.

5.1.3 Configuration 3: Stage 67 RANS parametric study

The primary set of analyses that were performed on the first Stage 67 were under the influence of pure bulk swirl. RANS simulations modeling one-flow passage of the Stage 67 with periodic BC on the side walls were carried out to assess the overall performance effects on the set of a rotor and stator. The key aim was to identify the effect of high bulk swirl angles on the stage operability, and any ambiguous behavior if the transonic rotor flow-field exhibits at these extreme swirl flow conditions. Also to note, this particular work was performed in a joint collaboration with a MSc student[62] working under supervision of the author in the year 2012-13.

Simulations were performed at constant N = 100% rotational speed, and the rotor was throttled from near choke to near stall operating condition by changing the choked nozzle areas (see Section 3.5.2). Each simulation was performed using a cluster of 48 CPUs. It required around 24 hours running time to reach the residual below $1x10^{-6}$, and the convergence criterion to be fulfilled.

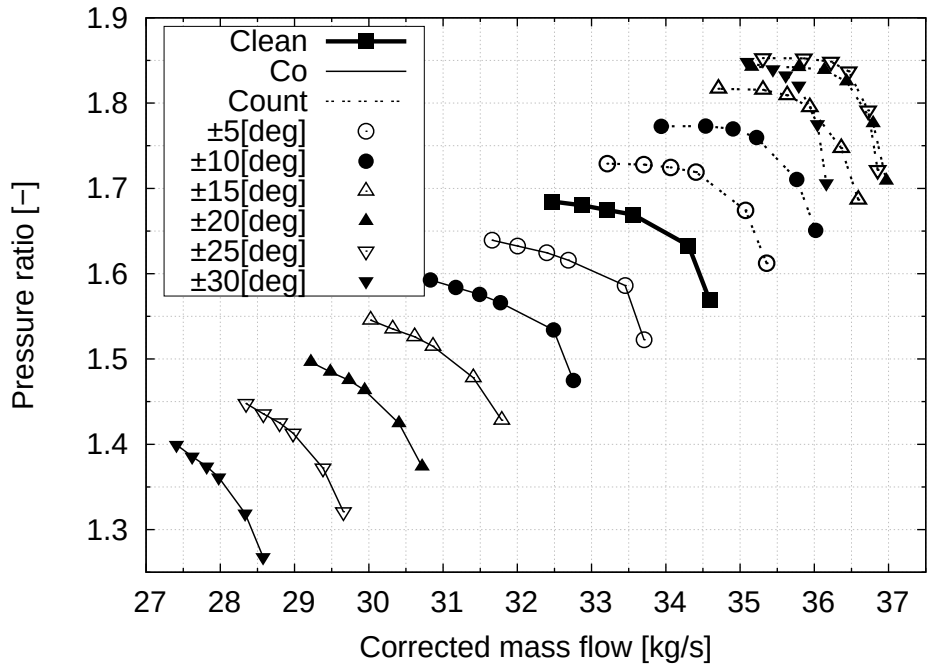

(a) Evolution of the rotor pressure ratio ($\overline{PR}$)

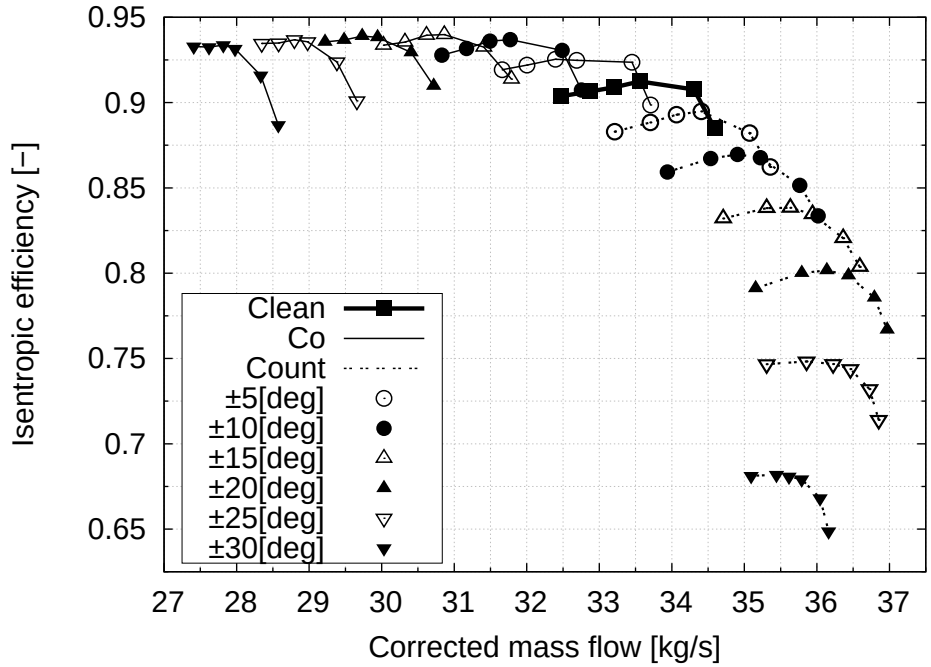

(b) Evolution of the rotor isentropic efficiency ($\overline{\eta}$)

Figure 5.9: Configuration 3: One flow passage Stage 67 RANS CFD. Both Co and Counter rotating bulk swirl. Performance maps.

5.1.3.1 Global performance

The compressor maps in Figure 5.9 show the results of both co and counter rotating bulk swirl on the rotor performance. At low swirl angles, the effect of ingesting a co-rotating swirl pattern is a reduction of the area-averaged pressure ratio ($\overline{PR}$) and the corrected mass flow ($\overline{W}_{correc}$), while a opposite trend is observed for the counter-rotating pure bulk swirl pattern. On the other hand, there is a slight increase in the isentropic efficiency ($\overline{\eta}$) for a co-rotating swirl, and a large reduction in $\overline{\eta}$ for the latter. This is a similar outcome that was observed on the previously described rotor configurations, when they were exposed with lower pure bulk swirl angles (i.e. upto 8[deg]).

However, at high swirl angles (i.e. $\alpha_{abs} \geq \pm 20$[deg]), there is a change in the flow-field characteristics, when simulated under both co and counter bulk swirl polarities. These are discussed in the following paragraphs.

The shift in the speed lines correspondent to a co-rotating bulk swirl angle from low to high (see Figure 5.9), has been found to exhibit a larger loss in $\overline{PR}$ and $\overline{W}_{correc}$, whereas the $\overline{\eta}$ remains almost unchanged but then starts to drop, when the swirl angle exceeds +15[deg]. The reader should also notice the change in the rotor speed-line slope, which takes place as the swirl angle increases. The rotor speed-line correspondent to +30[deg] is steeper than the undistorted (clean) one. This does not corresponds to the characteristics of low speed compressors. This is due to the lack of additional operating points of the speed-line, which could have been simulated by decreasing the outlet choke nozzle areas further for these particular simulations. However, the objective of the study was the identification of the flow phenomena which take place when the rotor is subjected to high swirl angles, and these extra operating points would not provide extra information at this stage. Therefore, the focus was then extended to the counter-rotating bulk swirl analyses.

The Figure 5.10 is illustrating solely the compressor rotor maps under the influence of counter-rotating bulk swirl. The transonic rotor exhibits similar characteristics as previously explained for a counter swirl pattern in the previous

sections until the swirl angle values of around -20[deg]. This includes shifting of the rotor speed-line rightwards and upwards, which is achieved by an increase in the values of $\overline{PR}$, $\overline{TR}$, and $\overline{W}_{correc}$ at the constant outlet throttle setting. While, there is a large drop in the values of $\overline{\eta}$ due to the increment in flow losses.

However, at high counter swirl angles, the flow-field exhibits a different characteristic. Lower than -20[deg] of counter swirl, which the author has defined as the critical counter-rotating swirl angle for the Rotor 67 configuration, the losses related with the higher Mach number (M_{rel}) are larger than the increase in the area-averaged pressure ratio ($\overline{PR}$) associated with a higher incidence angle (i). Therefore, speed-line drops in terms of the blade loading, and a large reduction in the operating mass flow range is also observed. The $\overline{\eta}$ drops dramatically (about 30% drop from clean condition) as the heat exchange and shock losses increases massively, making the compression system highly unstable and inefficient. A reduction in the $\overline{W}_{correc}$ can also be evidently observed at the swirl angle of -30[deg], and is the resultant of imbalance between the $\overline{PR}$ and $\overline{TR}$, and the necessity of keeping the outlet throttle setting constant.

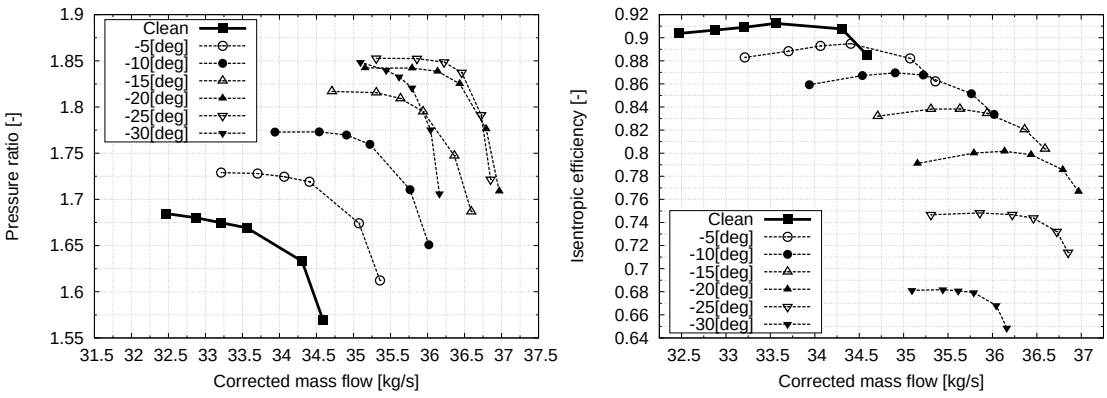

(a) Evolution of the rotor pressure ratio ($\overline{PR}$) (b) Evolution of the rotor isentropic efficiency ($\overline{\eta}$)

Figure 5.10: Configuration 3: One flow passage Stage 67 RANS CFD. Counter-rotating swirl results. Performance maps.

5.1.3.2 Flowfield features

The following paragraphs will describe in more detail the flow features that were mentioned in the global performance, and which limits the transonic rotor operation at high bulk swirl angles. First of all, the Figure 5.11 below shows the span-wise distribution of the incidence angle (i) for both co and counter-rotating bulk swirl test cases. From the incidence angle charts, the most prominent observation is the tendency of the rotor to operate at a unique incidence above a certain blade span. It tends to achieve this for most of the swirl angles, when under the influence of both co and counter swirl topology. From Figure 5.11(c), the relative Mach number for a clean (uniform axial flow) becomes sonic (i.e. $M_{rel} \geq 1$) at a blade span (s) of about 40%. Above this blade span, the rotor can be regarded to be operating at sonic conditions, and thus will self-contain a shock-wave system to accommodate the incoming flow.

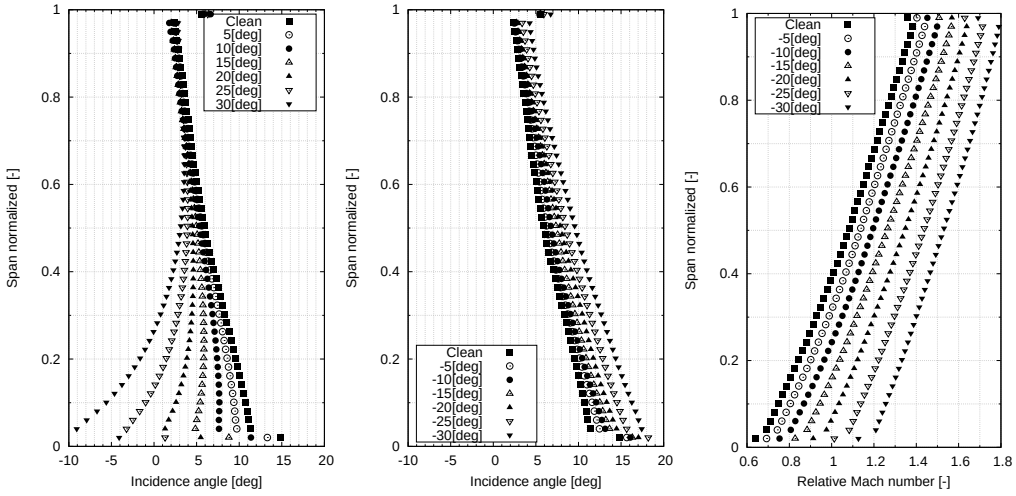

(a) Co-rotating (b) Counter-rotating (c) Counter-rotating

Figure 5.11: Span-wise distribution of the incidence angle (i), and relative Mach number (M_{rel}).

Thus, the flow behavior can be explained by first understanding the flow-field of the shock-wave system for the Rotor 67 configuration, which is highlighted in the Figure 5.12. The evolution of the shock-wave system is illustrated at 75% bade span for the three operating regions, namely, Near Choke (NC), Near Design

(ND), and Near Stall (NS). Also to note, as the Rotor 67 is a twisted blade geometry, it is designed in a such way that the shock becomes stronger as the blade span increases and the blade chord becomes smaller. However, the evolution of the shock-wave system at different operating conditions exhibits similar characteristics along the sonic blade span. At choking conditions, a weak bow shock at the blade's leading edge (LE), and a much stronger passage shock at near mid chord was observed. As the $\overline{PR}$ increases, the passage shock moves upstream, and becomes weaker in strength. While the bow shock becomes stronger, and starts to significantly separate from the blade's LE. At near stall conditions, the rotor only exhibits a single strong bow shock, and which is detached from the blade's LE.

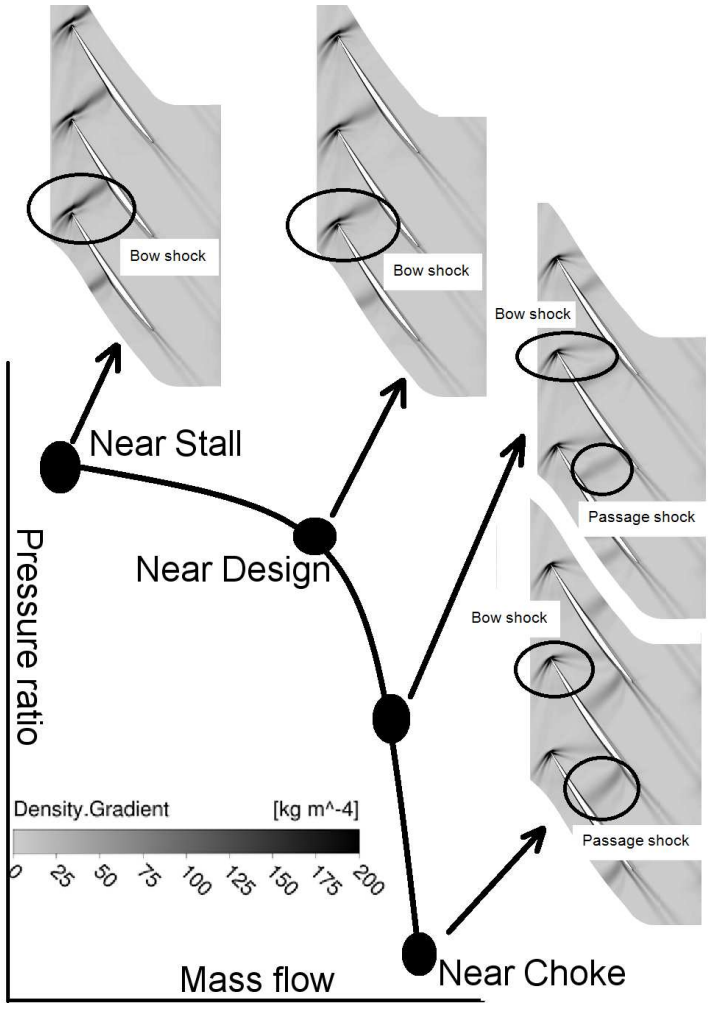

Figure 5.12: Rotor67 shock-wave system evolution at 75% blade span.

Returning back to the context, when the transonic rotor operates in a region where a bow shock and a passage shock exists, then the expansion waves have been found in between them[47]. During this flow operation, it is said the rotor operates at a *unique incidence*. The unique feature of this flow operation is the fact that the rotor operates at a constant incidence angle, regardless of the flow condition at the inlet. This explains the similar flow behavior that can be observed from Figure 5.11.

For a co-rotating bulk swirl (Figure 5.11(a)), the rotor is operating at a unique incidence from 40% blade span upwards for the swirl angles upto +15 [deg]. During this operation, the relative velocity (V_{rel}), the axial velocity (V_a) and the absolute swirl angle (α_{abs}) have to compensated in order to keep the relative inlet angle (α_{rel}) constant (see Figure 5.14). It means that the rotor is still trying to accommodate the incoming flow, and trying to maintain the stable operation without losing out in the performance. However, for swirl angles from +15 [deg] to +30 [deg], the flow exhibits a different characteristic. It can be observed from the Figure 5.11(a), the rotor is no longer operating at a unique incidence around the blade's mid-span region. But it is still trying to accommodate to a unique incidence near the tip region (also refer Figure 5.14). It means that the incoming distorted flow is changing the rotor shock-wave system near the mid-span region, where the shocks are much weaker. Thus, it's easier to diminish them when encountered by a co-rotating bulk swirl angle high enough to reduce the axial velocity to very low.

This flow observation is also highlighted in the density gradient plots (see Figure 5.13) of co-rotating swirl from low to high bulk swirl angles, shown at different blade spans. As high density gradient lines represents the shock structures within the blade passages, none can be observed at the high swirl angle angle of 30[deg]. It means that the rotor loading have been reduced to the minimal to accommodate the swirl flow. This also explains why the efficiency of the rotor starts to reduce at higher co-rotating swirl angles (see Figure 5.11(b)).

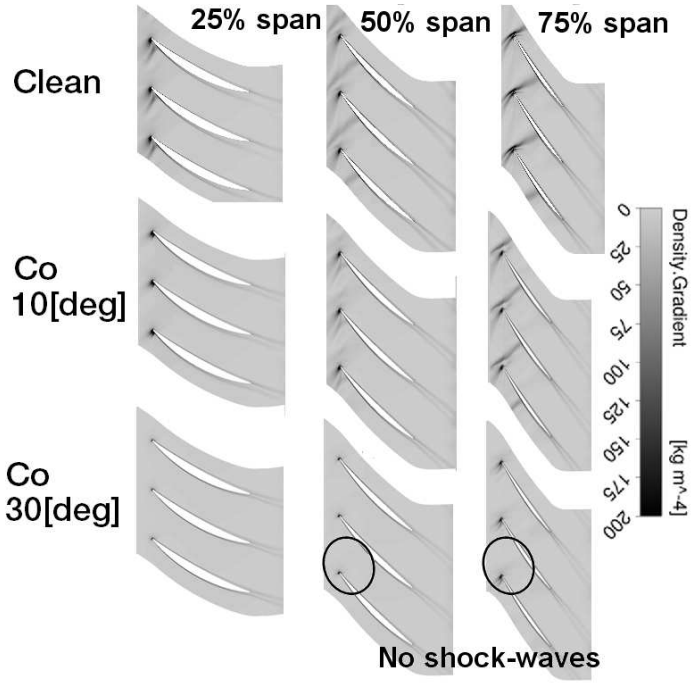

Figure 5.13: Density gradient span-wise contours illustrating the Rotor 67 passage's shockwave system. Near-design condition. Co-rotating bulk swirl.

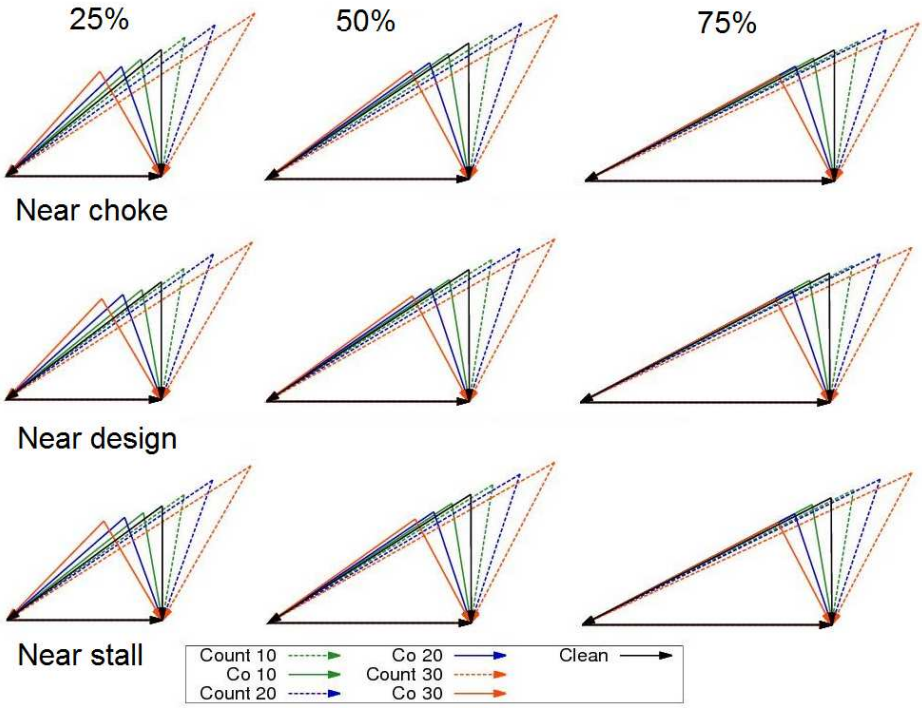

Figure 5.14: Velocity triangles at different blade spans. Ingestion of pure bulk swirl.

For the counter-rotating bulk swirl cases(Figure 5.11(b)), it seems like up to about -20[deg] , the bow shock at the rotor blade LE tried to accommodate the inlet α_{rel} to the desired unique incidence value, by increasing the V_a, and the V_{rel}, and decreasing the α_{abs}. This is also illustrated in Figure 5.14. This in return makes the shock system much stronger, and results in choking of the passage flow entirely from hub to tip. This strong bow shock attached inside the rotor passage can be seen in the density gradient plot in Figure 5.15. It can also be observed that for the counter swirl angles higher than -20[deg], the bow shock seems to be have been disturbed from its original position due to an interaction with some other flow feature near the blade suction side. This disturbance in the shock system induces a considerable amount of flow losses, which explains why the global performance (see Figure 5.10) showed the deterioration of the $\overline{PR}$ and the $\overline{\eta}$ beyond this *critical counter-rotating swirl angle*. This results in not obeying the unique incidence criterion at high counter-rotating swirl angles. This is also illustrated in the velocity triangles in Figure 5.14.

The amount of flow losses encountered under the influence of both co and counter rotating bulk swirl were quantified in terms of two parameters, namely, the loss coefficient ($\overline{\omega}$), and the relative pressure ratio ($\overline{P}_{rel}$). The Equations 5.4 and 5.5 were utilized. Where $\overline{P}_{1,rel}$ and $\overline{P}_{2,rel}$ refer to the area-averaged total pressure in the relative frame of reference at the blade aligned surfaces of revolution, and ($\overline{P}_{1,rel}\overline{p}_1$) is averaged value of the dynamic pressure at the aligned surface of revolution upstream of the rotor. The data was consistently generated by taking circumferential and radial area-averaged of the flow quantities. The measurement stations have been previously explained in the Section 3.7. The results are shown in Figure 5.16.

$$\overline{\omega} = \frac{\overline{P}_{1,rel} - \overline{P}_{2,rel}}{(\overline{P}_{1,rel} - \overline{p}_1)} \tag{5.4}$$

$$\overline{PR}_{rel} = \frac{\overline{P}_{2,rel}}{\overline{P}_{1,rel}} \tag{5.5}$$

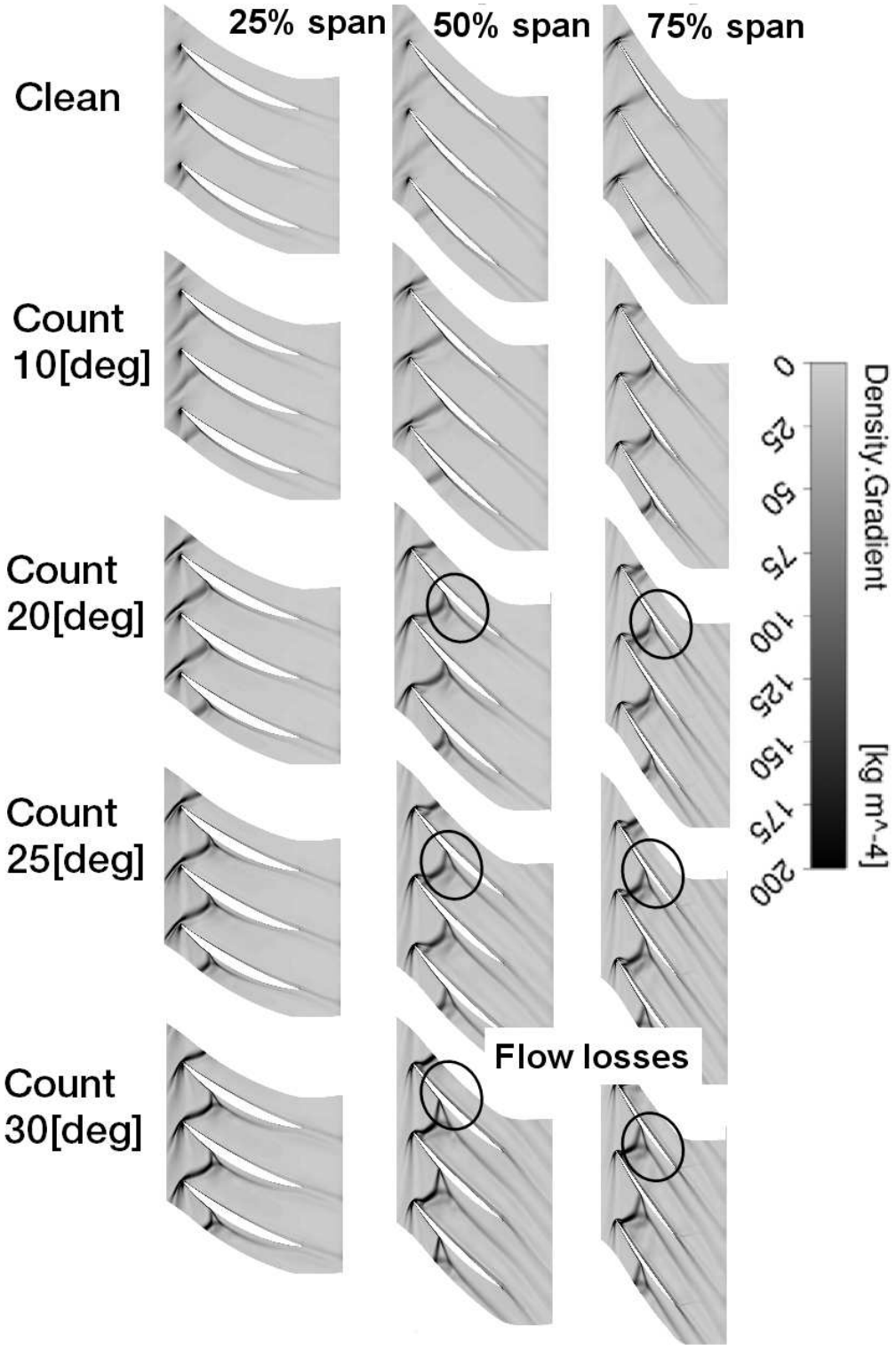

Figure 5.15: Density gradient span-wise contours illustrating the R67 passage's shockwave system. Near-design condition. Counter-rotating bulk swirl.

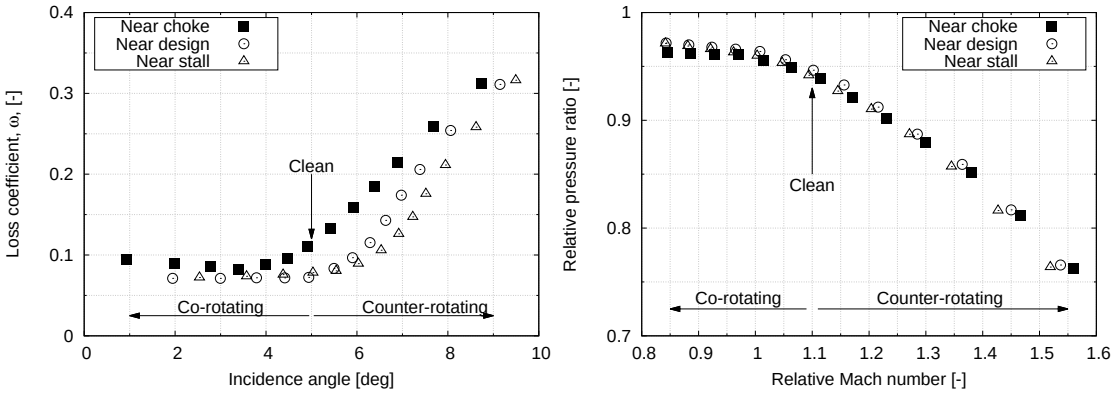

(a) Evolution of the loss coefficient ($\overline{\omega}$). (b) Evolution of the relative pressure ratio ($\overline{P}_{rel}$).

Figure 5.16: Configuration 3: Loss coefficient and relative pressure ratio. Co and counter-rotating bulk swirl.

From the above Figure 5.16, it can be clearly seen that when co-rotating bulk swirl angle is increased (i.e. the incidence angle is reduced), there is a slight reduction in the loss coefficient ($\overline{\omega}$), and an improvement in the relative pressure ratio ($\overline{P}_{rel}$). Only at very high co-rotating swirl angles, an increment in the flow losses were observed (i.e. when $\alpha_{abs} \geq 20$[deg]). Therefore, it can be stated that the ingestion of a co-rotating swirl doesn't induce noticeable flow losses in the compression system.

On the other hand, the counter-rotating bulk swirl analyses showed a completely different characteristic. There is a drastic increase in the flow losses observed with an ingestion of a counter-rotating swirl. For example, the loss coefficient ($\overline{\omega}$) increased from a value of 0.075 to 0.32, at near design operation, when encountered by a counter-rotating bulk swirl of -30 [deg]. This is an increase of flow losses by an amount of about 320%, and its an average of the whole blade passage. It clearly means that the reason of disturbance in the bow shock under high counter-rotating swirl angles is also inheriting a large amount of flow losses. Also, the shock losses are increased with an ingestion of counter swirl as the axial velocity is also increased.

A further detailed analyses of the flow-field were performed along the entire blade passage, and some interesting observations were made, as shown in the

Figures 5.17 and 5.18. A region of low-momentum and pressure was noticed where the interaction of bow shock takes places, as shown as an example in Figure 5.22. Also, the movement of the shock upstream show radial flow movement along the blade span. From Figure 5.18, a vortex can be clearly observed traveling from hub to tip on the suction side of the blade.

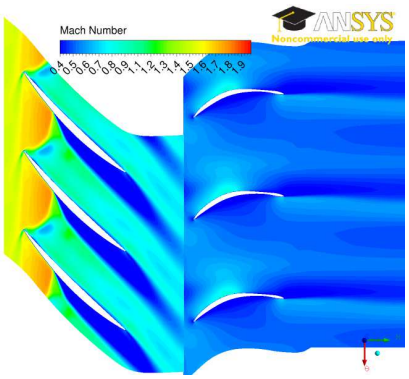

(a) Relative Mach number (M_{rel}).

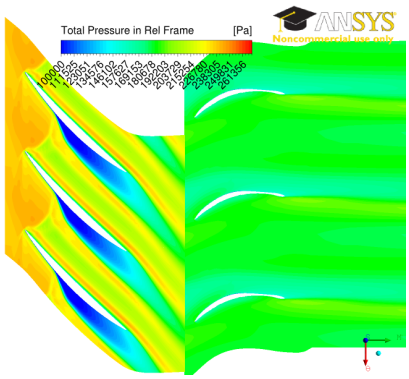

(b) Total pressure in stn frame (P_t).

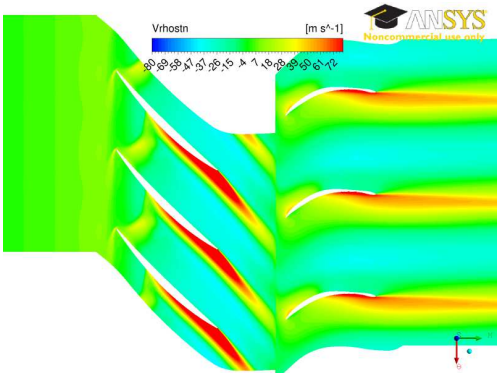

(c) Radial velocity (V_r).

Figure 5.17: 30[deg] counter-rotating bulk swirl ingested at mid-span. Near-design conditions.

This vortex is thought to be induced by an interaction between the strong bow shock, and the hub passage surface. Due to an increase intensity in the shock strength with the ingestion of high counter-rotating swirling flows, this vortex is generated where the bow shock attaches to the suction side of the rotor. Also, the strength of this hub corner vortex depends on the strength of the incoming counter-rotating bulk swirl. It can be observed that as the counter-

rotating bulk swirl angle is increased, this vortex travels with much higher radial velocity within the blade passages towards the tip region, and causing further passage flow losses along the way. The streamlines of the entropy for the α_{abs} = -30[deg] is shown in Figure 5.18(d). This clearly explain the reasons for the rotor performance deterioration at high counter-swirl angles. This may also trigger an early rotating-stall, as it fulfills one of the instability criterion, i.e. interaction of the passage flow with the tip gap flow.

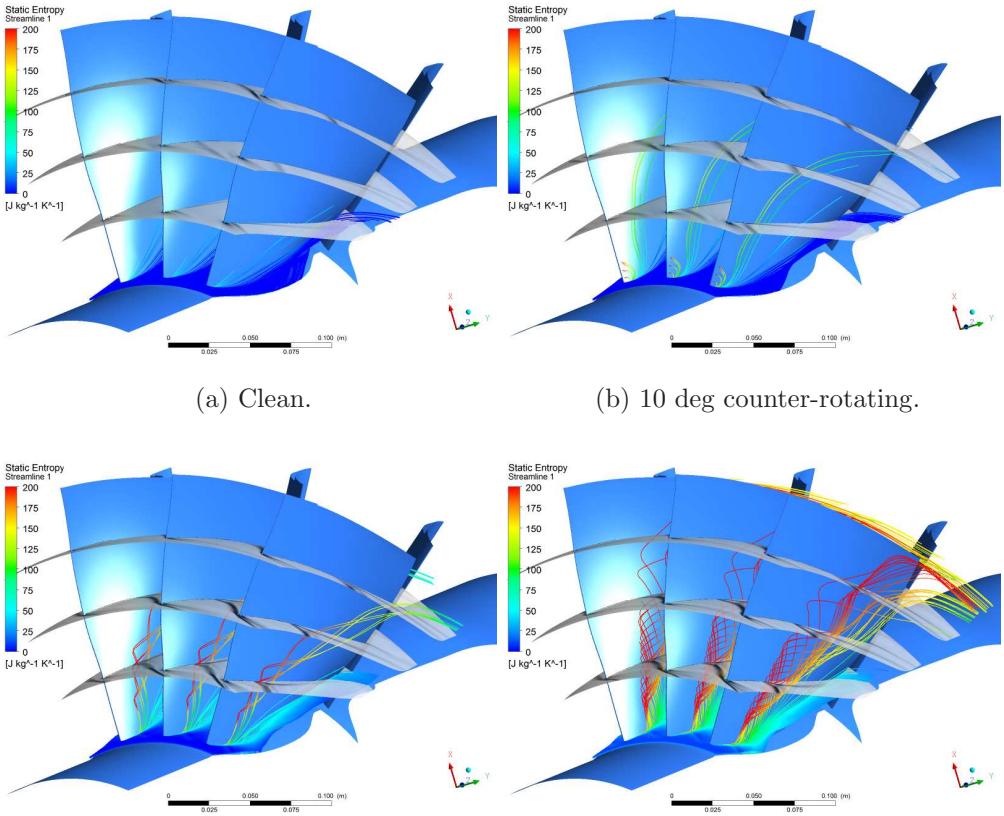

(a) Clean.

(b) 10 deg counter-rotating.

(c) 25 deg counter-rotating.

(d) 30 deg counter-rotating.

Figure 5.18: Identification of hub vortex under various counter-rotating swirl intensities using the static entropy flow streamlines. Near-design condition.

Comparison with the Rotor 37 (Configuration 2)

Another joint collaboration was made with a visiting MSc student[12] to validate the outcomes of the Stage 67 (Configuration 3) results with the Rotor 37 (Configuration 2). In this case study, only the rotor was simulated without any

downstream stator, and the static pressure (p_s) was used as the outlet BC. Very similar results to the Rotor 67 can be observed for the global performance, as shown in Figure 5.19 below. The co-rotating bulk swirl results in the continuous reduction of $\overline{PR}$, while an increment of the $\overline{\eta}$. To note, a higher increase in $\overline{\eta}$ was noticed for this case, when the co-rotating bulk swirl angle was increased.

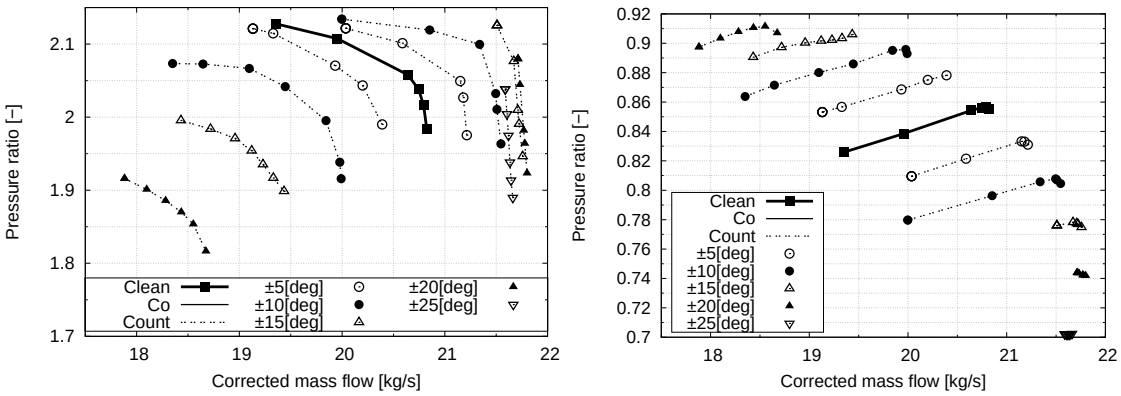

(a) Evolution of the pressure ratio ($\overline{PR}$). (b) Evolution of the isentropic efficiency ($\overline{\eta}$).

Figure 5.19: Compressor maps. Pure bulk swirl[12].

On the other hand, the counter-rotating bulk swirl also showed similar global performance effects, as for the Stage 67 configuration. After a certain counter-rotating bulk swirl angle, named as the critical counter-rotating swirl angle, the global performance showed a deterioration. For the Rotor 37, this critical swirl angle was found to be about -15[deg], and is smaller than the -20[deg] observed in the case of Rotor 67. Also, the reasoning behind the deterioration was found to be same as well, as shown in Figure 5.20.

The interaction of the shock structure with the hub surface resulted in the generation of a hub vortex on suction side of the blade. This vortex is again dependent on the incoming swirl intensity, and increases the flow losses across the rotor blade passage. However, as the Rotor 37 have a higher hub to tip ratio than the Rotor 67, and most of the blade span operates sonic even in the uniform axial flow conditions. Thus, this vortex was found to have more deteriorating effects on the rotor performance compared with the Rotor 67. This is highlighted in Figure 5.19, a counter-rotating swirl angle of -25 [deg] have a very steep line,

and is operating in choked conditions throughout its operation from choke to near stall. Thus, the Rotor 37 can be identified as much more sensitive to the counter-rotating swirling flow, and more unstable transonic rotor than the Rotor 67 when exposed to bulk swirl. However, the key conclusion is the fact that the underlying flow physics behind the performance effects of swirling flows on the transonic rotors are similar.

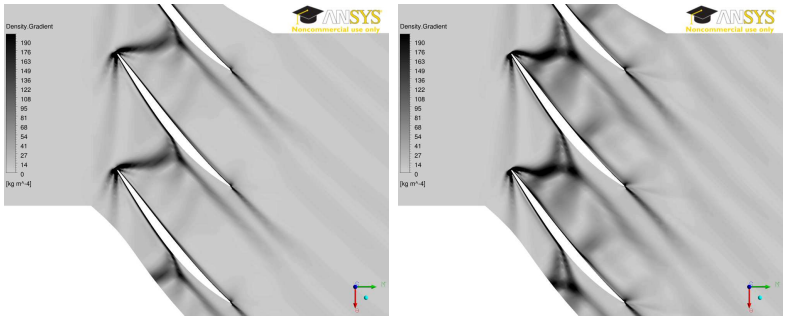

(a) Clean. (b) 20 deg counter-rotating.

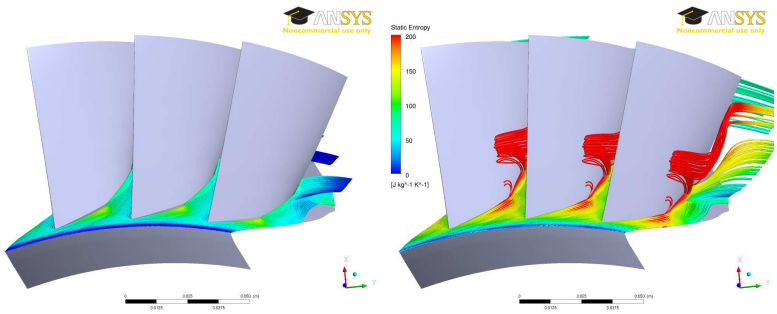

(c) Clean. (d) 20 deg counter-rotating.

Figure 5.20: Shockwave structure and the generated hub vortex. Near-design. At Mid-span[12].

5.1.4 Summary

The following can be recognized as the key findings from the bulk swirl CFD parametric study:

- The change in the inlet swirl angle in both co and counter rotating cases of the Stage 67 configuration was found to have evident effects on the turbomachinery performance (i.e. in terms of $\overline{PR}$, $\overline{W}$, $\overline{\eta}$, etc.). The effects

are similar to the previously discussed rotor configurations but at low bulk swirl angles.

- The transonic rotor tends to behave differently at high swirl angles, especially when a counter rotating bulk swirl is ingested.

- There is a large drop in the values of $\overline{PR}$, $\overline{TR}$, and a slight reduction in the $\overline{\eta}$, when a high co-rotating swirl angle is simulated.

- On other hand, the ingestion of a high counter-rotating bulk swirl completely changes the rotor characteristics. Large rotor losses are observed, when simulated lower than -20[deg] of bulk swirl for the Rotor 67, and around -15[deg] for the Rotor 37 configuration. These have been identified as the critical counter bulk swirl angles for the two rotor configurations.

- It has been found that these flow losses are induced at the rotor blade's suction side, and is located near the hub surface of the blade passage. A hub vortex is formed due to a strong interaction with the bow shock, and then which travels upstream towards the tip region. Thus, at high counter-rotating swirl angles, this can result in a large performance deterioration of the compression system, which may lead to the rotating stall or surge.

5.2 Vortex ingestion cases

This section discusses the performance effects of an ingestion of a tightly-wound vortex on the full-annulus rotor configurations. Both RANS and URANS approach have been tried and analyzed on the Rotor 67 configuration. Apart from this, a RANS parametric study altering the various vortex flow-field features have been carried out on the Stage 67 configuration, and is discussed in-detailed analyses. Thus, it is divided into two parts, first discussing the results of the Rotor 67 (with static pressure as outlet BC), and then the results of the vortex flow-field parametric study on the first Stage 67 (with a choked conv-diverg nozzle as outlet BC).

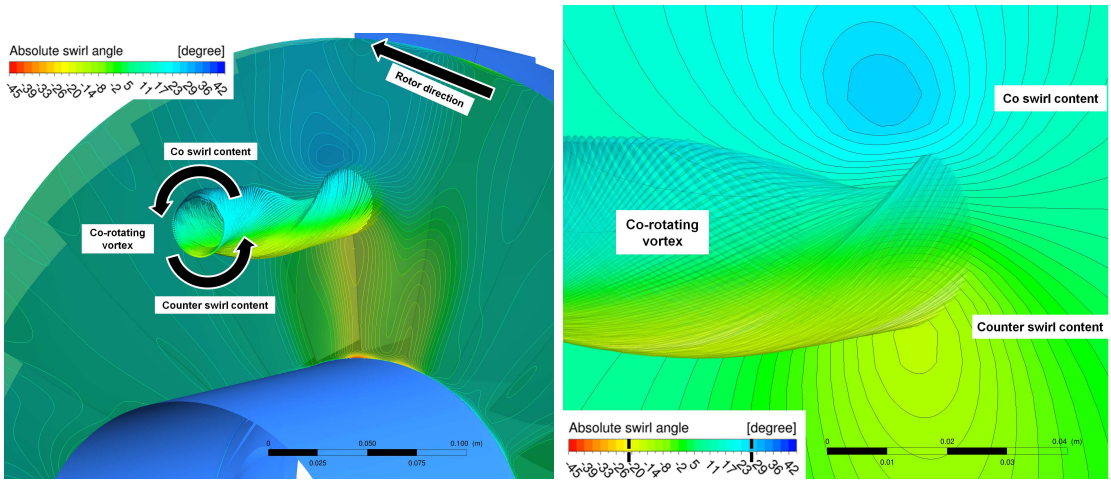

(a) α_{abs} topology with vortex streamlines. (b) Zoomed in view of, α_{abs} distribition.

Figure 5.21: Example of absolute swirl angle, α_{abs}. Near design. Co-rotating vortex ingestion at mid-span.

Before discussing the results from the CFD simulations, the above Figure 5.21 show a typical example of the vortex flow-field, upstream of the full-annulus rotor blade. This will help the reader to understand the local vortex flow-field, and it's differentiation with the flow-field of a pure bulk swirl pattern. Figure 5.21 is illustrating the absolute swirl angle (α_{abs}) topology that the rotor blade will experience during an ingestion of a co-rotating vortex. It can be noticed that both the co swirl (positive α_{abs}), and the counter swirl (negative α_{abs}) is present locally upstream of the blade. It is due to the small vortex core-size compared to the blade diameter. Thus, this distinguishes the vortex flow-field to the ingestion of a pure bulk swirl, where only one swirl direction is always present, i.e. either a positive or a negative α_{abs}.

Therefore, when analysing the results from the vortex ingestion cases, one has to keep in mind that both the co and the counter swirl contents will be present. These will affect the blade aerodynamics coherently, regardless of the absolute vortex direction. However, the absolute vortex direction will decide the radial position of these swirl contents. For an example, the ingestion of a co-rotating vortex at 50% blade span will result in a local co-rotating swirl content from about $50 - 75\%$ blade span. Whereas, from about $25 - 50\%$ blade span will still

experience a local counter-rotating swirl content. Also, consequently the local swirl-contents will become opposite in direction if the absolute vortex direction changes its polarity (i.e. from co to counter-rotating). The span-wise extent and the intensity of the swirl-contents is also dependent on the vortex-core size, and the circulation, respectively.

5.2.1 Configuration 1: Rotor 67 comparison of the RANS and URANS simulations of vortex ingestion

This section explains the effects of a single co and counter rotating vortex ingestion on the isolated Rotor 67 configuration, and both the RANS and URANS approach was used. The datum vortex circulation (see Section 3.6.2) of, $\Gamma = \pm 22.1[m^2.s^{-1}]$, was ingested near the hub (25% span) in both directions, co and counter-rotating to the rotor direction. The full-annulus rotor was simulated at, $N = 100\%$, spool speed and the effect of a vortex ingestion on the rotor global performance was studied (i.e. in terms of $\overline{PR}$, $\overline{W}$, $\overline{\eta}$, etc.). The differentiation between the results of the two numerical schemes (RANS and URANS) was also scrutinized.

To simulate the RANS cases, up to 64 parallel CPUs from the Cranfield High Performance Computing (CHPC) facility have been used, taking 1.5-2 days to reach a converge solution. The converged solution means the residuals of the flow variables within the domain reached at least below $1x10^{-6}$, and the fluctuations in the mass flow imbalance were below 0.1%. In general, it took an approximate 12 CPU days on the CHPC to get a full speed line, i.e. from near choke to near stall conditions. This was done by increasing the outlet static pressure. On the other side, the URANS simulations took much longer. Several unsteady CFD simulations were performed in the region from near-design to near-stall conditions. To simulate this, up to 96 parallel CPUs from the CHPC facility were used, taking 4-5 days per revolution to converge. Thus, for one converged quasi-steady state solution, it needed atleast 1.6 rotor revolutions near design, and much more at near stall conditions. As an approximation, it took around 65 days of 96 parallel

CPU's CHPC time to generate the part of counter-rotating vortex speed line from near-design to near-stall conditions (as shown in Figure 5.28).

A large post-processing database is also generated with these types of full-annulus CFD simulations. Around 25GB of data was obtained from each converged RANS simulation. On the other hand, URANS generated around 50GB per rotor rev, and as a result more than 3TB of data was obtained from this URANS study. Thus, several post-processing tools were developed in order to analyze the CFD results in a consistent manner.

Figure 5.22 show the swirl angle, α_{abs}, distribution upstream of the rotor inlet (at Plane 01, see Figure 3.25), for both co and counter-rotating vortex ingestion cases. The maximum local co and counter-swirl angles reached for the, $\Gamma = \pm 22.1[m^2.s^{-1}]$, in both cases α_{abs} was in the region of ± 25[deg] to $30 \pm$ [deg]. It is an interesting observation as the critical counter-swirl angle for the Rotor 67 as discussed in the last section was found to be in a similar swirl angle range. Thus, some flow losses were expected to be observed near the maximum counter-swirl content region.

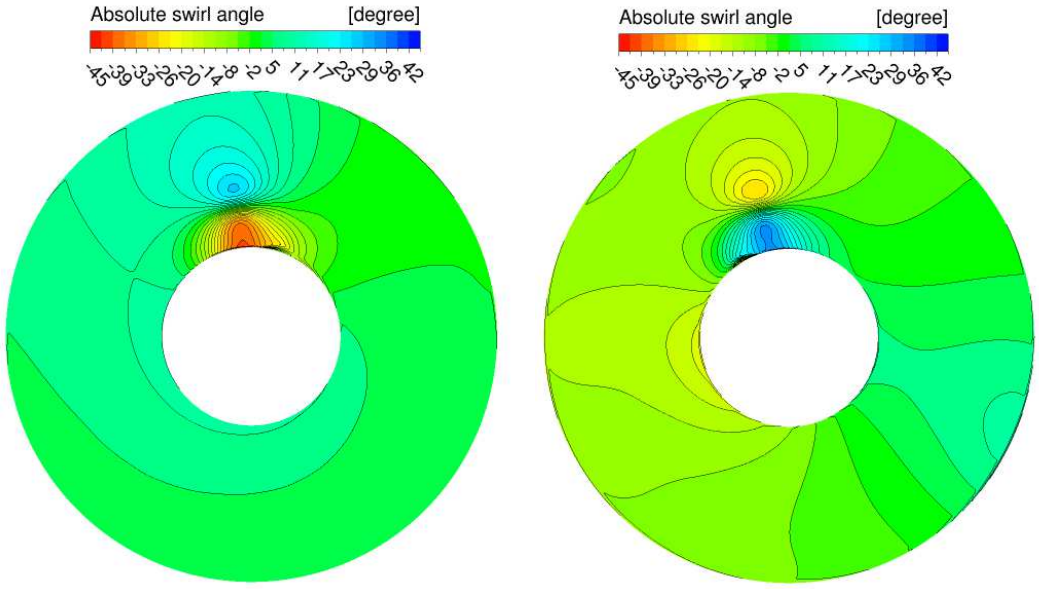

(a) Co-rotating vortex (b) Counter-rotating vortex

Figure 5.22: Absolute swirl angle, α_{abs}. Near design. Vortex at 25% blade span, $\Gamma = \pm 22.1[m^2.s^{-1}]$. At Plane 01 upstream of Blade LE.

5.2.1.1 Global performance

Observing Figure 5.23, the speed-lines of counter-rotating vortex in both the RANS and URANS are shifted to the right and upwards, where there is a larger $\overline{PR}$ and $\overline{W}$ compared with the undistorted (clean) flow conditions. On the other hand, co-rotating vortex distorted RANS speed line is shifted to the left and downwards. Also, the rate of deterioration of the rotor performance with the ingestion of co-rotating vortex is much more than the increase in $\overline{PR}$, and $\overline{W}$, observed with an ingestion of a counter-rotating vortex. Similar characteristics have been observed for the area-averaged temperature ratio ($\overline{TR}$) map, and opposite trends for the isentropic efficiency ($\overline{\eta}$). This is the characteristics of pure counter-rotating and co-rotating bulk swirls, with the bulk swirl angles higher than 15[deg]. This has been discussed in the last few sections. However, the reality of the vortex flow-field is not as straight forward as for the pure bulk swirl pattern.

As Rotor 67 is a twisted transonic rotor, first of all the blade loading increases from hub to tip (see Figure 4.5). So, for an example, when a counter-rotating vortex is ingested at 25% blade span, the majority of the blade is exposed to the counter-swirl content (negative α_{abs}). This can be observed in the Figure 5.22(b). Moreover, as the rotor blade loading increases span-wise, the part of the blade which is doing more work on the flow is exposed to the counter-swirl content. Thus, the overall effect on the rotor performance is similar to the pure counter-rotating bulk swirl.

However, it doesn't means that the co-swirl content is not affecting the rotor performance. Firstly, it can be observed from Figure 5.22(b), the intensity of the co-swirl content is intensified due to large interaction with the hub surface. Secondly, an example of the span-wise distribution of the total pressure ratio (PR), and the relative Mach number (M_{rel}) is shown for the vortex ingestion case at the mid-span (50% span) in Figure 5.24. For both co and counter-rotating vortex ingestion cases, the effects of both local swirl components is clearly visible. The effect of the co-swirl content within each case is illustrating more effect on the

rotor performance in terms of $\overline{PR}$. This is also observed in the global performance charts, following the same trend as in the vortex ingestion at 25% blade span.

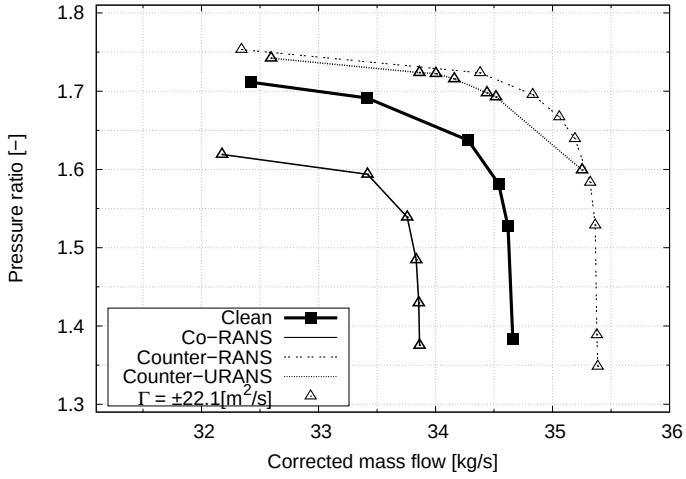

(a) Evolution of the rotor pressure ratio ($\overline{PR}$)

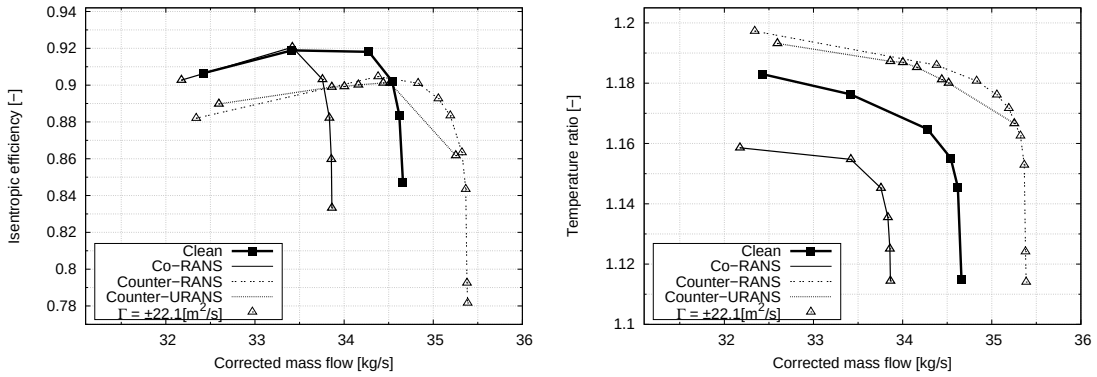

(b) Evolution of the rotor isentropic efficiency ($\overline{\eta}$)(c) Evolution of the rotor temperature ratio ($\overline{TR}$)

Figure 5.23: Configuration 3: Full-annulus Stage 67 vortex ingestion at 25% blade span, $\Gamma = \pm 22.1[m^2.s^{-1}]$. Performance maps.

When comparing the counter-rotating and co-rotating vortex ingestion cases, it can be clearly identified that the losses encountered with ingestion of counter-rotating vortex are much more, as the $\overline{\eta}$ decreases rapidly as well. This analysis will be explained in more detail in the next vortex flow-features parametric study section.

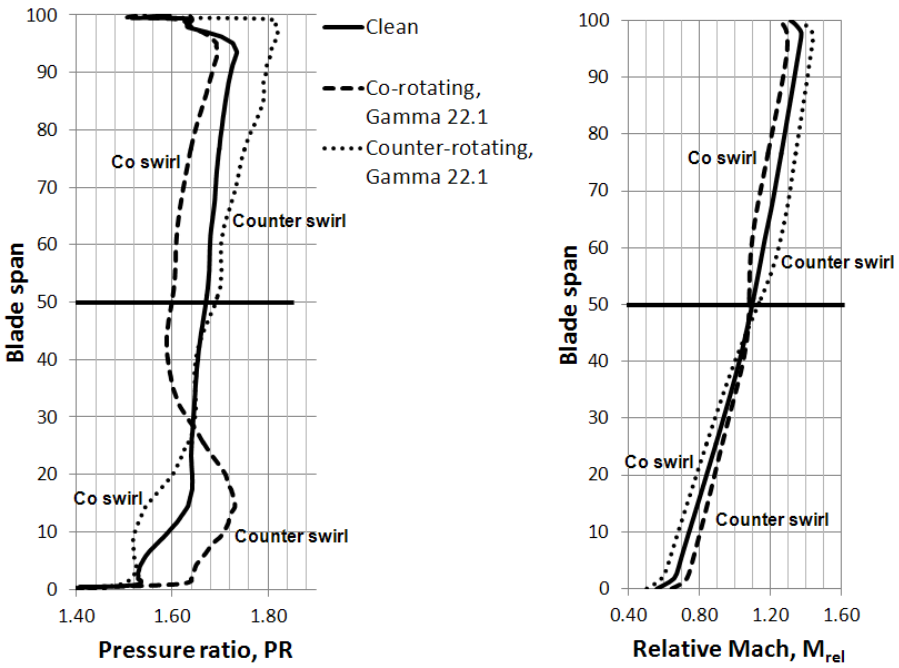

(a) Pressure ratio (PR)

(b) Relative Mach (M_{rel})

Figure 5.24: Span-wise distribution. Full-annulus Stage 67 vortex ingestion at 50% blade span. $\Gamma = \pm 22.1[m^2.s^{-1}]$.

One of the analysis that had to be performed within the context of this study was to identify the key differences between the RANS and URANS results. It can be observed from the global performance charts that there are very small differences in terms of the overall trend, and also the flow variable values. URANS method show a slight reduction in $\overline{PR}$, and $\overline{W}$, compared with the RANS results. This is due to one of the key flow-features that the URANS is taking into account, which is the inherent unsteady nature of the flow-field. The vortex is being chopped when it encounters the blade's LE. This is carried out in real psychical time-steps in the URANS calculations, which the user pre-defined per degree of rotor revolution and it has to be an appropriate small value to capture the required unsteady flows. However,it have to be kept in mind that the higher computing time is required if smaller time-steps are needed.

Hence, the flow-field downstream of the blade row is dependent of the actual position of the blade with respect to the vortex. Thus, this is the reason why

the global performance charts were evaluated by averaging the quasi-steady state solutions at different time-steps, and the differences with the RANS are thus reduced but not completely eliminated. On the other hand, RANS solution already gives the user a time-averaged solution of the flow-field, and in this particular case, it's over-predicting the values of $\overline{PR}$, and $\overline{W}$.

Therefore, it can be concluded that if the objective of the work is to very accurately predict the distorted flow propagation downstream (see Figure 5.25) and qualitative quantification of the associated flow losses, then the URANS becomes very important. Having said that, given the hefty computational time, and the costs involved to run URANS calculations, particularly if one's objective is the large number of simulations, these very small differences in the global performance results between RANS and URANS can be overlooked.

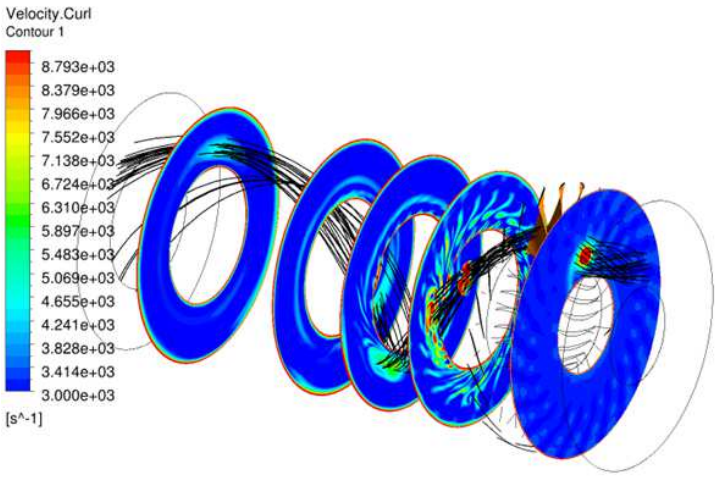

Figure 5.25: URANS full annulus vortex ingestion, $\Gamma = -22.1[m^2.s^{-1}]$: Vorticity propagation, Near-design condition, At $P_{s,out}$ constant.

5.2.1.2 Flow distortion propagation - URANS

Some additional simulations performed with the URANS method, keeping the vortex circulation and the direction same, but changing the radial location of the vortex. The following Figure 5.26 show the effect on $\overline{PR}$, and $\overline{W}_{correc}$, when the vortex is ingested from near hub to near tip. The near tip ingestion (75% blade span) of the vortex show almost no effect in the rotor global operating point,

when compared with the undistorted (clean) flow condition.

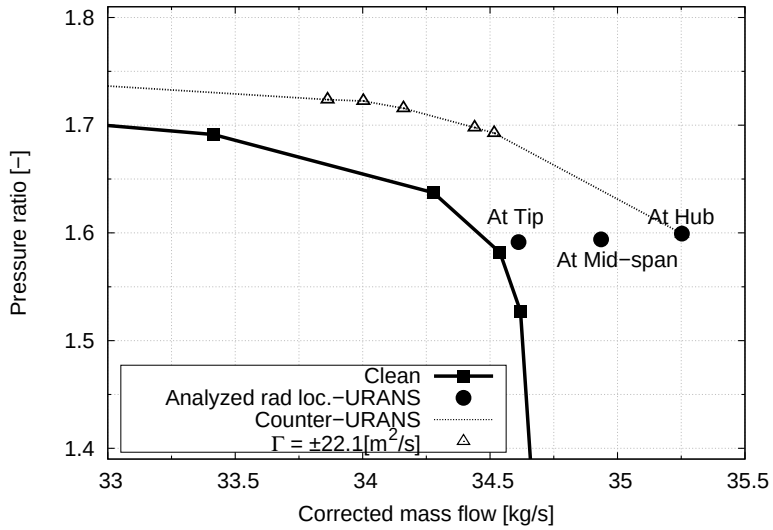

Figure 5.26: Configuration 3: Full-annulus Stage 67 vortex ingestion from 25% to 75% blade span. $\overline{PR}$ map. Near-design condition. $\Gamma = -22.1[m^2.s^{-1}]$.

In reality, it can be observed in Figure 5.27, the near tip vortex ingestion does have an effect in the rotor passage performance. The contours of the total-pressure (P_T) are illustrated for all the three URANS ingested cases. These have been compared with the uniform undistorted axial-flow (clean). This have been achieved by consistently eliminating the predicted downstream undistorted (clean) flow with each respective distorted case, thus representing only the time-averaged effects of only the distorted pattern on the rotor aerodynamics. All these have been performed at the constant outlet non-dimensional static pressure, P_s^* of 1.27.

By observing the near hub ingestion case in Figure 5.27 , a region of very low pressure downstream of the rotor passage is clearly visible. There is also a region of some high pressure compared with the clean case. In this case, as the majority of the blade span was exposed to the negative (counter) swirl content, in theory it should increase the blade loading. However, the region of higher pressure which is identified by grey circle is clearly dominated by the region of very low pressure (red circle). Very similar low pressure regions were observed for the mid-span, and near the tip vortex ingestion cases. All these low pressure regions were identified

near the vortex ingestion locations (i.e. at 25%, 50%, and 75% blade spans). To note, a vortex core itself contain around 20% less total-pressure compared with the ambient conditions. This in the combination with the vortex curl, and also the excess velocity within the core region is causing a considerable amount of flow losses within the rotor passage. This will be discussed more in next section.

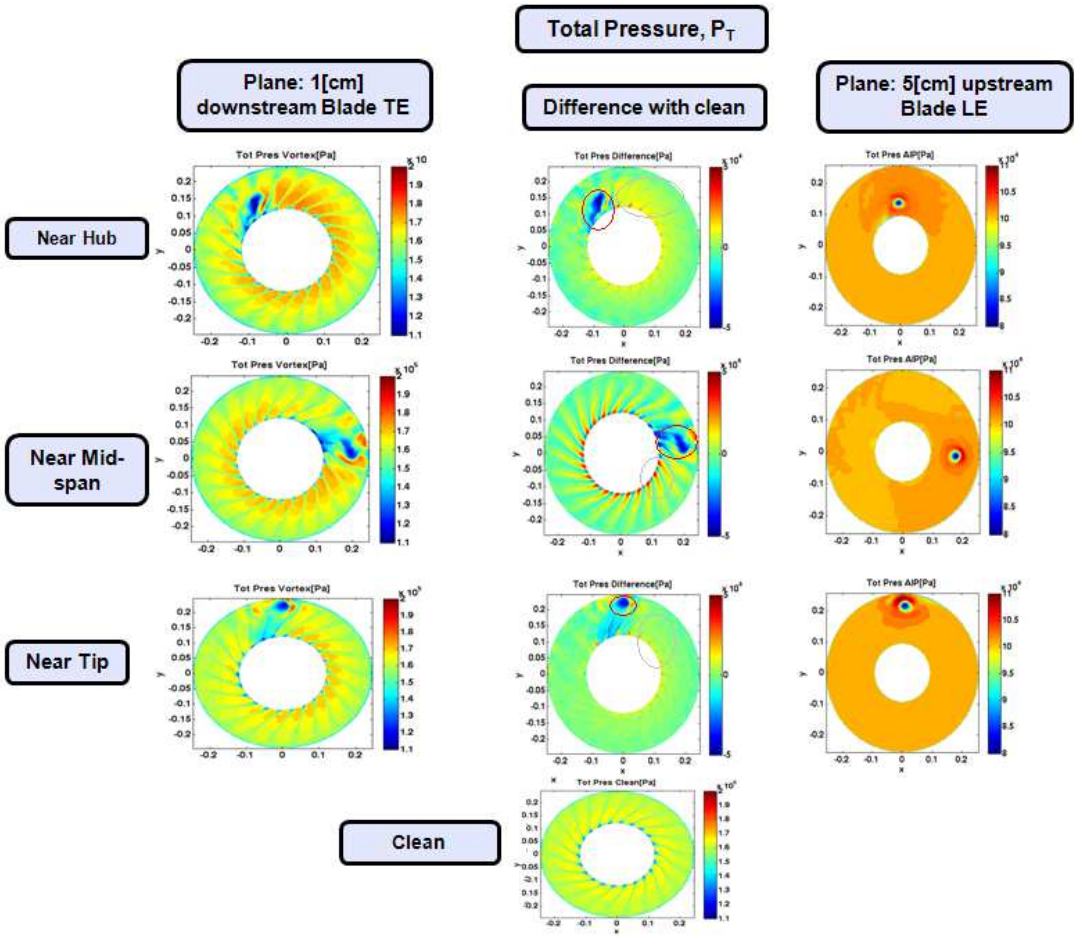

Figure 5.27: Downstream propagation flow analyses. URANS full annulus vortex ingestion at 25%, 50%, and 75% blade span, $\Gamma = -22.1[m^2.s^{-1}]$. Total pressure ($P_T$) contours.

One more key observation was made during these URANS analyses. Figure 5.28 show the tangential velocity (V_θ) contours for the three ingested cases. These are also time-averaged, and the differences with the clean case were post-processed at the constant P_s^* at the outlet. The propagation of the vortex curl at the rotor outlet is clearly visible. The red circles represents the negative (counter) V_θ

component, whereas the grey circles represents the positive (co) V_θ component. The mid-span ingestion case show two prominent co and counter V_θ at the rotor outlet. The other two cases show a less propagation of the V_θ components. It also indicates the fact that the interaction of the tangential velocity with the hub and tip surfaces are causing the vortex strength to decay as it passes through the rotor. Thus, it can be said that if more stages were present downstream of the rotor, the flow distortion in regards with the mid-span vortex would have travelled much further along the compressor domains due to higher tangential velocity at rotor outlet, when compared with the other two ingestion locations.

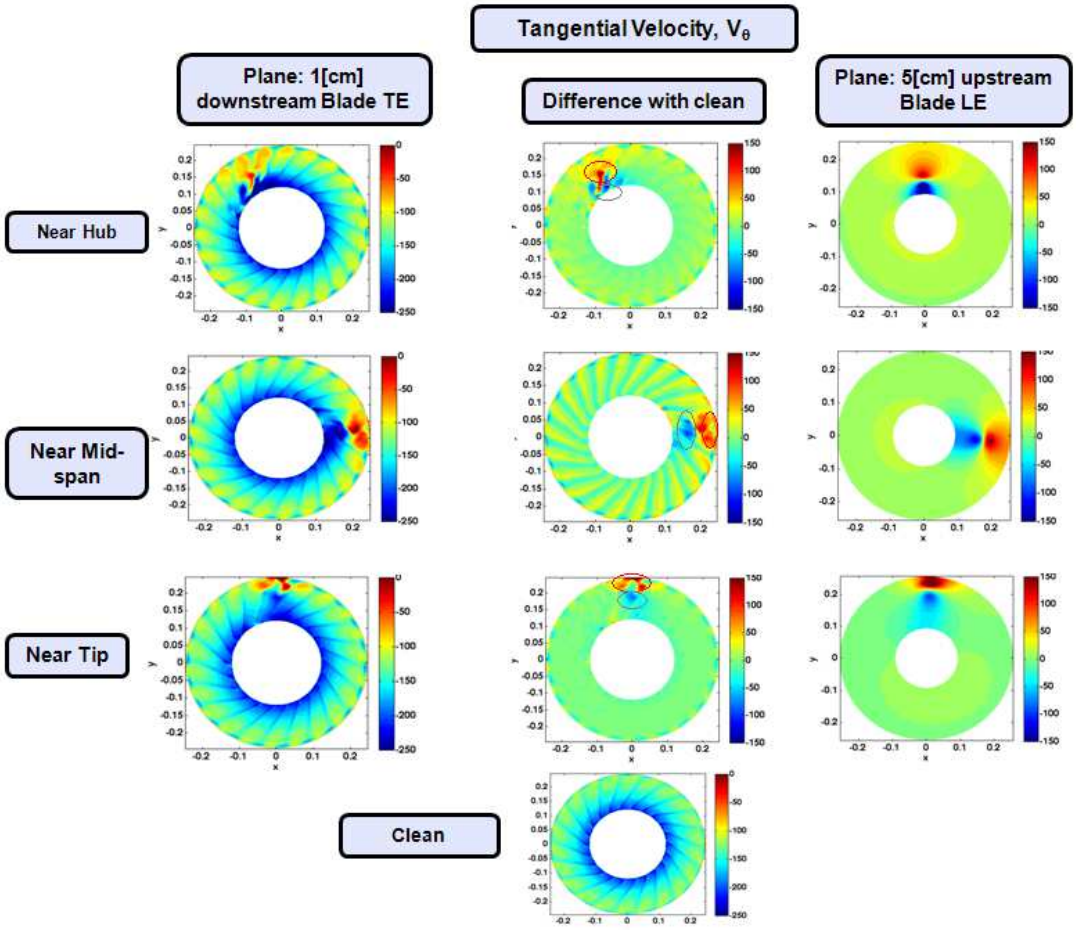

Figure 5.28: Downstream flow propagation analyses. URANS full annulus vortex ingestion at 25%, 50%, and 75% blade span, $\Gamma = -22.1[m^2.s^{-1}]$. Tangential velocity ($V_\theta$) contours.

In general, all these flow analyses show signs that if more stages were present

downstream of the rotor, they will be surely affected by the upstream ingestion of swirl distortion.

5.2.2 Configuration 3: Stage 67 RANS vortex flow feature parametric study

As stated earlier, one of the objectives of this research project was to examine the response of the turbomachinery components with respect to the different flow features of the ingested vortex. As there is still lack of knowledge in this area, the basic vortex parameters were considered, which are the vortex direction, the vortex strength, the vortex radial location, and the vortex core size. The Table D.2 in Appendix D lists all the RANS test cases that were simulated during this parametric study. These were simulated at two rotor spool speeds, i.e., $N = 100\%$, and $N = 90\%$. The first Stage 67 configuration, consisting of the Rotor 67 and Stator 67B, was used as the test geometry.

The section is divided into four parts, explaining the effect of each vortex parameter, i.e. the vortex direction, strength, radial position, and the size, on the transonic rotor performance. The global performance charts together with the flow-field contours are utilized, highlighting the key effects of the vortical flow on the turbo-machinery flow dynamics. To note, not all the simulation results are shown, just the required set of analyses to explain each effect is illustrated in the section. However, all the results were utilized in the swirl descriptor correlations, and is presented in the next flow descriptor chapter.

The choked convergent-divergent nozzle was used as the outlet BC. The nozzle throat areas (see Table 3.10) were varied to get the full operability range of the rotor, i.e. from near choke to near the stability limit, when under the ingestion of single tightly-wound vortices. The choked convergent-divergent nozzle also provided an advantage over the static-pressure outlet BC. It enabled to analyse the rotor response to vortex at the constant throttle settings (i.e. constant $NDMF_{out}$) to the undistorted (clean) flow conditions.

To simulate these cases, up to 76 parallel CPUs from the Cranfield High Per-

formance Computing (CHPC) facility have been used, taking 1-2 days for each simulation to reach a converge solution. All the residuals of the flow variables within the domain were made sure to reach atleast below $1x10^{-6}$, and the fluctuations in the mass flow imbalance were below 0.1%. In general, it took an approximate of 12 CPU days on the CHPC to get the full speed-line from near choke to the stability limit.

5.2.2.1 Effect of vortex direction

To show the effect of vortex direction, an example test case of vortex circulation, $\Gamma = \pm 11.01[m^2.s^{-1}]$, ingested at the mid-span have been chosen. The following Figure 5.29 show the swirl angle, α_{abs}, distribution upstream of the rotor inlet (at Plane 01), for both the co and counter-rotating vortex ingestion cases. The maximum local co and counter-rotating swirl angles (α_{abs}) in these test-cases were in the region of ± 15[deg] to ± 20[deg].

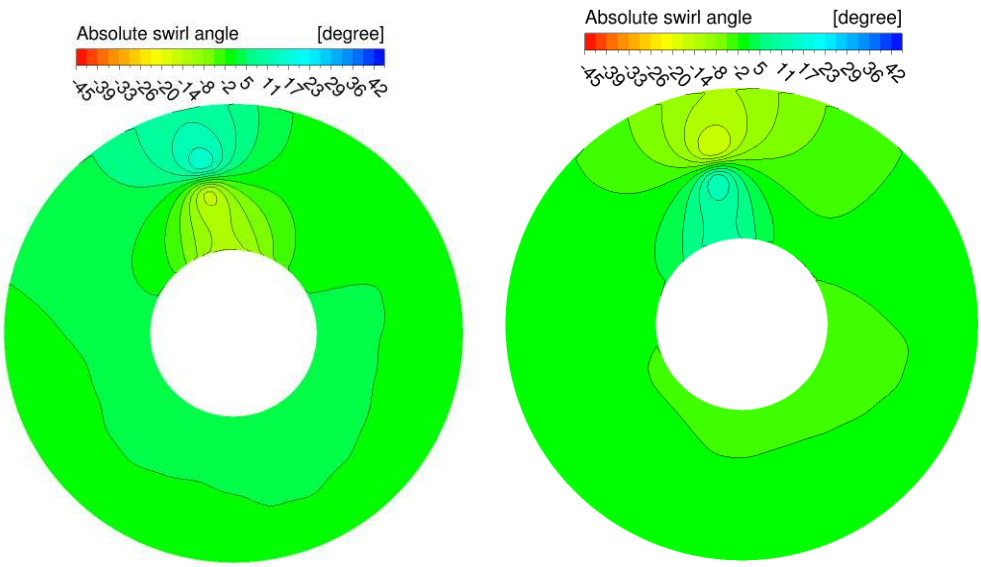

(a) Co-rotating vortex (b) Counter-rotating vortex

Figure 5.29: Inlet absolute swirl angle contours, α_{abs}. Near-design condition. Vortex at 50% blade span, $\Gamma = \pm 11.01[m^2.s^{-1}]$. Plane 01 upstream of Blade LE.

Figure 5.30 illustrates the global performance effects of the vortex ingestion. The ingestion of a counter-rotating vortex drives a rise in mass-flow ($\overline{W}$), pressure-

ratio ($\overline{PR}$) and temperature-ratio ($\overline{TR}$), while a co-rotating vortex causes the $\overline{W}$, $\overline{PR}$ and $\overline{TR}$ to drop. This is again a similar flow behaviour observed previously in the isolated Rotor 67 configuration. Also, the change in the performance parameters, i.e. $\overline{W}$, $\overline{PR}$ and $\overline{TR}$, from the undistorted (clean) flow conditions following the ingestion of a co-rotating vortex is much larger than in the case of a counter-rotating vortex ingestion. For an example, the change in $\overline{PR}$ is about 4-5% in the case of a co-rotating vortex, and only approximately -1% for the counter-rotating vortex ingestion.

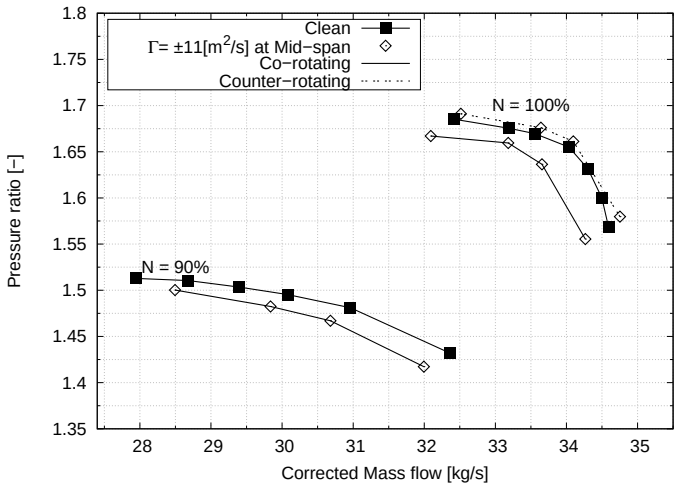

(a) Evolution of the rotor pressure ratio ($\overline{PR}$)

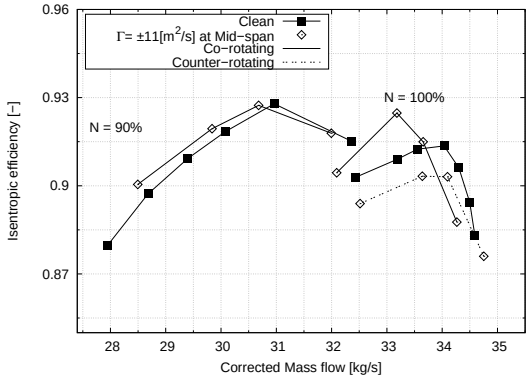

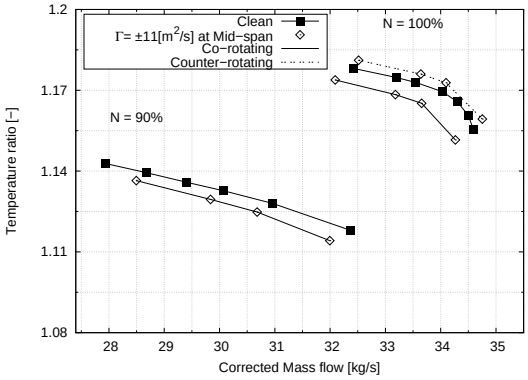

(b) Evolution of the rotor isentropic efficiency ($\overline{\eta}$)(c) Evolution of the rotor temperature ratio ($\overline{TR}$)

Figure 5.30: Configuration 3: Full-annulus Stage 67 vortex ingestion at 50% blade span. $\Gamma = \pm 11.01[m^2.s^{-1}]$. Performance maps.

On the other side, the results of the area-averaged isentropic efficiency ($\overline{\eta}$) is

exhibiting an opposite characteristics. A co-rotating vortex ingestion keeps the $\overline{\eta}$ of the rotor passage almost constant, even a slight improvement is also observed at the spool speed of, $N = 100\%$. It highlights the fact that the compression system is trying to accommodate the change in the inlet conditions without loosing the efficiency.

However, a counter-rotating vortex ingestion results in a large drop in the $\overline{\eta}$, highlighting the fact that there is a imbalance between the heat transfer and the pressure-rise across the rotor passage. In this case, as the counter swirl content is dominating the rotor blade span in the affected part of the annulus, this is resulting in flow losses.

These flow losses can be observed in the contours plots of Figure 5.31. It is illustrating the change in total entropy (Δs) of the flow across the rotor passage. The Equation 5.6 was used in a consistent manner from the rotor inlet to outlet to generate the distributions of Δs. This parameter gives an indication how much of the flow energy has been dissipated in the surroundings, when comparing at two defined planes. For the study, stations 1 and 2 (see Table 3.13), were used as the rotor inlet and outlet for the calculation of Δs. A grid of 1000x1000 cells per blade passage was used at both the rotor inlet and outlet for determining the total entropy changes between the two planes.

$$\Delta s = s_2 - s_1 = c_p \log \frac{T_{t,2}}{T_{t,1}} - R \log \frac{P_{t,2}}{P_{t,1}} \tag{5.6}$$

Where, R is the gas constant ($8.31[JK^{-1}mol{-}1]$), and c_p is the pressure coefficient and was assumed to be a constant value of around $1.005[kJkg^{-1}C]$.

An undistorted (clean) case is shown along with the two vortex ingestion cases to compare the flow losses across the rotor passage. The region of high losses have been highlighted in the contours by higher values of Δs. It can be clearly observe that the rotor experiences much higher flow losses in a region where the counter swirl content is present. The region of counter swirl content for the counter-rotating vortex ingestion case extends up to the tip surface. Thus, a large amount of tip gap flow losses can also observed for the counter-rotating vortex ingestion. Another region of the rotor annulus that experiences high flow

losses is the vortex core centre. Due to the excess velocity within the vortex core, it causes passage flow to choke, and therefore higher flow losses were noticed at the ingestion locations.

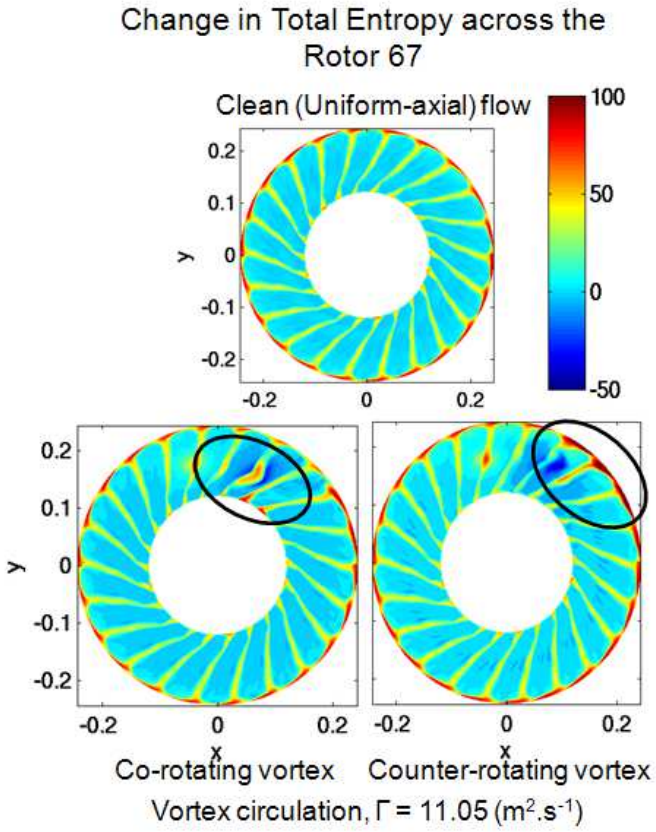

Figure 5.31: Delta total entropy, Δs, across the rotor 67 passage illustrating the regions of flow losses. Near-design condition. Vortex at 50% blade span, $\Gamma = \pm 11.01[m^2.s^{-1}]$. Using station Planes 1 and 2.

5.2.2.2 Effect of vortex strength

To show the effect of vortex strength, an example test case of vortex circulations, $\Gamma = \pm 11.01$, ± 16.0 and $\pm 22.1[m^2.s^{-1}]$, ingested at the near-hub (25% span) location have been chosen. Higher vortex strength is reflected in an increased swirl angle (α), and the higher radial and tangential velocities around the vortex centre. The core radius was kept constant and the circulation, Γ, was varied in these test-cases.

Figure 5.32 show the absolute swirl angle, α_{abs}, distribution upstream of the

rotor inlet, for both the co and counter-rotating vortex ingestion cases. As the Γ increases, the α_{abs} intensifies as well. The maximum local co and counter-rotating swirl angles (α_{abs}) for the circulation, $\Gamma = \pm 11.01[m^2.s^{-1}]$, were in the region of ±15[deg] to ±20[deg]. Whereas, in the case of, $\Gamma = \pm 22.1[m^2.s^{-1}]$, swirl angles as high as ±40[deg] was observed, especially near the hub surface.

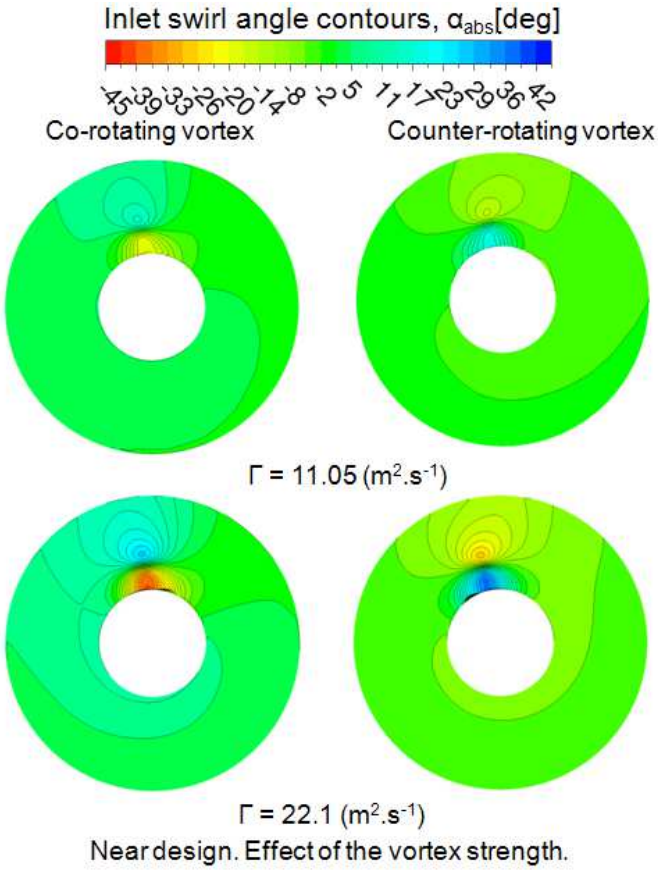

Figure 5.32: Inlet absolute swirl angle contours, α_{abs}. Near-design condition. Vortex at 25% blade span (near Hub), $\Gamma = \pm 11.01, 22.1[m^2.s^{-1}]$. At Plane 01 upstream of Blade LE.

The performance maps in Figure 5.33 illustrates the previously mentioned effects that the ingestion of a co-rotating vortex causes a loss in $\overline{PR}$ and a drop in $\overline{W}_{correc}$. In contrast, the $\overline{PR}$ and the $\overline{W}_{correc}$ increases in case of the counter-rotating vortex ingestion. These effects are shown to be intensified as the strength of the vortex rises under the co-rotating vortex. So, a larger drop in the $\overline{PR}$, $\overline{TR}$ and $\overline{W}_{correc}$ are observed, concisely as the Γ increases from +11.01

to $+22.1[m^2.s^{-1}]$. The area-averaged isentropic efficiency ($\overline{\eta}$) remains almost constant, and thus, the compression system seems to be coping with the augmented vortex strength in this case.

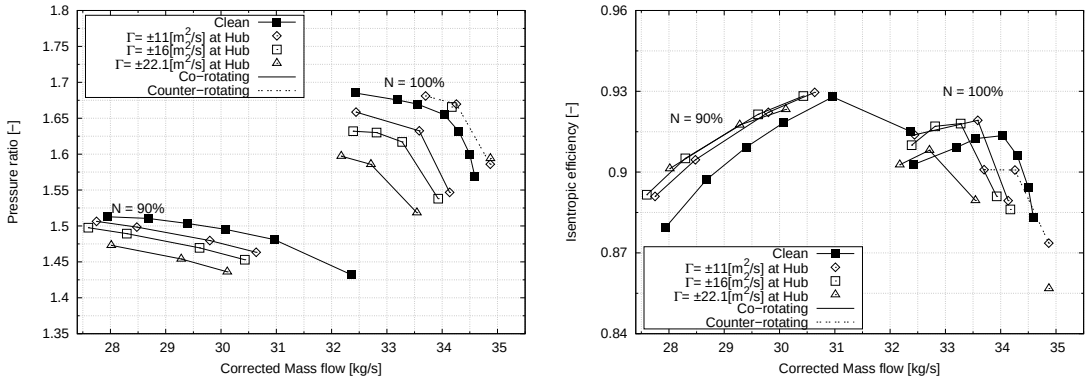

(a) Evolution of the rotor pressure ratio $\overline{PR}$ (b) Evolution of the rotor isentropic efficiency ($\overline{\eta}$)

Figure 5.33: Configuration 3: Full-annulus Stage 67 vortex ingestion at 25% blade span (near hub). $\Gamma = \pm 11.01, \pm 16.0$, and $22.1[m^2.s^{-1}]$. Performance maps.

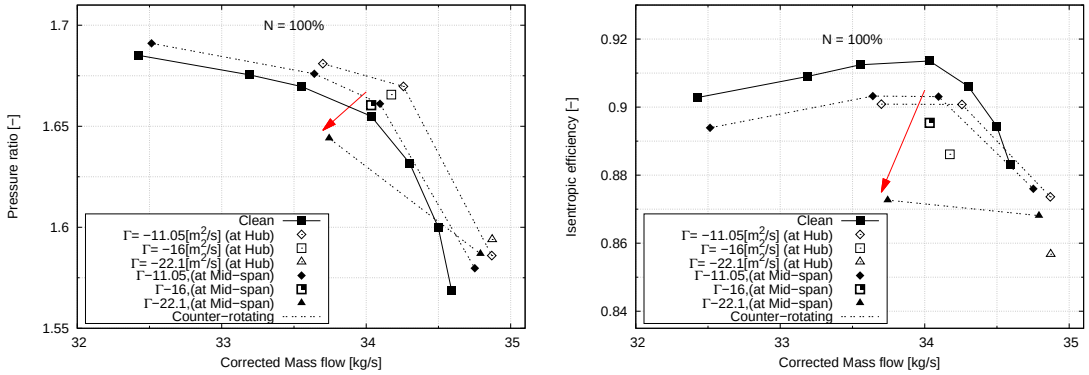

(a) Evolution of the rotor pressure ratio ($\overline{PR}$) (b) Evolution of the rotor isentropic efficiency ($\overline{\eta}$)

Figure 5.34: Configuration 3: Full-annulus Stage 67 counter-rotating vortex ingestion. Γ = -11.01, -16.0, and -22.1 $[m^2.s^{-1}]$. Performance maps at $N = 100\%$.

On the other hand, the vortex strength intensification in the case of counter-rotating vortex ingestion showed the signs of increased flow losses. As the Γ intensified from -11.01 to $-16.0[m^2.s^{-1}]$, the $\overline{PR}$ and $\overline{W}_{correc}$ remained almost same. However, a large drop in $\overline{\eta}$ was observed. A further investigation of the

vortex strength was performed in order to understand the flow dynamics taking place. Figure 5.34 illustrates the effect of the vortex strength, when ingested at the two radial locations (both counter-rotating vortex). If one can observe the mid-span vortex ingestion case, as the Γ increases from -11.01 to $-22.1[m^2.s^{-1}]$, a large drop in the $\overline{PR}$, $\overline{W}_{correc}$, and $\overline{\eta}$ is clearly noticeable.

Figure 5.35: Density gradient contour at 50% blade span illustrating the flow separation at the passage shock due to the counter swirl intensity. $\Gamma = -22.1[m^2.s^{-1}]$,

It is emphasizing on the key fact that it is easier for the blade operating in a transonic flow region to adjust to the incoming co-swirl content, and get an optimum flow condition by keeping the blade inlet relative angle to the desired values. It have been discussed before in the pure bulk swirl results that for the counter-rotating swirl, its much difficult for the blade shocks to adjust the incoming distorted flow. Therefore, in relation with the vortex ingestion cases, it means that the blade span is reacting to the co and counter-swirl contents in a similar manner to the pure bulk swirl. However, the radial velocity redistribution withinin the balde passage is much more intense than the bulk swirl cases. This is due to the inherent radial velocity component (V_r) of the vortex in the global coordinate system.

So, for the counter-rotating vortex ingestion case, the majority blade span is exposed to the counter-swirl content. Thus, it is much more difficult for the blade

to keep the incoming incidence angle to the desired values beyond a certain inlet absolute counter swirl angle,$-\alpha_{abs}$. Thus, the shock-wave system reveals a region of flow separation point near the blade suction surface. An example is shown in the density gradient blade-to-blade contour plots in Figure 5.35. The vortex of Γ of $-22.1[m^2.s^{-1}]$ is ingested at 25% blade span. The flow separation within the blade passage is shown at 50% blade span, where the maximum counter-swirl content exists. This region of flow separation causes considerable amount of flow losses, and have been discussed in the pure counter-rotating bulk swirl analysis. Thus, the flow passages surrounding the high counter swirl content are highly unstable in nature, and may cause rotor to trigger the rotating stall or even surge.

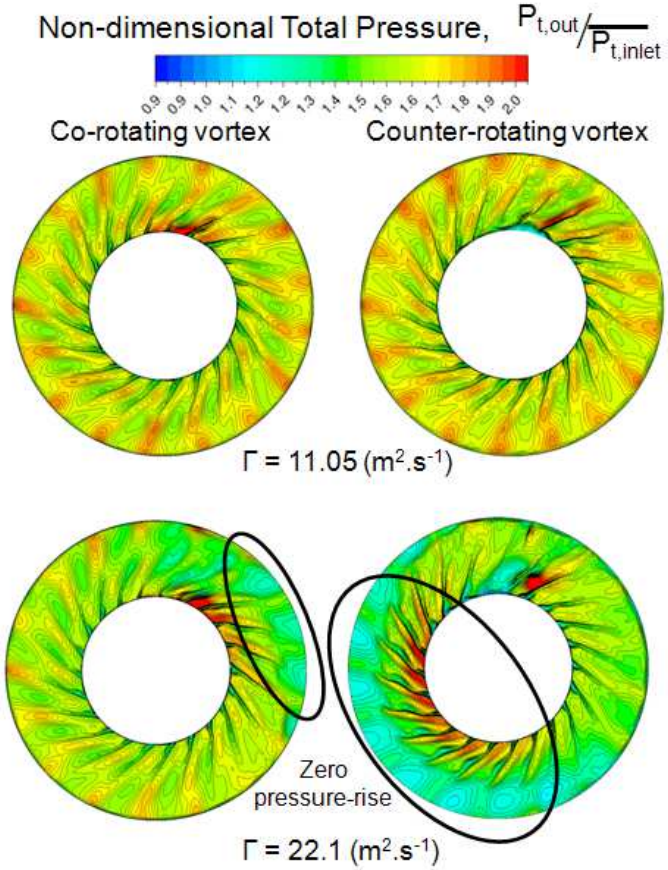

Figure 5.36: Non-dimensional total pressure, $\frac{P_{t,out}}{\overline{P_{t,in}}}$. Near-stall condition. Vortex at 25% blade span, $\Gamma = \pm 11.01 and \pm 22.1[m^2.s^{-1}]$. At Plane 2 downstream Blade TE.

The Figure 5.36 is demonstrating the non-dimensional total pressure rise across the rotor passage. All these have been plotted for near stall flow conditions. More flow separation for the higher vortex strengths is observed for both the co and counter-rotating vortex cases. However, the highest flow losses were noticed for the counter-rotating vortex ingestion case with Γ of $-22.1[m^2.s^{-1}]$. Almost, more than halve of the rotor annulus from 25% blade span to the tip surface have a zero total pressure rise across the rotor passage.

5.2.2.3 Effect of vortex radial location

Both co and counter-rotating vortices were ingested at the three different spanwise locations with respect to the axis of the compressor:
-At 25% blade span: Near the hub,
- At 50% blade span: At mid-span,
- At 75% blade span: Near the tip.

Figure 5.37 illustrates the effect of vortex radial location on the rotor global performance, with a lower strength vortex, i.e. Γ of $\pm 11.01[m^2.s^{-1}]$. A lower vortex circulation was chosen to show the vortex location consequences, as it is now known from the vortex strength analyses that at the higher vortex strengths, the rotor response to flow distortion changes. It takes place within the blade passage region which is exposed to the counter-swirl content. Thus, in order not to mix the two individual vortex effects, Γ of $11.01[m^2.s^{-1}]$ have been used for this set of analyses. Also, all the simulations at different radial locations have been performed at similar choked nozzle area variations at the outlet. Thus, they can be regarded at constant outlet throttle setting analyses, except some of the last stability points in each speed-line. The stability points were generated by closing down the back nozzle area until the stage exhibited any signs of mass-flow blockage, similar to the rotating-stall.

From the global performance charts, the reduction in $\overline{PR}$ and $\overline{W}_{correc}$ increases as the radial location of the ingested co-rotating vortex moves from the tip region towards the hub. The $\overline{\eta}$ is slightly improved, especially when vortex is located near the hub. On the other side, an increase in $\overline{PR}$ and $\overline{W}_{correc}$ was observed

as the radial location of the ingested counter-rotating vortex moves from the tip towards the hub region. A large drop in $\overline{\eta}$ is also observed for all the three counter-rotating vortex test-cases.

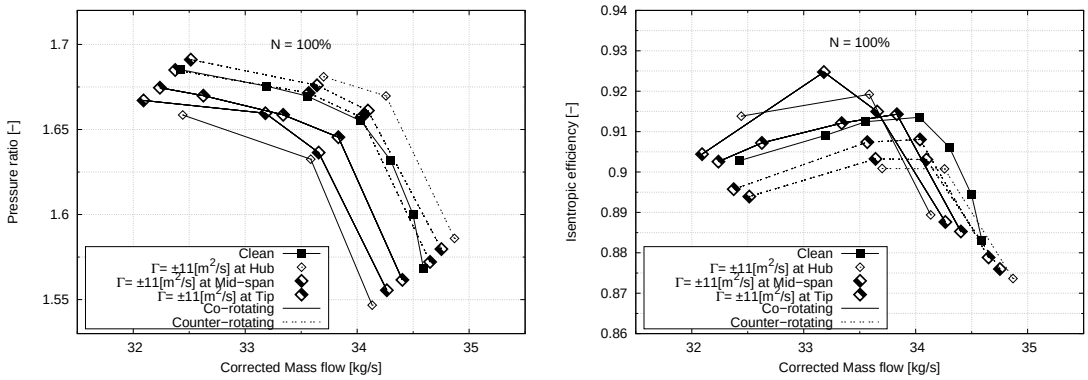

(a) Evolution of the rotor pressure ratio ($\overline{PR}$) (b) Evolution of the rotor isentropic efficiency ($\overline{\eta}$)

Figure 5.37: Configuration 3: Full-annulus Stage 67 vortex ingestion at three blade spans, 25%, 50% and 75%. $\Gamma = \pm 11.01[m^2.s^{-1}]$. Performance maps.

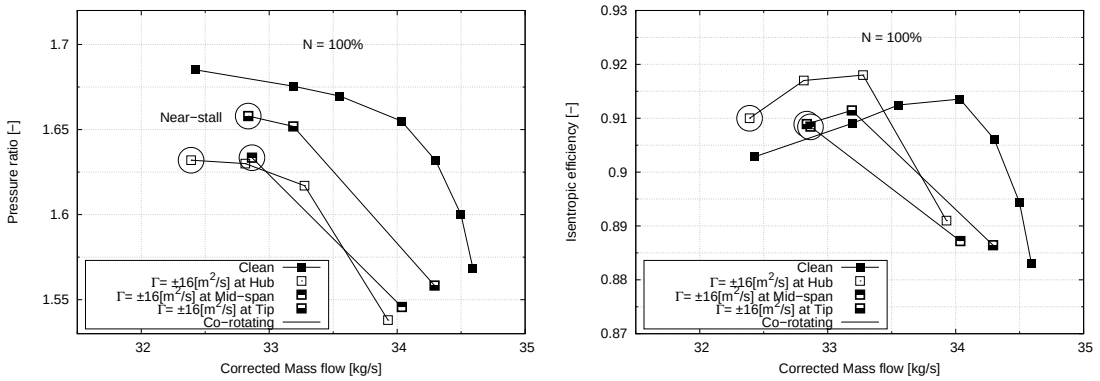

(a) Evolution of the rotor pressure ratio ($\overline{PR}$) (b) Evolution of the rotor isentropic efficiency ($\overline{\eta}$)

Figure 5.38: Configuration 3: Full-annulus Stage 67 co-rotating vortex ingestion at three blade spans, 25%, 50% and 75%. $\Gamma = +16.0[m^2.s^{-1}]$. Performance maps.

Both these opposite performance trends were expected, as they are dependent on the blade span-wise extents of local co and counter swirls. Also, the magnitude of the changes in $\overline{PR}$, $\overline{W}$,and $\overline{\eta}$ from the undistorted (clean) condition are much smaller in the case of the counter-rotating vortex. This flow behaviour of the counter-rotating vortex have already explained in the previous Secttion 5.2.2.1.

Figure 5.38 show the global performance of a case study of mid-strength co-rotating vortex ingestion ($\Gamma = +16.0[m^2.s^{-1}]$). The circled operating points are near stall conditions, and these were further post-processed using the blade-to-blade contours (see Figures 5.39-5.42).

Figure 5.39 describes the total-pressure (P_T) blade-to-blade contours at three different blade spans, i.e. 25%, 50% and 75%. All the three ingestion cases have been represented.

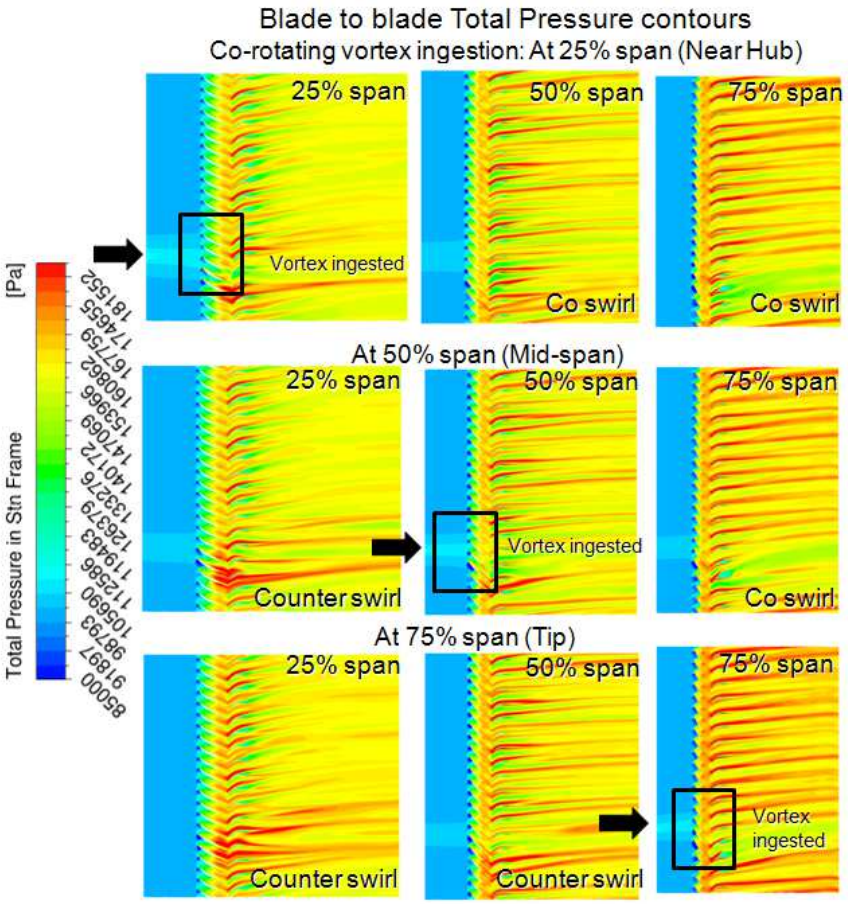

Figure 5.39: Blade-to-blade total-pressure (P_T)contours. Γ=$\pm$16.0$[m^2.s^{-1}]$. Near-stall.

For an example, when the co-rotating vortex was ingested at near hub location (25% span), it affected over an extent of about three blade passages. Also, the majority of the blade span was encountered with a co-swirl content. This resulted in a reduction of P_T, which can be noticed in the first row of the contour plots

in Figure 5.39 (see 50% and 75% span). Also, the vortex core region (see 25% span) results in a large reduction of P_T, when compared with the other parts of the stage annulus. The reason behind this reduction is the vortex flow-field simulated. The vortex core also contains a region of very low total-pressure, along with an excess axial velocity (refer Figure 3.24).

The excess axial velocity within the vortex core region can also observed in Figure 5.40. The blade-to-blade contours of axial velocity (V_a) is shown for the three ingested cases. In this plot, only the blade spans corresponding to the vortex ingestion locations are represented. For the near hub ingestion case, the excess velocity of the vortex core seems to have completely choked two of the blade passages due to very high axial-velocity. However, a region of flow separation over the suction side of one blade passage, which is directly exposed to the upstream vortex, can also be observed. This separated region is very similar to the previously described flow loss region on the blade suction side, and causes massive disturbances to the shock system.

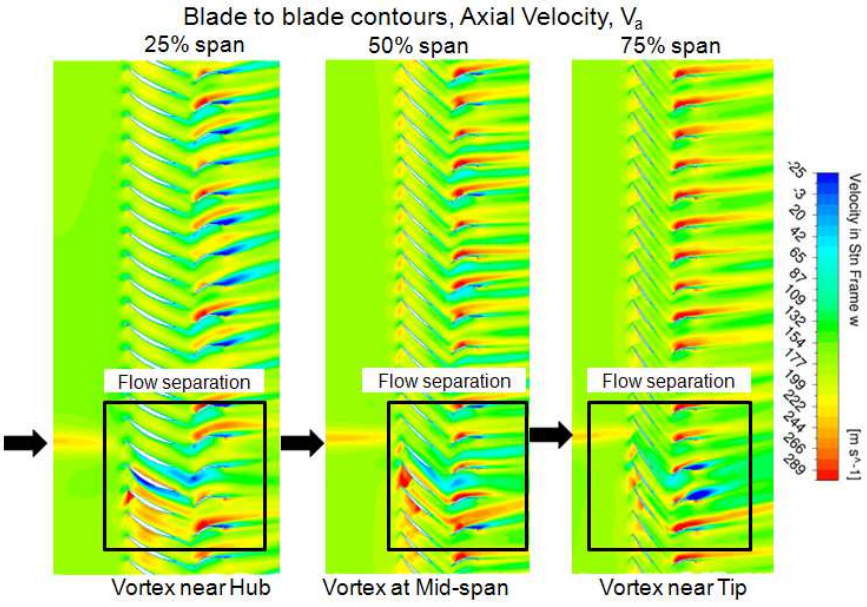

Figure 5.40: Blade-to-blade axial velocity (V_z) contours. Γ=$\pm$16.0$[m^2.s^{-1}]$. Near-stall.

The inlet relative angle (α_{rel}) should also be kept constant in the sonic blade span region to satisfy the unique incidence limitation. However, the worst affected

blade passages due to the vortex ingestion should show otherwise. This can be observed by the relative angle (α_{rel}) blade-to-blade contours plots in Figure 5.41, for all the three ingested cases. As stated above, the region where the vortex is ingested is unsuccessfully trying to accommodate the inlet swirl conditions. Thus, two of the blade passages for the hub ingestion case is not operating at the optimal incidence, as shown in the first row and first column plot in the Figure 5.41.

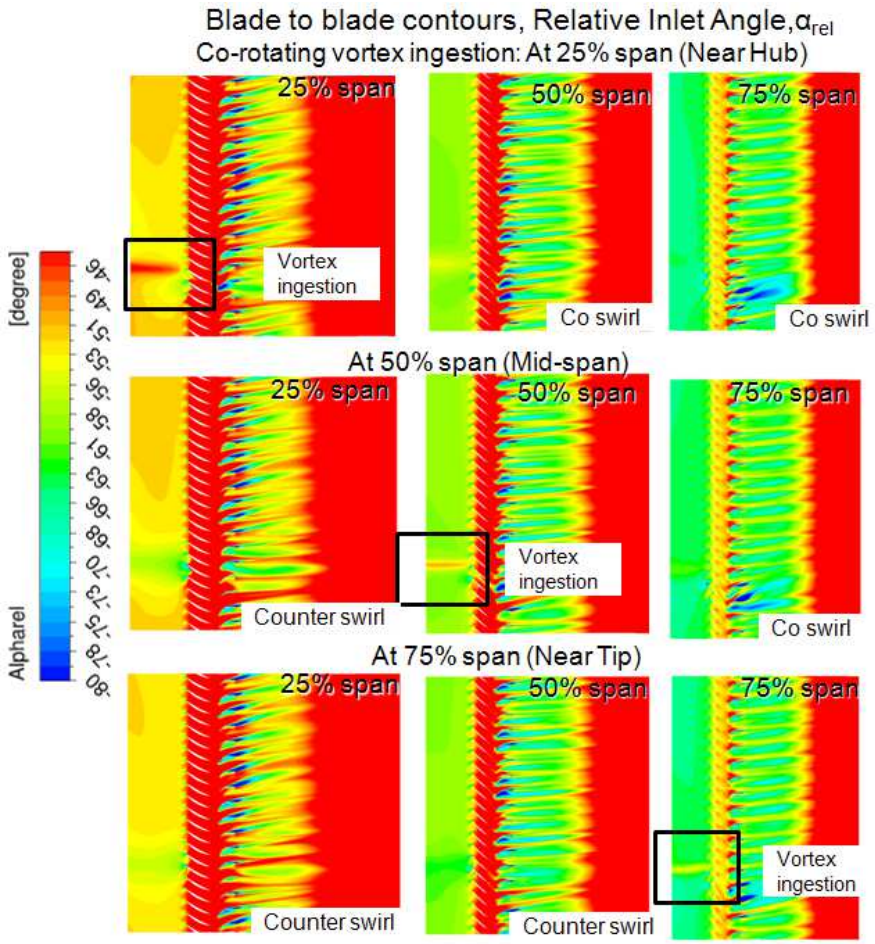

Figure 5.41: Blade-to-blade inlet relative angle (α_{rel}) contours contours. Γ=+16.0$[m^2.s^{-1}]$.

The entropy contour plots (Figure 5.42) for the ingested span locations supports the argument that the vortex core region is causing a considerable amount of flow losses.

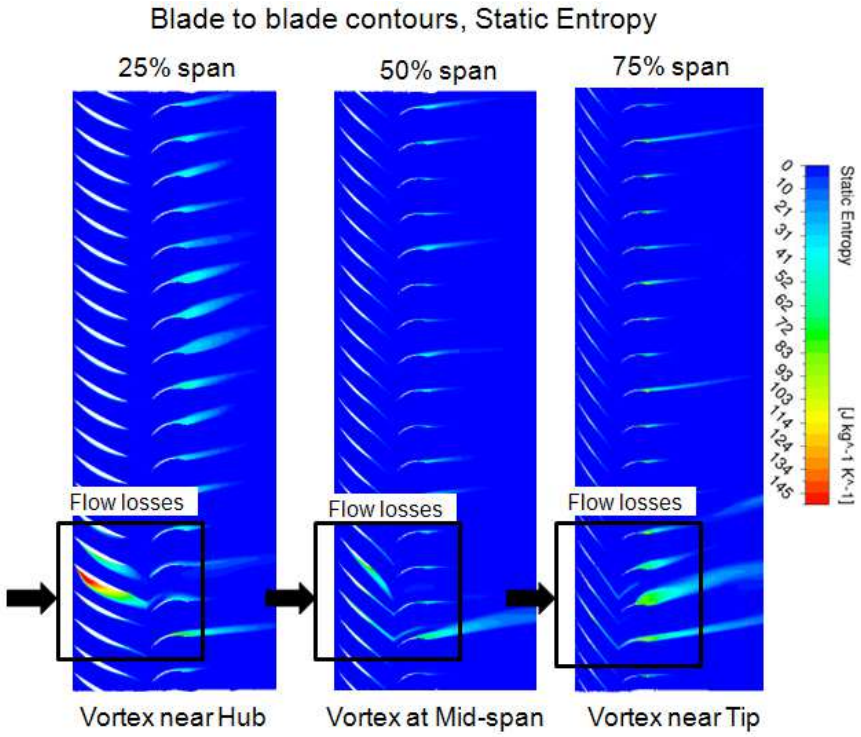

Figure 5.42: Blade-to-blade entropy (s) contours. Γ=$\pm$16.0$[m^2.s^{-1}]$. Near-stall.

As previously observed in the pure bulk swirl analysis, an increase in the radial velocity (V_r) is inherent with the flow separation of rotor passages. It can be observed from the Figure 5.43, due to an increase in the radial momentum within the distorted flow passages, the interaction with the tip-gap flow is intensified. The blade-to-blade contours of the tip-gap span is illustrated, and it can be clearly observed that a region of very low momentum in the tip gap region is created due to this intense flow interaction. This clearly satisfies one of the rotating-stall inception criterion[1,75], thus putting the compression system in the danger of stall or surge. The circumferential extent of this highly separated flow seems to be more augmented, when the vortex is ingested near the hub, and at the mid-span locations. This is due to the high entropy change near the ingested locations for these two cases (see Figure 5.42). Also, the radial flow, which is due to the suction side hub vortex (see Section 5.1.3.1), is formed due to the swirl distortion acting near the the hub surface. Therefore, in case of tip vortex ingestion, the likilehood of the suction side hub vortex is rare.

Also, from the Rotor 67 data[80], it is known that the strength of the shock-wave system intensifies with the blade span. Thus, the blade tip region experiences the strongest shock, as the M_{rel} reaches values upto 1.4 in an undistorted (clean) flow conditions. It can be argued then, when the vortex is ingested near the blade tip region, the deteriorating effects of the incoming vortex flow is lessened due to a stronger shock-wave system, and the vortex is just chopped downstream of the rotor. However, to note, as these are RANS simulations, the accurate picture of the instability inception have to be captured using the URANS method.

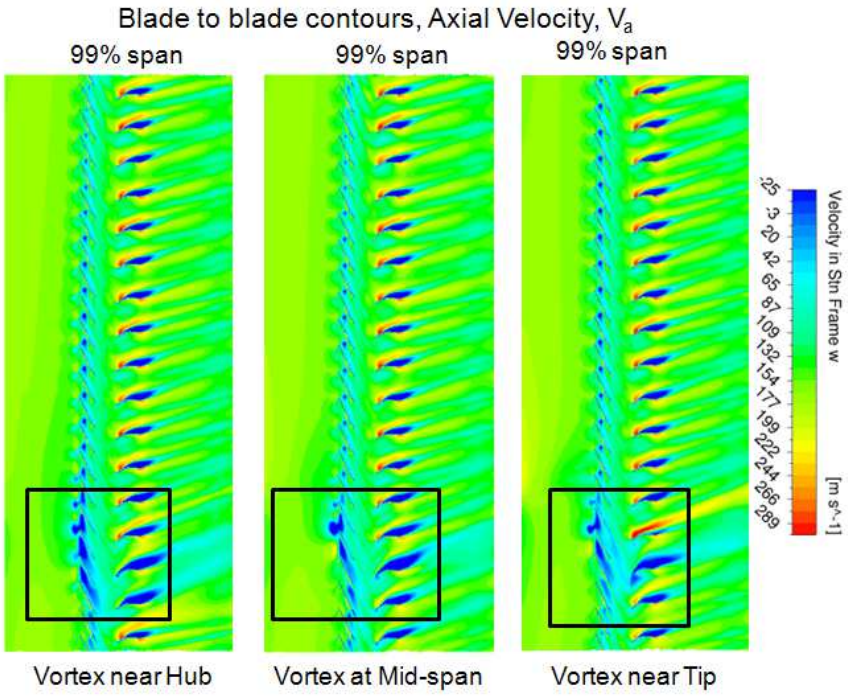

Figure 5.43: Blade-to-blade axial velocity (V_z) contours. $\Gamma = +16.0[m^2.s^{-1}]$. Near-stall conditions.

5.2.2.4 Effect of vortex core size

To show the effect of vortex core size, an example test case of co-rotating vortex circulations, Γ= +11.01, and $+22.1[m^2.s^{-1}]$, was ingested at the mid-span position. When the core size of a vortex is reduced to half radius and keeping the Γ constant, consequently the kinetic energy of the vortex will be more concentrated within a smaller space around the vortex core. And, the opposite will take place

if the vortex core size radius is doubled, while keeping the Γ constant. In this case, a wider spread of the kinetic energy around the vortex core was observed (see Figure 5.44), and therefore, results in smaller values of the swirl angle (α). These inlet vortex flow-features are illustrated in the contours plots in Figure 5.44. This may also be confirmed by examining the following equation whereby the circulation Γ is kept constant, and S is reduced in the case of a smaller core size. Thus, the vorticity ω must rise in this case.

$$\Gamma = \oiint_S \nabla \times \vec{v}.\vec{n}dS = \oiint_S \vec{\omega}.\vec{n}dS \tag{5.7}$$

The test cases were performed under two rotor speeds, i.e., $N = 100\%$, and $N = 90\%$. The global performance effects in terms of pressure ratio ($\overline{PR}$), and the isentropic efficiency ($\overline{\eta}$) are illustrated in Figure 5.44.

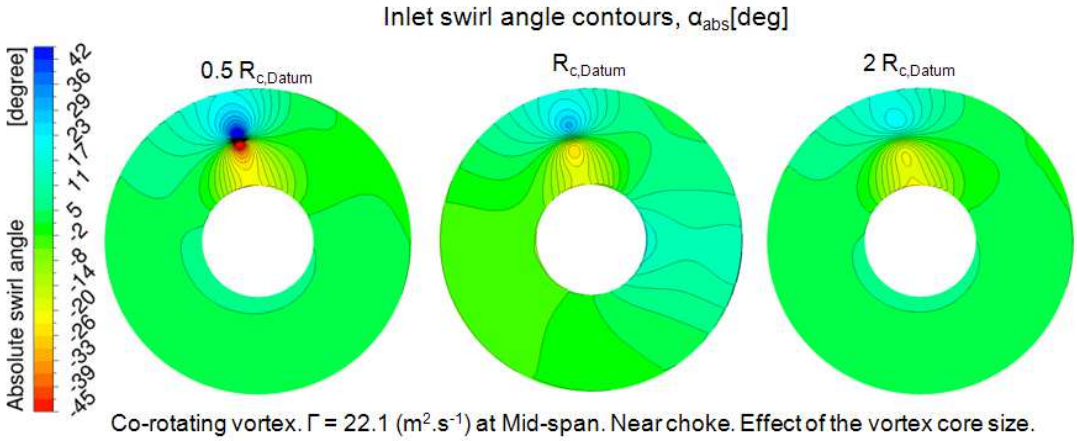

Figure 5.44: Inlet absolute swirl angle contours, α_{abs}. Near-choke condition. Vortex at 50% blade span (at Mid-span), $\Gamma = +22.1[m^2.s^{-1}]$. At Plane 01 upstream of Blade LE.

In terms of the isolated effect of the change in vortex core size, the vortex with a smaller core size causes the pressure ratio ($\overline{PR}$) and the mass flow ($\overline{W}$) to drop further compared with the higher vortex core size (see Figure 5.45). The isentropic efficiency ($\overline{\eta}$) is much more reduced for the smaller core-size vortex ingestions. This outcome is observe for both the values of vortex circulations, Γ= +11.01, and $+22.1[m^2.s^{-1}]$. The sensitivity of the rotor response is showing again to be dependant on the swirl angle distribution within the vortex core.

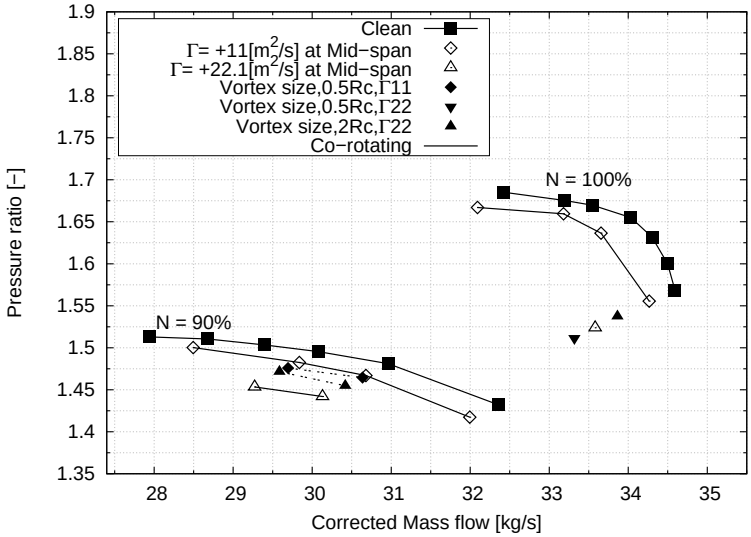

(a) Evolution of the rotor pressure ratio (PR)

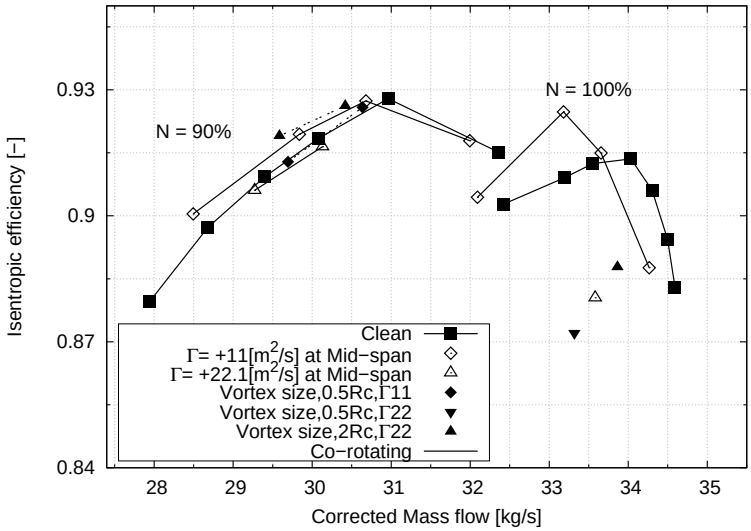

(b) Evolution of the rotor isentropic efficiency (η)

Figure 5.45: Configuration 3: Full-annulus Stage 67 co-rotating vortex ingestion at three blade spans, 25%, 50% and 75%. $\Gamma = \pm 11.01[m^2.s^{-1}]$. Performance maps.

This observation confirms the statement that a smaller size vortex with the same value of circulation is intensified, and thus is more concentrated in terms of the vorticity and the kinetic energy. Thus, it results in more rotor blade losses, and is shown in the Figure 5.46. Clearly, the smallest core size vortex is illustrating the most contribution in the turbo-machinery performance deterioration.

Also, the core size effects are amplified in the case of stronger strength vortex, i.e., Γ=+22.1$[m^2.s^{-1}]$. The sensitivity of the vortex core size on the rotor performance is higher, as the vortex strength increases. Thus, it can be stated that the compression system depends on the size, and the overall vortex circulation of the ingested vortices. An interesting observation is the fact that the swirl angle distributions (α) takes into account both of these vortex flow-features.

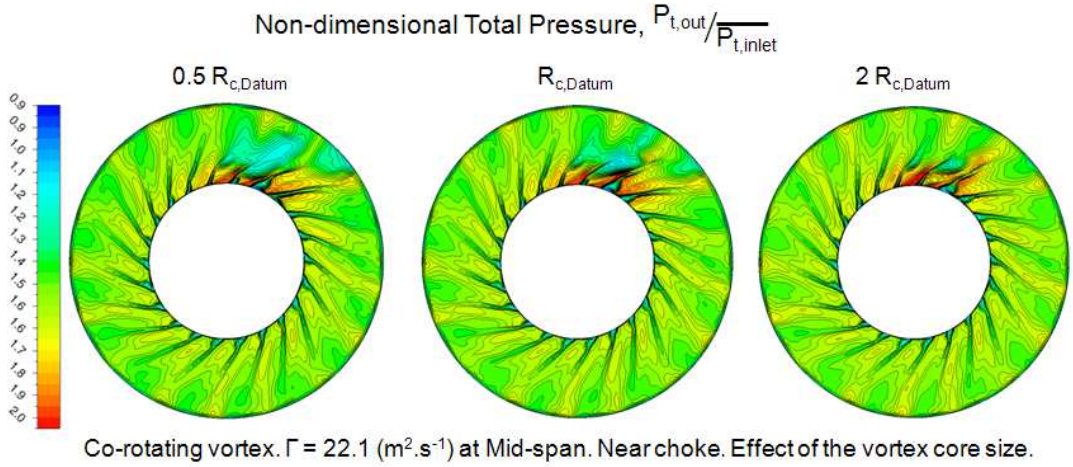

Figure 5.46: Non-dimensional total pressure, $\frac{P_{t,out}}{P_{t,in}}$. Near-choke condition. Vortex at 50% blade span (at Mid-span), $\Gamma = +22.1[m^2.s^{-1}]$. At Plane 01 upstream of Blade LE.

5.2.3 Summary

It was demonstrated in the vortex parametric study that high-strength, hub-ingested vortices caused the highest losses in compressor pressure ratio ($\overline{PR}$) and corrected mass flow ($\overline{W}_{correc}$). Both the co and counter rotating vortices showed signs of flow losses and system instabilities, especially when exceeding a certain value of the vortex circulation. Vortices with smaller core sizes (rc) have been shown to be more detrimental to the performance of the compressor than the larger vortices, if the circulation (Γ) is kept constant.

Following the study of the change in global performance, a closer investigation of the swirl effects across the blade span indicates that the rotor blade is exposed to two opposite swirl components, regardless of the vortex global direction. Thus,

the rotational direction of the rotor, with respect to each swirl direction, the strength of the swirl contents, and the radial location of the vortex center are decisive in determining the response of the compressor to vortex ingestion.

Furthermore, it was shown when the vortex was ingested near the hub region (25% span), the affected hub blade passages choked, causing the blade loading to become increasingly non-uniform. However, it was found that it is the radial swirl component impact within the blade span region, which induces the highest losses in the compression system. This causes considerable flow separation across the distorted blade span, and may cause the compression system to go towards the rotating stall region.

Some experiments that were performed by Mitchell[55] (see Section 2.6) with regards to the vortex ingestions showed similar results for the compressor response to the vortex polarity, and the ingestion location. From Mitchell[55] experimental study, it was concluded that both the co-rotating and counter-rotating vortices have an effect on the compressor stability. However, the co-rotating the vortices had the highest loss in terms of $\overline{PR}$ and $\overline{W}$, and also when ingested near the hub location. Similar observations of the vortex characteristics were also found in the current study.

Following the numerical investigation, quantification and discussion of the effects of different vortex features on the rotor performance, a methodology to correlate the changes in $\overline{PR}$ against the swirl parameters was developed. To do this, a number of swirl flow descriptors were generated, and were correlated against the changes in the compressor performance, i.e $\Delta\overline{PR}$, and $\Delta\overline{PRS}$. The results from this part of the research is shown in the next chapter.

Chapter 6

Flow Descriptors

6.1 Background

The key outcome of the research was to focus on the analysis of the swirl flow features which affect rotor performance through numerical tools, and their translation into the appropriate flow descriptors. For the latter, most of the numerical (CFD) database of the swirl distortion simulations on the Stage 67 (Configuration 3) was utilized.

To point out, all the results of pure bulk swirl simulations performed on the Stage 67 have been used as the dataset to use for flow descriptor correlations. This includes both the co and counter-rotating bulk swirl test-cases performed using the RANS approach (refer Appendix D, Table D.1). On the other hand, with regards to the vortex ingestion cases, only the co-rotating vortex ingestion RANS test cases on the Stage 67 have been used (refer Appendix D, Table D.2 for the test matrix). This is due to lack in number of performed counter-rotating vortex ingestion test cases, especially near the stall-conditions. However, the proposed methodology to asses the swirling flows with the help of flow descriptors is generic, and can be applied for both the global directions of the incoming vortex flow-field.

The overall aim was to generate an appropriate correlation methodology, which can then be used for the inlet-engine compatibility assessment under the influence of swirl distortion. The flow chart in Figure 6.1 layout the iterative

methods of the developed correlation methodology.

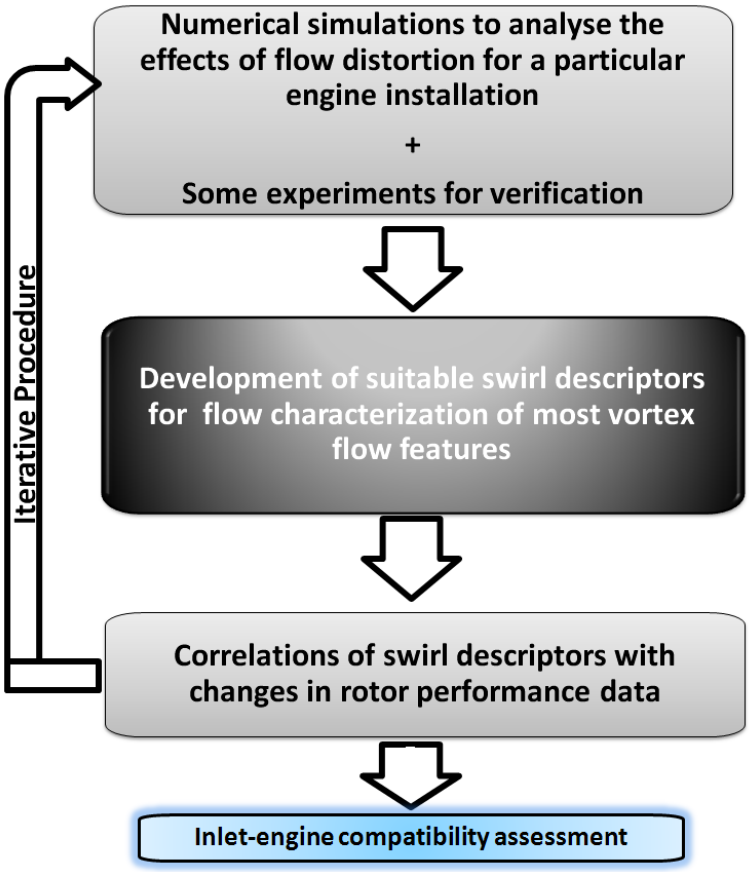

Figure 6.1: Flow descriptor correlation methodology.

A number of flow descriptors have been analysed over the course of the study, ranging from SAE proposed swirl descriptors[70] to some newly developed ones. This was performed to choose appropriate flow descriptors that take into account most of the swirl features, which were found to have an effect on the rotor performance during the post-analysis of numerical results.

The second goal was to generate methodologies in order to correlate the flow descriptors against the changes in compression system performance, e.g., change in ΔPR. This second task would help to feed information in to a broader industry goal of achieving a better inlet-engine compatibility assessment under the swirl distortion. For this, various methods have been analysed including the SAE recommended practices (see Chapter 2.6), and also more generic approaches has been studied. This chapter only contains the information of flow descriptors,

and the stability correlations, which the author found most appropriate within the context of the available numerical database, and also which shows the most promising results for future development.

6.2 Definition of parameters

This section lists the performance parameters, and the flow descriptors, along with the assumptions and techniques applied to generate a robust correlation methodology.

6.2.1 Performance parameters

As it has already been mentioned in the methodology chapter (Section 3.5.2) that the swirl distortion numerical studies on the Stage 67 has been performed at the constant outlet throttle settings. This means that the vortices were ingested at the inlet of a undistorted (clean) stage at the same throat area of the choked nozzle. Thus, the outlet Non-Dimensional Mass-Flow (NDMF) will remain constant for both the clean and the distorted cases.

This allows the user to evaluate the changes in compressor performance for each throttle setting independently, and generate a database that can then be used to create the descriptor correlations. The Section 2.5.1 discusses the two approaches which are widely used to asses the compressor response to distortion, i.e., at constant rotational speed and at constant mass flow. The constant rotational speed approach was adopted for the correlation analysis. It compliments the constant outlet throttle setting approach used in the numerical study, and also this technique can be used if there is lack of compressor performance data at a wide range of rotor speeds.

The compressor map sketch in the Figure 6.2(a) is illustrating a typical change in the clean speed-line, when encountered with an upstream flow distortion. It can be observed that there is a change in both the pressure ratio $\overline{PR}$, and the mass flow $\overline{W}$. The stability pressure ratio of a clean case, PRSC, has been shifted to a low value of PRSD. Additionally, by using the constant throttle setting

approach, pressure ratio of the new distorted operating point can be determined, which changes from $PR_{C,op}$ to $PR_{D,op}$. These particular operating points are simulated using the A6 nozzle area at the outlet, and is pointed out in Figure 6.2(b). It shows all the throttle settings nomenclature for the $N = 100\%$ spool speed. It ranges from A1 (near choke) to A10 (near stall) in clean uniform axial-flow conditions.

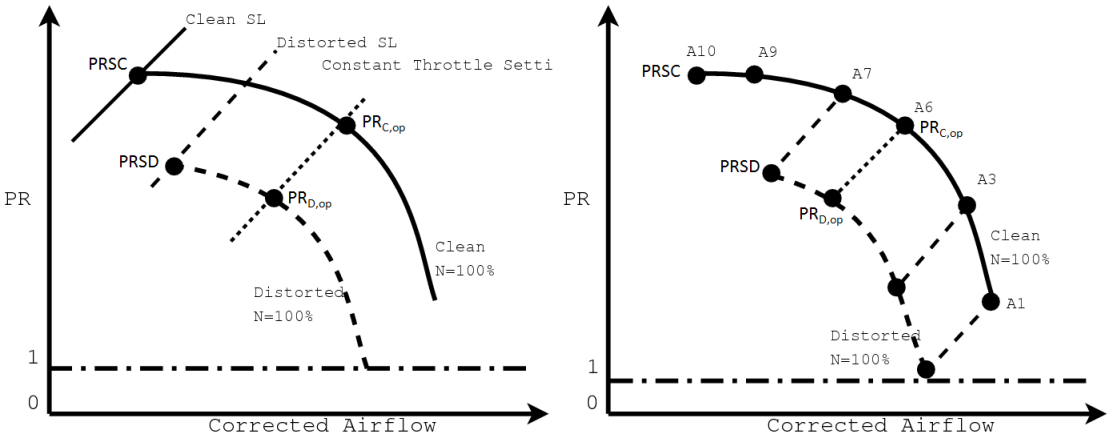

(a) Relevant points for stability definition (b) Constant throttle settings definition

Figure 6.2: Sketch: Quantification of compressor map parameters.

Two additional smaller nozzle areas were need for the $N = 90\%$ clean speed-line to reach the stability limit, which were A12 and A13. To note, the reduction in the nozzle areas (from A1 to A13) have been done in a consistent manner as shown in Table 3.10. Identifying the nomenclature of the throttle settings is important, as it will be later used in the correlations to described the compressor response to distortion in different flow regions.

Once all the key points in the compressor map have been recognized, the performance changes are evaluated in terms of three parameters. The first one is the change in pressure ratio (ΔPR) of a distorted compression system from the undistorted (clean) flow condition. The Equation 6.1 was used to determine ΔPR, where $\overline{PR_{C,t}}$ and $\overline{PR_{D,t}}$ are the area-averaged clean and the area-averaged distorted pressure-ratios, when both operating at similar constant throttle setting "t". Essentially, this parameter represents the loss in pressure ratio from the clean

case, non-dimensioned by the clean rise in pressure ratio. This method can be used to determine the ΔPR for the entire speed-line.

$$\Delta PR = \frac{\overline{PR_{C,t}} - \overline{PR_{D,t}}}{\overline{PR_{C,t}} - 1} \tag{6.1}$$

In order to track the changes in the surge line due to distortion, a second parameter can be used, i.e., the change in stability pressure ratio (ΔPRS). It is a modified version of the previous one, the constant throttle setting condition have been replaced by the stalling point in both the clean and the distorted speed-lines, as shown in the Equation 6.2. Thus, the PRSC and PRSD refer to the area-averaged clean and the area-averaged distorted stability pressure-ratios, respectively. This gives the user an idea of how much the stability line have been shifted due to the ingestion of inlet flow distortion.

$$\Delta PRS = \frac{PRSC - PRSD}{PRSC - 1} \tag{6.2}$$

The third performance parameter analysed is the change in surge margin (ΔSM) due to flow distortion, and is specified in Equation 6.3. It basically evaluates the difference between the clean and the distorted surge margins. The definition of surge margin (SM) has been taken from the SAE proposed SM list, i.e. the Equation 9 in Table 2.2.

$$\begin{cases} SM_{clean} = \frac{PRSC - PR_{C,op}}{PR_{C,op} - 1} \\ SM_{dist} = \frac{PRSD - PR_{D,op}}{PR_{D,op} - 1} \\ \Delta SM = SM_{clean} - SM_{dist} \end{cases} \tag{6.3}$$

The Figure 6.3 show an example of the performance parameter values, highlighting the changes in rotor performance, when encountered by different vortex flow features. The performance losses across the flow region from near choke to near stall is also tabulated. In this particular case, it showed that the rotor is most sensitive to the inlet flow distortion, when ingested near the hub location, and operating near the stability limit of the compression system. It is also illustrating the effect of the vortex strength on the performance parameters.

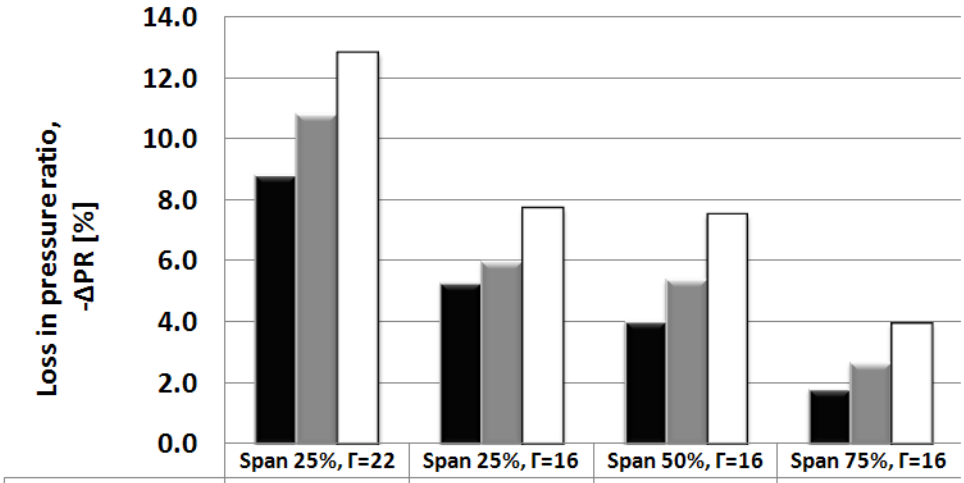

	Span 25%, Γ=22	Span 25%, Γ=16	Span 50%, Γ=16	Span 75%, Γ=16
Near choke (PR)	8.82	5.30	4.02	1.80
Near design (PR)	10.83	5.99	5.41	2.66
Stability limit (PRS)	12.83	7.74	7.53	3.96

Figure 6.3: Example of the performance parameters at various operating conditions. Vortex ingested at three radial locations. $\Gamma = +16$ and $+22.1[m^2.s^{-1}]$. At $N = 100\%$ spool speed.

6.2.2 Descriptors utilized

The second type of parameter required for the correlation analyses is definition of the flow descriptors. Several flow descriptors such as the, DC_{60}, SC_{60}, SI, SD, and SP have been previously described in Chapter 2.4.2. Most of these have been used and studied during the research study. However, only the flow descriptors that were utilized to generate the final correlation methodology is discussed over here.

Measurement setup

The grid discretisation for the flow descriptor definition is an important aspect for any robust correlation methodology. It lays out the foundation of the data collecting, and the averaging methods, which then have to be consistently used throughout the correlation study. Several averaging methods have been proposed in the past [68,70], and different values can be obtained if one follows an inconsistent approach.

The measurement Plane 1 (see Table 3.13) upstream of the blade's LE was

chosen as the Aerodynamic Interface Plane (AIP) for the Rotor 67 configuration. A study carried out by Cungo[19] on a similar rotor suggests that there has to be an adequate axial distance for the inlet flow not to be affected by the downstream Rotor 67 shock-wave system. From the study, it was found that the AIP location varies depending on the inlet flow, and also the rotor operating conditions. However, the measurement station plane 1 was chosen, which is about 0.32 hub chord upstream of the blade's LE. This was an appropriate upstream position of the AIP for not to be influenced by the downstream rotor shocks.

Figure 6.4 illustrates the annulus discretisation scheme used in the research study. The grid itself was subdivided into smaller annuli or rings. Additionally, the plane was subdivided into smaller circular sectors, also known as rakes. A grid dependency study was carried out on the number of rings and rakes required to capture the distorted flow-field accurately from the numerical database. A 400x400 grid was found to be well sufficient to precisely capture the full-annulus's flow-field. Currently, the non-intrusive measurement methods such as the particle image velocimetry (PIV) offers this kind of grid discretisation depth for the experimental testing[59].

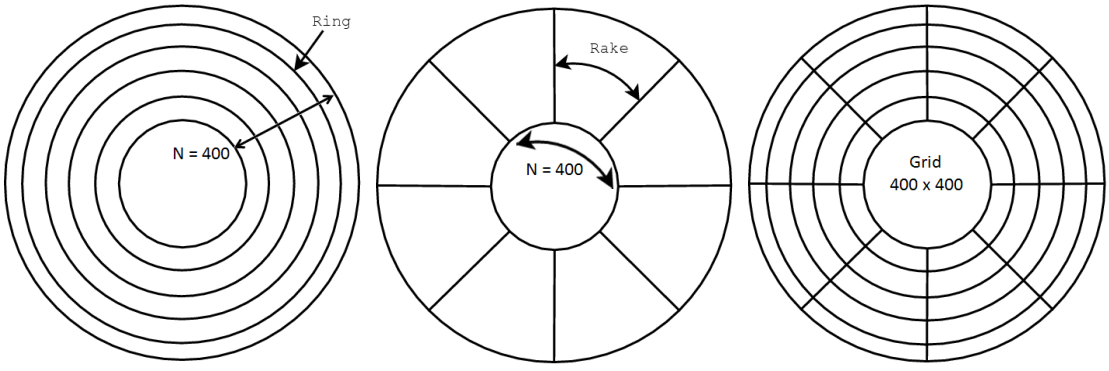

(a) Ring definition (b) Rake definition (c) Full definition

Figure 6.4: Annulus discretisation scheme: Ring and rake definition. At Plane 1.

Based on the described measurement grid, the following flow descriptors were developed from the numerical database.

Mean swirl intensity (SI)

It is one of the key SAE proposed flow descriptor for the swirl distortion[70] problem, and have been described in-detail previously (see Section 2.4.2). It essentially calculates an averaged swirl angle of distortion at the AIP plane. However, the calculation methodology have to be consistent, and robust enough to take into account the entire flow-field distribution accurately. To summarize, the following steps are needed to get the value of mean swirl intensity for the measurement grid.

Firstly, the Equation 6.4 describes the calculation of two sector swirls content along each one of the 400 (i) rings on the grid. Taking the area integral of the inlet swirl angle (α_x), sector swirls can be quantified for each measurement ring. The division of each ring in 400 rakes allows the user to use Equation 6.4 in its discrete formulation. The value can be either positive (SS_i^+) in the case of co-rotating swirl content, or negative (SS_i^-) in the case of counter-rotating swirl. Three input variables can be observed from the Equation 6.5.

The first two are the circumferential extents of the positive and the negative swirl angle (θ_i^+ and θ_i^-) along each i^{th} ring.

$$\begin{cases} SS_i^+ = \frac{1}{\theta_i^+} \int_{\theta_i^+} \alpha_x \left(\theta\right)_i \mathrm{d}\theta \\ SS_i^- = \frac{1}{\theta_i^-} \int_{\theta_i^-} \alpha_x \left(\theta\right)_i \mathrm{d}\theta \end{cases} \tag{6.4}$$

The third variable $\alpha_{x,i}$ is the swirl angle of interest along the each ring and rake. In the past, the absolute swirl angle (α_{abs}) have been used for the development of swirl intensity descriptor. However, when observing the distorted flow in the rotor blade's frame of reference, more types of swirl angles can be identified. These are illustrated in the Figure 6.5. The relative swirl angle (α_{rel}) is the angle that the rotor blade experiences, when exposed to the inlet flow. However, when a swirling flow is ingested at the inlet, the α_{rel} changes from the undistorted (clean) flow condition value. This change in α_{rel} causes the local blade incidence to increase or decrease depending on the swirl direction. The author have described this change in α_{rel} as $\alpha_{\Delta rel}$, and was calculated using the Equation 6.5, and the same measurement grid in the Figure 6.4.

$$\begin{cases} \alpha_{x,i} = \alpha_{abs} = atan\frac{V_{\theta,abs}}{V_x} \\ \alpha_{rel} = atan\frac{V_{\theta,rel}}{V_x} \\ \alpha_{x,i} = \alpha_{\Delta rel} = \alpha_{rel,Clean} - \alpha_{rel,Distorted} \end{cases} \tag{6.5}$$

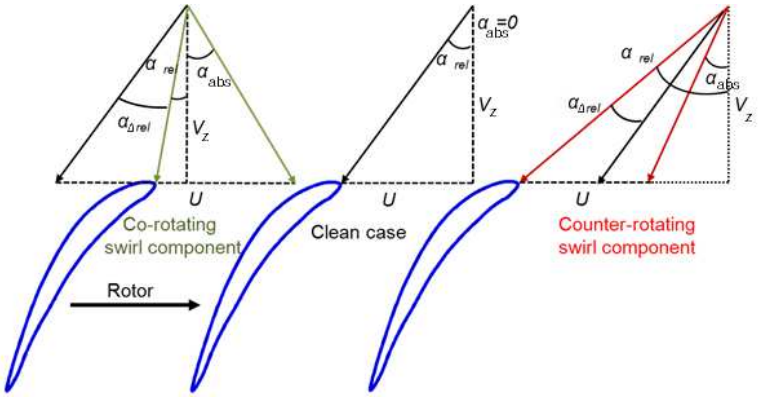

Figure 6.5: Sketch of nominal (clean) and distorted inlet velocity triangles. Definition of the change in inlet relative angle, $\alpha_{\Delta rel}$.

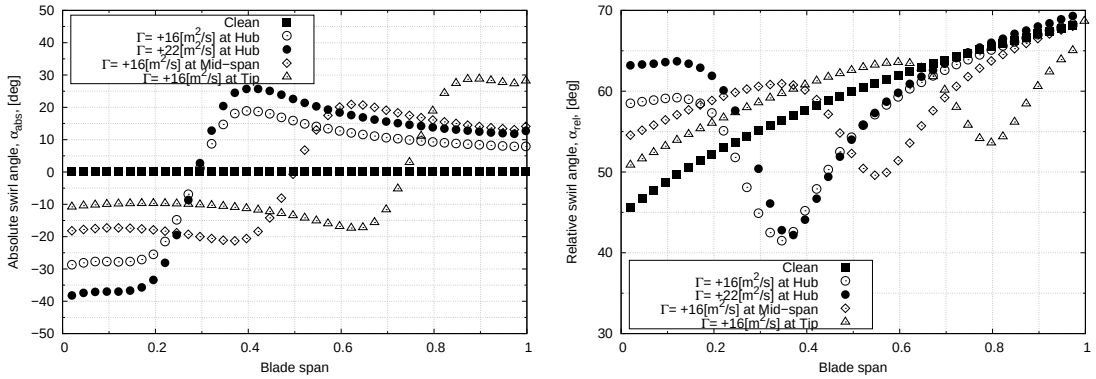

(a) Example of α_{abs} distribution.

(b) Example of α_{rel} distribution.

Figure 6.6: Example of span-wise angle distributions passing through the vortex centre. Vortex ingested at three radial locations. $\Gamma = +16$ and $+22.1[m^2.s^{-1}]$. At Plane 1 upstream of Blade LE.

Therefore, for the purpose of calculating the mean SI, two types of swirl angles were utilized in the study, which were the α_{abs} and the $\alpha_{\Delta rel}$. An example of the distribution of α_{abs} and α_{rel} passing through the vortex core center along the

blade span is shown in the Figure 6.6. As expected, the co-rotating and the counter-rotating swirl contents can be found along the blade span for the α_{abs} distribution. The latter is representing the α_{rel}, so all the values are positive. However, in order to calculate the $\alpha_{\Delta rel}$, the difference between the clean and the distorted have to performed. It will result in both the positive and the negative changes in local blade incidence, thus will exhibit a similar trend to the α_{abs}. The advantage of using the two types is the fact it takes into account both the absolute, and the relative frames of reference.

$$SI_i = \frac{SS_i^+ \cdot \theta_i^+ + \mid SS_i^- \mid \cdot \theta_i^-}{360} \tag{6.6}$$

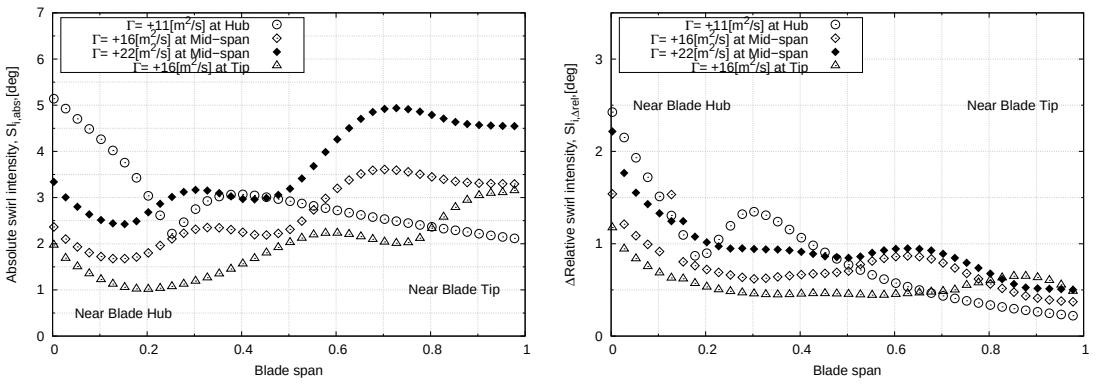

(a) Distribution of $SI_{i,abs}$.

(b) Distribution of $SI_{i,\Delta rel}$.

Figure 6.7: Example of span-wise flow descriptor definitions. Vortex ingested at three radial locations. $\Gamma = +16$ and $+22.1[m^2.s^{-1}]$, At Plane 1 upstream Blade LE.

The next step is to calculate the circumferentially averaged swirl intensity (SI) of the i^{th} ring, using the distributions of SS_i^- and SS_i^+. The following Equation 6.6 utilizes the positive and the absolute of negative sector swirls, thus it always generate positive values of SI_i along the blade span. Each value of SI_i can be defined as circumferentially average value of the absolute swirl angle along the analysed measurement ring i^{th}. It uses the circumferential extents (θ_i^+ and θ_i^-) to find the mean swirl angle in each ring. An example of SS_i^- distributions for

both types of angle inputs, α_{abs} and $\alpha_{\Delta rel}$, is shown in Figure 6.7. The effect of vortex strength and the radial location is clearly visible in both cases.

The final step in calculating the mean SI is the average SI_i along the blade span. Forthis purpose, different methods have been proposed in the past[68,69], and depends on number of factors, e.g. type of engine, rotor geometry, inlet configuration etc. Thus, SAE proposes the following Equation 6.7 for the preliminary generic correlations. It takes an arithmetic average of the SI_i along the blade span, where N represents the number of measurement rings.

$$SI = \frac{1}{N}\sum_{i=1}^{N} SI_i \tag{6.7}$$

Change in secondary kinetic energy coefficient (ΔCSKE)

A new flow descriptor for the flow distortion have been developed during the research study, and is called the change in secondary kinetic energy coefficient ($\Delta CSKE$). It utilizes the concept of coefficient of secondary kinetic energy (CSKE), which have been discussed by previous researchers[7] to determine the amount of flow losses due to the self-generated turbine vortices. The advantage of using the secondary kinetic energy is the fact that it is the kinetic energy associated with the non-streamwise flow components, i.e. the tangential (V_θ) and the radial (V_r) velocity components. Thus, the V_θ and the V_r velocity components due to the swirl distortion ingestion have some kinetic energy associated with it, and can be utilized in developing a robust swirl descriptor. A possible advantage of this flow descriptor over the SI is the fact that the SI only takes into account the angularity of the flow distortion, whereas $\Delta CSKE$ is basically a secondary flow energy equation term. Thus, by using two different approaches for the flow descriptors, a better insight to the swirl flow problem may be addressed.

$$SKE = \frac{1}{2}\rho\left(V_\theta^2 + V_r^2\right) \tag{6.8}$$

$$KE = \frac{1}{2}\rho\left(V_\theta^2 + V_r^2 + V_z^2\right) \tag{6.9}$$

$$CSKE = \frac{SKE}{KE} \tag{6.10}$$

$$\Delta CSKE = (CSKE)_{ave,dist} - (CSKE)_{ave,clean} \tag{6.11}$$

Equation 6.8 was used to determine the value of secondary kinetic energy (SKE) in each measurement probe. In order to obtain a consistent descriptor, the values of SKE are non-dimensionalized by the corresponding absolute kinetic energy (KE) (Equation 6.9). The output is the coefficient of the secondary kinetic energy (CSKE), as shown in Equation 6.10. The inlet flow-field in the non-streamwise direction is always influence by the downstream rotor, and therefore, the CSKE associated with the clean conditions but at constant throttle settings has to be subtracted (see Equation 6.11). In this way, the resultant $\Delta CSKE$ quantifies the secondary flows only contributed by the inlet swirl distortion. Once the value of $\Delta CSKE$ is calculated for the entire 400x400 measurement grid, an area average of the grid was performed. Thus, an absolute value of the $\Delta CSKE$ is calculated by circumferentially, and radially averaging the entire measurement plane.

6.3 Correlation analyses of pure bulk swirl

For bulk swirl analysis, the three flow descriptors introduced in the previous section, they have been correlated only against the loss in compressor pressure ratio ΔPR. The loss in stability pressure ratio (ΔPRS), and the change in surge margin (ΔSM) have not been correlated in this case. This is due to the fact that only one flow passage with the periodic BC was simulated under the influence of pure bulk swirl. Thus, to accurately capture the stability point is not feasible using this approach. However, the throttle settings away from the stability limit, i.e. from near choke to near stall have been illustrated, and discussed (see Figures 6.8-6.10).

6.3.1 Mean swirl intensity- Absolute (SI_{abs})

In this case study, the inlet absolute swirl angle (α_{abs}) was used to calculate the mean swirl intensity (SI_{abs}). The Figure 6.8 illustrates the correlations found with the ΔPR for both the co-rotating, and the counter-rotating bulk swirl. Three best fit lines have also been plotted in each correlation chart. The first one corresponds to near-stall (A10) throttle setting, second one is for near choke (A1), while the third one corresponds to the entire throttle setting data set. There is also a 2% deviation shading of the best fit line of the entire data-set.

From the correlation chart of co-rotating bulk swirl (see Figure 6.8(a)), it can be notice that the best fit lines in all the cases are almost linear. It means that as the swirl intensity (or α_{abs}) of the pure co-rotating bulk swirl increases at the inlet, the ΔPR goes up as well. As it is a pure bulk swirl pattern, the entire compressor face is exposed to the inlet bulk swirl. At the maximum co-rotating swirl angle (α_{abs}) of 30[deg], the compression system exhibits a loss of about 45% in the pressure ratio. Also, near-choke throttle setting exhibits a larger loss in pressure ratio than the near-stall condition. Due to the large drop in inlet relative Mach number (M_{rel}) at high SI_{abs}, i.e. $SI_{abs} \geq 20$[deg], the operation becomes significantly different between choke and stall.

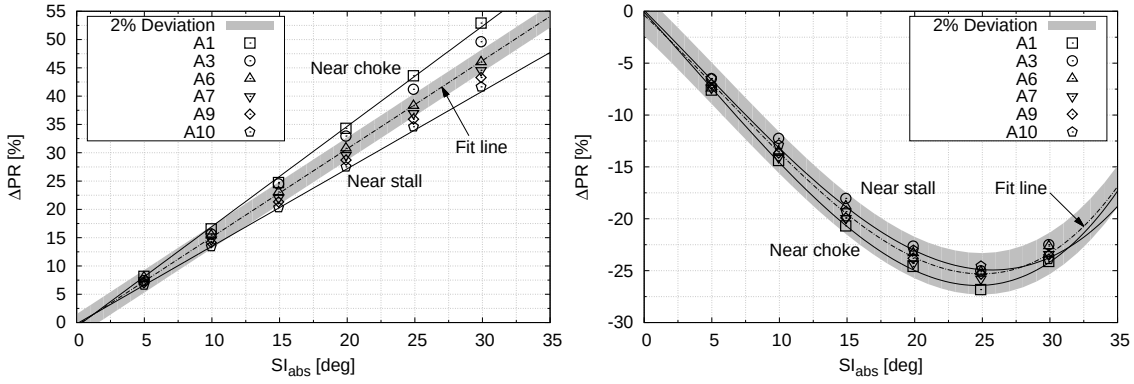

(a) Co-rotating bulk swirl.

(b) Counter-rotating bulk swirl.

Figure 6.8: Pure bulk swirl. Correlation between the loss in pressure ratio(ΔPR) and the mean swirl intensity-absolute(SI_{abs}).

On the other hand, correlation chart of the counter-rotating pure bulk swirl

(see Figure 6.8(b)) show a change in the trend. It is known from the last chapter that the pressure ratio increases when the counter-rotating swirl is ingested. Therefore, the values of ΔPR are negative till around 25[deg] of SI_{abs}. Until this point, the compression system exhibits an overall increase in ΔPR of about -25%. This is a lower rate of change in ΔPR, when compared with the value of about 38% for the co-rotating swirl, at the same 25[deg] of SI_{abs}. It means that the losses are much higher for the counter-rotating bulk swirl ingestion, even for SI_{abs} values upto around 25[deg]. Beyond this counter-rotating swirl angle, a complete shift in the shape of correlation can be observed. The flow losses within the blade passages exceeds massively, especially beyond the "critical" counter-rotating swirl angle of 20[deg](see Chapter 5.1.3.1). This causes the compressor to exhibit a reduction in $\overline{PR}$, thus the value of ΔPR increases from -25% to about -17.5%, when SI_{abs} increases from 25[deg] to 30[deg] respectively.

In the counter-rotating bulk swirl correlation (Figure 6.8(b)), the near choke and near stall throttle settings show very similar changes in the ΔPR. This is due to the high mass flow (W), and the inlet relative Mach number (M_{re}) associated with the counter-rotating pure bulk simulations. Thus, the operational margin for the compression system is much smaller compared the co-rotating bulk cases. A second order polynomial was found to be fit best for all the throttle settings in this set of correlations.

6.3.2 Mean swirl intensity-ΔRelative($SI_{\Delta rel}$)

In this case study, change in the inlet relative swirl angle (α_{rel}) was used to calculate the mean swirl intensity ($SI_{\Delta rel}$). Figure 6.9 illustrates the correlations found with the ΔPR for both the co-rotating, and the counter-rotating pure bulk swirl. As in the previous case, three best fit lines have also been plotted in each correlation chart. It can be noticed that the values of $SI_{\Delta rel}$ are much smaller than the SI_{abs}. It is because the values of $SI_{\Delta rel}$ are representing the changes in local blade incidence due to the swirl distortion. So, the charts are illustrating how much the compression system is deteriorating with these changes in the local

blade incidence.

From the chart of co-rotating bulk swirl (see Figure 6.9(a)), similar behaviour is observed in the correlation trend as previously in the SI_{abs} case. The correlation show a second order polynomial increase in the ΔPR with the $SI_{\Delta rel}$. However, at slight reduction in the values of $SI_{\Delta rel}$ for the near choke throttle settings (A1 and A3) are observed at high swirl angles cases, i.e., $SI_{\Delta rel} \geq 3$[deg].

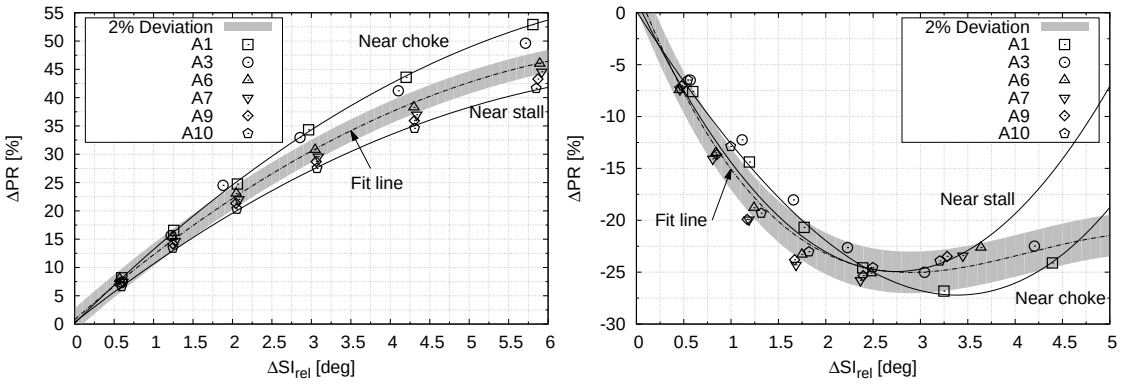

(a) Co-rotating bulk swirl.

(b) Counter-rotating bulk swirl.

Figure 6.9: Pure bulk swirl. Correlation between the loss in pressure ratio(ΔPR) and the mean swirl intensity-$\Delta relative(SI_{\Delta rel})$.

On the other hand, the correlation chart of the counter-rotating pure bulk swirl (see Figure 6.9(b)) exhibits a much different characteristics of the compression system. It have been discussed before the importance of the unique incidence angle in the transonic rotors. From the Figure 6.9(b), it can observed that at low counter swirl angles, i.e., $\alpha_{abs} \leq 10$[deg], the rotor is trying to keep the blade incidence (or $SI_{\Delta rel}$) constant. However, at high counter swirl angles, the rotor seems unable to achieve this state, and the scatter data of $SI_{\Delta rel}$ is the outcome. The cause is again related with the increased inlet relative Mach number (M_{rel}), which increases the shock-wave strength but also passage flow losses at high counter-rotating bulk swirl angles.

6.3.3 ΔSecondary kinetic energy coefficient- ΔCSKE

The final descriptor correlations for the pure bulk swirl is shown in Figure 6.10. In this case study, change in the inlet coefficient of the secondary kinetic energy ($\Delta CSKE$) was used to correlate against the ΔPR. Very similar trends to the SI_{abs} were observed. A second order polynomial trend is observed for both the co-rotating and the counter-rotating bulk swirl cases.

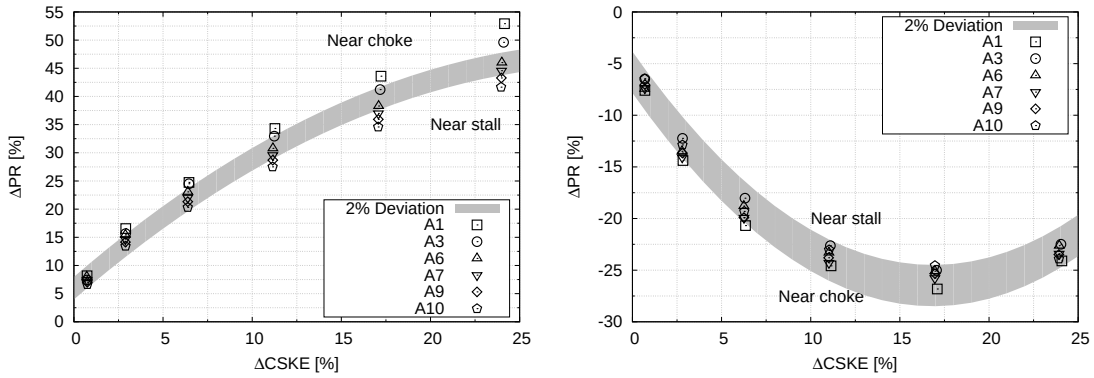

(a) Co-rotating bulk swirl.

(b) Counter-rotating bulk swirl.

Figure 6.10: Pure bulk swirl. Correlation between the loss in pressure ratio(ΔPR) and the Δcoefficient of secondary kinetic energy($\Delta CSKE$).

The only difference are the values of the $\Delta CSKE$, and their variations as the swirl angle changes. Unlike the SI_{abs} values, which are increasing linearly with the inlet swirl angle, the values of $\Delta CSKE$ seems to have a function with the inlet swirl angle. The term $\Delta CSKE$ takes into account both the tangential, and the radial velocity components, and therefore can be proven very useful for more complex swirl patterns, e.g, paired swirl, or vortices.

6.4 Correlation analyses of tightly-wound vortices

In this section, the changes in rotor performance under the influence of co-rotating vortex ingestion are correlated against the developed flow descriptors. Tightly

wound vortices are characterized by two regions of opposite swirl contents, i.e, the co and counter swirl content. Because of the interaction between these regions, and also the distortion in total pressure and axial velocity, the resultant effect on the turbomachinery is much more complex than the former. As a result, the correlation trends of a vortex ingestion slightly differs from the pure bulk swirl. However, all the different types of correlations are presented to give an overview of the study. To note, the performance database of both the rotational speeds, i.e., N=90% and 100%, was used, and the correlations are shown in this section.

6.4.1 Mean swirl intensity- SI

Figure 6.11 shows the evolution of the ΔPR with the SI_{abs} for all the throttle settings away from stalling. The effect of the throttle settings from near choke (A1) to near stall (A10 for N=100%, and A13 for N=90% in clean conditions) can be observed. For both spool speeds, most of the distorted test cases stalled before the clean stability throttle settings of A10, and A13, respectively. A second order polynomial trend can be fit in the correlation. Figure 6.11(b) describes the same data set but illustrating each rotational speed separately. A 1.5% deviation from the best fit line of the entire data set of the ΔPR is also plotted. It can be noticed that both the SI_{abs}, and the ΔPR values are much smaller compared with the bulk swirl correlations. This was expected as unlike the pure bulk swirl, the vortex ingestion mainly affects only part of the rotor annulus (3-4 rotor passages). Thus, the average SI_{abs}, and the effect on the rotor ΔPR is less than the former. However, it doesn't mean the ΔPRS should follow the same trend.

The ΔPR correlations show dependency on the swirl strength, the core size, the radial location, and also the spool speed of the tested compression system. The SI_{abs} flow descriptor seems to be taking into account all these vortex flow-features, and generating a correlation that fits quite well in a second order polynomial. The maximum ΔPR from the undistorted (clean) flow conditions were observed for the rotor speed, N=100% test cases, which ranges upto about 12%. In general, the trend show higher values of the ΔPR for the higher strength (Γ)

vortices. Also, when the radial vortex ingestion location changes from near tip to near hub, the values of SI_{abs} and the ΔPR increases. As expected, a smaller vortex core size (i.e. when Γ is kept constant) also showed a higher value of SI_{abs}, and correspondingly a larger loss in the rotor performance (ΔPR).

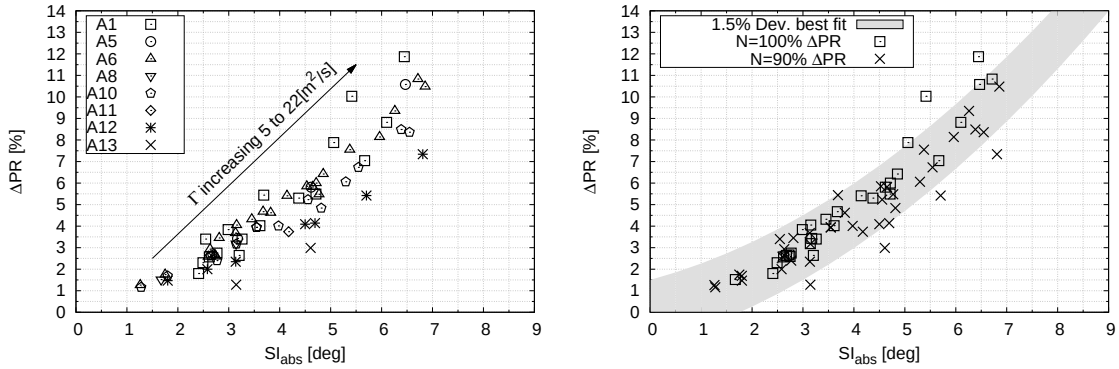

(a) Throttle settings illustration.

(b) Spool speed illustration.

Figure 6.11: Single vortex ingestions. Correlation between the loss in pressure ratio(ΔPR) and the mean swirl intensity-absolute(SI_{abs}).

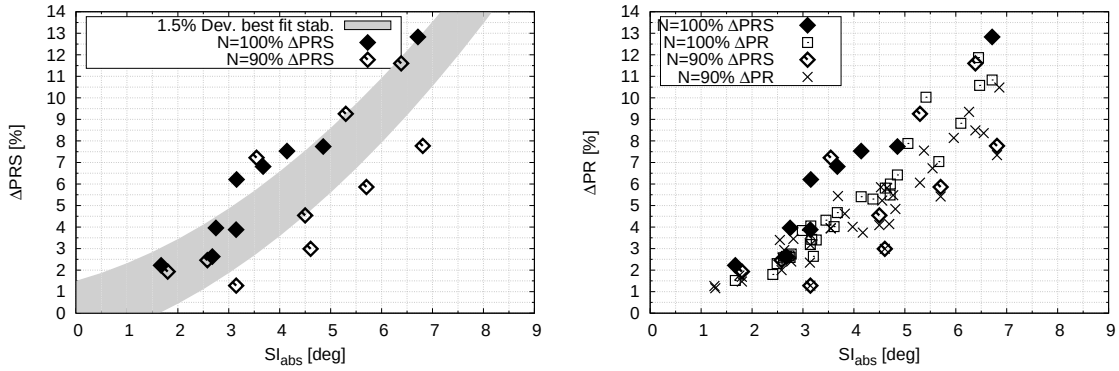

(a) Stability limit.

(b) Combined anlysis.

Figure 6.12: Single vortex ingestions. Combined ΔPR and ΔPRS correlations against the mean swirl intensity-absolute (SI_{abs}).

Figure 6.12(a) illustrates the correlation of SI_{abs} against the stability pressure ratio (ΔPRS) for the previous mentioned test cases. A 1.5% deviation from the best fit line (2^{nd} order polynomial) of the data set of ΔPRS is also plotted. From

the correlation, it can be clearly observed that the values of ΔPRS are higher for the higher spool speed, i.e., when N=100%. The stability line represents the maximum change in the stability pressure ratio that the rotor exhibits before going into the unstable operation (e.g. the rotating stall or surge). Thus, from the ΔPRS correlation, it can be said that the Rotor 67 is exhibiting higher performance losses, at N=100%. This is also an expected observation as the transonic rotors are more loaded at higher spool speeds, and thus, exhibiting more sensitivity to the inlet vortex ingestion. The combined ΔPR and ΔPRS correlations against the SI_{abs} is also illustrated in Figure 6.12(b). In general, the combined analyses show promising results for the use of SI_{abs} as a flow descriptor in this type of swirl distortion scenario.

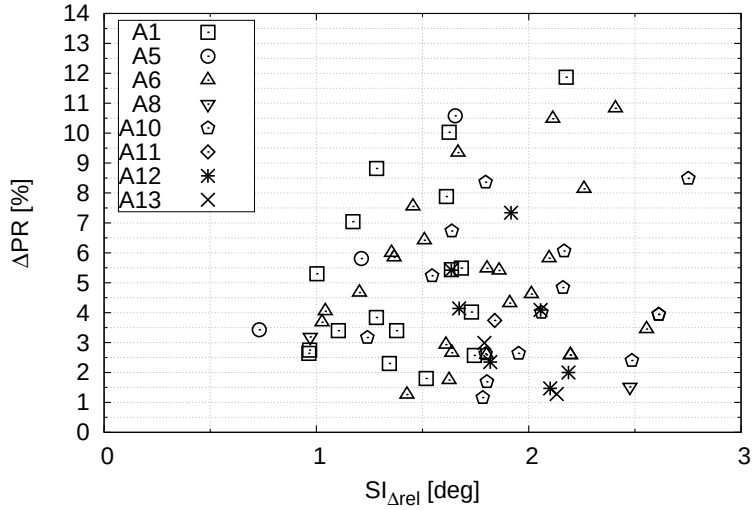

Figure 6.13: Single vortex ingestions. Correlation between the loss in pressure ratio(ΔPR) and the mean swirl intensity-$\Delta relative(SI_{\Delta rel})$.

In the previous section, another type of SI flow descriptor using the change in the inlet relative angle of the rotor was correlated. It was named as $SI_{\Delta rel}$, and Figure 6.13 shows the correlation found with the ΔPR for the vortex ingestion test cases. A large scatter of the data can be seen at all the throttle settings (A1 to A13), and no kind of correlation trend is observed from the analysis. This is due to the fact that the vortex flow-field is much more complex than the bulk swirl pattern, it is due to distorted flow regions of the total pressure, the axial and

the radial velocities which resulting in a flow redistribution just upstream of the blade LE[28](see Chapter 4.3). This causes the small changes in the inlet relative angle (α_{abs}) to change constantly, as the distorted flow reaches the blade's LE. Thus, to use this type of flow descriptor for the distorted patterns that inherits distortion variables other than the swirl angle was found to be less useful.

Equation 6.3 illustrates the definition of surge margin for the undistorted (clean), and the distorted cases. This is one of the key performance parameters that the industry uses often in determining the safety margins of an engine at different operating conditions. To note, the operating points (op) in the definitions of SM_{clean} and $SM_{distorted}$ are achieved by keeping the outlet throttle setting (t) constant between the two cases.

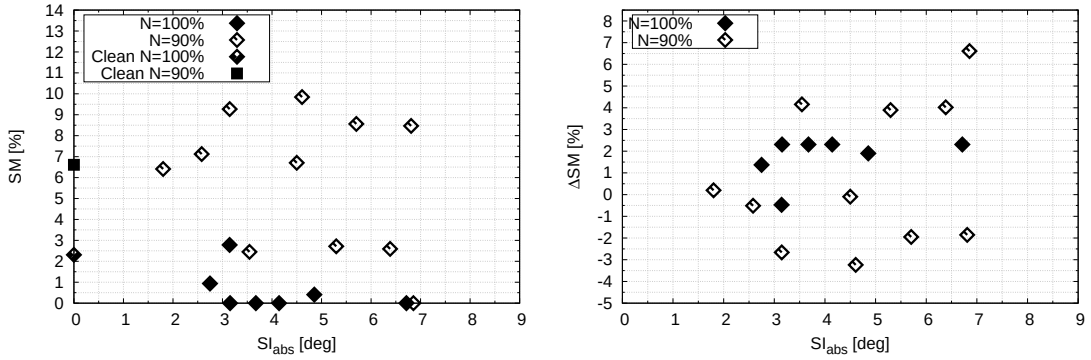

(a) Surge margin (SM).

(b) Change in surge margin (ΔSM).

Figure 6.14: Single vortex ingestions. Correlation between the loss in pressure ratio(ΔPRS) and the SM definitions.

Figure 6.14 show the correlation of SM and ΔSM against the SI_{abs} for the vortex ingestion cases. From the chart, it can be observed that the SM for N=100% is much lower than N=90%. With the ingestion of the vortex, the SM reduces for most of the cases at higher spool speed. Only one case showed an improvement in the SM, which was simulated at a lower vortex circulation. On the other hand, N=90% spool speed was more tolerant to the vortex ingestions in terms of SM, and a slight improvement was observed in low to medium vortex circulation test cases (i.e., Γ 11.01, and 16.0 $[m^2.s^{-1}]$. This is the due to an

increase in the mass-flow range ($\Delta\overline{W}$) with an ingestion of a co-rotating vortex that causes an increase in the values of SM. This is a characteristic of a pure co-rotating bulk swirl pattern that results in an drop of ΔPRS and an increase in SM[10,72].

However, its not a surprise that no correlation was found between the SM or ΔSM with the flow descriptors (i.e., SI_{abs}, $SI_{\Delta rel}$ etc.) . The reason is the shape of the transonic rotor speed-line that changes with the amount of the inlet airflow. Thus, a performance parameter that depends on two operating points in a speed-line, such as the SM, is currently beyond the scope for the descriptor correlations, that needs various different speed-lines database. The SAE[68,70] also always proposes ΔPRS to be used as the stability parameter for the inlet-engine compatibility assessments. From the study, it was also observed that for the constant rotor speed approach, the use of ΔPRS as a performance parameter for the flow descriptor correlations was found to be more attractive.

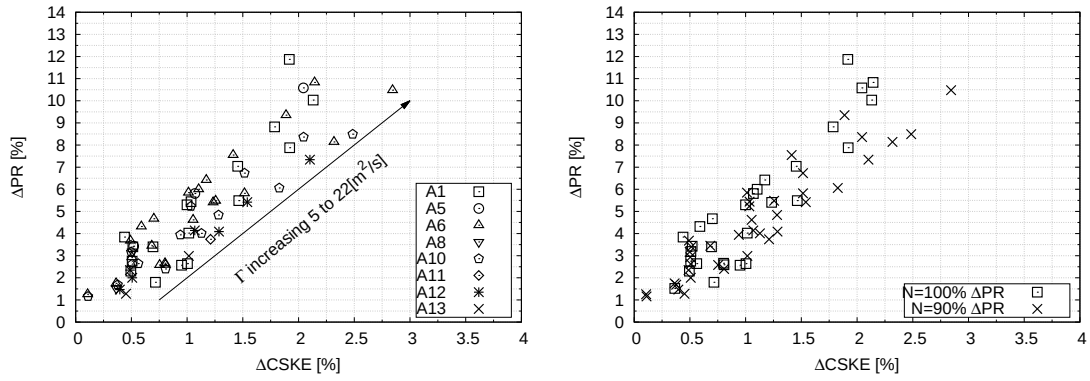

(a) Throttle settings illustration.

(b) Spool speed illustration.

Figure 6.15: Single vortex ingestions. Correlation between the loss in pressure ratio(ΔPR) and the Δcoefficient of secondary kinetic energy($\Delta CSKE$).

6.4.2 ΔSecondary kinetic energy coefficient- ΔCSKE

The final set of flow descriptor correlations for the vortex ingestion cases are shown in Figures 6.15-6.16. In Figure 6.15, the changes in the inlet coefficient of the secondary kinetic energy ($\Delta CSKE$) are correlate against the ΔPR. Very

similar correlation trends to the SI_{abs} were again observed using this type of flow descriptor. However, the correlations of both speed-lines (see Figure 6.15(b)) are much closer together compared with the SI_{abs} (see Figure 6.11(b)) correlations.

For the vortex ingestion cases, the values of $\Delta CSKE$ are also much lower than the SI_{abs}, and show more linear trends against the ΔPR (Figure 6.15), and the ΔPRS (Figure 6.16). The reason might be the radial and the axial velocity components of the inlet flow, which is been taken into account in the CSKE formulation. Equations 6.8-6.10 describes the steps in calculating the CSKE. From Equation 6.8, during the calculation of SKE, the radial velocity (V_r) component is included, and then non-dimensioned by the KE (Equation 6.9). The term KE calculates the total kinetic energy of the flow, thus also taking into consideration the axial velocity (V_a) component. The tightly-wound vortices have a considerable amount of distortion in the V_r, and the V_a components. Thus, the use of $\Delta CSKE$ flow descriptor seems advantageous for this type of the swirl distortion. It also shows a slightly better correlation against the performance parameters than the SI_{abs}.

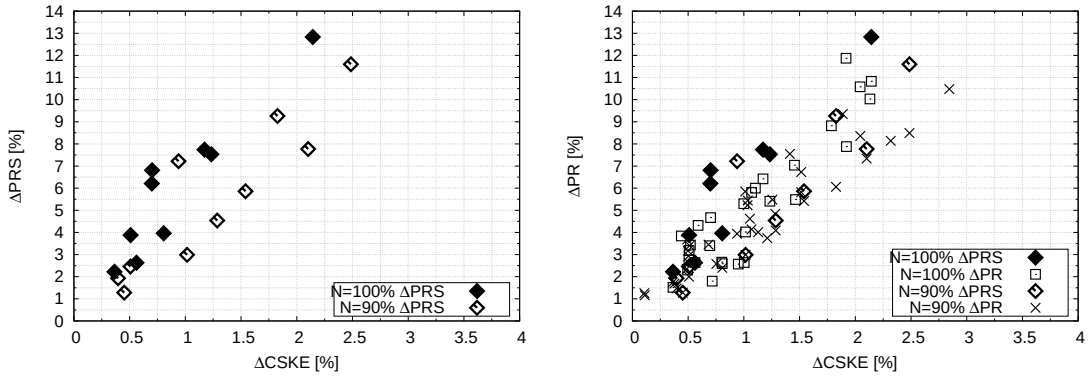

(a) Stability limit.

(b) Combined anlysis.

Figure 6.16: Single vortex ingestions. Stability limit. Correlation between the loss in pressure ratio(ΔPRS) and the Δcoefficient of secondary kinetic energy($\Delta CSKE$).

6.5 Combined bulk and tightly-wound vortex correlation analysis

Previous sections highlighted the correlation trends for the pure bulk swirl, and the single vortex ingestion separately. This section analyses the combined correlation trends for the both types of swirl distortion. Moreover, a numerical work was carried out by Pardo[62] on the multiple vortex ingestions, and the development of similar flow descriptor correlations. To compare the effect of a single and multiple vortex ingestion, the results from this study are also included. Also, some simulations were performed on the Rotor 37 (Configuration 2) to compare the correlation trends for the two different types of transonic rotors.

To note, only the results of $N = 100\%$ rotational speed are shown in this section, the reason being the numerical work carried on the multiple vortices[62], and also the Rotor 37 was limited at this spool speed. For the Rotor 37 configuration, four numerical test-cases were performed, increasing in number of the ingested vortices from one to four. The vortex circulation, $\Gamma = 11.01[m^2.s^{-1}]$, was chosen, and was ingested at the mid-span in these cases. Only the ΔPRS values for the Rotor 37 are illustrated.

6.5.1 Single and multiple tightly-wound vortices

This section compares the changes in the trends of flow descriptor correlations due to the multiple vortex ingestion. The data provided by Pardo[62] of the multiple vortex ingestion on a similar rotor includes different types of co-rotating vortices.

In the above correlations, the ΔPR stands for the changes in pressure-ratio at the all the throttle settings away from stall, where as the ΔPRS is illustrating the changes in stability pressure-ratios for the single and multiple vortex ingestion. Similar correlation trends were observed when comparing a single and, the multiple vortex ingestion cases. Figure 6.17 illustrates the evolution of the ΔPR, and the ΔPRS, with the SI_{abs}. It can be noticed that for a given SI_{abs}, the effect of a single vortex is slightly higher than the other. The work done on the

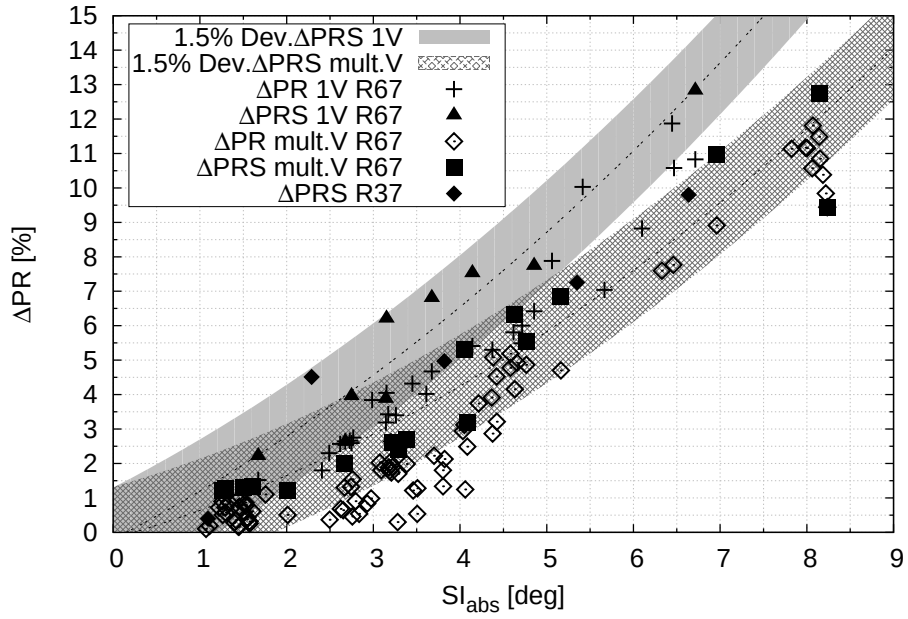

Figure 6.17: Comparison between the single (1V) and multiple (multi.) vortex ingestion. Correlation of the ΔPR, and the ΔPRS, against the SI_{abs}.

multiple vortices[62] suggest that the rate of loss in the rotor performance reduces with an increase in number of the ingested vortices.

Thus, it can be said that the response of a single vortex ingestion at a given SI_{abs} is higher. Both best fit lines of the stability-limit data (ΔPRS) show a second order polynomial trend, and thus, shows viability of the flow descriptor SI_{abs} for these types of swirling flows.

Also, the values of ΔPRS for the Rotor 37 configuration falls within the predicted correlations trends of the Rotor 67. Thus, results of the Rotor 37 suggests that the SI_{abs} correlation methodology works well for both types of the transonic rotors.

Similar correlation curves for both types of vortex ingestion were also observed using the ΔCSKE flow descriptor. The results are shown in Figure 6.18. The ΔCSKE flow descriptor also show a second order polynomial curve from the correlation data-set. The effect of a single vortex on the ΔPR at a given ΔCSKE is again higher than the other. Thus, both these flow descriptors (SI_{abs} and ΔCSKE) show consistent trends by taking into account most of the vortex flow

features, i.e., the vortex strength (Γ), radial location (span), size (rc), number, and also the compressor rotational speed (N).

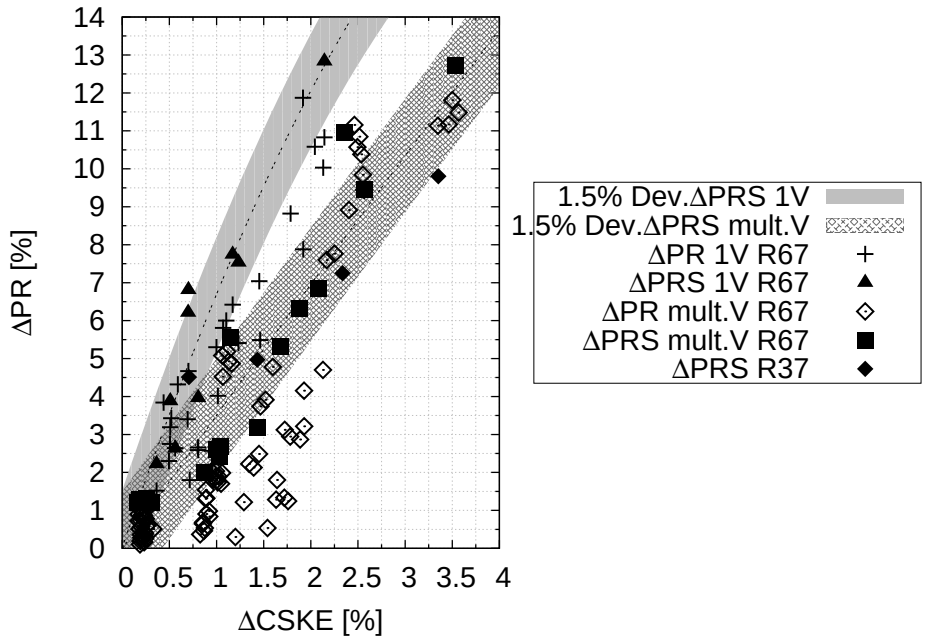

Figure 6.18: Single and multiple vortex ingestions. Correlation of the ΔPR, and the ΔPRS, against the $\Delta CSKE$.

6.5.2 Pure bulk swirl and tightly-wound vortices

Finally, the combined correlations generated for the tightly-wound vortices and, the pure bulk swirl are illustrated in Figure 6.19. Because of the limitations of one flow passage simulations for bulk swirl test-cases, the correlations obtained refer to the throttle settings away from stalling only.

Figure 6.19(a) shows the evolution of the ΔPR with the SI_{abs} taking into consideration the entire correlation dataset. As mentioned earlier, the values of SI_{abs} and the ΔPR obtained for the pure bulk swirl are much higher. The pure bulk swirl pattern is a type of swirl distortion that affects the entire rotor annulus. While, the vortex ingestion takes place locally in some blade passages, and only affects part of the compressor. The correlation trends show that the flow descriptors are capable of taking this into consideration, as the dataset for the highest vortex circulation results into SI_{abs} of about 9[deg]. Whereas, the

bulk swirl angle ranges upto 30[deg].

From Figure 6.19(b), which is within the range of tightly wound vortex map, the correlation obtained for the bulk swirl fits well within the tightly-wound vortex cases. A single vortex ingestion still shows the highest sensitivity in terms of the ΔPR, compared with the multiple or the pure bulk swirl pattern. However, the differences are small, and the overall correlation trends is exhibiting a promising correlation methodology. It is also showing that by only simulating less complex swirl patterns, i.e., a pure bulk swirl pattern, general correlation trends for the swirl distortion problem can be obtained for the specific compression system.

6.6 Summary

In this section, several correlations between the rotor performance loss (i.e. the ΔPR, and the ΔPRS), and the magnitude of the distortion (e.g. SI_{abs}, and $\Delta CSKE$) have been generated and assessed. The analysis have been made at constant throttle settings, and at the stability limit of the test cases. The constant rotor speed approach have been used in the development of correlations. It has allowed the representation of the entire speed-line in a series of the flow descriptor correlation maps.

The correlations generated for the bulk swirl showed promising polynomial trends, when using the SI_{abs}, and the $\Delta CSKE$, against the changes in performance for both the co-rotating and the counter-rotating swirl.

However, for the tightly-wound vortices, only the database of co-rotating vortices was used. The correlations obtained exhibited good second order polynomial trends, taking into account the rotor's rotational speed, and also the geometry. Additionally, combined correlations for the bulk-swirl, the single vortex, and the multiple vortices ingestion has been compared. The results show that the response of the rotor to the ingestion of a single vortex is slightly higher than the rest of the distorted patterns. In general, the combined correlations showed the viability of the proposed descriptor correlation methodology.

The flow descriptors, i.e., SI_{abs}, and the $\Delta CSKE$ showed that it can take

into account several swirling flow parameters. These include the swirl strength, polarity, position, overall size, and also the rotational speed of the compression system.

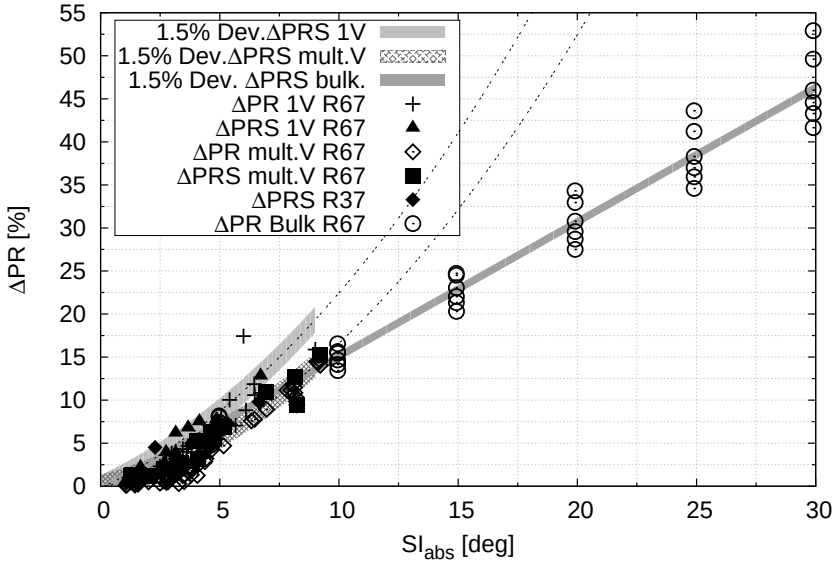

(a) Complete chart.

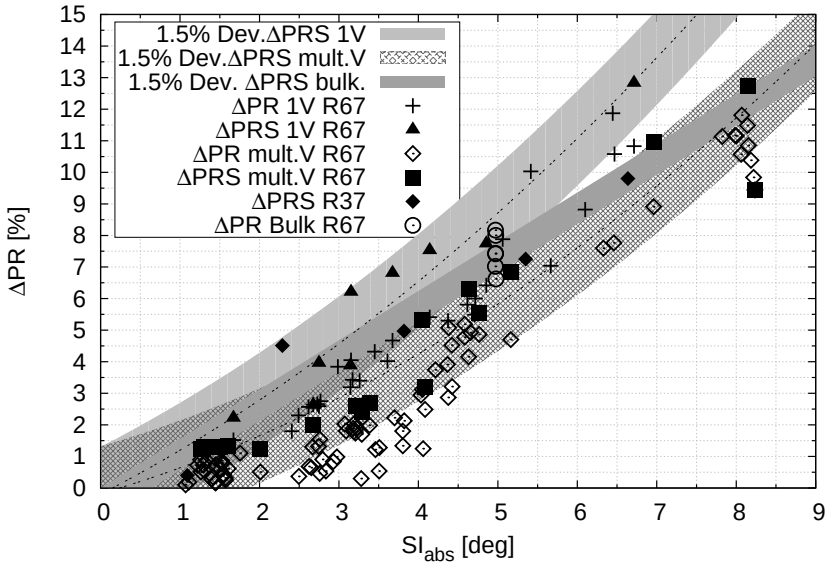

(b) Within the vortex ingestion range.

Figure 6.19: Pure bulk swirl and vortex ingestion correlations. Correlation of the ΔPR, and the ΔPRS, against the SI_{abs}.

Chapter 7

Summary, novelty and future work

This chapter, summarizes the major contribution done out of the research topic, and some recommendations for future work.

7.0.1 Research topic summary and novelty

In the introductory part of the document, the key objectives of the research were outlined. The aim was to broaden knowledge of the swirl distortion effects on the turbo-machinery performance, and propose methods for the correlation of the performance changes using the flow descriptors.

The CFD was used as a tool for generating the database of two types of swirl distortion, i.e., the pure bulk swirl and the discrete vortices. Two different transonic rotor, i.e. the Rotor 67 and 37, were used as the test-domains. Various swirl flow-features parametric studies were performed to address the swirl problem.

The following can be recognized as the key outcomes from the research study:

- A boundary condition (BC) methodology is proposed that can be used to numerically simulate various swirl patterns, such as, the pure bulk swirl, and the discrete vortices, as an inlet condition of a compression system. This allow the users to save considerable computational time, and the costs

involved by eliminating the need to model the upstream distortion generators, if not required by the study.

- For the first time, a comparison of the steady (RANS), and the unsteady (URANS), CFD capability under the influence of swirl distortion have been assessed. Away from the stability limit, both approaches exhibit similar results. Due to the unsteady nature of flow near the stall conditions, the URANS have been found to provide a better insight into the unsteady interactions, especially when under the influence of a swirling flow. However, the computational time fourfold with the URANS CFD, and if one objective is to generate a large database of the swirl distortion effects quickly, this approach may become infeasible.

- The turbo-machinery was found to have evident effects in the performance flow variables (such as the, $\overline{PR}$, $\overline{W}$, $\overline{\eta}$, etc.) due to the ingestion of both co-rotating, and counter-rotating pure bulk swirl. The magnitude, and the polarity of the swirl pattern exposed at the rotor inlet were found to be the key factors in determining the rotor response. Also, as reported previously in [70,72], the polarity of the bulk swirl pattern have opposing aerodynamic effects on the compression performance. A co-rotating bulk swirl reduces the compressor pressure ratio ($\overline{PR}$), and the mass-flow ($\overline{W}$), while the $\overline{\eta}$ remains almost unchanged. Whereas, in the case of counter-rotating bulk swirl, there is an increase in the values of $\overline{PR}$, $\overline{W}$, $\overline{TR}$, and a reduction in the values of $\overline{\eta}$. However, from the research, this was found to be only true, when under the influence of low bulk swirl angles.

- The transonic rotor was found to behave differently at high bulk swirl angles due to inherit changes in the shock-wave system. When a high intensity co-rotating bulk swirl was ingested, a much larger rate of drop in the values of $\overline{PR}$, $\overline{W}$, $\overline{TR}$, and a reduction in the $\overline{\eta}$ was observed. On the other hand, the ingestion of a high intensity counter-rotating swirl completely changes the rotor characteristics. Beyond a certain counter-rotating bulk swirl angle at the inlet, a large amount of flow losses were observed within the infected

rotor passages. This has been identified as the critical counter bulk swirl angle, and exhibited a different value for each transonic rotor.

- These flow losses have been found to be induced at the rotor blade's suction side, and forms a hub vortex due to a strong interaction between the bow shock, and the hub boundary due to the incoming counter-rotating swirling flow. This generated vortex then travels radially upwards towards the tip region, causing the flow spillage at the rotor tip gap. At high counter-rotating swirl angles, this can result in a large performance deterioration of the compression system, which may lead to the rotating stall or even surge. This is a new finding in reference to the previous studies on the pure bulk swirl, and was found to be directly linked with the shock-wave system of the investigated transonic rotors.

- With regards to the vortex ingestion, it was concluded that the vortex strength (Γ), the radial location (r_v), the polarity, and the vortex core-size (r_c), all plays a vital role in determining the rotor response to flow distortion. This had been a research area, where very little information existed in the past.

- Two-opposite swirl contents (co and counter) was found to be present with the ingestion of small tightly-wound vortices, regardless of the vortex global direction. Thus, it was found that the local effect of the vortex depends all the above mentioned parameters coherently. In general, it was observed that the vortices ingested near the hub cause the highest flow losses, and the losses incremented as the vortex strength intensified. Comparing, the co-rotating, and the counter rotating vortices, the latter showed signs of more flow losses, and the system instabilities, especially when exceeding a certain value of the vortex circulation (Γ). Also, the vortices with smaller core sizes (with constant Γ) showed more detrimental to the performance of the compressor than the larger size vortices.

- The effect of rotor's rotational-speed was also found to be important in un-

derstanding the response of vortex ingestion. At higher spool speeds, more performance losses were observed. This was due to the shock-wave system of the transonic rotors, which exhibits stronger shocks at higher spools speeds. This consequently results in more passage flow losses, especially near the vortex ingestion locations.

- Various flow descriptors were developed to generate a viable correlation methodology for the inlet-engine system compatibility. The SI_{abs}, and the $\Delta CSKE$ flow descriptors were found to be most suitable for the two types of swirl patterns studied. These two flow descriptors can take into account most of the pure bulk, and the vortex ingestion flow-features. The ΔPR, and the ΔPRS were used as the performance parameters, and were correlated against the flow descriptors. This is the first in-detail publication that show swirl descriptors correlations with the changes in the compression system, and also, for more than one type of the swirl distortion. Various swirl descriptors have been proposed in the past[70,71] but never before a full inlet-engine compatibility assessment have been published on specific compression systems.

- Most of the correlations obtained showed good second order polynomial trends, taking into account the rotor's rotational speed. These were also compared with a different rotor geometry. The combined correlation analyses showed that the sensitivity of rotor to the ingestion of a single vortex is more than the other types of distorted patterns. In general, the viability of the proposed correlation methodology is promising, and most of the future work is pointing towards this direction.

7.0.2 Recommendations for future work

As it happens with every research course, not all the questions can be answered by its end. Unavoidably, the following are some of the author suggestions in different research areas for future work.

- The boundary condition (BC) methodology for the vortex ingestion cases have some assumptions. For example, a value of an excess axial velcoity was assumed, and was used for all the different vortex simulations. However, from previous work both the excess[16] and the deficit of the axial velocity[25] have been reported. Thus, the BC's of total pressure, and the axial velocity can be developed further.

- The descriptor correlation database is based on the RANS calculations performed in the study. The author would recommend few URANS test-cases to compare the two approaches, especially near stability limit of the rotor configurations. As, observed during the instability URANS simulations that the unsteady effects play a vital role for the instability inception. Thus, to develop the credibility of the proposed correlation methodologies, this can be considered as one of the vital future task in the research. Also, analyzing the changes in compressor efficiency with the flow descriptors correlations will shed more light into the internal losses due to swirl distortion.

- Also, only the first Stage 67 of the two sage fan has been simulated. Moreover, the mesh size of the stator was limited due to the available computational resources. Therefore, a further improvement in mesh count of the stator, and also the inclusion of the second stage is recommended. This will allow the complete one compressor unit (i.e. the complete fan Stage 67 (LPC)) to be analysed under the influence of swirl distortion. It will also help in understanding the swirl distortion propagation across the different rotor stages, and will assist in determining the transportation distortion index. This might help in improving the proposed flow descriptor correlation methodology for the swirl distortion.

- Only the co-rotating vortex ingestion database for flow descriptor correlations has been utilized. This was due to lack in number of simulations performed under the influence of counter-rotating vortex. In order to respect the time-scales of the research programme, this aspect had to be left out. To have a comprehensive methodology, it is still necessary to per-

form the counter-rotating vortex simulations and include the outcome in the generated correlation database. This might shed some new information regarding the swirling flows as the counter-rotating cases which were performed showed the highest signs in terms of system instabilities.

- In terms of the flow descriptor definitions, the combined effect of swirl and total-pressure distortion on turbo-machinery still needs to be addressed. In the past[70], the swirl distortion problem have been tackled using only the swirl components of the incoming flow. However, from the study of vortex ingestions, it has been found that the total-pressure distortion within the vortex core region can also have some notable adverse effects on the stability of compression systems. Thus, the combination of the two show more promising future for the tightly-wound vortex inlet-engine compatibility assessments.

- Some interesting future perspective in the analytical tools for the use in assessing the non-uniform inlet flows in turbo-machinery is emerging. These include the parallel compressor theory that has been used in the past for only pure bulk analyses[20]. Due to hefty costs involved for the full inlet-engine experiments under the influence of swirl flow distortion, the combination of both the analytical and the numericals tools show more promise in addressing swirl distortion problem in the future.

References

[1] Adamczyk, J., M. Celestina, and E. Greitzer (1993). The role of tip clearance in high-speed fan stall. *Journal of turbomachinery Vol. 115*(No. 1), pp. 28–39.

[2] Ameri, A. (2009, January). Nasa rotor 37 cfd code validation glenn-ht code. *AIAA 47th AIAA Aerospace sciences meeting Orlando, Florida Vol. 1060*.

[3] Anderson, J. D. (1995). *Computational fluid dynamics*, Volume 206. McGraw-Hill New York.

[4] Anderson, J. D. (2007). *Fundamentals of Aerodynamics* (4th ed ed.). New York: McGraw-Hill.

[5] ANSYS, I. (2010). Ansys-cfx solver theory guide. *ANSYS CFX Release Vol. 11*, pp. 69–118.

[6] Arima, T., T. Sonoda, M. Shirotori, A. Tamura, and K. Kikuchi (1999). A numerical investigation of transonic axial compressor rotor flow using a low-reynolds-number k-epsilon turbulence model. *Journal of turbomachinery Vol. 121*, pp. 44–58.

[7] Bellancourt, L. (2010). Engine integration aerodynamics vortex ingestion investigation. Master's thesis, Cranfield Univesity.

[8] Bhagwat, M. J. and J. G. Leishman (2002). Generalized viscous vortex model for application to free-vortex wake and aeroacoustic calculations. In *Anual Forum Proceedings of Amercian Helicopter Society*, Volume 58, pp. 2042–2057.

[9] Biollo, R. and E. Benini (2009). Shock/boundary-layer/tip-clearance interaction in a transonic rotor blade. *Journal of Propulsion and Power Vol. 25*(No. 3), pp. 668–677.

[10] Bouldin, B. and Y. Sheoran (2007). Impact of complex swirl patterns on compressor performance and operability using parallel compressor analysis. In *proceedings of International Association of Airbreathing Engines ISABE*, Volume 1140.

[11] Brix, S., G. Neuwerth, and D. Jacob (2000). The inlet vortex system of jet engines operating near the ground. *AIAA Journal*, pp. 75–85.

[12] Cailler, M. (2013). Personal communication.

[13] Calahan, G. M. and A. H. Stenning (1971). Attenuation of inlet flow distortion upstream of axial flow compressors. *Journal of Aircraft Vol. 8*(No. 4), pp. 227–233.

[14] Castaneda, J., A. Mehdi, D. di Cugno, and V.Pachidis (2011). A preliminary numerical cfd analysis of transonic compressor rotors when subjected to inlet swirl distortion. In *ASME Turbo Expo proceedings*.

[15] Chima, R. (1996). Calculation of tip clearance effects in a transonic compressor rotor. Technical report, NASA Glenn Research Center.

[16] Chow, J. S., G. G. Zilliac, and P. Bradshaw (1997). Mean and turbulence measurements in the near field of a wingtip vortex. *AIAA Journal Vol. 35*(No. 10), pp. 1561–1567.

[17] Cousin, W. (2003). Inlet distortion testing and analysis of a high-bypass ratio turbofan engine the f119-pw-100 engine. In *proceedings of International Association of Airbreathing Engines ISABE*.

[18] Cousin, W. and M. Davis (June 2011). Evaluating complex inlet distortion with a parallel compressor model: Part 1 concepts, theory, extensions, and limitations. In *in proceedings of ASME Turbo Expo*.

[19] Cungo, D. (2013). *Tightly-Wound Vortex and Self-Generated Intake Distortion Effects on Turbomachinery Performance*. Ph. D. thesis, Cranfield University.

[20] Davis, M., D. Beale, K. Boyer, and D. O'Dowd (2006, December). An example for integrated gas turbine engine testing and analysis using modeling and simulation. In *proceedings of ITEA*, Volume 10.

[21] Davis, M. W. and D. S. Kidman (2010). Prediction and analysis of inlet pressure and temperature distortion on engine operability from a recent t-38 flight test program. In *proceedings of ASME Turbo Expo, Glasgow*.

[22] Day, I. (1993). Stall inception in axial flow compressors. *ASME Journal Turbo-machinery Vol. 115*, pp. 1–9.

[23] Day, I. and C. Freeman (1994). The unstable behavior of low and high speed compressors. *ASME Journal of Turbo-machinery Vol. 116*, pp. 194–201.

[24] Denton, J. (1997). Lessons from rotor 37. *Journal of Thermal Science Vol. 6*(No. 1), pp. 1–13.

[25] Devenport, W. J., M. C. Rife, S. I. Liapis, and G. J. Follin (1996). The structure and development of a wing-tip vortex. *Journal of Fluid Mechanics Vol. 312*(No. 67), pp. 106.

[26] Dunham, J. (1998). Cfd validation for propulsion system components. agard advisory report (355). Technical report, North Atlantic Treaty Advisory Group for Aerospace Research, Development Propulsion, and Energetics.

[27] Edwin, J. G. and B. Willis (1974). Summary of recent investigations of inlet flow distortion effect on engine stability. Technical Report NASA TM X- 71505, NASA TECHNICAL MEMORANDUM.

[28] Fidalgo, V. J., C. A. Hall, and Y. Colin (2010). A study of fan-distortion interaction within the nasa rotor 67 transonic stage. In *proceedings of ASME Turbo Expo*, Number GT2010-22914.

[29] Gelder, F., F. Schmidt, L. Suder, and D. Hathaway (1989). Design and performance of controlled-diffusion stator compared with original double-circular-arc stator. Technical report, Lewis research center, NASA.

[30] Goldsmith, E. L. and J. M. Seddon (Sep 1993). *Practical Intake Aerodynamic Design* (ISBN-10: 0632031034 ed.).

[31] Gong, Y. (1999, February). *A computational model for rotating stall and inlet distortions in multistage compressors*. Ph. D. thesis, Massachusetts Institute of Technology (MIT).

[32] Gorrel, S. E., J. Yao, and A. R. Wadia (2008). High fidelity urans analysis of swirl generation and fan response to inlet distortion. In *proceedings of Joint AIAA/ASME/SAE/ASEE Propulsion Conference and Exhibit, 44rd, Hartford*.

[33] Gorrell, S. E., J. Yao, and A. R. Wadia (2008). High fidelity urans analysis of swirl generation and fan response to inlet distortion. *AIAA Journal Vol. 4985*.

[34] Goutines, M. and H. Joubert (1987). Compatibilit entre d'air-moteur: impact des mthodes thoriques et exprimentales. In *AGARD conference proceedings*, pp. 400–413.

[35] Green, S. (1995). *Fuid Vortices*. Springer.

[36] Hah, C. (2009). Large eddy simulation of transonic flow field in nasa rotor 37. Technical report, NASA Glenn Research Center.

[37] Hah, C., D. C. Rabe, T. J. Sullivan, and A. R. Wadia (1998a). Effects of inlet distortion on the flow field in a transonic compressor rotor. *Journal of turbomachinery Vol. 120*.

[38] Hah, C., D. C. Rabe, T. J. Sullivan, and A. R. Wadia (1998b). Effects of inlet flow distortion on the flow field in a transonic compressor rotor. *Journal of Turbomachinery Vol. 120*, pp. 233–246.

[39] Hale, A., M. Davis, and J. Sirbaugh (2006, July). A numerical simulation capability for analysis of aircraft inlet-engine compatibility. *Journal of turbomachinery Vol. 128*, pp. 473–480.

[40] Hercock, R. G. Effects of intake flow distortion on engine stability. Technical report, Installation Aerodynamics group, Rolls-Royce Limited, Bristol.

[41] Johns, C. J. (2002). The aircraft engine inlet vortex problem. *AIAA Journal AIAA's Aircraft Technology, Integration, and Operations (ATIO), California*(No. 5894).

[42] Kampungkai (2012). A330-300-egr engine ground run - http://kampungkai.blogspot.co.uk/.

[43] Kidman, D. S., P. V. Reagan, and D. J. Malloy. Comparison of inlet compatibility results from subscale wind tunnel and full-scale flight tests of the f/a-22 aircraft with the f119-pw-100 engine. In *proceedings of International Association of Airbreathing Engines ISABE*, Volume 1169.

[44] Kurzke, J. (2008). Effects of inlet flow distortion on the performance of aircraft gas turbines. *Journal of Engineering for Gas Turbines and Power Vol. 130*(No. 4).

[45] Launder, B. E. and D. Spalding (1974). The numerical computation of turbulent flows. *Computer Methods in Applied Mechanics and Engineering Vol. 3*(No. 2), pp. 269–289.

[46] Leishman, J. G. (2000). *Principles of Helicopter Aerodynamics*. Cambridge, England: Cambridge University Press.

[47] Licthfus, J. and H. Starken (1976). Supersonic cascae flow. Technical report, Institut fiir Luftstrahlantriebc, Porz-Wahn, Dcutschland.

[48] Longley, J. P. and E. M. Greitzer (1992). Inlet distortion effects in aircraft propulsion system integration. *AGARD Lecture Series 183, June*.

[49] Longley, J. P. and T. P. Hynes (1990). Stability of flow through multistage axial compressors. *Journal of turbomachinery Vol. 112*, pp. 126–132.

[50] Lotter, K. W. and J. Jarg (1982). The effect of intake flow disturbances on apu compressor blade high cycle fatigue in the airbus a300. *ICAS Journal Vol. 82*, pp. 1072–1081.

[51] Ludwig, G. (October 1989). Tomahawk engine/inlet compatibility study for f107-wr-400/402 engines. Technical Report 5003-2025, Williams International Report.

[52] Macmunus, D. G. (2012). Personal communication.

[53] McLelland, G., D. di Cugno, D. MacManus, and V. Pachidis (2012, June). Boundary conditions for vortex cfd simulations. In *proceedings of ASME Turbo Expo, Copenhagen, Denmark*, Number GT2012-68718.

[54] Mentor, F. R. (1994). Two-equation eddy-viscosity turbulence models for engineering applications. *AIAA Journal Vol. 32*(No. 8), pp. 15981605.

[55] Mitchell, G. A. (1975). Effect of inlet ingestion of a wing tip vortex on compressor face flow and turbojet stall margin. Technical Report Nasa TM X-3246, NASA Lewis Research Center, Ohio.

[56] Motycka, D. L. (1976, April). Ground vortex-limit to engine/reverser operation. *ASME Journal, pages=pp. 258-264*.

[57] Motycka, D. L. and W. A. Walter (1975). An experimental investigation of ground vortex formation during reverse engine operation. *AIAA Journal Vol. 1245*, pp. 4.

[58] Motycka, D. L., W. A. Walter, and G. L. Muller (1973). An analytical and experimental study of inlet ground vortices. *AIAA Journal Vol. 1313*, pp. 4.

[59] Murphy, J. (2008). *Intake Ground Vortex Aerodynamics*. Ph. D. thesis, Cranfield University.

[60] Murphy, J., D. G. MacManus, and M. D. Taylor (2007). A quantitative study of inlet ground vortex. In *proceedings of International Association of Airbreathing Engines ISABE*, Volume 1209.

[61] Niazi, S. (2000). *Numerical simulation of rotating stall and surge alleviation in axial compressors*. Ph. D. thesis, Georgia Institute of Technology.

[62] Pardo, A. C. (2013). Effect of inlet swirl distortion on turbomachinery. Master's thesis, Cranfield Univesity.

[63] Pazur, W. and L. Fottner (1991). Influence of inlet swirl distortions on the performance of a jet propulsion two-stage axial compressor. *Journal of Turbomachinery Vol. 113*(No. 2), 233–240.

[64] Reid, C. (1969). The response of axial flow compressors to intake flow distortion. In *in proceedings of ASME expo*.

[65] Reid, L. and D. Moore (1978). Design and overall performance of four highly loaded, high-speed inlet stages for an advanced high-pressure-ratio core compressor. Technical report, Lewis research center, NASA.

[66] Ruffino, N. (2011). Phase transition thermodynamics-http://theaviationist.com/tag/thermodynamics/.urjjnr3krsg.

[67] SAE (1978). Gas turbine engine inlet flow distortion guidelines. Technical Report ARP1420b, S16 Turbine Engine Inlet Distortion Committee.

[68] SAE (1983). Inlet total-pressure-distortion considerations for gas-turbine engines. Technical Report AIR 1419, S16 Turbine Engine Inlet Distortion Committee.

[69] SAE (1991). A current assessment of the inlet/engine temperature distortion problem. Technical Report AIR 5687, S16 Turbine Engine Inlet Distortion Committee.

[70] SAE (2007). A methodology for assessing inlet swirl distortion. Technical Report AIR5686, S16 Turbine Engine Inlet Distortion Committee.

[71] Sheoran, Y. and B. Bouldin (2002). Inlet flow angularity descriptors proposed for use with gas turbine engines. In *proceedings of Society of Automotive Engineer (SAE) Technical Conference*, Volume 2919.

[72] Sheoran, Y., B. Bouldin, and P. Krishnan (2012). Compressor performance and operability in swirl distortion. *Journal of turbomachinery Vol. 134* (No. 4).

[73] Sheoran, Y., B. Bouldin, and P. M. Krishnan (2009, June). Advancements in the design of an adaptable swirl distortion generator for testing gas turbine engines. *ASME Journal of Turbomachinery*, pp. 23–30.

[74] Sheoran, Y., M. Davis, and D. Beale (2008). Integrated test and evaluation techniques as applied to an inlet swirl investigation using the f109 gas turbine engine. In *in proceedings of ASME Turbo expo*, Number GT2008-50657.

[75] Simpson, A. and J. Longley (2007). An experimental study of the inception of rotating stall in a single stage low-speed axial compressor. In *proceedings of ASME Turbo Expo, Montreal, Canada*.

[76] Spakovszky, Z. and C. Roduner (2007). Spike and modal stall inception in an advanced turbocharger centrifugal compressor. In *proceedings of ASME Turbo Expo, Montreal, Canada*.

[77] Spector, D. (2012). Commercial aircraft of the future will be unbelievably quiet and fuel-efficient webpage: Businessinsider.com.

[78] Stevens, C. H., E. D. Spong, and M. S. Hammock (June 1987). F-15 inlet/engine test techniques and distortion methodologies studies, vol i technical discussion. Technical Report NASA CR-144866.

[79] Stocks, C. P. and N. C. Bissinger (May 1981). The design and development of the tornado engine air intake. Technical Report Paper 10, AGARD CP-301.

[80] Strazisar, J., R. Wood, D. Hathaway, and L. Suder (1989). Laser anemometer measurements in a transonci axial-flow fan rotor. Technical Report Technical paper 2879, Lewis research center, NASA.

[81] Tan, C., I. Day, S. Morris, and A. Wadia (2010). Spike-type compressor stall inception, detection, and control. *Annual Review of Fluid Mechanics Journal Vol. 42*, pp. 275–300.

[82] Vo, H., J. Cameron, and S. Morris (2008). Control of short length-scale rotating stall inception on a high-speed axial compressor with plasma actuation. In *proceedings of ASME Turbo Expo, Berlin, Germany.*

[83] Vo, H., C. Tan, and M. Greitzer (2008b). Criteria for spike initiated rotating stall. *ASME Jouranl of Turbo-machinery Vol. 130*, pp. 1–8.

[84] Williams, D. (2010). Airframe engine integration lectures notes; cranfield university thermal power course), institution=Cranfield University. Technical report.

[85] Wu, J. Z., H. Ma, and M. D. Zhou (2006). *Vorticity and Vortex Dynamics.* Heidlberg, Germany: Springer.

[86] Wu, Y. L., E. Y. K. Ng, and K. Wong (2007). Numerical study of the swirl flow in f-5e intake with subsonic speeds. *Elsevier Journal Mathematical and computer modelling, Vol. 48*, pp. 448–469.

[87] Yao, J., S. E. Gorrel, and A. R. Wadia (2007). A time-accurate cfd analysis of inlet distortion induced swirl in multistage fans. In *proceedings of Joint AIAA/ASME/SAE/ASEE Propulsion Conference and Exhibit, 43rd, Cincinatti.*

[88] Zhang, Y., X. Lu, W. Chu, and J. Zhu (2010). Numerical investigation of the unsteady tip leakage flow and rotating stall inception in a transonic compressor. *Journal of Thermal Science Vol. 19*(No. 4), pp. 310–317.

Appendix A

Ground vortex

Ground vortex is a type of a tightly-wound vortex that has been the starting case study in this work. The formation mechanism and methods for characterizing of a vortex for modelling purposes is explained in this section.

Figure A.1: Ground vortex ingestion during:**a)** Airbus A330-300 EGR engine maintenance at high power setting ©Kampungkai[42] **b)** Eurofighter Typhoon taxiing ©N.Ruffino[66]

A.1 Criteria and formation mechanism

Figure A.1 show two examples of ground vortex ingestion in both civil and military aircraft. The criteria for a vortex to be ingested from the ground surface depends on number of factors, which include engine power setting, ambient conditions, ground clearance and the engine diameter. Following two key non-

dimensional terms have been recognized necessary for understanding the formation of ground vortices.

- U_{in}/U_{∞}, the velocity ratio is a measure of the streamtube contraction ratio, assuming the flow is incompressible (Eq.A.1).

- H/D_i, the non-dimensional height-to-diameter is the ratio of engine height (H) from ground surface and the highlight diameter (D_i) of the intake.

$$\begin{cases} \rho_{\infty} A_{\infty} U_{\infty} = \rho_{in} A_{in} U_{in} \\ \frac{A_{\infty}}{A_{in}} = \frac{U_{in}}{U_{\infty}} \end{cases} \tag{A.1}$$

There are some key elements necessary for any vortex formation. This includes the identification of stagnation point, the source of vorticity around the stagnation line and the presence of engine airframe and gas turbine itself. However, the velocity contraction ratio U_{in}/U_{∞} and the height-to-diameter ratio H/D_i can used as an indicator of the capture streamtube size and interaction with ground clearance of the intake as shown in Figure A.2.

Thus, high velocity ratios and low non-dimensional heights will lead to a strong interaction of the streamtube with the ground and therefore vortex formation. Many researchers have use the dependency of these two parameters on the formation of ground vortices and proposed correlations through vortex/no vortex maps. These are currently the established industrial design method to avoid the formation of vortices for a particular aircraft. As shown in Figure A.3, the chart relate values of the non-dimensional height with the velocity ratio for which the vortex formation occurs or not.

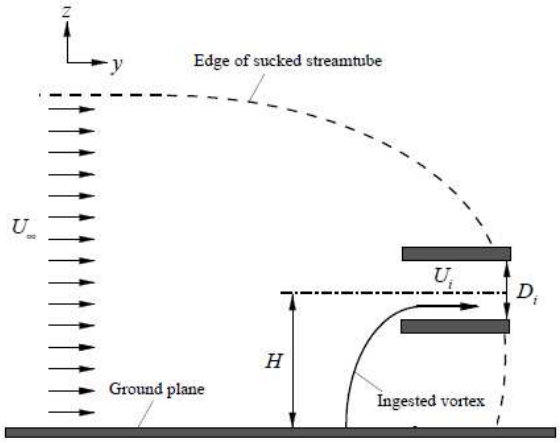

Figure A.2: Illustration of the sucked streamtube interaction with the ground plane[59].

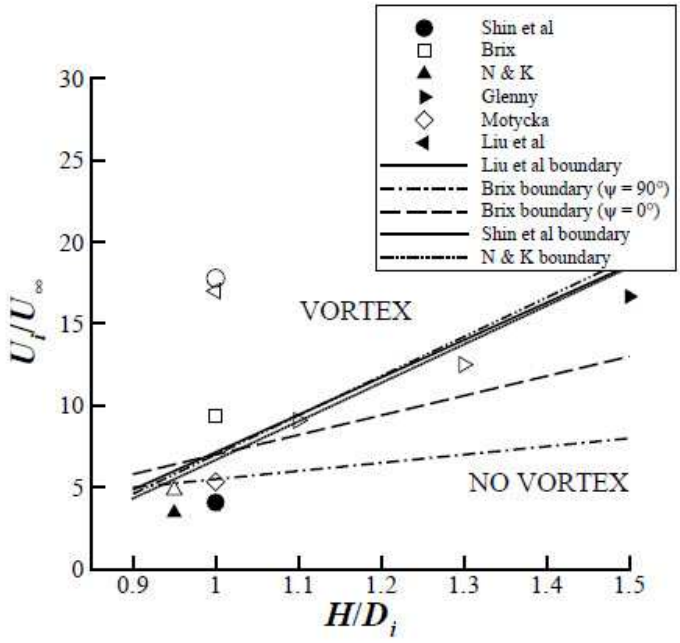

Figure A.3: Correlation of velocity ratio and non-dimensional height showing a region of vortex formation and no-vortex formation (filled symbols represents a data point in which no vortex is seen, and unfilled symbols are points in which vortices are observed)[11,59].

A complete understanding of the vortex formation mechanisms are yet to be fully understood and several classifications of these exists in the literature[11,41,59].

However, there are two basic flow mechanisms[60] that have been reduced for ground vortex formation depending on the wind direction. The first one is concerned to headwind and quiescent(no-wind) conditions. The latter focuses on the crosswind configuration.

1. **Headwind and quiescent mechanism**

   Headwind mechanism is applicable to an intake with its axis parallel to the flow direction. The basis of vortex formation lies at certain U_{in}/U_{∞} due to magnification of the ambient vorticity in the upstream boundary layer. The velocity gradient inside the boundary layer acts as a source of vorticity and thereby, the creation of vortex lines. Therefore, engine intake system work as a vacuum pump, and along with sucking the capture streamtube these vortex lines are also ingested at the inlet. One of the distinct features of these vortex lines is the conservation of the angular momentum ($m\omega r^2$). As the vortex lines are stretched before entering the intake, a higher angular velocity is achieved. Figure A.4 below illustrates the vorticity formation and the ingestion of two contra-rotating vortex lines for this particular headwind case. But the rotation and number of vortices seen at the fan face depends on the direction, deformation and convection of the ambient vortex lines associated with the dominant vorticity source[59].

   In quiescent(no wind) conditions, the ingestion of airflow from all directions is the main source of vorticity in the surrounding flowfield. In particular, the flow coming from underneath the engine has to be turned 90 degrees before being sucked. This induced vorticity is the source for the vortex and by definition this formation mechanism requires no ambient vorticity. Brix et al.[11] reported this domination of the flow behind and between the intake and the ground. Figure A.5 illustrates the consequence of this dominant flow as it stretches and deforms the associated vortex lines. This scenario is very similar to the headwind mode, the exception been the opposite direction of the vorticity source, and the fact that it is a direct consequence of the intake induced flowfield rather than the approaching flow. Therefore,

the vortices formed at the fan face in quiescent mode rotate in the opposite direction to that formed under headwind conditions but have similar formation mechanisms.

2. **Crosswind mechanism**

The vortex formation mechanism in crosswind mode is slightly more complex than the former. In this case not only a ground vortex is formed but also a trailing vortex appears at the leeward lip of the inlet (see Figure A.6). Velocity gradients in the upstream boundary layer are again the main vorticity source but in this case the gradients are associated with the yaw angle introduced by the crosswind's tangential velocity component. To note that as the yaw angle diminishes, the crosswind mechanism will be partially offset by the headwind up to a certain value below which the headwind mechanism becomes dominant[60]. Also from previous studies it is found that as the velocity ratio U_{in}/U_{∞} diminishes the vortex strength increases up to a maximum value. However, a further reduction of the velocity ratio will result in a sudden drop of the vortex circulation.

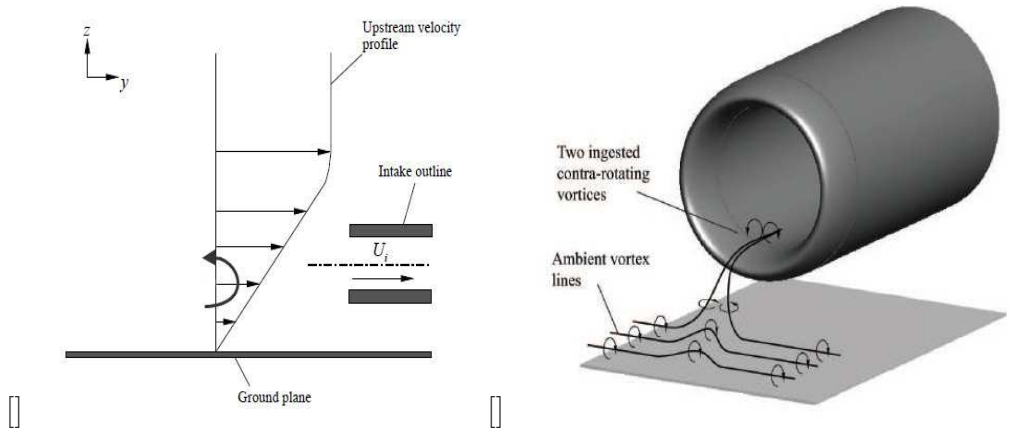

Figure A.4: First mechanism of vortex formation[59]:**a)** Upstream atmospheric boundary layer **b)** Generation and ingestion of vortex lines

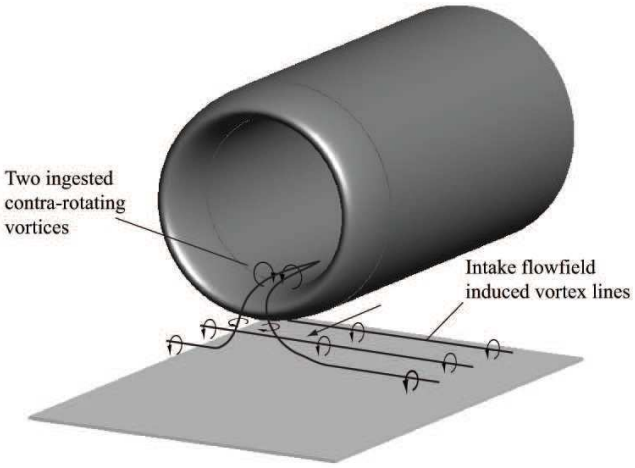

Figure A.5: Vortex formation and ingestion under quiescent(no wind) conditions[59]

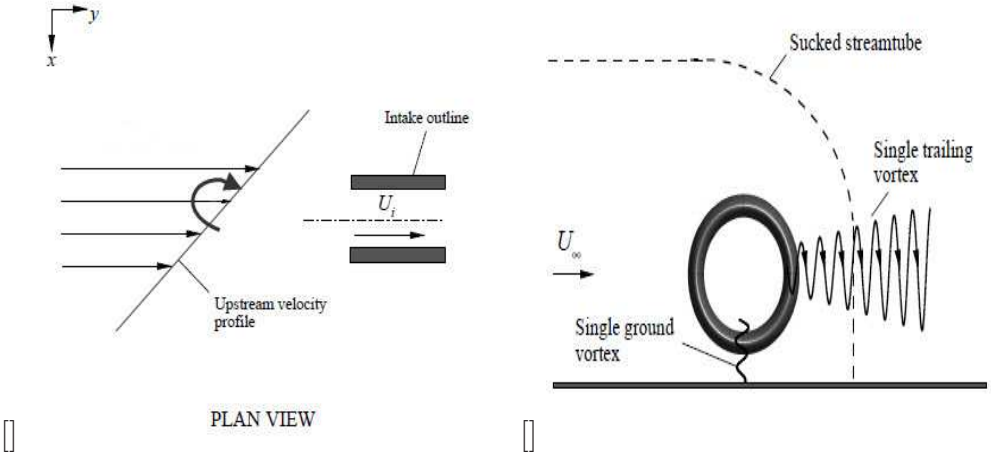

Figure A.6: Crosswind mechanism of vortex formation[59]:**a)** Upstream atmospheric velocity profile **b)** Generation and ingestion of vortex lines

Appendix B

Vortex Models

Many vortex model definitions can be found in the literature[4,35,46,85], developed for different types of vortex flow fields. For the purpose of this study, the vortex models relevant to tightly-wound vortices that may effect the aero-propulsion systems are discussed.

1. **Lamb-Oseen vortex**

   Oseen (1912) and Lamb (1932) investigated a two-dimensional vortex line which decays due to viscosity. They used the vorticity equation (Equation B.1) for an incompressible Newtonian fluid assuming constant viscosity and with only potential body forces.

$$\frac{D\vec{\omega}}{Dt} = (\vec{\omega}.\nabla)\vec{u} + v\nabla^2\vec{\omega} \tag{B.1}$$

   For a two dimensional vortex field, this vorticity equation can lead to the following tangential velocity and vorticity distributions. From Figure B.1, the motion of the vortex core resembles a solid body rotation, whereas the velocity distributions away from core are substantially unaffected. However, there are certain limitations to the applicability of this model in real viscous flow scenarios ,as discussed by Green[35].

$$\omega_z(r,t) = \frac{\Gamma_o}{4\pi vt} exp(\frac{-r^2}{4vt}) \tag{B.2}$$

$$V_\theta(r,t) = \frac{\Gamma_o}{2\pi r}[1 - exp(\frac{-r^2}{4vt})] \tag{B.3}$$

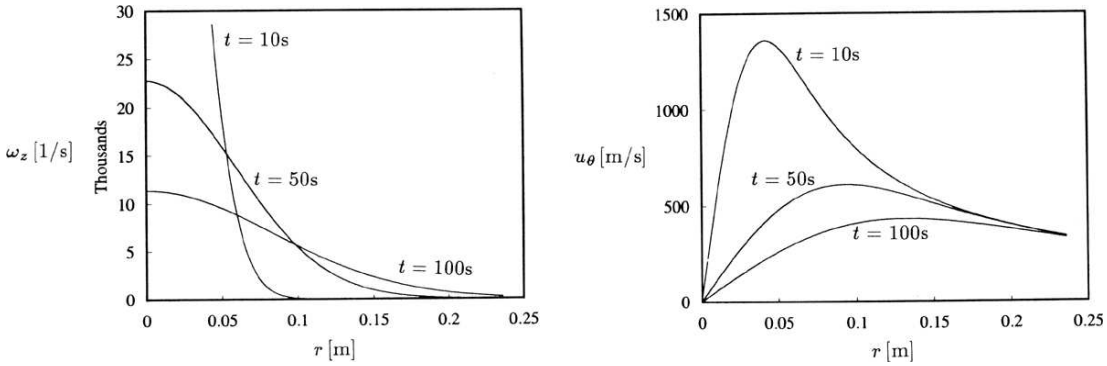

Figure B.1: Vorticty (left) and tangential velocity (right) distribution of the Lamb Oseen model[35]

2. **Rankine vortex**

The Rankine model describes a vortex flow field through the combination of a solid body rotation in the vortex core, and an irrotational vortex in the outer region. The vortex dynamics are described in terms of the tangential velocity V_θ, and the axial velocity V_a components. The radial velocity V_r component is small, and can be neglected when describing the vortex in the local frame. The tangential velocity distribution is a function of radius as shown in Equation B.4. Also, the radial momentum EquationB.5, can be used to derive an expression for the pressure distribution (Equation B.5), assuming an incompressible fluid. An example of the distribution of the tangential velocity using Rankine vortex model is shown in Figure B.2.

$$V_\theta = \begin{cases} \frac{\Gamma}{2\pi r_c^2} r & \text{if } r \leq r_c \\ \frac{\Gamma}{2\pi r} & \text{if } r > r_c \end{cases} \tag{B.4}$$

$$\frac{\delta p}{\delta r} = \rho \frac{V_\theta^2}{r} \tag{B.5}$$

3. **Vatistas vortex**

A newer model as compared with others, Vatistas (1991) proposed his vortex model taking into account the viscous effects of the fluid. This is the vortex model that have been used for the research study. It is based on the concept that in real flows the shearing forces generated by the fluid viscosity will act to diffuse the vorticity. So, the discontinuity in the tangential velocity as observed in Rankine vortex (Figure B.2) at the transition point from solid body rotation to irrotational vortex should not exist in real viscous flows.

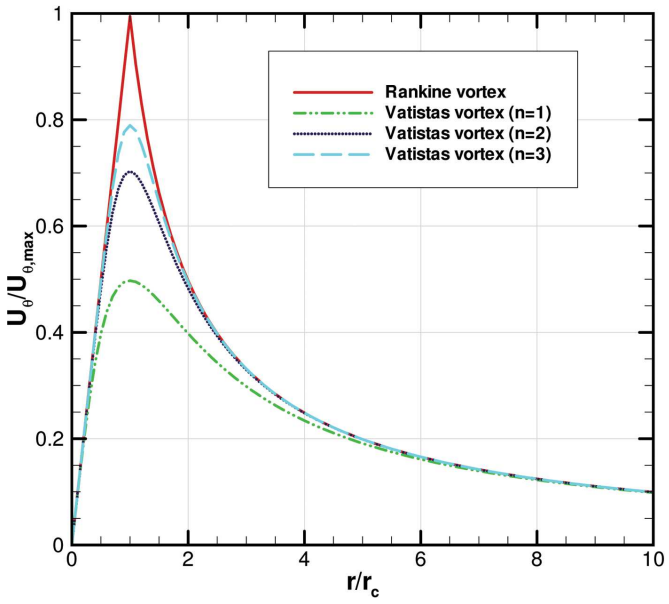

Figure B.2: Tangential velocity distributions of Rankine and Vatistas vortex models

Figure B.2 illustrates the tangential velocity distributions for the Vatistas model, when using three different Vatistas shape factors n. The shape factor n is an integer that has been developed by Vatistas, and using Biot-Stavart law, an expression for the tangential velocity V_θ can be derived as shown in Equation B.6. Reader might notice the expression resemblance to the tangential velocity of Rankine model (Equation B.4), whereby n tend towards infinity.

$$V_\theta(r) = \frac{\Gamma}{2\pi r_c^2} \left\{ \frac{r}{(1 + (\frac{r}{r_c})^{2n})^{1/n}} \right\} \tag{B.6}$$

The value of n can be determined experimentally and varies for different applications. Murphy[59] found in his work, the value of $n = 1$ is the most suitable for ground vortices, which is the datum case study of the current work, while $n = 2$ provides a good approximation for tip vortices (see Figure B.3).

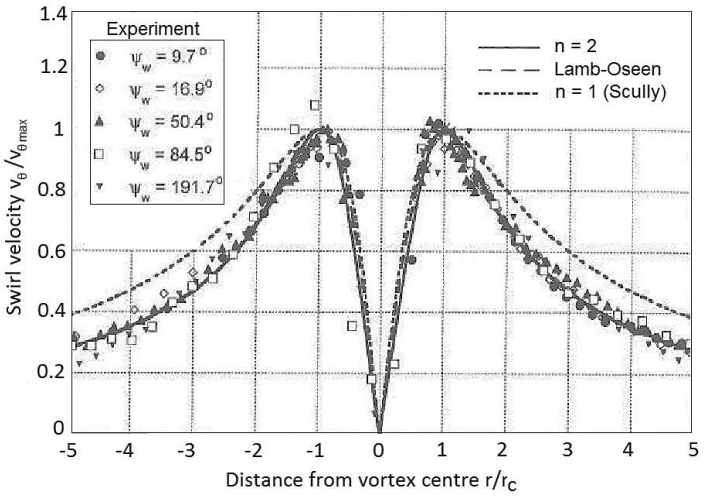

Figure B.3: Comparison of vortex models with experimental tip vortex V_θ measurements[46]

By implementing the assumption of the Vatistas tangential velocity model in the following Equation B.7 derived by Bhagwat and Leishman[8], the following axial V_z (Equation B.8), and the radial V_r (Equation B.9) velocity components of the vortex fluid have been proposed.

$$V_r \frac{\delta V_\theta}{\delta r} + V_z \frac{\delta V_\theta}{\delta z} + V_r \frac{V_\theta}{r} = 0 \tag{B.7}$$

$$V_r(r) = -\frac{Ar}{2z^2}\left\{1 - \frac{r^2}{(r_c^{2n} + r^{2n})^{1/n}}\right\} \tag{B.8}$$

$$V_z(r) = -\frac{A}{z}\left\{1 - \frac{r^2}{(r_c^{2n} + r^{2n})^{1/n}}\right\} \tag{B.9}$$

Where, A is a constant and z is the axial distance downstream from a selected position (e.g. an engine inlet or a wing tip trailing edge). The

contribution of radial velocity V_r is usually of a lower order of magnitude as compared with other velocity components. On other hand, axial velocity is either modelled with an excess or a deficit at the vortex centre. Both possibilities can be found in the literature, excesses up to 77%[16], and deficits of 15%[25] have been reported for wing tip vortices.

Appendix C

Vortex circulation prediction tool

Murphy[59] carried out sub-scale intake experimental work on ground vortex ingestion during his doctoral research. One of his key research outcome was the development of an empirical vortex circulation model in order to predict the swirl patterns produced by various ground vortex ingestion cases. Wind tunnel tests of a $1/30^{th}$ scale model intake were carried out to investigate the conditions at which the previously mentioned three types of ground vortex are formed. SPIV (Stereoscopic Particle Image Velocimetry) and total pressure measurements enabled a thorough investigation of the flow field and the development of a very useful tool to describe the vortex characteristic at the entrance of an intake.

Thus, the possibility of imposing as a boundary condition the vortex structure at the inlet of a compression system can be very attractive. This allows for CFD purposes modelling only the turbomachinery components and saves considerable computational time for not having to simulate the ground and the intake domains as well. In this way, using Murphy[59] empirical model to predict the vortex strength depending on ambient conditions and the ground clearance, a methodology was established. Apart from the vortex circulation, the swirl distribution also has to be ascertained and for this purpose various vortex models are available such as the Vatistas' vortex model.

Vatistas' vortex model have proven especially for ground vortices of being the one which best fits the required pattern as compared with experimental measure-

ments. However, there are some additional terms such as shape factor (n) and vortex core size (r_c) which also needs to be addressed for full swirl distribution of a ground vortex (see Eq.B.6-B.9). The r_c has found to be roughly 6% of the intake inner diameter, D_i and the Vatistas shape factor, n, is on average 1 for ground vortices[60]. This is explained in more detail as a part of inlet boundary conditions implementation in next section.

The prediction of a datum vortex circulation is performed for a fixed U_{in}/U_∞ and H/D_i. The method for headwind or/and quiescent conditions are very similar to the cross-wind configuration and the cross-wind case performed is actually the extended version of the former. Just to clarify that the findings in which the method is based on will not be explained, but which the inputs are and how it works will be shown by an illustration below. A detailed explanation of the experimental data from which the method was built can be found in[59].

As it was aforementioned at the beginning of this section, the key parameters for defining the features of a ground vortex are the velocity ratio U_{in}/U_∞ or U^* and the non-dimensional height H/D_i, and as expected these are the main inputs for this empirical model. The algorithm structure for the prediction of vortex circulation can be observed in Figure C.1.

From Figure C.1, U^*_{crit} stands for the velocity at which the vortex vanishes, having been related to the velocity at which the streamtube lifts from the ground and usually refer to as blow away conditions. This velocity can be found from mass continuity considerations. For the calculation of this velocity, the inlet Mach number M_i, the non-dimensional height $\frac{H}{D_l}$ and the ratio of the inlet diameter to the highlight diameter $\frac{D_l}{D_{in}}$ have to be known and then following expressions can be used to derive U^*_{crit}.

$$\rho^* = \frac{\rho_\infty}{\rho_{in}} = \left\{1 + \frac{\gamma - 1}{2} M_i^2\right\}^{1/(\gamma-1)} \tag{C.1}$$

$$U^*_{crit} = 4\rho^* \left(\frac{D_l}{D_{in}} \frac{H}{D_l} + \frac{D_l}{2D_{in}}\right)^2 \tag{C.2}$$

Once U^*_{crit} is known, an empirical expression relates the velocity at which the

circulation peaks, U^*_{max}, to U^*_{crit} by utilizing experimental results and is as follows:

$$U^*_R = \frac{U^*_{crit}}{U^*_{\max}} = 0.65 \tag{C.3}$$

Another empirical relationship associates the value of U^*_{max} and the corresponding maximum non-dimensional circulation Γ^*_{max} by:

$$\Gamma^*_{\max} = 0.83(U^*_{\max})^{-0.7} \tag{C.4}$$

Finally, in order to calculate the vortex strength for the velocity ratio U^* in question is computed via Eq.C.5, and then using Eq.C.6 the non-dimensional circulation Γ^* for the particular value of the inputs can be obtained.

$$U^{\sim} = \frac{U^*/U^*_{\max} - U^*_R}{1 - U^*_R} \tag{C.5}$$

$$\frac{\Gamma^*}{\Gamma^*_{\max}} = \frac{2^{1/k} U^{\sim}}{\left[1 + U^{\sim 2k}\right]^{1/k}} \tag{C.6}$$

The Γ^* can then be converted to dimensional circulation Γ by the following expression.

$$\Gamma^* = \frac{\Gamma}{U_{in} D_l} \tag{C.7}$$

As the reader may have inferred, there has been no input of the yaw angle in any of the formulations, therefore the previous method described upto the calculation of Γ can only be applied to a headwind condition. However, an extension to a crosswind configuration can be performed yet again by use of some more empirical relationships[59]. Firstly, the level of distortion $DC_{60}^{\psi=0}$ for a null yaw angle must be calculated from Eq.C.8. Once this is known and using Eq.C.9, the level of distortion for a yaw angle of 90 degrees $DC_{60}^{\psi=90}$ can also be obtained.

$$DC_{60}^{\psi=0} = 0.0567\Gamma^* + 0.0141 \tag{C.8}$$

$$DC_{60}^{\psi=90} = \left(-25.3\left(\frac{h}{D_l}\right) + 15.3\right) * DC_{60}^{\psi=0} \tag{C.9}$$

Finally, the correlation between the non-dimensional circulation Γ^* and the DC_{60} at 90 degrees as shown in Eq.C.10 can be used to calculate the Γ^* for a pure cross-wind condition. Further correlation exists (see Eq.C.11) to calculate Γ^* for cases with particular values of the yaw angle different from 90 degrees.

$$\Gamma^*_{\psi=90} = 1.11 DC_{60}^{\psi=90} + 0.0075 \tag{C.10}$$

$$\begin{cases} \varsigma = \frac{DC_{60}^{\psi} - DC_{60}^{\psi=0}}{DC_{60}^{\psi=90} - DC_{60}^{\psi=0}} = \sin^6\psi \\ \eta = \frac{\Gamma^*_{\psi} - \Gamma^*_{\psi=0}}{\Gamma^*_{\psi=90} - \Gamma^*_{\psi=0}} = \sin^3\psi \end{cases} \tag{C.11}$$

The methodology for subscribing vortices as a boundary condition for numerical simulations cannot only consider the value of circulation predicted from the above model and then utilizing a suitable vortex model to derive its swirl characteristics. But in fact some further inputs are still needed such as the direction and number of vortices generated for each vortex mechanism. In order to take into account the topology of the flow field for each vortex configuration, vortex visualizations were carried out by Brix et al.[11], Murphy et al.[60]. Some of the key features of these configurations are discussed below as it directly contributes to the type of swirl pattern imposed at the engine face.

- **Quiescent:** The swirl angle pattern is unsteady due to the complexity of the flow field, as the flow coming from far downstream interacts with the one travelling from far upstream. At first two counter rotating vortices are observed but as the time passes by a single vortex becomes dominant. Beyond this point, the flow gets locked in this mode.

- **Headwind:** In this configuration, two counter-rotating vortices of a higher strength than the former case are observed. Figure C.2 shows how the swirl pattern changes as the velocity ratio does and the particular direction of rotation of each mode.

- **Crosswind:** If the wind has a certain tangential velocity component (crosswind), the strength of the vortex formed can be three times higher than the previous cases. Furthermore, lip separation has also been observed which may increase the overall distortion level at the engine face. Nonetheless, the level of total pressure drop inside the vortex is more severe than the one associated with the flow separation[59]. A yaw angle of 90 degrees (pure crosswind) represents the most hazardous case forming a very strong single vortex. The circulation variation with the yaw angle can be fitted using a sin^3 trend. 90 degrees (pure crosswind) mode was chosen to be the maximum strength vortex case for the research.

- **Take-off and thrust reverse operation:** From the experimental observations[56,57], two counter-rotating vortices were reported for thrust reversal operation. The main source of vorticity came due to the deceleration of the aircraft and the reverse flow jets, which creates high strength tailwind. Although values of circulation were not reported for thrust reverse conditions, the levels of total pressure drop were compared to the ones provided for headwind mode[59]. Circulation values can be inferred to be slightly higher than in the case of headwind which may be due to the considerable level of tailwind during the deceleration of the aircraft.

  The take-off configuration can be seen as the opposite case to thrust reverse mode. Experimental work by Murphy[59] showed again two contra-rotating vortices having vorticity levels lower than in the case of headwind condition.

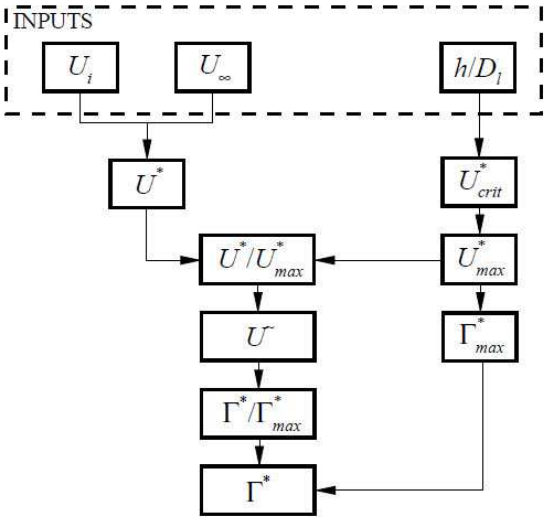

Figure C.1: Algorithm to calculate vortex circulation under headwind conditions[59]

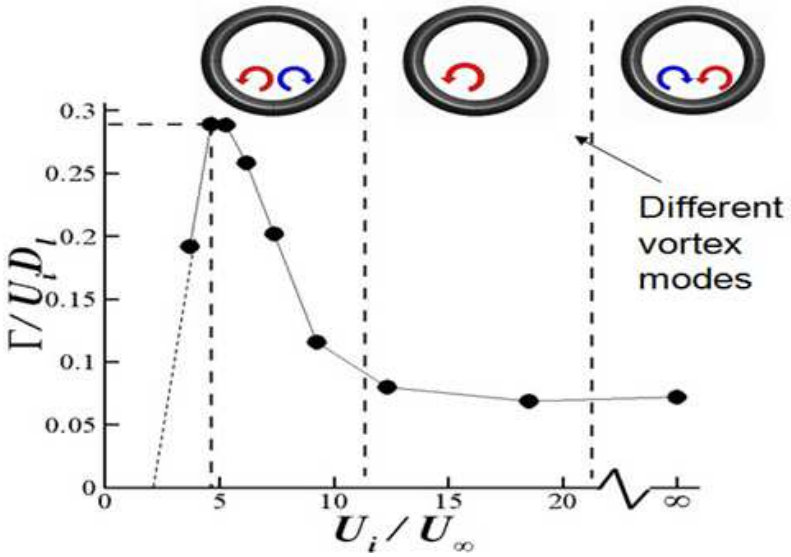

Figure C.2: Transition from quiescent to headwind conditions showing the vortex pattern[59]

Appendix D

Matrix of cases

Bulk swirl angles (degrees) @ 100% rot. speed						
Rotor 37(Configuration 2)- RANS	±5°					
Rotor 37(Configuration 2)- URANS	±5°					
Rotor 67(Configuration 1)- RANS	+2°	+4°	±5°	+6°	+8°	
Stage 67(Configuration 3)-RANS	±5°	±10°	±15°	±20°	±25°	±30°

Table D.1: Matrix of bulk swirl cases - Co rotating (+) and Counter rotating(-)

Case No.	Rot. speed	Γ $[m^2/s]$	Vortex core size, $\frac{r_c}{s}$	Direction	Span-wise ingestion location	No. vortices,N_v
1	90%	11	9%	Co	25%	1
2	90%	16	9%	Co	25%	1
3	90%	19	9%	Co	25%	1
4	90%	22	9%	Co	25%	1
5	90%	5	9%	Co	50%	1
6	90%	11	9%	Co	50%	1
7	90%	11	4.5%	Co	50%	1
8	90%	16	9%	Co	50%	1
9	90%	19	9%	Co	50%	1
10	90%	22	9%	Co	50%	1
11	90%	22	14%	Co	50%	1
12	90%	25	9%	Co	50%	1
13	90%	11	9%	Co	75%	1
14	90%	16	9%	Co	75%	1
15	90%	19	9%	Co	75%	1
13	90%	22	9%	Co	75%	1
14	100%	11	9%	Co	40%	1

15	100%	13	9%	Co	40%	1
16	100%	16	9%	Co	40%	1
17	100%	11	9%	Co	25%	1
18	100%	16	9%	Co	25%	1
19	100%	16	4.5%	Co	25%	1
20	100%	22	9%	Co	25%	1
21	100%	22	4.5%	Co	25%	1
22	100%	22	14%	Co	25%	1
23	100%	33	9%	Co	25%	1
24	100%	11	9%	Co	50%	1
25	100%	16	9%	Co	50%	1
26	100%	16	4.5%	Co	50%	1
27	100%	19	9%	Co	50%	1
28	100%	22	9%	Co	50%	1
29	100%	22	4.5%	Co	50%	1
30	100%	22	14%	Co	50%	1
31	100%	33	9%	Co	50%	1
32	100%	11	9%	Co	75%	1
33	100%	16	9%	Co	75%	1

34	100%	16	4.5%	Co	75%	1
35	100%	22	4.5%	Co	75%	1
36	100%	22	14%	Co	75%	1
37	100%	11	9%	Counter	25%	1
38	100%	16	9%	Counter	25%	1
39	100%	22	9%	Counter	25%	1
40	100%	33	9%	Counter	25%	1
41	100%	11	9%	Counter	50%	1
42	100%	11	9%	Counter	75%	1
43	100%	16	9%	Counter	75%	1
44	100%	22	9%	Counter	75%	1

Table D.2: Case studies: Configuration 3; Tightly-wound vortex analysis